11-2-2018 2:15 PM

The Electrochemical Study of Simulated Spent Nuclear Fuel (SIMFUEL) Corrosion under Permanent Disposal Conditions

Ziyan Zhu, *The University of Western Ontario*

Supervisor: Shoesmith, David W., *The University of Western Ontario*
Co-Supervisor: Noël, James J., *The University of Western Ontario*
A thesis submitted in partial fulfillment of the requirements for the Doctor of Philosophy degree in Chemistry

Abstract

The safety assessment of spent nuclear fuel under permanent disposal conditions requires examination of the corrosion of the spent fuel waste form (UO_2) inside a failed waste container. The objective of this research project was to develop a detailed mechanism of the UO_2 corrosion process when exposed to groundwater. The redox conditions within a failed container in a deep geologic repository will be complex. The oxidant, H_2O_2, produced by the α-radiolysis of groundwater, will be the main driving force for fuel corrosion. However, the efficiency of fuel dissolution will be determined by the competition between UO_2 corrosion and H_2O_2 decomposition to the much less reactive O_2. As a consequence, the corrosion of the UO_2 will be determined by the relative importance of 3 reactions, the anodic oxidation of UO_2 and H_2O_2 both of which will be coupled to the cathodic reduction of H_2O_2 under corrosion conditions.

The relative importance of the two anodic reactions was studied electrochemically on SIMFUEL (simulated spent fuel) in HCO_3^-/CO_3^{2-} solutions. It was found that both reactions were suppressed by the formation of U^{VI} surface films at low HCO_3^-/CO_3^{2-} concentrations. When the formation of these films was prevented at higher HCO_3^-/CO_3^{2-} concentrations both reactions occurred readily on the sublayer of $U^{IV}_{1-2x}U^{V}_{2x}O_{2+x}$. At high potentials H_2O_2 was directly oxidized on the noble metal (ε) particles in the SIMFUEL which were rendered catalytic by preoxidation (e.g., Pd to Pd^{II}).

The reduction of H_2O_2 has been studied on a range of UO_2 electrodes such as RE(III)-doped and non-stoichiometric (UO_{2+x}) electrodes and SIMFUEL. It was found that reduction on a UO_2 surface proceeded through a two-step reaction sequence, the chemical oxidation of U^{IV} to U^{V} followed by the electrochemical reduction of the surface back to U^{IV}. The rate of H_2O_2 reduction decreased in the order $UO_{2.002}$ ~ $UO_{2.5}$ ~ SIMFUEL > Gd-UO_2 ~ Dy-UO_2 > $UO_{2.1}$. The

low reduction rate on RE(III)-doped electrodes was attributed to the stabilized UO_2 matrix by the formation of RE(III)-O_V clusters. The reduction rate may be catalyzed by ε-particles in SIMFUEL electrodes.

The coupling of these anodic and cathodic reactions was also studied under corrosion conditions. H_2O_2 was found to decompose to O_2 and H_2O both homogeneously and heterogeneously accompanied by a minimal amount of UO_2 corrosion. Homogeneous decomposition proceeded via a peroxycarbonate (CO_4^{2-}) intermediate while heterogeneous decomposition was catalyzed by the reversible $U^{IV} \rightleftharpoons U^{V}$ redox transformation in a thin $U^{IV}_{1-2x}U^{V}_{2x}O_{2+x}$ surface layer. The rate of the heterogeneous decomposition reaction depended on whether U^{VI} surface species were allowed to accumulate on the surface blocking access of H_2O_2 to the catalytic surface layer.

A series of computational analyses were performed using a model previously developed to describe fuel corrosion inside a failed container. The influences on fuel corrosion of fuel defect geometry, ε-particle distribution and H_2O_2 decomposition on UO_2 corrosion rate were investigated. The defect geometries, in the form of pores and fractures, was found to exert only a minor influence on the rate of fuel corrosion rate. Similarly, changes in the number of ε-particles exerted only a minimal effect. Decomposition of H_2O_2 caused a significant decrease in fuel corrosion rate since the slowly reacting O_2 was dominantly lost by transport out of the defects.

Keywords

Uranium Dioxide, Corrosion, Electrochemistry, Fission Products, Hydrogen Peroxide, Decomposition, SIMFUEL.

Co-Authorship Statement

Chapter 3 contains the contribution of Dr. Linda Wu, who developed the dissolution experiments at earlier studies.

Chapter 5 contains the contribution from Malin Ly who assisted me with experiments and data processing.

Chapter 6 contains contribution from Dr. Nazhen Liu and Dr. Zack Qin, who developed the previous version of COMSOL model, Dr. Nazhen Liu provided Figure 6.6 and Figure 6.7.

This is dedicated to my parents

Huanyu Zhu
朱焕育
Yufen Zhang
张玉芬

Acknowledgement

First and foremost, I would like to thank my supervisors Dr. David Shoesmith and Dr. Jamie Noël. Words can't describe how much I am grateful to Dave. Over the past 4 years, he has always been there for me, his patience, encouragement, and guidance made this thesis possible. His work ethic and positive attitude will always inspire me to be a better self. I am so grateful to him for reading and commenting on countless revisions of this thesis. I would like to thank Jamie for always taking time out of his busy schedule to discuss electrochemistry and corrosion science. He was not only a mentor and a supervisor, but also a good friend who always brought me peonies at office, and gave me many gardening tips.

I would like to thank Dr. Dimitrij Zagidulin for being there for me whenever I encountered technical problems and helping me get back on my feet and Dr. Nazhen Liu and Dr. Zack Qin for the help with developing COMSOL model and providing guidance when I was lost. I want to thank all the Shoesmith and Noël group members for creating such an enjoyable working atmosphere and providing valuable feedback for my work. I will always cherish our friendship. I am also grateful to Dr. Jiju Joseph and the Wren group with providing extremely helpful expertise to all the UV-vis experiments performed in the Wren lab.

I would like to thank Dr. Mark Biesinger, Mr. Brad Kobe, Dr. Heng-Yong Nie, Dr. Sridhar Ramamurthy, and Ms. Mary Jane Walzak from Surface Science Western for their expertise and assistance with surface analyses.

I am grateful to the Nuclear Waste Management Organization (NWMO, Toronto) and the Natural Sciences and Engineering Research Council (NSERC, Ottawa) who funded this research under an Industrial Research Chair agreement with the University of Western Ontario.

My deepest gratitude goes to my family. My parents for the endless love and support, especially my mom for always being there for me, having long Skype calls with me disregarding the 12-hour time difference.

My most special thanks go to my husband, Landon Hang, for supporting me unconditionally, and for being my best friend and my life partner, I couldn't have done this without him.

"It was the best of times,

it was the worst times.

it was the age of wisdom,

it was the age of foolishness"

-Charles Dickens

Table of Contents

List of Figures

List of Tables

List of Symbols and Acronyms

at.%	Atomic percent
AECL	Atomic Energy Canada Limited
BE	Binding Energy
b	Radiation zone thickness
CSV	Cathodic stripping voltammetry
CV	Cyclic voltammogram
D_i	Diffusion coefficient for species i
E	Potential
e^-	Electron
E_{CORR}	Corrosion potential
$[Fe^{2+}]_{bulk}$	Bulk concentration of Fe^{2+}
F	Faraday constant
g_i	g-value for species i
δ	Diffusion layer thickness
$[H_2]_{bulk}$	Bulk concentration of H_2
$[H_2]_{crit}$	Critical $[H_2]$ that can completely suppress fuel corrosion
ICP-AES	Inductively coupled plasma atomic emission spectroscopy
ICP-MS	Inductively coupled plasma atomic mass spectroscopy
j	Current density
k	Reaction rate constant
K_{eq}	Equilibrium constant
L	Diffusion boundary used in model calculation

LPR	Linear polarization resistance
NWMO	Nuclear Waste Management Organization
Q_A	Anodic charge
Q_c	Cathodic charge
Q	Electric charge
R	Resistance
R_P	Polarization resistance
RE	Rare earth fission products
WE	Work electrode
SCE	Saturated calomel electrode
SEM	Scanning electron microscopy
SIMFUEL	Simulated nuclear fuel
s_0	Noble metal particle coverage slope
T	Temperature
t	Time
XPS	X-ray photoelectron spectroscopy
ε-particles	Noble metal fission product
ρ	Density
ω	Angular frequency
wt.%	Weight percent
η	Overpotential
ε	Numerical coefficient
ν	Kinematic viscosity

Chapter 1

1 Introduction

1.1 Project Motivation

Nuclear energy represents the world's largest energy source for electricity with minor emissions and has a very low environmental impact. Despite these advantages, the issue of spent fuel disposal is very complex, and has been the focus of much international research for decades. The primary high level waste form generated by nuclear energy is the spent fuel. As of June 30, 2016, Canada had ~2.7 million used fuel bundles, sufficient to fill seven hockey rinks, from the ice surface to the top of the boards.[1] Due to the possibility of the release to the environment of long-lived radionuclides, the disposal of nuclear fuel must be carefully managed, and many countries are considering deep geological repositories (DGR) for permanent disposal.

Canada's long-term plan for used nuclear fuel is the Adaptive Phased Management (APM) process developed by the Nuclear Waste Management Organization (NWMO) in 2005 and approved by the Government of Canada in 2007.[2] This approach involves interim storage until final disposal in the DGR. Safe disposal in a DGR is based on a multi-barrier approach comprised of the used fuel bundles, a carbon steel vessel with a layer of copper, a clay buffer, and a deep stable geological environment, as illustrated in Figure 1.1.

While the prospects for the development of long-lived nuclear waste containers are very promising, it is judicious to assess the consequences of their failure which could result in

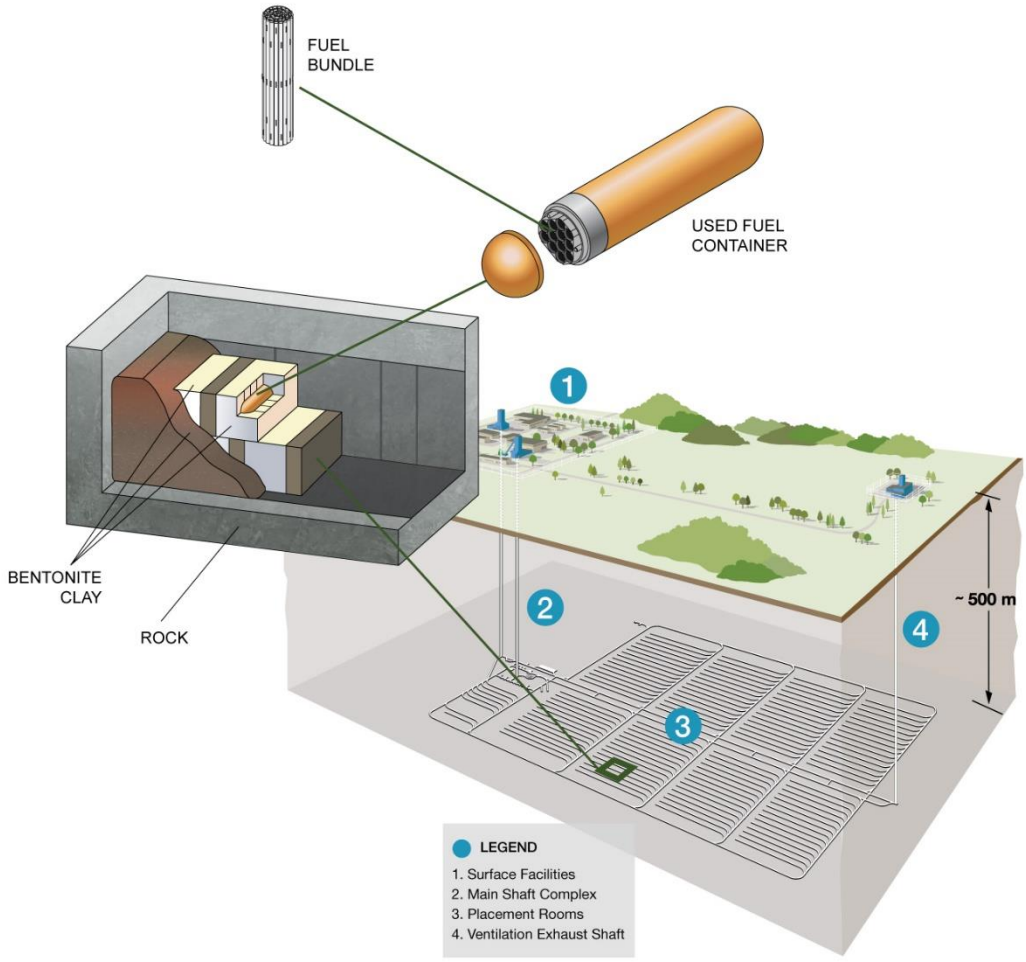

Figure 1.1: Illustration of the deep geological repository concept showing the fuel bundle, metallic canister, emplacement room, and the tunnel layout.[2]

exposure of the spent fuel to ground water and potentially to oxidizing conditions at the fuel surface. This would lead to corrosion of the fuel.[3] The development of performance assessment models for deep geological disposal requires a fundamental understanding of the process of fuel corrosion which could lead to the release of harmful radionuclides to the geosphere from a failed container.[4]

1.2 Project Overview

As the majority of radionuclides produced during in-reactor irradiation are located in the fuel matrix, their release rate to the environment will be controlled by the UO_2 corrosion rate. The solubility of UO_2 is extremely limited under reducing conditions (~10^{-15} mol.L^{-1}),[5, 6] but increases by orders of magnitude under oxidizing conditions, making the dissolution rate of spent fuel very sensitive to redox conditions, Figure 1.2.

At repository depths (~500 m underground), the concentration of oxidants is expected to be extremely low. Any O_2 introduced during the repository construction and trapped on sealing will be consumed by corrosion of the Cu container and mineral/biological reactions in the surrounding clays.[7, 8] However, the radiation fields associated with the decay of fission products and actinides will remain significant for up to 10^5 years making water radiolysis a primary source of oxidants,[9-11] Figure 1.3. While the groundwater will be anoxic when first

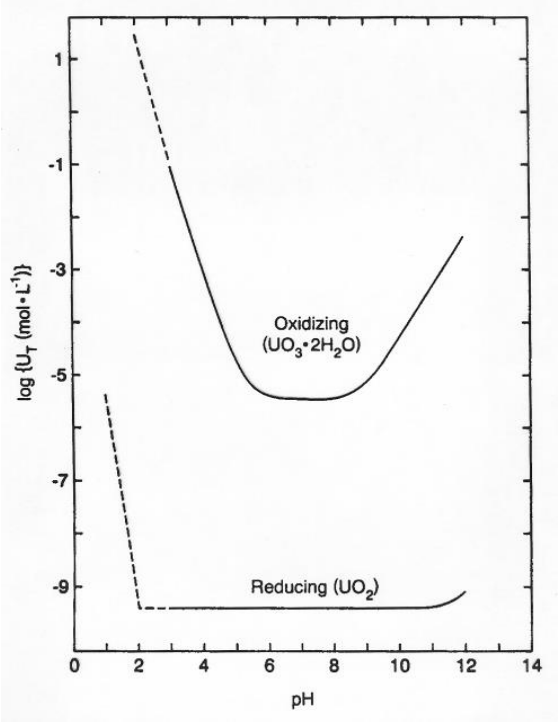

Figure 1.2: Solubility of uranium dioxide (UO_2) and schoepite ($UO_3 \cdot 2H_2O$) as a function of pH at 25°. U_T indicates the total uranium in the solution.[5]

contacting the fuel, the radiolysis of water can produce a number of reactive species with the dominant molecular products being H_2O_2, H_2, and O_2.[11, 12] H_2O_2 has been shown to be the primary radiolytic oxidant capable of driving fuel corrosion leading to the formation of the soluble U^{VI} state (as UO_2^{2+}).[4] The rate of production of radiolytic species is determined by the dose rate of the spent fuel. As the radiation fields decay, conditions will become less oxidizing, and the corrosion rate will correspondingly decrease. The corrosion rate will be influenced by the formation of corrosion product deposits, which can partially block the fuel corrosion process. However, groundwater ions, in particular HCO_3^-/CO_3^{2-}, can form uranyl complexes, which increase the solubility and prevent corrosion products deposition thereby accelerating the corrosion process.

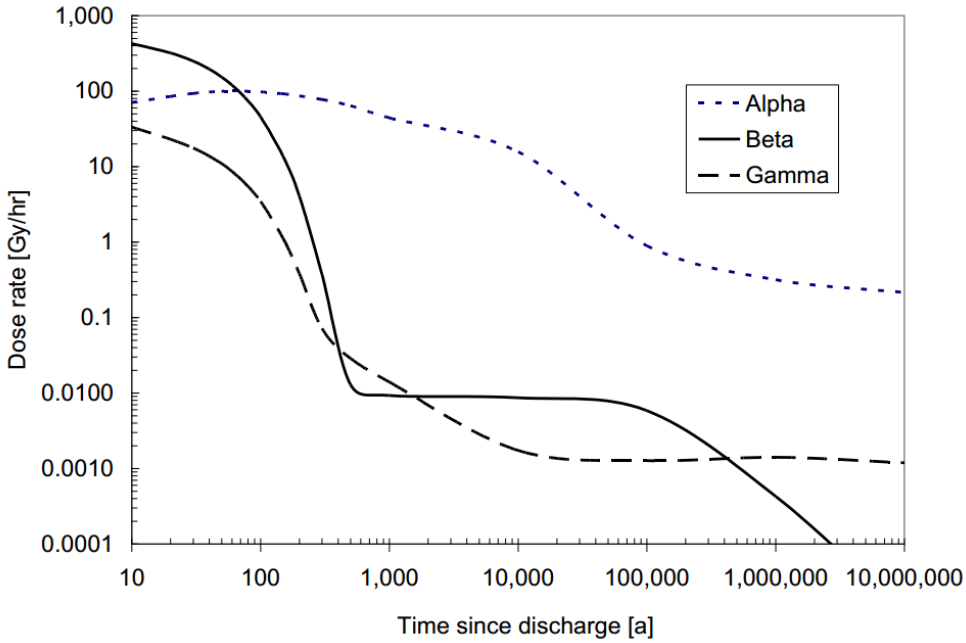

Figure 1.3: Alpha, beta, and gamma radiation dose rates calculated with respect to time for a layer of water in contact with a CANDU fuel bundle with a burn up of 220 MWh/kgU. The details of alpha, beta and gamma radiation dose rate calculations was described in reference [11].

1.3 Basic Properties of UO_2

1.3.1 Structural Properties

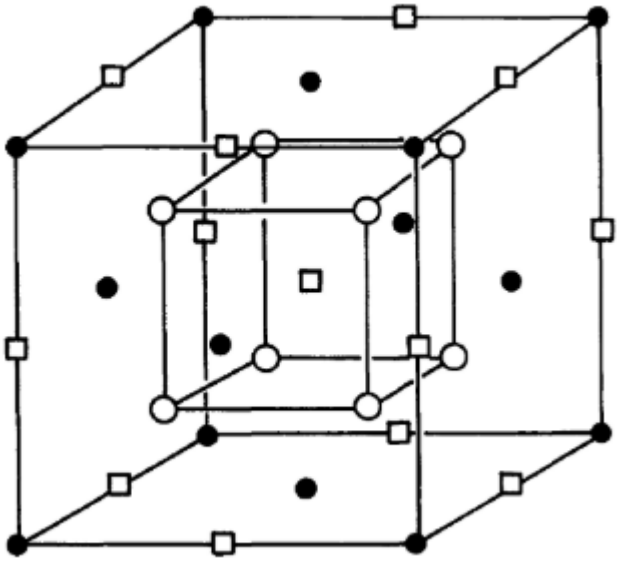

Figure 1.4: Fluorite crystal lattice structure of UO_2. (●) U atoms; (○) O atoms; (□) empty lattice interstitial sites.

Crystalline UO_2 adopts the fluorite lattice structure which can be described as a simple cubic O^{2-} sublattice within a face centered cubic (fcc) lattice of U^{4+} ions, Figure 1.4.[14, 15] Each U atom is coordinated by eight neighboring O atoms, while the O atoms are surrounded by four U atoms. The unit cell parameter is a = 5.470 Å, with ionic radii of $r_{U^{4+}} = 0.97$Å and $r_{O^{2-}} = 1.40$ Å.[16, 17] The oxidation of UO_2 involves the injection of O^{2-} ions with the appropriate number of U^{4+} ions being oxidized to higher oxidation states (U^{V}/U^{VI}) in order to maintain charge neutrality.[14] An important feature of the fluorite lattice structure is the large and cubically coordinated interstitial sites which can accommodate additional O atoms up to a composition near $UO_{2.33}$, with only a small distortion of the lattice structure.

X-ray photoelectron spectroscopy and neutron diffraction studies have shown that, from $UO_{2.13}$ to $UO_{2.25}$, the incorporation of additional O atoms leads to a significant structural rearrangement. The displacement of interstitial oxygen atoms in the <110> direction leads to a movement of oxygen atoms from normal lattice sites in the <111> directions without affecting the U sublattice.[14, 18-22] The resulting defect structure is called a Willis cluster which contains two O' atoms, two O vacancies and two O" atoms, and is referred to as a 2:2:2 cluster, Figure 1.5. $UO_{2.33}$ has a tetragonally distorted fluorite structure and is the end of fluorite lattice structure range, with further oxidation causing a transformation to a more layered-like configuration with a significantly lower density.[18] In the composition range from U_2O_5 to

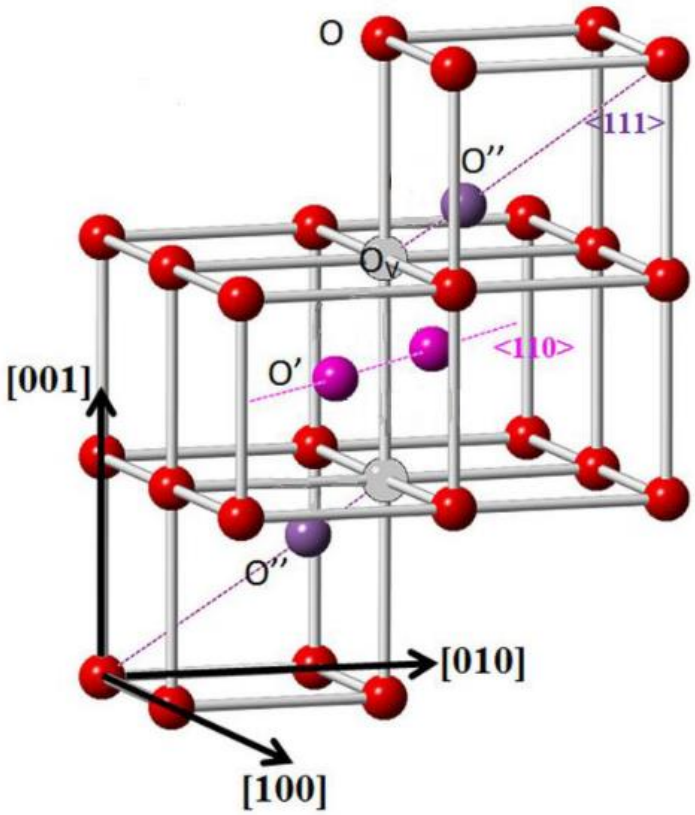

Figure 1.5: Illustration of 2:2:2 cluster in UO_{2+x}.[19]

U_3O_8, 12 distinct phases have been reported. All these intermediate uranium oxides are electrically conductive, whereas the end member, UO_3, is an insulator.[23]

1.3.2 Electrical Properties

Electrochemical studies of UO_2 require the solid semiconductor to conduct electric current. When slightly non-stoichiometric, UO_2 is a p-type semiconductor, Figure 1.6, the rate-determining step for oxidation being charge transfer to form the ionic species (UO_2^{2+}), which can subsequently transfer to solution.[24] Thus, the solid-state conductivity is the major factor in determining the kinetics of dissolution.

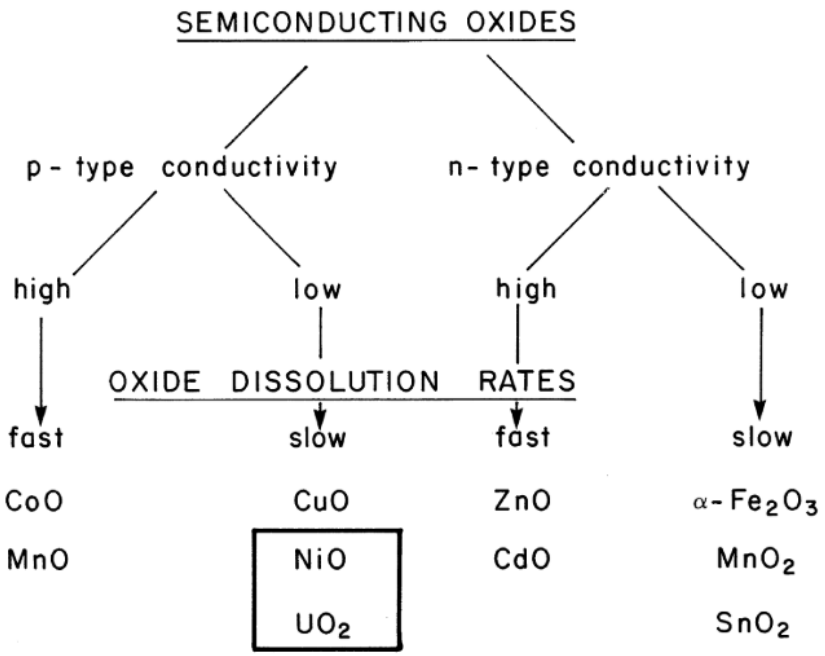

Figure 1.6: Categorization of oxides according to their conductivity type and dissolution behavior.[23]

Stoichiometric UO_2 is described as a Mott-Hubbard insulator,[25-27] which is characterized by a partially filled cationic shell with a sufficient energy bandwidth that the movement of electrons in the 5f level is restricted by Coulomb interactions.[28] Electronic

conductivity can only be activated when the normally localized electrons move to the next cation in a series of small thermally assisted jumps, a process known as small polaron hoping.[29-31]

Figure 1.7 shows a schematic UO_2 energy-level diagram derived from spectroscopic and electrochemical data.[10] The U 5f band contains two electrons per U atom for stoichiometric UO_2 and is located between the filled valence band and the empty conduction band. The valence band is filled with electrons with mainly O 2p character, while the conduction band contains overlapping of U 7s, 6d and 5f states. For perfectly stoichiometric UO_2, electronic conductivity requires the promotion of electrons from the U 5f level to the conduction band. The activation energy of ~1.1eV required makes this process unlikely to occur at room temperature.[29] UO_2 fuel is slightly oxidized during the fabrication procedure, with excess oxygen atoms present as O^{2-} at interstitial sites, and an appropriate number of U^{IV} oxidized to U^{V}/U^{VI}. This process creates holes in the narrow U 5f band, which migrate by a polaron hopping process with a low activation energy ~0.2 eV.[32-34]

Replacing a small fraction of U^{IV} ions in UO_2 with lower-valent species, such as rare earth (RE^{III}) elements, will lead to the formation of U^{V} to maintain charge neutrality. This also creates holes in the narrow U 5f band despite the absence of interstitial O^{2-} ions, leading to an increased conductivity.[35, 36] Used fuel contains significant amounts of fission products, and its conductivity should be enhanced compared to unirradiated fuel.

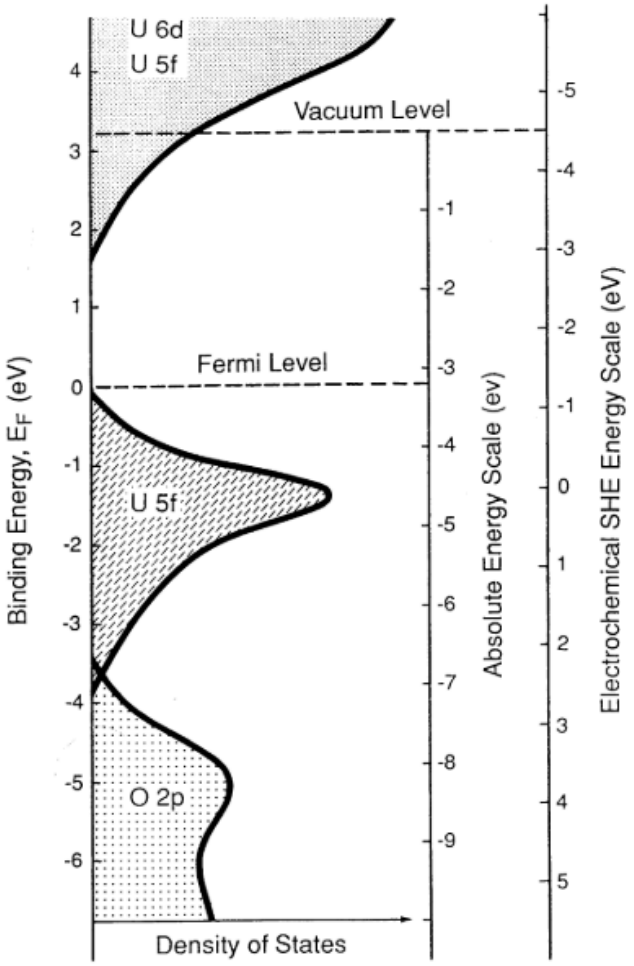

Figure 1.7: Illustration of UO_2 energy levels and band structure, derived from spectroscopic and electrochemical data.[9]

1.3.3 Thermodynamic Properties

Figure 1.8 shows a potential (E)-pH diagram for the U-H_2O system demonstrating the stable phases and solution soluble species.[37] For $6 \leq pH \leq 9$, the anticipated range under disposal conditions, UO_2 is stable and extremely insoluble at non-oxidizing potentials. as shown in Figure 1.2. At higher potentials dissolved UO_2^{2+} becomes the dominant species, and can be extensively hydrolyzed in aqueous solution yielding a range of species, $(UO_2)_x(OH)_y^{2x-y}$. When complexing ions, such as carbonate and phosphate are present, uranyl complexes are formed

over a wide pH range. At low pH (<1), the unoxidized U^{4+} can be complexed by sulfate and fluoride ions leading to increased solubility.[38, 39] The overall impact of groundwater ions on U^{IV} and U^{VI} solubility is highly dependent on the nature of the complexing anion and the pH range.

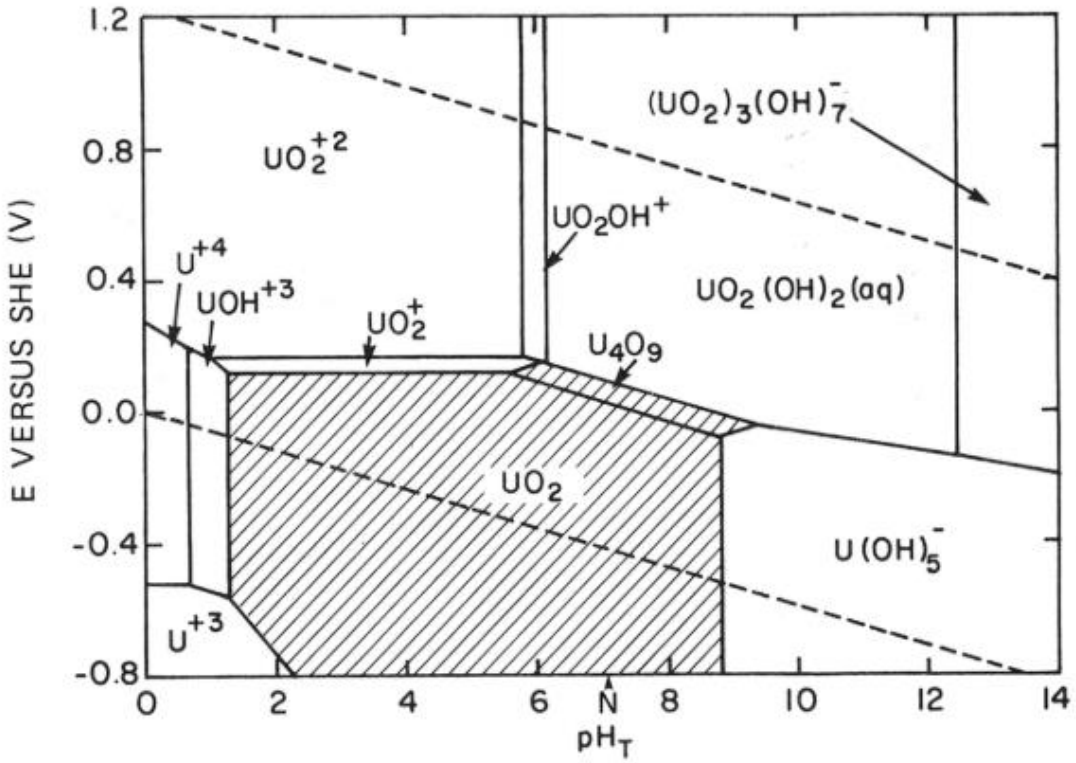

Figure 1.8: Potential-pH diagram for the U/H_2O system at 25ºC. The dissolved species concentration is 10^{-9} M.[37]

1.3.4 Electrochemical Properties

Figure 1.9 shows a Cyclic Voltammogram (CV) recorded on a UO_2 electrode in a slightly alkaline solution.[4] Various oxidation stages are indicated in the current response observed. On the forward scan, Figure 1.9, peak 1 arises in the potential range -0.8 to -0.4 V (vs. SCE). In this range, the bulk UO_2 is thermodynamically stable and oxidation should not occur. It has been proposed that oxidation in this region can be attributed to the presence of non-stoichiometry in the UO_2 surface, possibly within grain boundaries.[40] At low potential, the oxidation of UO_2

appears to be reversible, since 100% of the oxidation charge can be recovered when the potential scan is reversed for $E \leq -0.4$ V.

Peak II is attributed to the oxidation of the surface of the UO_2 matrix and involves the corporation of O^- ions into the UO_2 matrix interstitial sites, to produce a $U^{IV}_{(1-2x)}U^{V}_{2x}O_{2+x}$ layer, Figure 1.4. At $E > -0.4$ V, the oxidation of UO_2 becomes irreversible, with a stoichiometry $\geq UO_{2.25}$ achieved around $E = -0.1$ V. Further oxidation causes tetragonal distortions leading to dissolution as uranyl ions (III).[41] On the reverse scan, peak IV is sometimes observed around

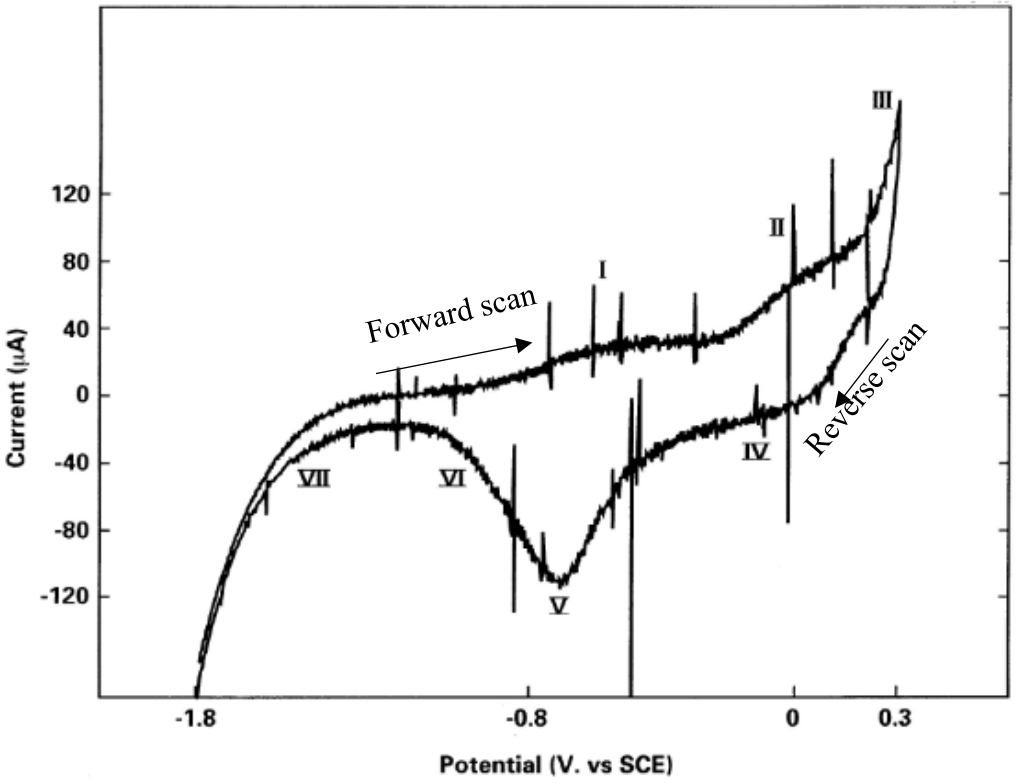

Figure 1.9: Cyclic voltammogram recorded on a rotating UO_2 disc electrode at a scan rate of 10 mV s^{-1} using IR compensation, rotation rate = 16.7 Hz, in an electrolyte solution of 0.1 mol L^{-1} $NaClO_4$ (pH = 9.5). The Roman numbers represents the various stages of oxidation or reduction, and the two arrows indicate the scan direction.[4]

~0.1 V, which is associated with the reduction of absorbed surface species formed at anodic potentials. Peak V is attributed to the reduction of the oxidized surface layer formed on the forward scan. The significant cathodic current increase in the potential region VII is caused by the reduction of H_2O.

Based on a wide range of electrochemical and surface analytical experiments, the behavior of UO_2 as a function of corrosion potential (E_{CORR}) has been determined and is summarized in Figure 1.10.[42, 43] The potential ranges for the important electrochemical processes occurring on UO_2, is shown in Figure 1.9. The anticipated potential range inside a failed container, calculated using a Mixed Potential Model,[44] is indicated by the arrow A. When E < -0.4 V (vs. SCE), UO_2 exists in its stoichiometric form, and the chemical dissolution rate is extremely low due to the low UO_2 solubility. The vertical dash line in Figure 1.10 indicates the thermodynamic threshold, above which UO_2 oxidation becomes possible, and the U^V content of the surface

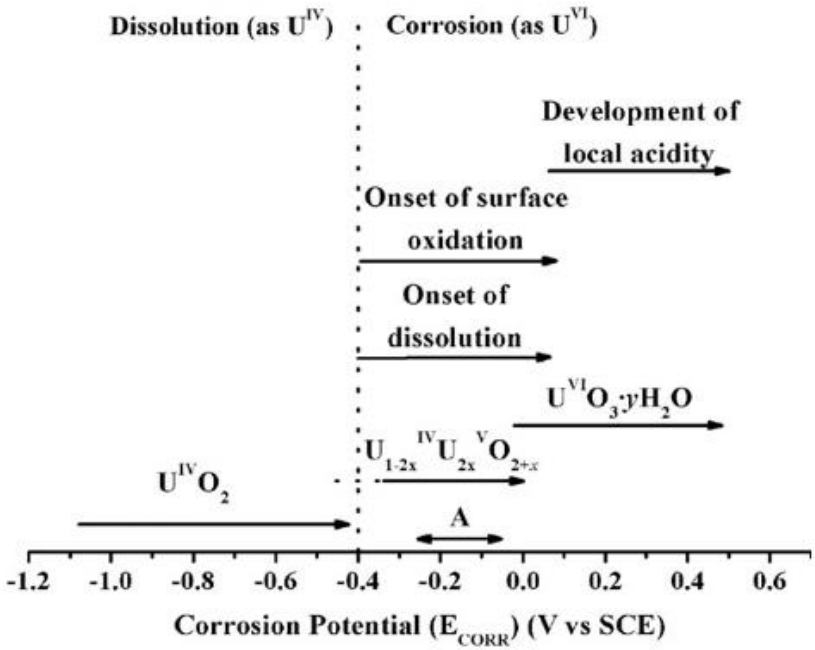

Figure 1.10: Composition and corrosion behavior of UO_2 as a function of UO_2 corrosion potential (E_{CORR}), measured in neutral to slightly alkaline solutions.[42]

increases as measured by X-ray photoelectron spectroscopy and confirmed by previous studies.[4, 45]

1.4 Spent Fuel

CANDU fuel pellets are fabricated by sintering pressed compacts of fine-grained unenriched UO_2 powder (^{235}U = 0.71%) at ~ 1700ºC under a reducing atmosphere produced by a constant flow of H_2 gas. A typical fuel bundle is shown in Figure 1.11.[46] During in-reactor irradiation the fuel undergoes a number of microstructural and compositional changes. The individual grains grow, and a wide range of fission products are produced distributed within the UO_2 fuel matrix. Volatile fission products can diffuse to the tube/UO_2 interface and into grain boundaries to form gas bubbles, as illustrated in Figure 1.12.[47-49]

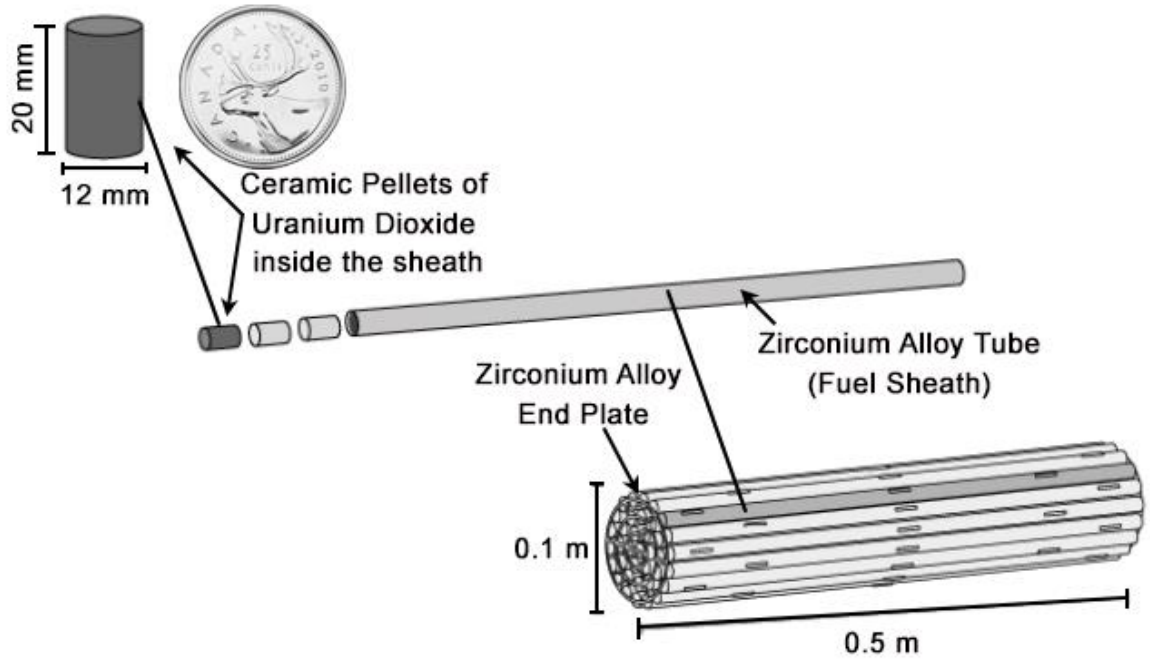

Figure 1.11: Typical CANDU fuel bundle. (Image adapted from reference [46])

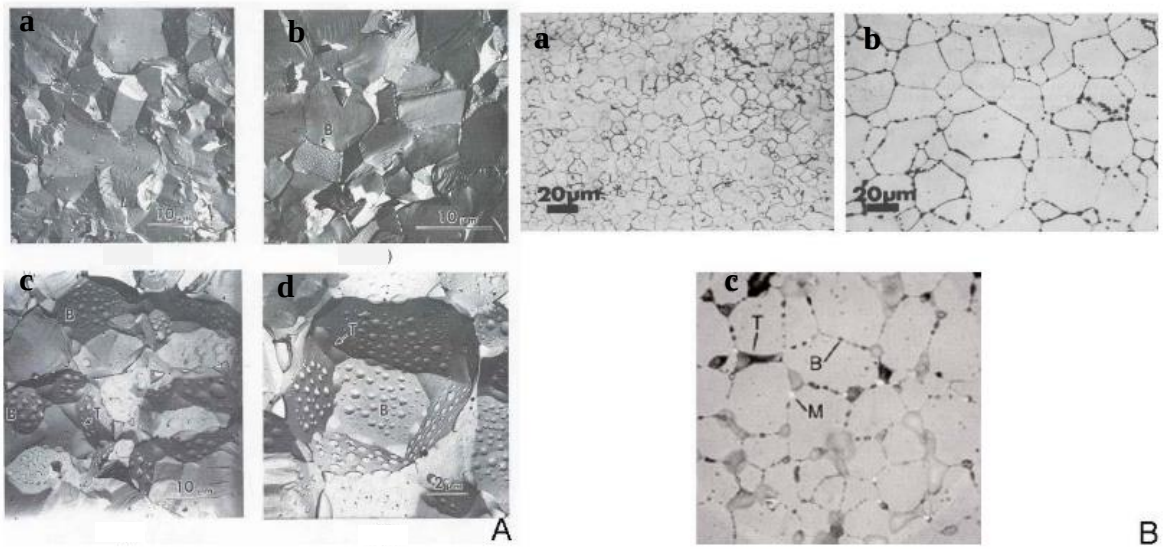

Figure 1.12: (A) Scanning electron microscope images of UO_2 fuel, (a) typical structure of unirradiated UO_2; (b) irradiated at low power (< 45kW/m); (c) and (d) magnified view of irradiated high power fuel (> 50 kW/m), showing the growth of fission gas bubbles. (B) Optical images of polished and etched UO_2 fuel, (a) unirradiated UO_2 with sintering porosity; (b) irradiated UO_2 at low burnup (20 MWh/kgU at 52 kW/m), noted the increase of UO_2 grain size; (c) irradiated UO_2 at high burnup (770 MWh/kgU at 52 kW/m), note the development of tunnels (T) and gas bubbles (B).[47-49]

On removal of fuel from the reactor, the radioactivity level and the fuel composition are determined by the extent of burnup (a measure of the energy released per unit mass of the initial fuel, measured in gigawatt days/metric ton of heavy metal (GWd/tHM)).[49] Spent fuel contains > 95% UO_2, the reminder being the radioactive fission products and actinides produced in reactor. More than 90% of the fission products and actinides formed remain close to the location of their formation in the UO_2 matrix, while some are redistributed as a consequence of the high temperatures. The species formed can be categorized as follows based on their chemical

states. Figure 1.13 summarizes the distribution of fission products and actinides in spent fuel after in-reactor irradiation.[50-52]

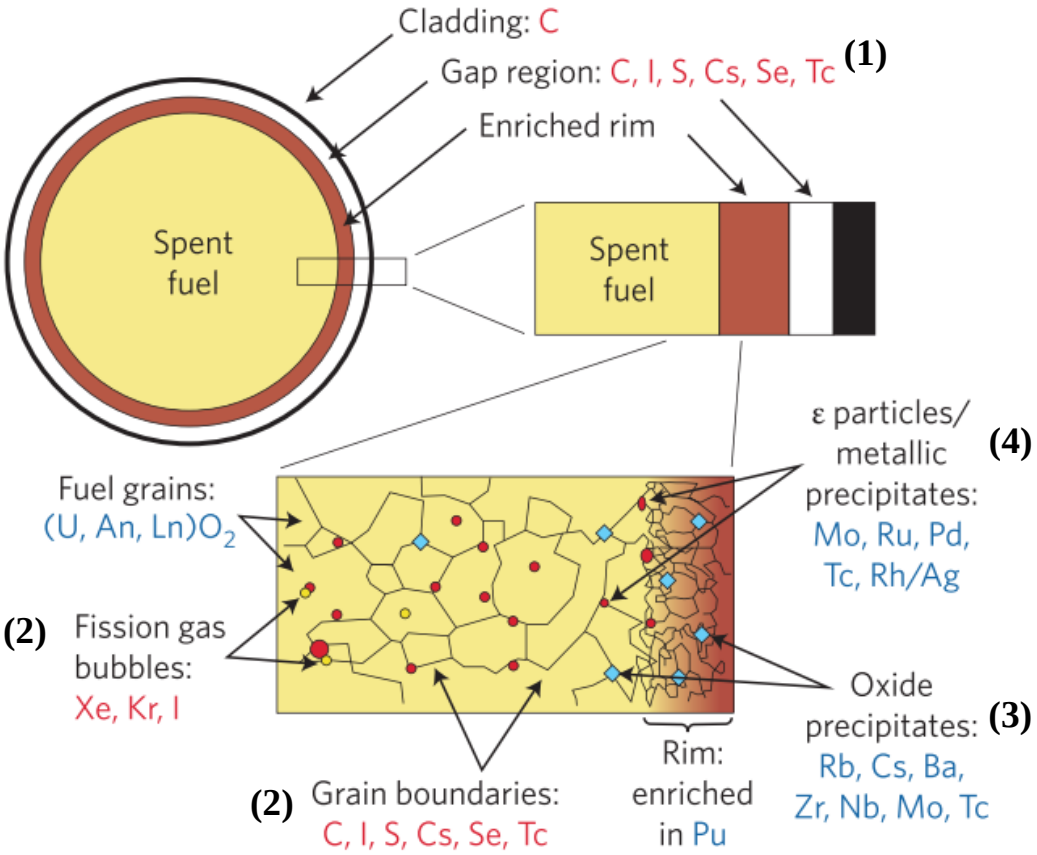

Figure 1.13: Illustration of spent fuel microstructure and the distribution of fission products and actinides after in-reactor irradiation. Image adapted from references [50] and [51].

(1) The gap inventory, such as C, I, Cs, comprising volatile fission products which migrate during reactor operation to the fuel/sheath gap due to their relatively high diffusion coefficients.

(2) Fission products that are volatile which can migrate to grain boundaries in the fuel at high in-reactor temperatures, e.g., Xe, Kr.

(3) Fission products that are stable as oxides, but incompatible with UO_2 matrix (Rb, Cs, Ba, Zn, Mo, Te, Sr, Nb), can segregate into secondary phases. They tend to have the general oxide composition of ABO_3, and to adopt a cubic perovskite structure, with Ba, Sr and Cs in the A sites, Zn, Mo, U and rare earth elements in the B sites.

(4) Fission products that are not stable as oxides (e.g., Mo, Ru, Pd) can segregate to grain boundaries and form intermetallic particles (ε-particles).

(5) Fission products that remain in the fuel matrix as substitutional ions such as actinides (Np, Pu, Am, Cm) and rare earths (La, Ce, Pr, Nd, Pm, Sm, Eu, Gd, Y).

The radionuclides can also be grouped based on their anticipated release mechanism under disposal conditions.

(1) The gap inventory (1 in Figure 1.13) would be expected to be soluble and released on contact with groundwater and is termed the instant release fraction.

(2) The grain boundary inventory (2, in Figure 1.13) will depend on the chemical and physical properties of individual grain boundaries and could be retained for protracted period of exposure to groundwater. However, they are commonly assumed to be quickly released as part of the instant release fraction.

(3) The release of radionuclides retained in fuel matrix would be controlled by the corrosion/dissolution of the fuel.

On discharge from the reactor, the fuel is highly radioactive, but the activity level decreases very rapidly. For CANDU fuel, the overall radioactivity decreases to ~1% of the initial radioactivity in 10 years.[49] The β/γ radiation will decay to an insignificant level within a few hundred years. Beyond this period the radioactivity would be dominated by α-radiation, Fig.1.4.[11] If it is assumed that the container will protect the spent fuel from contact with

groundwater over the time when β/γ irradiation are still significant, α-radiation would be the key source of radiolytic oxidants inside a failed waste container.

1.5 UO_2 Surface Reactions

1.5.1 Kinetics of H_2O_2 Reactions

If container failure occurred while γ/β radiation fields were significant, Figure 1.3, fuel corrosion would be driven by both radical and molecular oxidants.[4] However, while radical oxidants (e.g., $OH^{\bullet}$) are highly reactive,[53] their steady-state concentrations will be low and fuel corrosion will be predominantly driven by molecular oxidants, such as O_2 and H_2O_2 which will be present at substantially larger concentration.[53, 54] If container failure is delayed until only α-radiolysis is the significant source of oxidants then H_2O_2 will be the dominant oxidant. The coupling of H_2O_2 reduction and UO_2 oxidation serves as the main driving force for corrosion.

$$H_2O_2 + 2e^- \rightarrow 2OH^- \qquad \textbf{1.1}$$

$$UO_2 \rightarrow UO_2^{2+} + 2e^- \qquad \textbf{1.2}$$

Besides reaction 1.1, H_2O_2 can also undergo reduction, reaction 1.3, and the coupling between reaction 1.1 and 1.3 results in H_2O_2 decomposition to produce H_2O and the alternative oxidant, O_2, reaction 1.4.

$$H_2O_2 \rightarrow O_2 + 2H^+ + 2e^- \quad \textbf{1.3}$$

$$2H_2O_2 \rightarrow O_2 + H_2O \quad \textbf{1.4}$$

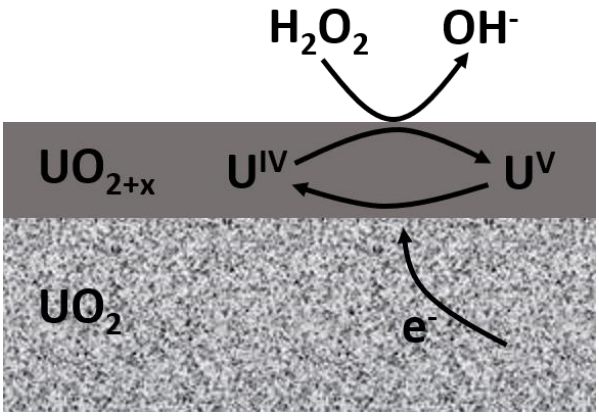

Figure 1.14: Illustration showing the electrochemical reduction of H_2O_2.

The electrochemical reduction of H_2O_2 has been found to be markedly faster (200 times) than that of O_2, and has been extensively studied on UO_2.[4, 55, 56] This higher rate was attributed to the ability of H_2O_2 to create U^{IV}-U^V donor-acceptor states, Figure 1.14, rather than rely on their pre-existence as was the case for the electrochemical reduction of O_2[4, 57]

Under cathodic polarization, H_2O_2 reduction involves chemical oxidation of the UO_2 surface i.e., the creation of U^{IV}-U^V sites[58]

$$2U^{IV} + H_2O_2 \rightarrow 2U^V + 2OH^- \quad \textbf{1.5}$$

followed by their subsequent electrochemical reduction,

$$2U^{V} + 2e \rightarrow 2U^{IV} \qquad \textbf{1.6}$$

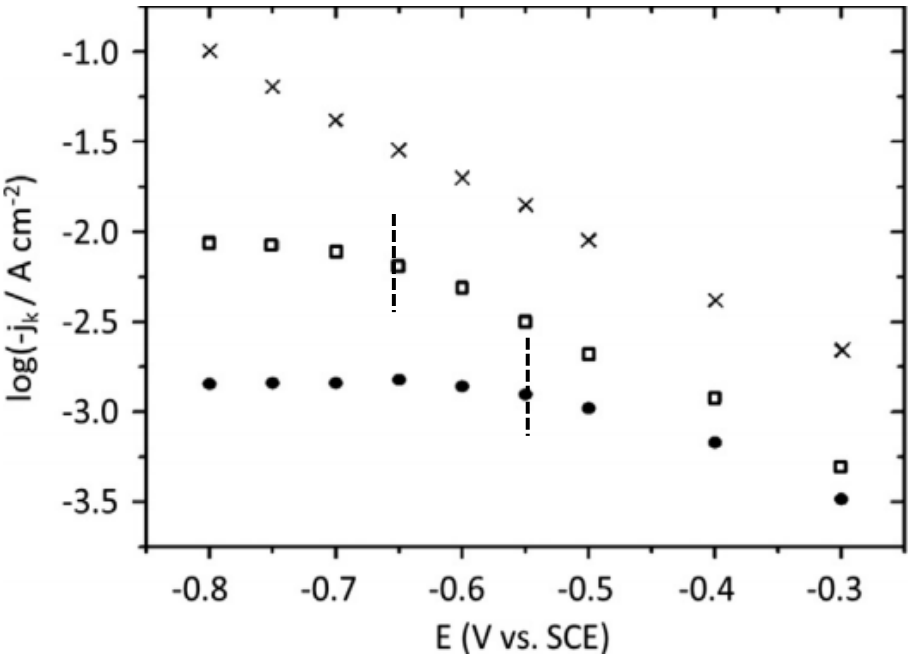

Figure 1.15: Tafel plots (transport-corrected) recorded on SIMFUEL (no noble metal particles) in 0.1 mol.L^{-1} NaCl (pH = 9.7) containing various [H_2O_2]; (full circle) 1.3 × 10^{-4} mol.L^{-1}; (open square) 4.0 × 10^{-4} mol.L^{-1}; (x) 4.3 × 10^{-3} mol.L^{-1}. The dash lines indicate the transition from rate control by reaction 1.6 to rate control by reaction 1.5.[59]

This reaction sequence led to large Tafel slopes (-200 to -400 mV^{-1}) and fractional reaction orders as a consequence of the potential dependent surface coverage by active sites. Since reaction 1.5 was dependent on [H_2O_2] and reaction 1.6 on applied potential, the rate controlling reaction changed from electrochemical control at high [H_2O_2], when the initial chemical reaction was fast, to chemical control when the [H_2O_2] was lower and the applied potential sufficiently negative, as indicated in Figure 1.15.[58] The vertical dashed lines indicate the transition between these two rate-controlling steps.

H_2O_2 reduction could be catalyzed on both RE^{III}-doped surfaces and on noble metal (ε) particles. However, electrochemical studies detected no discernible influence of RE^{III} doping,

and only a minor influence of ε-particles.[58] Thus, at the low burnups achieved in spent CANDU fuel (~1.5 at.%), no significant influence of ε-particles on H_2O_2 reduction in support of UO_2 corrosion would be anticipated. This is thought to be a direct consequence of the ability of H_2O_2 to create U^{IV}-U^{V} states making the kinetics of reduction on the UO_2 surface and on ε-particles only marginally different.

Wu et. al. studied H_2O_2 oxidation on a UO_2 surface at applied anodic potentials in solutions with a wide range of pH.[59-61] It was found that the oxidation current of H_2O_2 is independent of $[H_2O_2]$ in the absence of CO_3^{2-}/HCO_3^-, when the deposition of corrosion product ($UO_3 \cdot yH_2O$) would be expected. This indicates the H_2O_2 oxidation rate on UO_2 surface is determined by surface composition.[61] In alkaline solution (pH = 11), H_2O_2 oxidation increases with $[H_2O_2]$ even without the presence CO_3^{2-}/HCO_3^-. At a sufficiently high potential, the anodic current increases significantly which was attributed to H_2O_2 oxidation on the ε-particles in the SIMFUEL.[59]

Under corrosion conditions, the behaviour of H_2O_2 is complicated since it can both decompose as well as drive fuel corrosion. At sufficiently high $[H_2O_2]$ in neutral to alkaline conditions, surface oxidation was found to be rapid with the potentially catalytic $U^{IV}_{1-2x}U^{V}_{2x}O_{2+x}$ surface layer becoming covered in an insulating $U^{VI}O_{3.y}H_2O$ layer. When this insulating layer was present both UO_2 corrosion and H_2O_2 decomposition were limited.

Attempts have been made to elucidate the mechanism of these surface reactions at the corrosion potential (E_{CORR}).[4, 62, 63] Figure 1.16 shows the variation of E_{CORR} as a function of $[H_2O_2]$ in a solution not containing HCO_3^-/CO_3^{2-}. At low $[H_2O_2]$, E_{CORR} increases with $[H_2O_2]$, but becomes independent of $[H_2O_2]$ over the intermediate $[H_2O_2]$ range, 10^{-4} to 5×10^{-4} mol.L^{-1}. This suggests the dominant surface reaction is H_2O_2 decomposition rather than H_2O_2 driven UO_2 corrosion. For $[H_2O_2] > 5 \times 10^{-3}$ mol.L^{-1}, E_{CORR} increases linearly with $[H_2O_2]$, suggesting that the rate of fuel corrosion increases relative to the rate of decomposition.

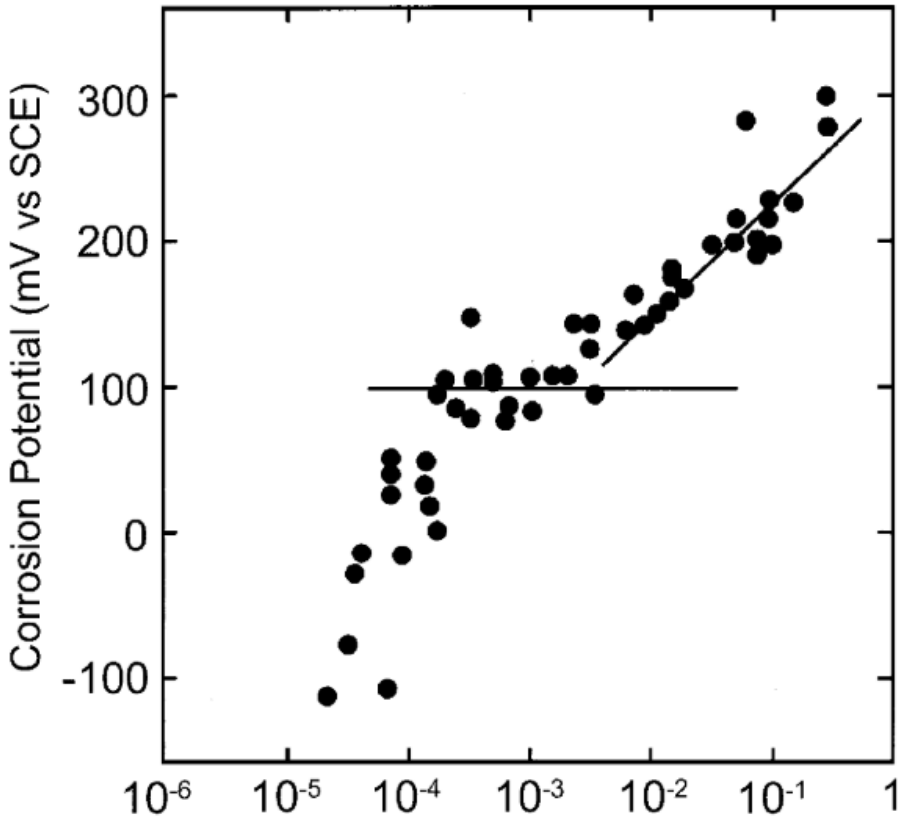

Figure 1.16: Corrosion potential (E_{CORR}) for UO_2 as a function of $[H_2O_2]$ in a 0.1 mol.L^{-1} $NaClO_4$, pH = 9.5.[63]

1.5.2 H_2O_2 Decomposition

1.5.2.1 Homogenous Decomposition in Groundwater

In a previous study, the H_2O_2 decomposition rate was studied in solutions and also in the presence of UO_2 pellets, it was found that the H_2O_2 decomposition rate is highest in CO_3^{2-} solutions compared with SO_4^{2-} and SiO_2.[64] Many studies [65-69] have suggested H_2O_2 decomposes in strong alkaline (pH = 12) solution through the formation of an intermediate, perhydroxyl ion (HO_2^-) species, which can catalyze the H_2O_2 decomposition process (equation 1.7-1.8).

$$H_2O_2 + OH^- \rightarrow HO_2^- + H_2O \qquad \textbf{1.7}$$

$$HO_2^- + OH^- \rightleftharpoons O_2 + H_2O + 2e^- \qquad \textbf{1.8}$$

Spalek et al. [67] studied H_2O_2 decomposition in NaOH and KOH solutions. They also suggested H_2O_2 decomposition proceeds through the formation of HO_2^- in the absence of metal catalysts, and the H_2O_2 decomposition rate is dependent on the total alkalinity and $[H_2O_2]$. The proposed mechanism involved interactions between HO_2^- and H_2O_2 which weaken the H-O bond and catalyze the decomposition reaction.

Flanagan et al. [70] used Raman spectroscopy to demonstrate the formation of peroxocarbonate ions when HCO_3^-/CO_3^{2-} was present in H_2O_2 solutions in the pH range 7.0 to 9.5. Navarro et al.[71] observed that the H_2O_2 decomposition rate in HCO_3^-/CO_3^{2-} solutions reaches a maximum at pH values between 11.5 and 11.7, when the solution contains mainly CO_3^{2-} ions.

1.5.2.2 Catalyzed H_2O_2 Surface Reactions

De Pablo et al.[72] measured the amount of U released to solution to be less than the amount of H_2O_2 consumed, suggesting H_2O_2 decomposition was also occurring. This was consistent with earlier studies which showed that the H_2O_2 consumed in UO_2 dissolution experiments could not all be accounted for.[61, 62] Many of these early studies were conducted at high [H_2O_2] (> 10^{-4} mol.L^{-1}) in solutions containing no HCO_3^-/CO_3^{2-}, and hence, were complicated by corrosion product deposition on the UO_2 surface. When HCO_3^-/CO_3^{2-} was present, and dissolution unimpeded by deposits,[73] ~ 80% of the H_2O_2 was consumed by decomposition.[74, 75] A combination of experimental and density functional theory investigations[76, 77] suggested decomposition proceeded via a mechanism involving $OH^{\bullet}$ radicals. Electrochemical studies[55] suggested the reaction was catalyzed by U^{IV}/U^{V} surface states on UO_2, i.e., on the catalytic $U^{IV}_{1-2x}U^{V}_{2x}O_{2+x}$ layer. More recent observations showed that H_2O_2 maintained a low E_{CORR} (-0.35V) independent of [H_2O_2] (10^{-8} to 10^{-5} mol.L^{-1}) as would be expected if decomposition was poising the potential, Figure 1.14.[78] Recent electrochemical studies demonstrated that decomposition did occur on a $U^{IV}_{1-2x}U^{V}_{2x}O_{2+x}$ surface, XPS analyses showing that pre-oxidized UO_2 accelerated the decomposition reaction.[78, 79]

Based on experiments in which the production of $OH^{\bullet}$ was monitored on UO_2, doped UO_2 and SIMFUEL it was claimed that the decomposition rate was effectively independent of matrix doping. Comparison of the H_2O_2 consumption rate to the U^{VI} dissolution rate showed decomposition was the major reaction pathway, not H_2O_2-promoted UO_2 corrosion.[74, 75] The dissolution yield on UO_2 was 14% compared to only 0.2% on SIMFUEL, consistent with electrochemical observations that the UO_2 lattice is stabilized by RE^{III}-doping.[80]

In addition, the noble metal particles aggregated at grain boundaries can also sustain H_2O_2 decomposition. Although there are a number of studies on transition metal catalyzed H_2O_2 decomposition, only a few of them focus on the ε-particles in UO_2 system. Nilsson et al.[75] suggested for a similar amount of H_2O_2 consumption, U dissolution rates of SIMFUEL pellets are significantly less compared with UO_2 samples due to the catalyzed decomposition of H_2O_2 on ε-particles. Lousada et al.[77] have confirmed the reduction of oxidative dissolution yield for SIMFUEL pellets compared with that of pure UO_2.

1.5.3 O_2

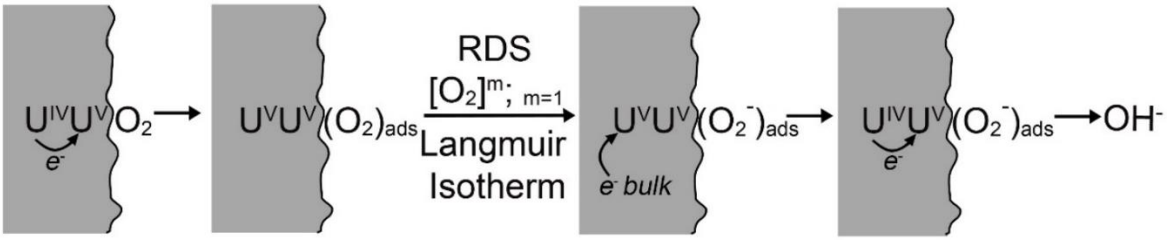

Figure 1.17 Schematic of the O_2 reduction process on UO_2.[4]

The cathodic reduction of O_2 is notoriously slow due to the need to break the O-O bond. On UO_2, the kinetics are accelerated when the surface is oxidized to $U^{IV}_{1-2x}U^{V}_{2x}O_{2+x}$ in aerated solution.[81] The reaction was found to be first order with respect to $[O_2]$ and thought to be initiated by O_2 adsorption under Langmuir isotherm conditions involving the interaction of the π and/or sp^2 orbitals of O_2 with partially filled U5f orbitals present in $U^{IV}_{1-2x}U^{V}_{2x}O_{2+x}$. It was

claimed the catalysis was achieved by the formation of donor-acceptor sites. This catalytic process is illustrated in Figure 1.18.[4]

On non-stoichiometric UO_{2+x} electrodes, O_2 reduction currents were suppressed and exhibited both a square root dependence on $[O_2]$ and large Tafel slopes, Figure 1.178.[82, 83] These results suggest the rate-determining first electron transfer was coupled with O_2 adsorption under Temkin conditions. The O_2 reduction current was also reduced by competition for U^V surface locations in HCO_3^-/CO_3^{2-} solutions.[83] Since the reaction order with respect to $[O_2]$ and the Tafel slopes were apparently unaffected by HCO_3^-/CO_3^{2-}, the overall reduction mechanism appeared to be unaltered, although ring-disc experiments showed that H_2O_2 was released to

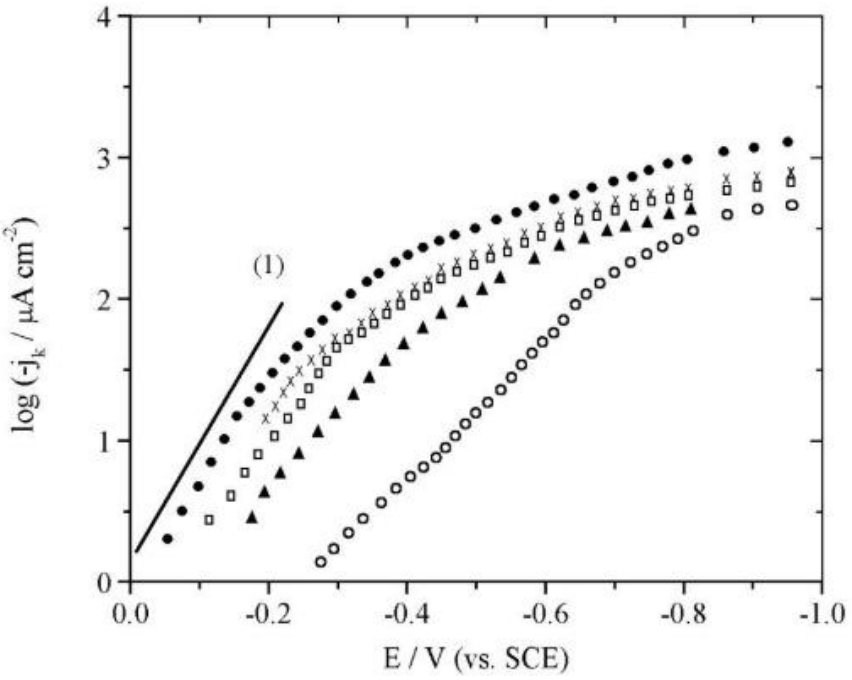

Figure 1.18: O_2 reduction currents recorded on different SIMFUEL electrodes in a 0.1 mol.L^{-1} NaCl solution (pH = 9.5) sparged with O_2, (○) electrode doped with only rare earth metals, no ε-particles; (▲) 1.5 at.% burn-up SIMFUEL; (□) 3 at.% SIMFUEL; (●) 6 at.% SIMFUEL; (x) 3 at.% SIMFUEL contains only ε-particles, no rare earth metals.[83]

solution indicating its rapid desorption due to displacement from the donor-acceptor sites by HCO_3^-/CO_3^{2-}.[81, 83]

The influence of both RE^{III} doping and the presence of noble metal (ε) particles on the kinetics of O_2 reduction have been studied, Figure 1.18.[43] Fission product doping (with RE^{III} the major influence) had only a marginal effect on the kinetics but an increase in number and size of noble metal particles present in SIMFUELs (over the simulated burn-up range 1.5 at.% to 6 at.%) systematically increased the reduction rate of O_2. This is not surprising since these particles contain the noble metals Ru, Rh and Pd all of which have been shown to catalyze the O_2 reduction reaction. As a consequence, O_2 reduction in support of fuel corrosion inside a failed container would be expected to occur preferentially on these particles.

1.5.4 The Influence of HCO_3^-/CO_3^{2-} on UO_2 Corrosion

The rate of fuel corrosion depends not only on redox conditions but also on the groundwater composition. In a Canadian DGR, the major groundwater species are expected to be $Ca^{2+}/Na^+/Cl^-/SO_4^{2-}$ with a small amount of HCO_3^-/CO_3^{2-} (10^{-4} to 10^{-3} mol.L^{-1}).[84] The key groundwater species likely to influence fuel dissolution is HCO_3^-/CO_3^{2-}, which is a strong complexing agent for the uranyl ion (UO_2^{2+}), reaction 1.10. This leads to a considerable increase in solubility. The influence of HCO_3^-/CO_3^{2-} is very dependent on redox conditions, with reaction 1.9 being rate-determining under less oxidizing conditions.

$$UO_2 \rightarrow UO_2^{2+} + 2e^- \qquad \textbf{1.9}$$

$$UO_2^{2+} + 3HCO_3^- \rightarrow UO_2(CO_3)_2^{2-} + 2H^+ \qquad \textbf{1.10}$$

Under more oxidizing conditions, the formation of UO_2CO_3 occurs on the fuel surface, reaction 1.11, and the rate of dissolution becomes controlled by the chemical dissolution reaction 1.12, whose rate depends on the concentration of $[CO_3^{2-}]$

$$UO_2 + CO_3^{2-} \rightarrow UO_2CO_3 + 2e^- \quad \textbf{1.11}$$

$$UO_2CO_3 + CO_3^{2-} \rightarrow UO_2(CO_3)_2^{2-} \quad \textbf{1.12}$$

The sequence of UO_2 oxidation/dissolution reactions in slight alkaline carbonate solutions also involves OH^- ions[85]

$$UO_2 + HCO_3^- \rightarrow (UO_2HCO_3)_{ads} + e^- \quad \textbf{1.13}$$

$$(UO_2HCO_3)_{ads} + OH^- \rightarrow (UO_2CO_3)_{ads} + e^- + H_2O \quad \textbf{1.14}$$

$$(UO_2\ CO_3)_{ads} + HCO_3^- \rightarrow [UO_2(CO_3)^2]^{2-} + H^+ \quad \textbf{1.15}$$

The influence of HCO_3^-/CO_3^{2-} has been investigated in both chemical[86-88] and electrochemical experiments[36, 41, 61, 62, 89]. The overall corrosion reaction in HCO_3^-/CO_3^{2-} solutions is complicated since the anodic and cathodic reactions appear to be convoluted. UV-Vis spectrophotometric evidence suggested dissolution can be accelerated by the formation of soluble uranylperoxocarbonate, $U^{VI}O_2((O_2)_x(CO_3)_y^{2-2x-2y}$,[90, 91] and EIS evidence indicated a similar surface intermediate, may catalyze the cathodic reaction.[89]

1.6 Scavenging Radiolytic Oxidants

Inside a failed container, corrosion processes will occur on both the fuel surface and the inner surface of the steel container with the latter process yielding the potential redox scavengers, Fe^{2+} and H_2.

1.6.1 The Influence of Fe^{2+}

The influence of Fe and Fe corrosion products on fuel corrosion has been extensively studied[92] and showed both the corrosion and radionuclide release rates were suppressed. Since

there will be no contact between the steel and the fuel inside a container, the dominant scavenging reaction involving Fe^{2+} will be either the Fenton reaction for H_2O_2

$$Fe^{2+} + H_2O_2 \rightarrow Fe^{3+} + OH^{\bullet} + OH^- \quad \textbf{1.16}$$

$$Fe^{2+} + OH^{\bullet} \rightarrow Fe^{3+} + OH^- \quad \textbf{1.17}$$

or its oxidation by O_2

$$O_2 + 4Fe^{2+} + 2H_2O \rightarrow 4Fe^{3+} + 4OH^- \quad \textbf{1.18}$$

a reaction known to regulate redox conditions in natural waters.[93]

Since the influences of Fe^{2+} and H_2 cannot be separated in experiments with Fe, more direct attempts have been made to determine the influence of Fe^{2+} on fuel corrosion[92] both experimentally and via model calculations.[44, 94-96] Calculations based on experimentally determined rate constant[97] indicated the consumption of H_2O_2 by the Fenton reaction lead to substantial suppression of UO_2 dissolution. By contrast, calculations using a mixed potential model[98] indicated only a minor effect of Fe^{2+}. The difference between these two calculations is the presence of a corrosion product deposit in the latter, but not the former calculation.

1.6.2 The Influence of H_2

The measured steel corrosion rates under simulated granitic conditions were found to be in the range 0.05 to 0.1 µm/year.[92] In sealed repositories, this would lead to H_2 pressures > 5 MPa, and dissolved concentrations in the 10 to 100 mmol.L^{-1} range.[99] In addition to H_2 from steel corrosion, water radiolysis can also produce H_2 inside a failed container. Suppression of fuel corrosion and radionuclide release in the presence of H_2 has been consistently observed in both chemical and electrochemical experiments.[42, 100-105] A number of mechanisms have been either demonstrated or proposed, all of which involve activation of H_2 to produce the

strongly reducing H• radical which can scavenge radiolytic oxidants and, hence, suppresses fuel corrosion.[40]

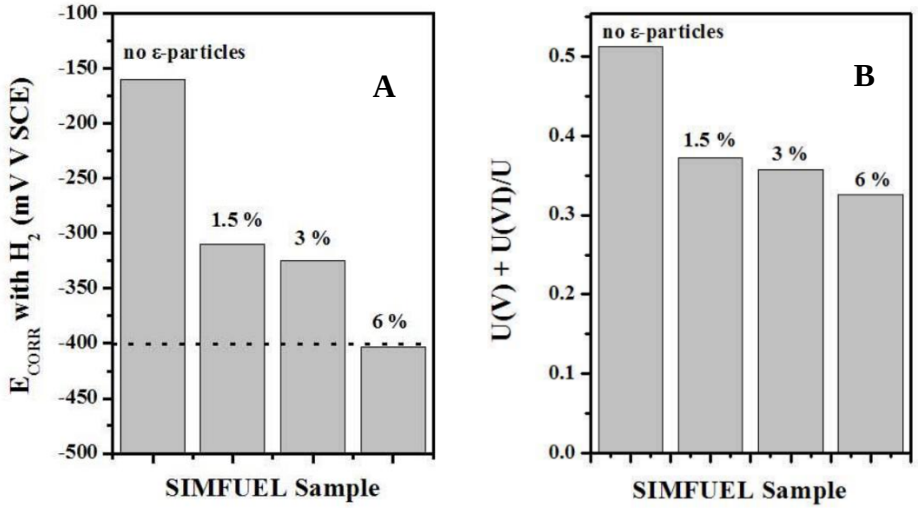

Figure 1.19: The influence of the increasing number and size of *ε*-particles in SIMFUELS with different degrees of simulated burnup on the corrosion potential (E_{CORR}) and the degree of oxidation of the surface in H_2-purged 0.1mol.L^{-1} KCl. The horizontal line indicates the potential threshold below which the corrosion of the UO_2 surface will not occur. [43]

The activation of H_2 on noble metal particles has been demonstrated electrochemically on SIMFUELs with different levels of simulated burnup, with the corrosion rate being significantly supressed by an increase in the number of ε-particles.[42, 43, 92, 104] This was not surprising since noble metals are well known catalysts for the $H_2/H^{\bullet}/H^+$ reaction with exchange currents in the range 10^{-4} to 10^{-3} A.cm^{-2}.[106] Even for small $[H_2]$, E_{CORR} decreases as the number and size of noble metal particles increases eventually reaching the thermodynamic threshold for UO_2 oxidation, Figure 1.19A. XPS analyses confirm that the extent of oxidation of the UO_2 surface is reduced, this could be attributed to the reversible dissociation of H_2 (to $H^{\bullet}$ radicals) on the ε-particles which act as galvanically-coupled anodes protecting the fuel from oxidation, Figure 1.20.[104] There is another possible way H_2 can supress corrosion rate by scavenging the radiolytic oxidant H_2O_2 on both ε-particles (Figure 1.21A) and the fuel surface (Figure 1.21B).[78] Both surfaces appeared able to activate H_2 (i.e., produce $H^{\bullet}$) on the SIMFUEL surfaces which then consumed the $OH^{\bullet}$ radicals, produced by dissociation of H_2O_2, to produce H_2O. The mechanism by which this occurs has not been elucidated, although there is

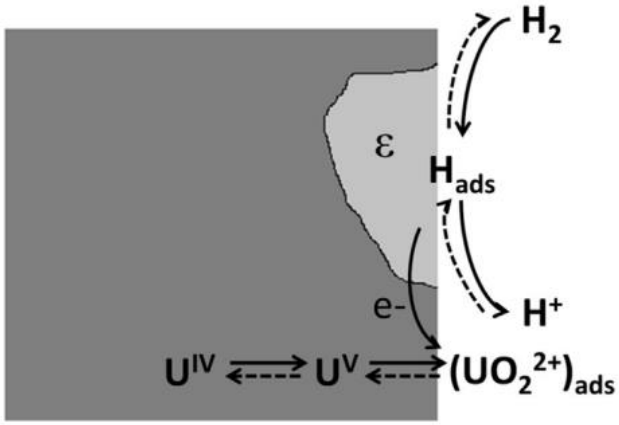

Figure 1.20: Illustration showing H_2 oxidation on noble metal (ε) particles galvanically coupled to the UO_2 matrix and inhibiting its oxidation.[104]

electrochemical evidence to indicate $H^{\bullet}$ can directly reduce U^{V} states in the surface region of $UO^{IV}_{1-2x}U^{V}_{2x}O_{2+x}$.[78]

Recent computational modelling results have shown the importance of H_2 in suppressing the UO_2 corrosion even within fractures in the fuel.[107] Liu et al. calculated that, fuel corrosion could be totally supressed within a wide range of defect geometries if the [H_2] produced by steel container corrosion reaches ~5.7 µmol.L^{-1}. Liu also found that radiolytically produced H_2 could dominate the suppression of fuel corrosion as the depth of fractures in the fuel increases due to the accumulation of radiolytically produced H_2 at the base of the cracks.[107]

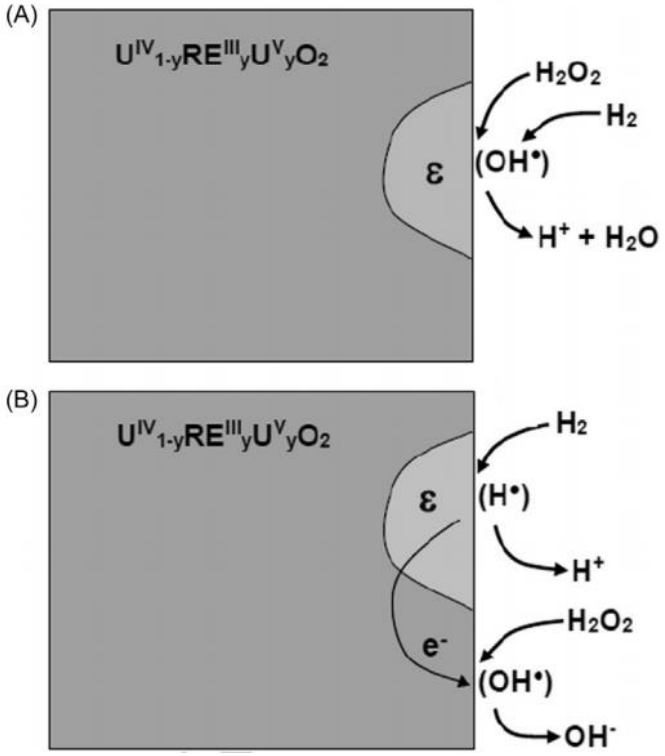

Figure 1.21: Schematic illustration of the possible reaction pathways for the consumption of H_2O_2 by reaction with H_2 on a SIMFUEL surface: (A) on noble metal (ε) particles; and (B) by H_2 oxidation on noble metal particles coupled to H_2O_2 on the galvanically coupled oxide surface.[78]

1.7 Thesis Goals and Outline

The focus of this project is to develop a detailed understanding of the corrosion mechanism of UO_2 in solutions containing the main radiolytic oxidant, H_2O_2. Many variables, such as potential, $HCO_3^-/CO_3^{2-}$and fission products, can influence the reactivity of H_2O_2. Their influences on the surface composition and electrical conductivity of UO_2 will affect surface redox reaction rates and significantly alter the overall fuel corrosion rate. Electrochemical methods allow us to separate a corrosion reaction into two constituent half reactions and determine the rate dependence on potential for each half reaction. Chemical and surface/analytical techniques can link the electrochemical/chemical process to the surface compositional and structural changes on UO_2 electrodes. In this project, attempts have been made to investigate the H_2O_2 decomposition, oxidation and reduction mechanisms on various UO_2 electrodes to determine the resulting effects on fuel corrosion.

Chapter 2 briefly reviews the principles and theory of the experimental techniques used in this research.

In chapter 3, the effects of ε-particles on H_2O_2 oxidation, studied electrochemically, are described. The balance between H_2O_2 oxidation and UO_2 oxidation was investigated, and the oxidative dissolution of UO_2 was monitored by Inductively Coupled Plasma Atomic Emission Spectroscopy (ICP-AES).

In chapter 4, describes the study of H_2O_2 decomposition and H_2O_2 driven fuel corrosion using chemical, electrochemical and surface/solution techniques, in particular X-ray Photoelectron Spectroscopy (XPS) and Inductively Coupled Plasma Mass Spectroscopy (ICP-MS). A small electrochemical cell was designed to accurately monitor H_2O_2 and U concentration

changes with time, while the corrosion potential and polarization resistance were monitored at the same time to determine the relative corrosion rates.

Chapter 5 describes a study of H_2O_2 reduction on UO_2 electrodes with different compositions. Six different electrodes were used to investigate the effect of rare earth dopants, noble metal particles and non-stoichiometry on the reaction mechanism and kinetics. Rotating disc electrodes (RDE) were employed to control the diffusion of bulk H_2O_2 to UO_2 surface. The reduction reaction of H_2O_2 was studied by applying a cathodic potential to the electrodes and measure the corresponding current responses.

In chapter 6, the results of a series of sensitivity analyses using a pre-developed model for UO_2 corrosion are described. The influences of defect geometry and changes in the ε-particles coverage of the fuel surface were calculated.

1.8 Reference

[1] Nuclear Wate Management Organization, Progress through collaboration triennial report 2014 to 2016, NWMO, 2017, 13.

[2] Nuclear Waste Management Organization, Choosing a Way Forward, http://www.nwmo.ca, (2010).

[3] P.A. Gierszewski, J; Calder, N; D'Andrea, A;, Garisto, F; Kitson, C; Melnyk, T; Wei, K; Wojciechowski, L, Third case study-postclosure safety assessment Ontario Power Generation, Intera Engineering, AECL, 2004

[4] D.W. Shoesmith, Fuel corrosion processes under waste disposal conditions, Journal of Nuclear Materials, 282 (2000) 1-31.

[5] L.O. Werme, L. Johnson, V. Oversby, F. King, K. Spahiu, B. Grambow, D. Shoesmith, Spent fuel performance under repository conditions: A model for use in SR-Can, SKB2004.

[6] I. Grenthe, J. Fuger, R.J. Konings, R.J. Lemire, A.B. Muller, C. Nguyen-Trung, H. Wanner, Chemical thermodynamics of uranium, North-Holland Amsterdam1992.

[7] F. King, M. Kolar, The copper container corrosion model used in AECL's second case study, Ontario Power Generation report, (2000).

[8] F. King, M. Kolar, Analysis of the effect of cladding on the oxidative dissolution of used nuclear fuel using the mixed-potential model of fuel dissolution (MPM Version 1.2), Ontario Power Generation Report, (2000) 01200-10022.

[9] F. Garisto, Fourth case study: features, events and processes, Canada: Nuclear Waste Management Organization, (2012).

[10] D. Shoesmith, S. Sunder, W. Hocking, Electrochemistry of UO_2 nuclear fuel, Electrochemistry of Novel Materials (edited by J. Lipkowski and PN Ross), VCH Publishers, New York, (1994) 297-337.

[11] S. Sunder, Alpha, beta and gamma dose rates in water in contact with used CANDU UO_2 fuel, AECL, Canada, 1995, pp. 27.

[12] A. Henglein, J. W. T. Spinks. R. J. Woods: An Introduction to Radiation Chemistry, Third Edition, John-Wiley and Sons, Inc., New York, Toronto 1990. ISBN 0-471-61403-3. 574 Seiten, Preis: DM 91, 45, Berichte der Bunsengesellschaft für physikalische Chemie, 95 (1991) 451-451.

[13] G.R. Choppin, J.-O. Liljenzin, J. Rydberg, Radiochemistry and nuclear chemistry, Butterworth-Heinemann2002.

[14] B.T. Willis, Crystallographic studies of anion-excess uranium oxides, Journal of the Chemical Society, Faraday Transactions 2: Molecular and Chemical Physics, 83 (1987) 1073-1081.

[15] D.J.M. Bevan, I.E. Grey, B.T.M. Willis, The crystal structure of β-U_4O_{9-y}, Journal of Solid State Chemistry, 61 (1986) 1-7.

[16] F. Grønvold, High-temperature X-ray study of uranium oxides in the UO_2□U_3O_8 region, Journal of Inorganic and Nuclear Chemistry, 1 (1955) 357-370.

[17] T. Cardinaels, K. Govers, B. Vos, S. Van den Berghe, M. Verwerft, L. de Tollenaere, G. Maier, C. Delafoy, Chromia doped UO_2 fuel: Investigation of the lattice parameter, Journal of Nuclear Materials, 424 (2012) 252-260.

[18] P.A.T. G. C. Allen, Ordered defects in the oxides of uranium, Proceedings of the Royal Society of London. A. Mathematical and Physical Sciences, 406 (1986) 325-344.

[19] B. Willis, The defect structure of hyper-stoichiometric uranium dioxide, Acta Crystallographica Section A: Crystal Physics, Diffraction, Theoretical and General Crystallography, 34 (1978) 88-90.

[20] G. Allen, P. Tempest, J. Tyler, Coordination model for the defect structure of hyperstoichiometric UO_{2+x} and U_4O_9, Nature, 295 (1982) 48.

[21] G.C. Allen, P.A. Tempest, The accommodation of oxygen clusters in hyperstoicheiometric uranium dioxide and its effects on crystal structure, Journal of the Chemical Society, Dalton Transactions, (1983) 2673-2677.

[22] J. Wang, R.C. Ewing, U. Becker, Average structure and local configuration of excess oxygen in UO_{2+x}, Scientific reports, 4 (2014) 4216.

[23] D. Smith, B. Scheetz, C. Anderson, K. Smith, Phase relations in the uranium-oxygen-water system and its significance on the stability of nuclear waste forms, Uranium, 1 (1982) 79-111.

[24] R.L. Segall, P.S. Turner, Oxide surfaces in solution, Elsevier, Amsterdam, 1988.

[25] P.W. Winter, The electronic transport properties of UO_2, Journal of Nuclear Materials, 161 (1989) 38-43.

[26] S.M. Gilbertson, T. Durakiewicz, G.L. Dakovski, Y. Li, J.-X. Zhu, S.D. Conradson, S.A. Trugman, G. Rodriguez, Ultrafast photoemission spectroscopy of the uranium dioxide (UO_2) Mott insulator: evidence for a robust energy gap structure, Physical Review Letters, 112 (2014) 087402.

[27] L.E. Roy, T. Durakiewicz, R.L. Martin, J.E. Peralta, G.E. Scuseria, C.G. Olson, J.J. Joyce, E. Guziewicz, Dispersion in the Mott insulator UO_2: A comparison of photoemission spectroscopy and screened hybrid density functional theory, Journal of Computational Chemistry, 29 (2008) 2288-2294.

[28] Y. Baer, J. Schoenes, Electronic structure and coulomb correlation energy in UO_2 single crystal, Solid State Communications, 33 (1980) 885-888.

[29] P. Ruello, K.D. Becker, K. Ullrich, L. Desgranges, C. Petot, G. Petot-Ervas, Thermal variation of the optical absorption of UO_2: determination of the small polaron self-energy, Journal of Nuclear Materials, 328 (2004) 46-54.

[30] J.M. Casado, J.H. Harding, G.J. Hyland, Small-polaron hopping in Mott-insulating UO_2, Journal of Physics: Condensed Matter, 6 (1994) 4685.

[31] A.J.E. Rettie, W.D. Chemelewski, D. Emin, C.B. Mullins, Unravelling small-polaron transport in metal oxide photoelectrodes, The Journal of Physical Chemistry Letters, 7 (2016) 471-479.

[32] J.L. Bates, C.A. Hinman, T. Kawada, Electrical conductivity of uranium dioxide, Journal of the American Ceramic Society, 50 (1967) 652-656.

[33] J. Tateno, The dielectric properties at 9.1 GHz and nature of small polarons in nonstoichiometric uranium oxides, The Journal of Chemical Physics, 81 (1984) 6130-6135.

[34] P. Nagels, J. Devreese, M. Denayer, Electronic conduction in single crystals of uranium dioxide, Journal of Applied Physics, 35 (1964) 1175-1180.

[35] H. He, P.G. Keech, M.E. Broczkowski, J.J. Noël, D.W. Shoesmith, Characterization of the influence of fission product doping on the anodic reactivity of uranium dioxide, Canadian Journal of Chemistry, 85 (2007) 702-713.

[36] M. Razdan, Shoesmith D.W., The electrocheical reacivity of 6.0 wt.% Gd doped UO_2 in aquous carbonate-bicarbonate solutions, Journal of The Electrochemical Society, 4 (2014) H225-H234.

[37] J. Paquette, R.J. Lemire, A Description of the Chemistry of Aqueous Solutions of Uranium and Plutonium to 200°C Using Potential-pH Diagrams, Nuclear Science and Engineering, 79 (1981) 26-48.

[38] D. Gorman-Lewis, P.C. Burns, J.B. Fein, Review of uranyl mineral solubility measurements, The Journal of Chemical Thermodynamics, 40 (2008) 335-352.

[39] D.L. Clark, D.E. Hobart, M.P. Neu, Actinide carbonte complexes and their importance in actinide environmental chemistry, Chemical Reviews, 95 (1995) 25-48.

[40] B.G. Santos, J.J. Noël, D.W. Shoesmith, The effect of pH on the anodic dissolution of SIMFUEL (UO_2), Journal of Electroanalytical Chemistry, 586 (2006) 1-11.

[41] N. Liu, H. He, J.J. Noël, D.W. Shoesmith, The electrochemical study of Dy_2O_3 doped UO_2 in slightly alkaline sodium carbonate/bicarbonate and phosphate solutions, Electrochimica Acta, 235 (2017) 654-663.

[42] M.E. Broczkowski, J.J. Noël, D.W. Shoesmith, The influence of dissolved hydrogen on the surface composition of doped uranium dioxide under aqueous corrosion conditions, Journal of Electroanalytical Chemistry, 602 (2007) 8-16.

[43] D. Shoesmith, Used fuel and uranium dioxide dissolution studies–a review, Report NWMO TR-2007-03, Nuclear Waste Management Organization, Toronto, ON, (2007).

[44] D.W. Shoesmith, M. Kolar, F. King, A mixed-potential model to predict fuel (uranium dioxide) corrosion within a failed nuclear waste container, CORROSION, 59 (2003) 802-816.

[45] B.G. Santos, H.W. Nesbitt, J.J. Noël, D.W. Shoesmith, X-ray photoelectron spectroscopy study of anodically oxidized SIMFUEL surfaces, Electrochimica Acta, 49 (2004) 1863-1873.

[46] Nuclear Waste Managment Organization, Canada's used nuclear fuel, Nulcear Waste Management Organization, Toronto.

[47] I. Hastings, Structures in irradiated UO_2 fuel from Canadian reactors, Atomic Energy of Canada Limited(AECL), Report AECL-MISC-249, (1982).

[48] J. Novak, I.J. Hastings, Ontario hydro experience with extended-burnup power reactor fuel, Atomic Energy of Canada Limited (AECL), Report: AECL-10388, 1991.

[49] D.W. Shoesmith, The chemistry/electrochemistry of spent nuclear fuel as a wasteform, Uranium: Cradle to Grave, Mineralogical Society of Canada, Short Course Series, 43 (2013) 337-368.

[50] E.C. Buck, B.D. Hanson, B.K. McNamara, The geochemical behaviour of Tc, Np and Pu in spent nuclear fuel in an oxidizing environment, Geological Society, London, Special Publications, 236 (2004) 65-88.

[51] J. Bruno, Spent Nuclear Fuel, Elements (Quebec), 2 (2006) 343-349.

[52] R.C. Ewing, Long-term Storage of Spent Nuclear Fuel, Nature Materials, 14 (2015) 252-257.

[53] E. Ekeroth, O. Roth, M. Jonsson, The relative impact of radiolysis products in radiation induced oxidative dissolution of UO_2, Journal of Nuclear Materials, 355 (2006) 38-46.

[54] O. Roth, S. Nilsson, M. Jonsson, Radiation enhanced reactivity of UO_2, Journal of Nuclear Materials, 354 (2006) 131-136.

[55] J. Wren, D. Shoesmith, S. Sunder, Corrosion behavior of uranium dioxide in alpha radiolytically decomposed water, Journal of the Electrochemical Society, 152 (2005) B470-B481.

[56] D.W. Shoesmith, S. Sunder, M.G. Bailey, G.J. Wallace, The corrosion of nuclear fuel (UO_2) in oxygenated solutions, Corrosion Science, 29 (1989) 1115-1128.

[57] J.S. Goldik, H.W. Nesbitt, J.J. Noël, D.W. Shoesmith, Surface electrochemistry of UO_2 in dilute alkaline hydrogen peroxide solutions, Electrochimica Acta, 49 (2004) 1699-1709.

[58] J.S. Goldik, J.J. Noël, D.W. Shoesmith, The effects of simulated fission products in the reduction of hydrogen peroxide on simulated nuclear fuel electrodes, Journal of The Electrochemical Society, 153 (2006) E151-E159.

[59] L. Wu, The Electrochemistry of Hydrogen Peroxide on Uranium Dioxide and the Modelling of Used Nuclear Fuel Corrosion under Permanent Disposal Conditions, (2014).

[60] L. Wu, D.W. Shoesmith, An electrochemical study of H_2O_2 oxidation and decomposition on simulated nuclear fuel (SIMFUEL), Electrochimica Acta, 137 (2014) 83-90.

[61] J.S. Goldik, L. Wu, D.W. Shoesmith, The anodic reactions on simulated spent fuel (SIMFUEL) in H_2O_2 solutions: effect of carbonate/bicarbonate, Journal of Electrochemical Society, 161 (2014) C363-C371.

[62] S. Sunder, N.H. Miller, D.W. Shoesmith, Corrosion of uranium dioxide in hydrogen peroxide solutions, Corrosion Science, 46 (2004) 1095-1111.

[63] D.W. Shoesmith, S. Sunder, An electrochemistry-based model for the dissolution of UO_2, Pinawa, Man.: Atomic Energy of Canada Limited 1991.

[64] M. Amme, J. Svedkauskaite, W. Bors, M. Murray, J. Merino, A kinetic study of UO_2 dissolution and H_2O_2 stability in the presence of groundwater ions, Radiochimica Acta, 95 (2007).

[65] J. Abbot, D.G. Brown, Kinetics of Iron-catalyzed decomposition of hydrogen peroxide in alkaline solution, International Journal of Chemical Kinetics, 22 (1990) 963-974.

[66] W.D. Nicoll, A.F. Smith, Stability of dilute alkaline solutions of hydrogen peroxide, Industrial & Engineering Chemistry, 47 (1955) 2548-2554.

[67] O. Spalek, J. Balej, I. Paseka, Kinetics of the decomposition of hydrogen peroxide in alkaline solutions, Journal of the Chemical Society, Faraday Transactions 1: Physical Chemistry in Condensed Phases, 78 (1982) 2349-2359.

[68] R. Venkatachalapathy, G.P. Davila, J. Prakash, Catalytic decomposition of hydrogen peroxide in alkaline solutions, Electrochemistry Communications, 1 (1999) 614-617.

[69] K.C.T. E. L. Littauer, Catalytic decomposition of hydrogen peroxide in alkaline solution, Journal of Electrochemical Society, 126 (1979) 1924-1927.

[70] J. Flanagan, D.P. Jones, W.P. Griffith, A.C. Skapski, A.P. West, On the existence of peroxocarbonates in aqueous-solution Journal of the Chemical Society-Chemical Communications, (1986) 20-21.

[71] J.A. Navarro, M.A. de la Rosa, M. Roncel, F.F. de la Rosa, Carbon dioxide-mediated decomposition of hydrogen peroxide in alkaline solutions, Journal of the Chemical Society, Faraday Transactions 1: Physical Chemistry in Condensed Phases, 80 (1984) 249-253.

[72] J. Pablo, Casas, I., Clarens, F., Aamrani, F., & Rovira, M. , The Effect of Hydrogen Peroxide Concentration on the Oxidative Dissolution of Unirradiated Uranium Dioxide, MRS Proceedings, 663 (2000).

[73] E. Ekeroth, M. Jonsson, Oxidation of UO_2 by radiolytic oxidants, Journal of Nuclear Materials, 322 (2003) 242-248.

[74] R. Pehrman, M. Trummer, C.M. Lousada, M. Jonsson, On the redox reactivity of doped UO_2 pellets – influence of dopants on the H_2O_2 decomposition mechanism, Journal of Nuclear Materials, 430 (2012) 6-11.

[75] S. Nilsson, M. Jonsson, H_2O_2 and radiation induced dissolution of UO_2 and SIMFUEL pellets, Journal of Nuclear Materials, 410 (2011) 89-93.

[76] C.M. Lousada, A.J. Johansson, T. Brinck, M. Jonsson, Mechanism of H_2O_2 decomposition on transition metal oxide surfaces, The Journal of Physical Chemistry C, 116 (2012) 9533-9543.

[77] C.M. Lousada, M. Trummer, M. Jonsson, Reactivity of H_2O_2 towards different UO_2-based materials: The relative impact of radiolysis products revisited, Journal of Nuclear Materials, 434 (2013) 434-439.

[78] M. Razdan, D.W. Shoesmith, The influence of hydrogen peroxide and hydrogen on the corrosion of simulated spent nuclear fuel, Faraday Discussions, 180 (2015) 283-299.

[79] M. Razdan, D.S. Hall, P.G. Keech, D.W. Shoesmith, Electrochemical reduction of hydrogen peroxide on SIMFUEL (UO_2) in acidic pH conditions, Electrochimica Acta, 83 (2012) 410-419.

[80] M. Razdan, D.W. Shoesmith, Influence of trivalent-dopants on the structural and electrochemical properties of uranium dioxide (UO_2), Journal of The Electrochemical Society, 161 (2014) H105-H113.

[81] W.H. Hocking, J.S. Betteridge, D.W. Shoesmith, The cathodic reduction of oxygen on uranium dioxide in dilute alkaline aqueous solution, Journal of Electroanalytical Chemistry, 379 (1994) 339-351.

[82] D.W. Shoesmith, S. Sunder, M.G. Bailey, N.H. Miller, Corrosion of used nuclear fuel in aqueous perchlorate and carbonate solutions, Journal of Nuclear Materials, 227 (1996) 287-299.

[83] W. Hocking, J.S. Betteridge, D.W. Shoesmith, The cathodic reduction of oxygen on uranium dioxide in dilute alkaline aqueous solution, Atomic Energy of Canada Limited Report, 1991.

[84] J. McMurry, Reference water compositions for a deep geologic repository in the Canadian Shield, Ontario Power Generation, Nuclear Waste Management Division Report, (2004).

[85] P.G. Keech, J.J. Noël, D.W. Shoesmith, The electrochemical reduction of hydrogen peroxide on uranium dioxide under intermediate pH to acidic conditions, Electrochimica Acta, 53 (2008) 5675-5683.

[86] J. De Pablo, I. Casas, J. Giménez, M. Molera, M. Rovira, L. Duro, J. Bruno, The oxidative dissolution mechanism of uranium dioxide. I. The effect of temperature in hydrogen carbonate medium, Geochimica et Cosmochimica Acta, 63 (1999) 3097-3103.

[87] J. De Pablo, I. Casas, J. Gimenez, V. Marti, M. Torrero, Solid surface evolution model to predict uranium release from unirradiated UO_2 and nuclear spent fuel dissolution under oxidizing conditions, Journal of Nuclear Materials, 232 (1996) 138-145.

[88] M.M. Hossain, E. Ekeroth, M. Jonsson, Effects of on the kinetics of UO_2 oxidation by H_2O_2, Journal of Nuclear Materials, 358 (2006) 202-208.

[89] J.S. Goldik, J.J. Noël, D.W. Shoesmith, Surface electrochemistry of UO_2 in dilute alkaline hydrogen peroxide solutions, Electrochimica Acta, 51 (2006) 3278-3286.

[90] G.S. Goff, L.F. Brodnax, M.R. Cisneros, S.M. Peper, S.E. Field, B.L. Scott, W.H. Runde, First identification and thermodynamic characterization of the ternary U (VI) species, $UO_2(O_2)(CO_3)_2^{4-}$, in $UO_2{-}H_2O_2{-}K_2CO_3$ solutions, Inorganic chemistry, 47 (2008) 1984-1990.

[91] S.M. Peper, L.F. Brodnax, S.E. Field, R.A. Zehnder, S.N. Valdez, W.H. Runde, Kinetic study of the oxidative dissolution of UO_2 in aqueous carbonate media, Industrial & engineering chemistry research, 43 (2004) 8188-8193.

[92] D.W. Shoesmith, Used Fuel and Uranium Dioxide Dissolution Studies – A Review, Nuclear Waste Mangement Organization, 2007.

[93] W. Stumm, G.F. Lee, Oxygenation of ferrous iron, Industrial & Engineering Chemistry, 53 (1961) 143-146.

[94] L. Johnson, P. Smith, The interaction of radiolysis products and canister corrosion products and the implications for spent fuel dissolution and radionuclide transport in a repository for spent fuel, National Cooperative for the Disposal of Radioactive Waste (NAGRA), 2000.

[95] L. Wu, Y. Beauregard, Z. Qin, S. Rohani, D.W. Shoesmith, A model for the influence of steel corrosion products on nuclear fuel corrosion under permanent disposal conditions, Corrosion Science, 61 (2012) 83-91.

[96] L. Wu, N. Liu, Z. Qin, D.W. Shoesmith, Modeling the radiolytic corrosion of fractured nuclear fuel under permanent disposal conditions, Journal of The Electrochemical Society, 161 (2014) E3259-E3266.

[97] M. Jonsson, F. Nielsen, O. Roth, E. Ekeroth, S. Nilsson, M.M. Hossain, Radiation induced spent nuclear fuel dissolution under deep repository conditions, Environmental Science & Technology, 41 (2007) 7087-7093.

[98] M. Kolar, King F., , The mixed-potential model for UO_2 dissolution, Ontario Power Generation.

[99] P. Carbol, J. Cobos-Sabate, J. Glatz, C. Ronchi, V. Rondinella, D. Wegen, T. Wiss, A. Loida, V. Metz, B. Kienzler, The effect of dissolved hydrogen on the dissolution of 233U doped UO, (2005).

[100] M. Trummer, M. Jonsson, Resolving the H_2 effect on radiation induced dissolution of UO_2-based spent nuclear fuel, Journal of Nuclear Materials, 396 (2010) 163-169.

[101] E. Ekeroth, M. Jonsson, T.E. Eriksen, K. Ljungqvist, S. Kovács, I. Puigdomenech, Reduction of UO_2^{2+} by H_2, Journal of Nuclear Materials, 334 (2004) 35-39.

[102] S. Nilsson, M. Jonsson, On the catalytic effects of UO_2(s) and Pd(s) on the reaction between H_2O_2 and H_2 in aqueous solution, Journal of Nuclear Materials, 372 (2008) 160-163.

[103] M. Trummer, O. Roth, M. Jonsson, H_2 inhibition of radiation induced dissolution of spent nuclear fuel, Journal of Nuclear Materials, 383 (2009) 226-230.

[104] M. Broczkowski, J. Noël, D. Shoesmith, The inhibiting effects of hydrogen on the corrosion of uranium dioxide under nuclear waste disposal conditions, Journal of Nuclear Materials, 346 (2005) 16-23.

[105] M. Broczkowski, P. Keech, J. Noël, D. Shoesmith, Corrosion of uranium dioxide containing simulated fission products in dilute hydrogen peroxide and dissolved hydrogen, Journal of the Electrochemical Society, 157 (2010) C275-C281.

[106] J.K. Nørskov, T. Bligaard, A. Logadottir, J. Kitchin, J.G. Chen, S. Pandelov, U. Stimming, Trends in the exchange current for hydrogen evolution, Journal of the Electrochemical Society, 152 (2005) J23-J26.

[107] N. Liu, L. Wu, Z. Qin, D.W. Shoesmith, Roles of radiolytic and externally generated H_2 in the corrosion of fractured spent nuclear fuel, Environmental science & technology, 50 (2016) 12348-12355.

Chapter 2

2 Experimental Techniques and Details

In this chapter, the principles of the experimental techniques used in this project are briefly reviewed. For electrochemical experiments, more detailed information on experimental parameters will be provided in the individual experimental sections found in subsequent chapters.

2.1 UO_2 Materials

The UO_2 materials used in the experiments in chapters 3 and 4 are simulated spent nuclear fuel (SIMFUEL) provided by Atomic Energy of Canada Limited (AECL, Chalk River, Canada)*. All materials were received in pellet form. For chapter 5, the three hyper-stoichiometric UO_{2+x} materials (x represents the average degree of the non-stoichiometry, x = 0.002, 0.05, and 0.1) used were also fabricated at AECL. The 12.9 wt.% Dy-doped UO_2 (Dy-UO_2) and 6.0 wt.% Gd-doped UO_2 (Gd-UO_2) specimens were provided by Cameco (Port Hope, Canada).

2.1.1 SIMFUEL

SIMFUEL is an analogue of CANDU spent nuclear fuel composed of UO_2 doped with non-radioactive fission products to simulate the chemical and physical effects of spent fuel after in-reactor burnup without the associated radiation levels.[1]

* Atomic Energy of Canada Limited is now Canadian Nuclear Laboratories

Two features of SIMFUEL are particularly important to this study: (i) the rare earth elements (RE^{III}) (Y, Ce, Nd, La) which dissolve in the UO_2 matrix and can influence the structure and reactivity of UO_2; (ii) the noble metal (Pd, Ru, Rh) dopants, which segregate into noble metal (ε) particles in the UO_2 matrix. Of the other elements added to SIMFUEL, Sr, Zr, and Ba form oxides which segregate as a separate perovskite-type phase which appears to be inert. The added Mo, which can be present in both metallic and oxides forms, tends to be incorporated into the noble metal particles.[2] The microstructure of SIMFUEL has been studied extensively using SEM, EDX and XPS,[1, 3, 4] and is very similar to that of a CANDU fuel pellet with UO_2 grains ~8-15 μm in size. The noble metal particles exist as small spherical precipitates distributed mainly along grain boundaries. The SIMFUEL used in this project possessed a 3 at.% simulated burnup, which is higher than that of standard CANDU fuel (1.5 at.% burnup).

2.1.2 Hyper-Stoichiometric UO_{2+x}

Three hyper-stoichiometric UO_{2+x} samples were studied with nominal O/U ratios of 2.002, 2.05 and 2.1. The non-stoichiometry was achieved by annealing a disc of near-stoichiometric UO_2 in a gas mixture with controlled ratios of $Ar/H_2/O_2$ at around 1600 K. Raman spectroscopy, Scanning Electron Microscopy (SEM), X-ray Powder Diffraction (XRD) and Scanning Electrochemical Microscopy (SECM) have been used to study the microstructure, conductivity, and electrochemical reactivity of individual grains in these non-stoichiometric materials, and showed that the composition is not uniform.[2, 5-7]

2.1.3 Dy-UO_2 and Gd-UO_2

SEM, EDX and Raman spectroscopy studies have been used to determine the composition and microstructure of the Dy-UO_2 and Gd-UO_2 materials.[8] Both materials possessed a rough surface morphology. EDX maps show that the doping elements, Dy and Gd, were homogeneously distributed. No separation of Gd (as Gd_2O_3) and Dy (as Dy_2O_3) was observed.

2.2 Electrochemical Experimental Techniques

2.2.1 Electrode Preparation

All the UO_2 electrodes were cut into discs, 2-3 mm in thickness, using a saw with a diamond blade. One surface of the electrode was then polished and electroplated with a thin layer of Cu to provide good electrical contact to an external measuring circuit. The electroplating cell is shown in Figure 2.1A and illustrated schematically in Figure 2.1B. The UO_2 disc was secured in the end of a piece of rubber tubing and immersed in 0.1 $mol.L^{-1}$ $CuSO_4$ solution. A piece of Cu metal was used as the CE, and electronic grade Hg was poured into rubber tubing to facilitate the electric contact. A Cu wire was used to connect the Hg to the external circuit. A 10 mA current was applied for 5 minutes using a DC power supply (GPR-30H10D) to form a thin, evenly distributed, layer of Cu on the UO_2 surface.

A threaded stainless steel shaft, with a diameter similar to that of the UO_2 electrode was then bonded to the Cu-plated UO_2 surface using silver epoxy (Hysol KS0004). The disc was then either fixed in a RDE Teflon holder using a casting compound (Hysol EE4183) to make a rotating disc electrode (RDE), or the sides were coated with Amer coat (90HS, Amercoat

Canada) to make small non-rotating electrodes. All electrodes were polished (wet) using 1200 SiC paper, rinsed with distilled de-ionized water before performing experiments.

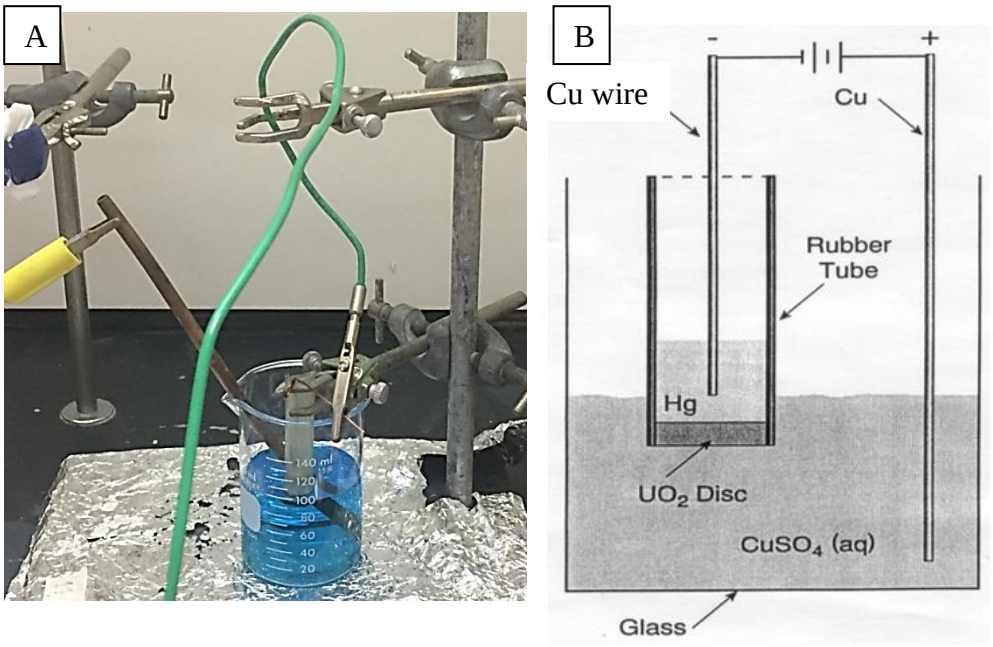

Figure 2.1: (A) Image of laboratory setup, and (B) a schematic illustration of the electroplating of Cu onto one face of a UO_2 disc electrode.

2.2.2 Electrochemical Cell

Two different electrochemical cells were used in this project. Experiments with a rotating disc electrode (RDE) were performed in an 800 mL, three-compartment cell shown in Figure 2.2. The main chamber of the cell was separated from the reference and counter electrode compartments by dense glass frits. A Luggin capillary was used to minimize the ohmic potential drop caused by the solution resistance between the reference electrode (RE) and the working electrode (WE). A Pt foil spot welded to a Pt wire was used as the counter electrode (CE) and a saturated calomel electrode as RE. The second cell used was a 40 mL single-compartment cell, Figure 2.3. The CE was a Pt wire which was placed in a glass tube and separated from the main

cell compartment by a dense glass frit, and the RE was a Ag/AgCl (Saturated KCl). The cells were placed in a Faraday cage while running experiments to minimize interference from external noise. The RDE rotation rate was controlled using an analytical rotator from Pine Instrument (model ASR). All the electrochemical experiments were performed with a Solartron 1287 potentiostat controlled by CorrWare Version 2.7 software.

2.2.3 Solutions

All solutions were prepared with Type 1 water (resistance of 18.2 MΩ.cm), purified using a Millipore Milli-Q Plus unit, to remove organic and inorganic impurities, and then passed through a Milli-Q-plus ion exchange column. All the experiments were conducted at room temperature and purged with Ar (ultra-high purity, Praxair) for at least 30 minutes prior to experiments. Purging was then continued for the duration of an experiment. Experiments were conducted in a 0.1 $mol.L^{-1}$ NaCl solution with the pH adjusted to 9.7 by adding a NaOH solution. When required, $NaHCO_3$ and H_2O_2 (3% and 30%) were added in the quantities required to achieve the desired concentration. All chemicals were reagent grade and purchased from Fisher Scientific.

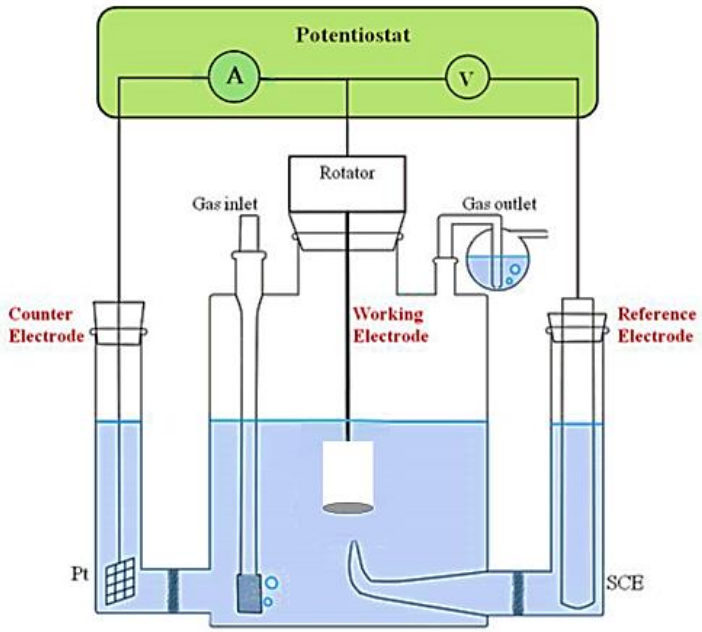

Figure 2.2: Diagram of the three-compartment electrochemical cell used in RDE experiments.

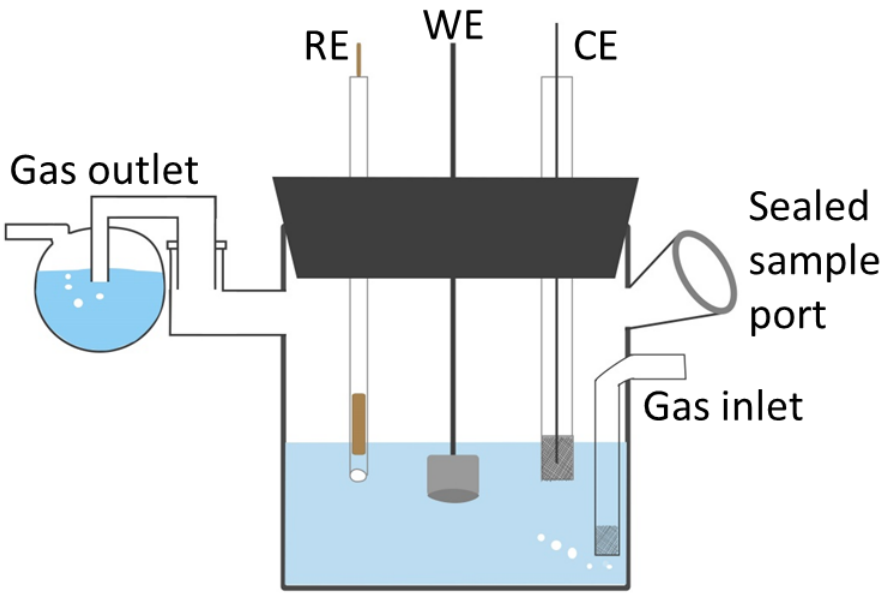

Figure 2.3: Diagram of the single-compartment electrochemical cell used in corrosion experiments.

2.2.4 Corrosion Potential (E_{CORR}) Measurements

The corrosion of UO_2 in aqueous solution involves the coupling of the anodic oxidation of UO_2 with the cathodic reduction of an available oxidant,

$$UO_2 + Ox \rightarrow UO_2^{2+} + Red \qquad \textbf{2.1}$$

where Ox is the oxidant and Red is the reduced form. Since the anodic and cathodic half reactions involve electron transfer, the reaction rate can be expressed as a corrosion current, i_{CORR}. The corrosion reaction is a short circuit electrochemical reaction with both reactions occurring on the UO_2 surface with

$$i_{CORR} = \sum i_a = -\sum i_c \qquad \textbf{2.2}$$

where i_a and i_c are the currents for the anodic and cathodic half reactions, respectively.

$$UO_2 \rightarrow UO_2^{2+} + 2e^- \quad (E_e)_{UO_2^{2+}/UO_2} \qquad \textbf{2.3}$$

$$Ox + ne^- \rightarrow Red \qquad (E_e)_{Ox/Red} \qquad \textbf{2.4}$$

and $(E_e)_{UO_2^{2+}/UO_2}$ and $(E_e)_{Ox/Red}$ are the equilibrium potentials for the two half-reactions(2.3 and 2.4), given by the Nernst equation and written by convention as reduction reactions. The thermodynamic requirement for reaction 2.1 to be spontaneous is,

$$(E_e)_{UO_2^{2+}/UO_2} < (E_e)_{Ox/Red} \qquad \textbf{2.5}$$

When each half-reaction is controlled by the rate of electron transfer, the relationship between current and potential can be expressed by the Butler-Volmer equation,[9]

$$j = j_o \left[\exp\left\{\frac{\alpha F}{RT}\eta\right\} - \exp\left\{\frac{(1-\alpha)F}{RT}\eta\right\}\right] \qquad \textbf{2.6}$$

where j_o is the exchange current density, α is the transfer coefficient, F is the Faraday constant, R is the gas constant, T is the temperature, and η is the overpotential, defined as

$$\eta = E - E_e \qquad \textbf{2.7}$$

where E is the applied potential.

At the equilibrium potential, E_e, $\eta = 0$, and no net current flows although the equilibrium is considered dynamic, $j_a = -j_c = j_o$. For a corrosion process, the anodic half of one reaction is coupled with the cathodic half of another reaction. Each half reaction, equations 2.3 and 2.4, can be represented kinetically by a Butler-Volmer relationship as shown in Figure 2.4. Since corrosion is a short-circuit reaction, the total anodic current must be equal and opposite in sign to the cathodic current. Figure 2.4 shows this criterion can only be met at a single potential, termed the corrosion potential (E_{CORR}), which lies between the equilibrium potentials for the two half reactions.

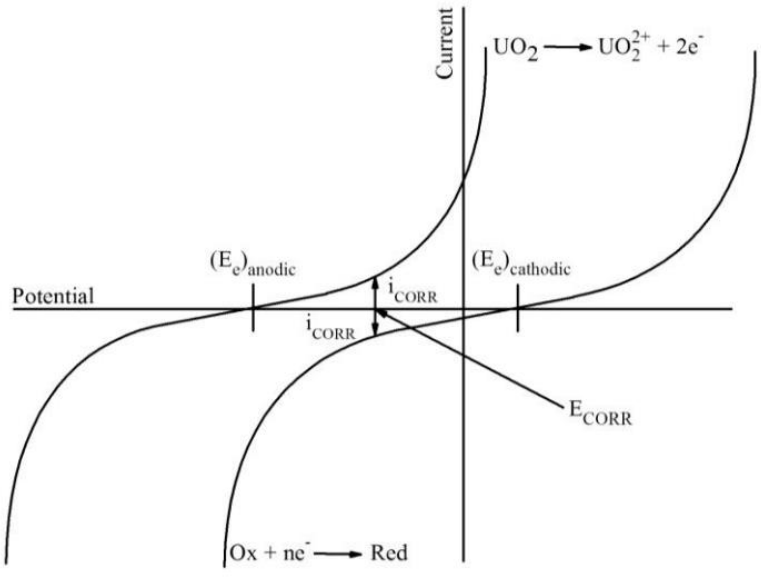

Figure 2.4: Current-potential relationships for the UO_2 dissolution and oxidant reduction reactions indicating the corrosion potential (E_{CORR}) at which they couple.

$$(E_e)_{anodic} < E_{CORR} < (E_e)_{cathodic} \qquad \textbf{2.8}$$

While the E_{CORR} is thermodynamically restricted according to equation 2.8, its value provides qualitative information about the kinetics of the system, since the value of E_{CORR} is determined by the shapes of the current-potential curves (Figure 2.4) for the coupled reactions. Providing E_{CORR} is far from both equilibrium potentials, the UO_2 oxidation and oxidant reduction reactions can be considered to be proceeding irreversibly.

The currents in Figure 2.4 can be plotted as log(i) versus E to generate an Evans diagram, Figure 2.5, where the intersection of the two curves gives the I_{CORR} and E_{CORR} values. The two linear portions of the plots yield the Tafel regions for each half reaction with slopes of

$$b_a = \frac{2.303\ RT}{\alpha nF} \qquad \textbf{2.9}$$

and

$$b_c = \frac{-2.303\ RT}{(1-\alpha)nF} \qquad \textbf{2.10}$$

As indicated by equation 2.6, the exchange current for the two reactions can be determined by extrapolating the Tafel regions back to the respective equilibrium potentials. The overall measurable current is given by the sum of the two half reactions and yields a modified Butler-Volmer relationship termed the Wagner-Traud equation

$$i = i_{CORR}\left[\exp\left\{\frac{\alpha_A F}{RT}(E - E_{CORR})\right\} - \exp\left\{\frac{(1-\alpha_C)F}{RT}(E - E_{CORR})\right\}\right] \qquad \textbf{2.11}$$

E_{CORR} values can not be predicted from the E_e values of the two half reactions, since they are determined by the shapes of the current-potential relationships, hence, by the kinetic parameters i, α and n. The overall rate of corrosion will be controlled by the kinetically slowest half reaction.

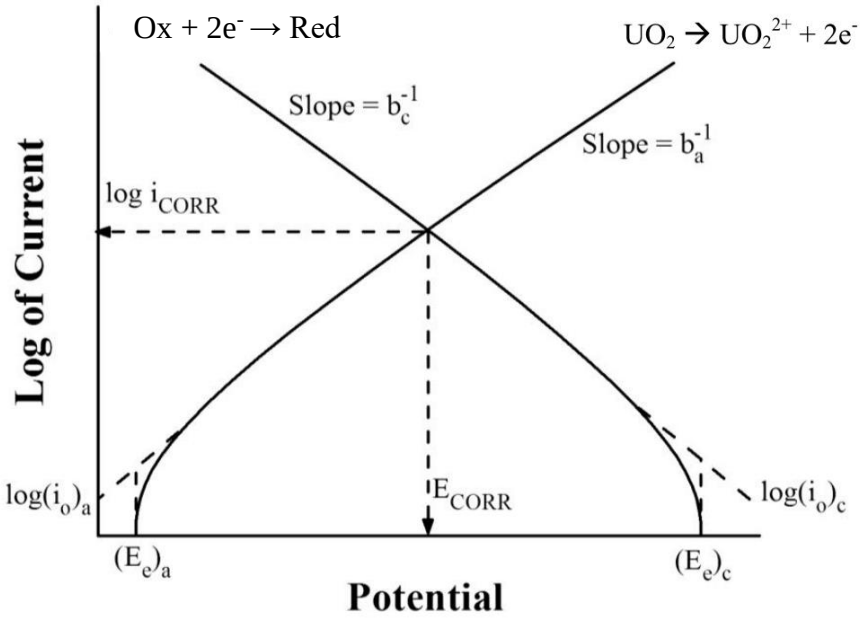

Figure 2.5: An Evans diagram for the corrosion process on UO_2.

2.2.5 Rotating Disc Electrode (RDE) Technique

An electrochemical reaction occurring at an electrode-electrolyte interface is two-dimensional, and the reaction rate can depend on the mass transfer of reactants and/or products to/from the electrode surface. The rate of mass transfer of substance i is proportional to its concentration gradient according to Fick's first law of diffusion[9]

$$-J_i(x,t) = D_i \frac{\partial c_i(x,t)}{\partial x} \qquad \textbf{2.12}$$

where $J_i(x,t)$ is the flux of species i at a distance x from the electrode surface at time t, and D_i is the diffusion coefficient of i at x ,and $\frac{\partial c_i(x,t)}{\partial x}$ is the concentration gradient at x at time t.

The Nernst diffusion layer approximation can be used for steady-state transport conditions. The flux is considered to become constant at a transition point between the bulk solution and diffusion layer (the region within which the concentration gradient exists), Figure 2.6. The distance from the electrode surface to the transition point is the diffusion layer thickness

(δ). Using a rotating disc electrode, the dimensions of the diffusion layer can be controlled and determined using the equation

$$\delta = 1.6 D_i^{2/3} \nu^{1/6} \omega^{-1/2} \qquad \textbf{2.13}$$

where D is the diffusion coefficient ($cm^2.s^{-1}$), ν is the kinematic viscosity of the solution ($cm^{-2}.s^{-1}$) and ω is the rotation rate of the RDE ($rad.s^{-1}$). An increase in ω reduces the diffusion layer thickness, thereby increasing the flux of species i to the electrode surface.

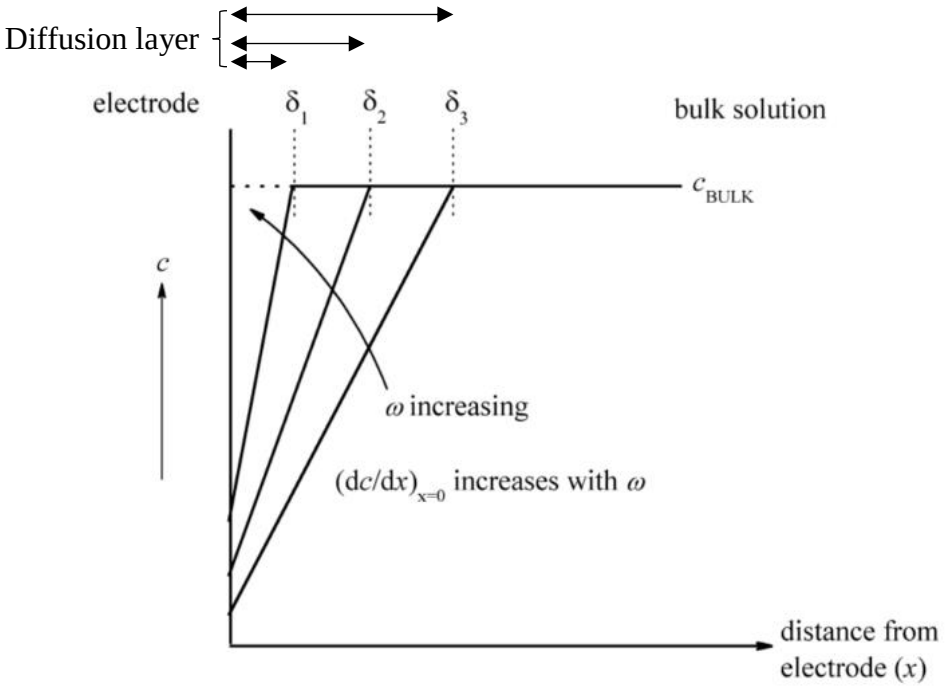

Figure 2.6: Diagram showing the steady-state concentration gradients (d_c/d_x) near an electrode/solution interface as the electrode rotation rate (ω) is increased; δ is the Nernst diffusion layer thickness.

For a general electrochemical reaction,

$$A \pm ne^- \xrightarrow{k} \text{Products} \qquad \textbf{2.14}$$

the reactant species A must diffuse from the bulk solution to the electrode surface before experiencing electron transfer. Assuming that A is the only reacting species, and that the reaction is irreversible, the current density (j) can be related to the diffusion limited current (j_d) by:

$$j = j_d \frac{(c_b - c_s)}{(c_b)} \qquad \textbf{2.15}$$

where c_b is the bulk concentration of species A, c_s is the electrode surface concentration and j_d is the diffusion-limited current density given by the Levich Equation.

$$j_d = n\xi FAc_b D^{2/3} \nu^{-1/6} \omega^{1/2} \qquad \textbf{2.16}$$

where ξ is a numerical coefficient.

The current density can also be related to the surface concentration by

$$j = nFAkc_s^m \qquad \textbf{2.17}$$

in which A is the electrode surface area, and m is the reaction order with respect to the reactant. The kinetic current (j_k, the current in the absence of any mass transport contribution) can be defined as,

$$j_k = nFAkc_b^m \qquad \textbf{2.18}$$

when the surface concentration is the same as the bulk concentration.

These equations can be combined to yield the current measured when the reaction is under mixed kinetic and diffusion control to generate the Koutećky-Levich (K-L) equation

$$\left(\frac{1}{j}\right)^{1/m} = \left(\frac{1}{j_k}\right)^{1/m} + \frac{(j)^{1-1/m}}{B\omega^{1/2}} \qquad \textbf{2.19}$$

where B is given by

$$B = n\xi FAc_b D^{2/3} \nu^{-1/6} \qquad \textbf{2.20}$$

A plot of $\left(\frac{1}{j}\right)^{1/m}$ versus $\omega^{-1/2}$ will yield a linear relationship which can be extrapolated to infinite ω to yield a value for j_k. The log of j_k can then be plotted as a function of applied potential E to yield a Tafel relationship.

The K-L equation is rather insensitive to the value of m, the reaction order, since straight lines are obtained whether m = 1/2, 1 or 2. Thus, the K-L equation alone can not be used to determine the reaction order. An alternative method is to plot data according to the equation,

$$\log(j) = \log(j_k) + m \cdot \log\left(1 - \frac{j}{j_d}\right) \qquad \textbf{2.21}$$

In order to use equation 2.21, the diffusion-limited current must be measured experimentally or calculated from equation 2.16 providing all the other quantities are accurately known.

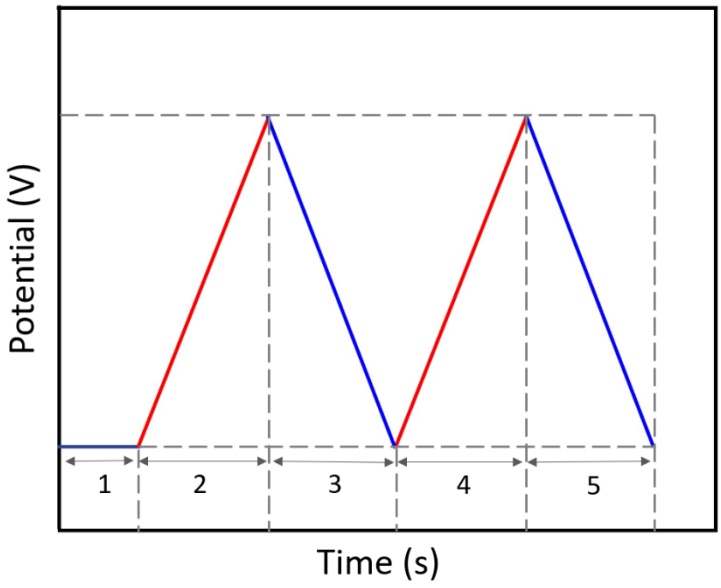

Figure 2.7: The potential-time profile used to record two cyclic voltammograms, t1: cathodic cleaning, t2~t5: two cyclic voltammetric scans with t2 and t4 (red solid lines) representing the forward scans, and t3 and t5 the reverse scans (blue solid lines).

2.2.6 Electrochemical Polarization Techniques

2.2.6.1 Cyclic Voltammetry (CV)

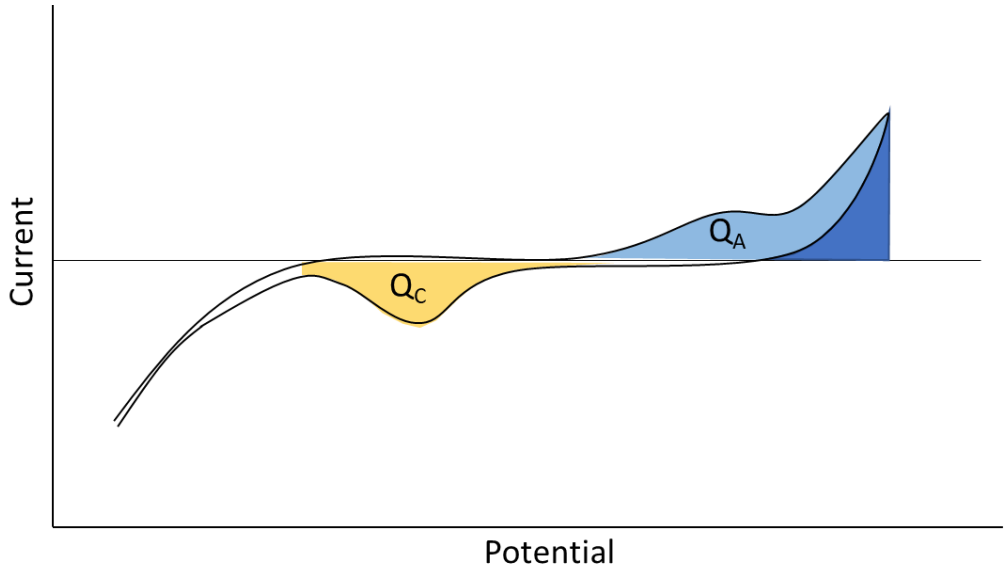

Figure 2.8: A schematic cyclic voltammogram showing the integrated area Q_A and Q_C.

Dynamic polarization curves were generated by sweeping at a constant scan rate between two potentials. The potential profile for a typical double CV scan is shown in Figure 2.7. On a UO_2 electrode, cathodic reduction was performed at -1.2 V vs. SCE to reduce the U^V/U^{VI} oxides present due to air oxidation (t1) followed by a scan up to 0.4 V. Figure 2.8 shows a schematic illustration of a CV recorded on UO_2, showing oxidation to form surface films and dissolved UO_2^{2+} on the forward scan and the reduction of films and deposits on the reverse scan. Integration of the current associated with the current on the forward scan yields a measure of the extent of oxidation (Q_A). The integration of the current on the reverse scan yields an additional contribution to Q_A (the dark shaded area) and a measure of the extent of film formation (Q_C). The difference Q_A-Q_C indicates the amount of oxidized product lost to solution by dissolution. The charge obtained by integration of a current peak can be used to determine the amount of

oxidation and for reduction which occurred within a specific potential interval. The peak positions are an indication of the stage of oxidation and help determine the oxidation mechanism of the electrode material (UO_2 in the present case). The positions of the peaks on the reverse scan indicate whether the oxidized species formed during the forward scan are retained on the electrode surface and available to be reduced, or lost to solution by dissolution and unavailable for reduction. Changing the forward scan potential limit allows the extent and degree of oxidation to be controlled.

2.2.6.2 Potentiostatic Polarization

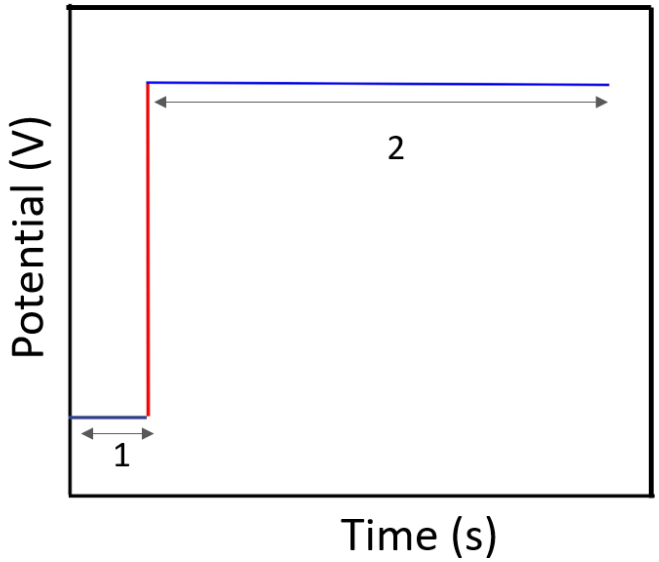

Figure 2.9: The potential-time profile used in a potentiostatic polarization experiment, t1: cathodic reduction at -1.2 V vs. SCE for 2 minutes; t2: a period of oxidation.

Figure 2.9 shows a potential profile used in potentiostatic experiments. The electrode (UO_2) was first cathodically cleaned for 2 minutes at -1.2 V, and then a constant potential (E) was applied to the sample and the current recorded as a function of time. In this project, the potential used in region t2 ranged from +0.15 V to +0.4 V (vs. SCE).

2.2.6.3 Linear Polarization Resistance Measurements

The polarization resistance (R_P) is a measure of resistance to charge transfer at the electrode surface. To measure R_P, a small potential perturbation over a potential range of ± 10 mV, is applied at a slow scan rate of 0.01 $mV.s^{-1}$ starting at the E_{CORR}, Figure 2.10. The slope of the resulting linear current-potential relationship around E_{CORR} yields the R_P value, which is inversely proportional to the rate of interfacial charge transfer $i_{interface}$,

$$R_P = \left(\frac{\Delta E}{\Delta i_{interface}}\right)_{\Delta E \to 0} \qquad \textbf{2.22}$$

In this study, the R_P value is a measure of two simultaneous reactions, UO_2 corrosion and H_2O_2 decomposition, and the $i_{interface}$ is given by

$$i_{interface} = i_{UO_2} + i_{H_2O_2} \qquad \textbf{2.23}$$

where i_{UO_2} and $i_{H_2O_2}$ are the currents due to the UO_2 and H_2O_2 reactions. When positive, $i_{interface}$ is dominated by the currents for the anodic oxidation of UO_2 and H_2O_2, and, when negative, by the cathodic reduction of H_2O_2.

It should be noted that the current-potential relationship plotted in Figure 2.10 is the sum of the current from both anodic and cathodic reactions. For a potential close to E_{CORR}, the exponential relationships comprising the Wagner-Traud equation (2.11) can be linearized to yield the expression;

$$i_{interface} = 2.303 \left\{\frac{b_a b_c}{b_a + b_c}\right\} \frac{1}{R_P} \qquad \textbf{2.24}$$

where b_a and b_c are the two Tafel slopes defined by equation 2.9 and 2.10. This expression can be rearranged to yield

$$R_P = 2.303 \left\{\frac{b_a b_c}{b_a + b_c}\right\} \frac{1}{i_{interface}} \qquad \textbf{2.25}$$

If the Tafel slopes are known, the measured R_P can be converted to $i_{interface}$ using equation 2.25. If these values are unknown, R_P can still be used as a qualitative parameter to compare the interfacial rates.

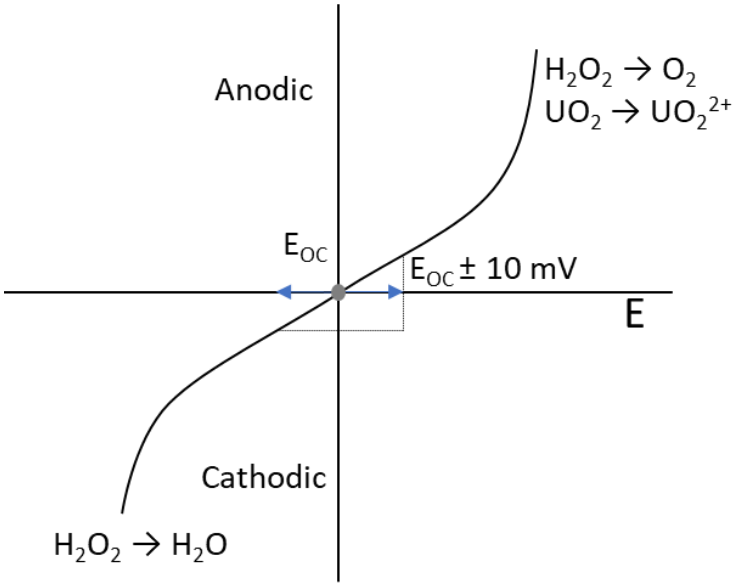

Figure 2.10: Schematic illustration showing the linearization of the Wagner-Traud relationship for a potential E_{OC} ±10 mV. For UO_2 in an H_2O_2 solution both UO_2 corrosion ($UO_2 \rightarrow UO_2^{2+}$) and H_2O_2 decomposition occur ($H_2O_2 \rightarrow H_2O + O_2$).

2.3 X-Ray Photoelectron Spectroscopy (XPS)

2.3.1 Principle of XPS

XPS was used to quantitively analyze the oxidation states of U on the surface of UO_2 electrodes before and after experiments. XPS is a surface sensitive technique that utilizes irradiation by a fixed low-energy X-ray to eject electrons from the core energy levels of the elements comprising the surface of the material, Figure 2.11.

When the sample is irradiated with x-rays with a known energy (hν), electrons with a discrete binding energy (E_b) are ejected from the core levels of the elements with a kinetic energy of E_{kin}. The kinetic energy of the photoelectron is the difference between the energy of the x-ray and the binding energy of the electron plus the work function (∅, the minimum energy required to extract an electron from the surface into a vacuum),

$$E_{kin} = h\nu - (E_b + \emptyset) \qquad \textbf{2.26}$$

Since electrons excited within the sample surface have a low inelastic mean-free path, only electrons from a depth between 0.5 and 3 nm escape with a discrete energy, making XPS a surface sensitive technique.

A valuable feature of XPS is its ability to discriminate between the different oxidation states and chemical environments of an element since the binding energy of the electron for that state will be different. Hence, each element will give rise to a characteristic set of peaks in the

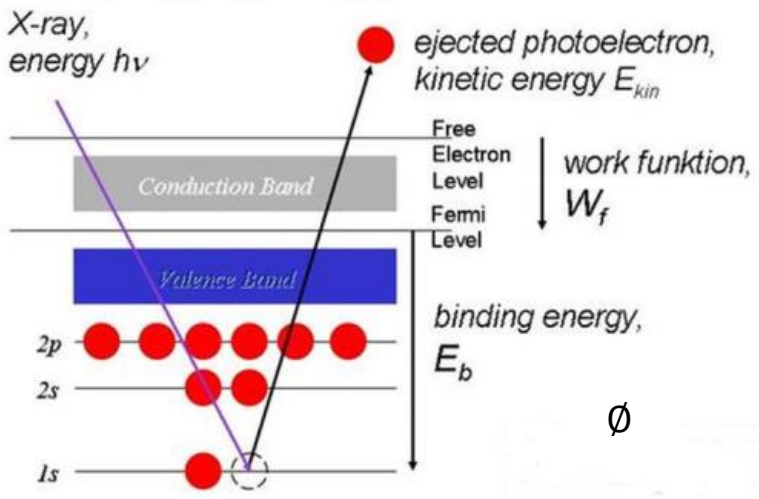

Figure 2.11: Schematic representation of the excitation of a core level (1s) electron by an X-ray of known energy, and the subsequent generation of a photoelectron. (Image source: www.ifw-dresden.de)

photoelectron spectrum. The intensity of the peaks is related to the concentration of the element within the analyzed region. Distinct chemical oxidation states can be analyzed by obtaining high-resolution spectra and using peak fitting programs to deconvolute the spectra and yield the percent composition of each state.

Figure 2.12 shows a representative low-resolution survey photoelectron spectrum recorded on a freshly polished SIMFUEL UO_2 electrode. The Al Kα X-ray source can generate several characteristic U lines, but the principal lines are the U 4f peaks since those are the most intense. The spectrum is a plot of the signal intensity vs. binding energy. The U 4f, U 4d and U 5d peaks all appear as doublets, while the O 1s and C 1s peaks are singlets. This is expected according to spin-orbit splitting.[10]

Additional small peaks are present in close proximity to the U 4f peaks on the high binding energy side and are known as satellite peaks. These satellite peaks are commonly interpreted as shake-up satellites, which result from charge transfer processes. The position and

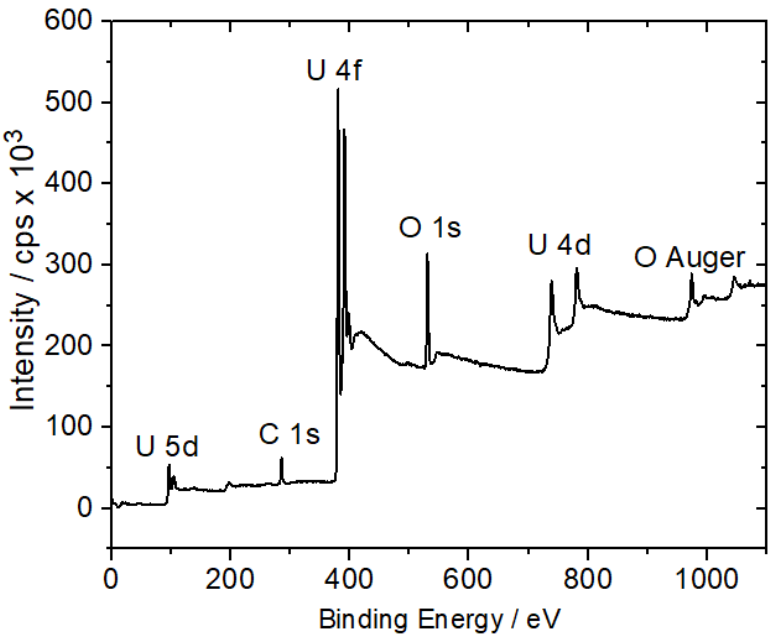

Figure 2.12: Survey spectrum of a freshly polished 3 at.% SIMFUEL electrode. The source of the most prominent lines is indicated on the graph.

shape of these satellite peaks is reproducible and commonly used to confirm the identity of the oxidation states present in the element.

2.3.2 XPS Experimental Details

All XPS spectra were collected using a Kratos Axis NOVA spectrometer with a monochromatic Al Kα source (1486.6 eV). The instrument work function was calibrated to give a binding energy of 83.96 eV for the Au $4f_{7/2}$ line for metallic Au and the spectrometer dispersion was adjusted to give a binding energy of 932.62 eV for the Cu $2p_{3/2}$ line of metallic Cu. Survey spectra were recorded for the energy range of 0-1100 eV on a surface area of 300 × 700 μm^2 with a pass energy of 160 eV. High resolution spectra were recorded over an area of 300 × 700 μm^2 using a pass energy of 20 eV. When necessary, spectra were charge-corrected by reference to the main line of C 1s at 285 eV. All analyses and fitting procedures were performed using Casa XPS software (version 2.3.14).

The U4f peaks are the most intense and best resolved peaks in the U spectrum, and were used to analyze the oxidation state of U on the surface.[11-13] High-resolution scans were performed for the spectral region including the U $4f_{5/2}$ and U $4f_{7/2}$ peaks and their satellites, and the U 5f valence band region.

The fitting procedure used to analyze the U 4f and O 1s spectral regions involved a 50% Gaussian and 50 % Lorentzian fitting routine with a Shirley background correction. The fractions of U^{IV}, U^{V} and U^{VI} were determined from the fitted U 4f spectra. The fitting procedure was based on published reference spectra.[14-17] The U $4f_{5/2}$ and U $4f_{7/2}$ peaks were located at ~ 391 eV and 380 eV with the spin-orbital interaction causing a separation of 10.9 eV, Figure 2.13. The binding energies for U^{IV}, U^{V} and U^{VI} in the U $4f_{7/2}$ peak for mixed-valent U compounds vary with the chemical composition of the compounds. The energy separations are relatively

consistent., i.e., 0.5-0.9 eV between U^{IV} and U^{V} and 0.8-1.1 eV between U^{V} and U^{VI}. The satellite peaks associated with the U^{IV}, U^{V} and U^{VI} components are also characteristic of the U 4f spectrum. The reported distance between the main peak and the satellite peak is relatively consistent, i.e., 6-7 eV for U^{IV}, 8-9 eV for U^{V} and 4 eV and 10 eV for U^{VI}.

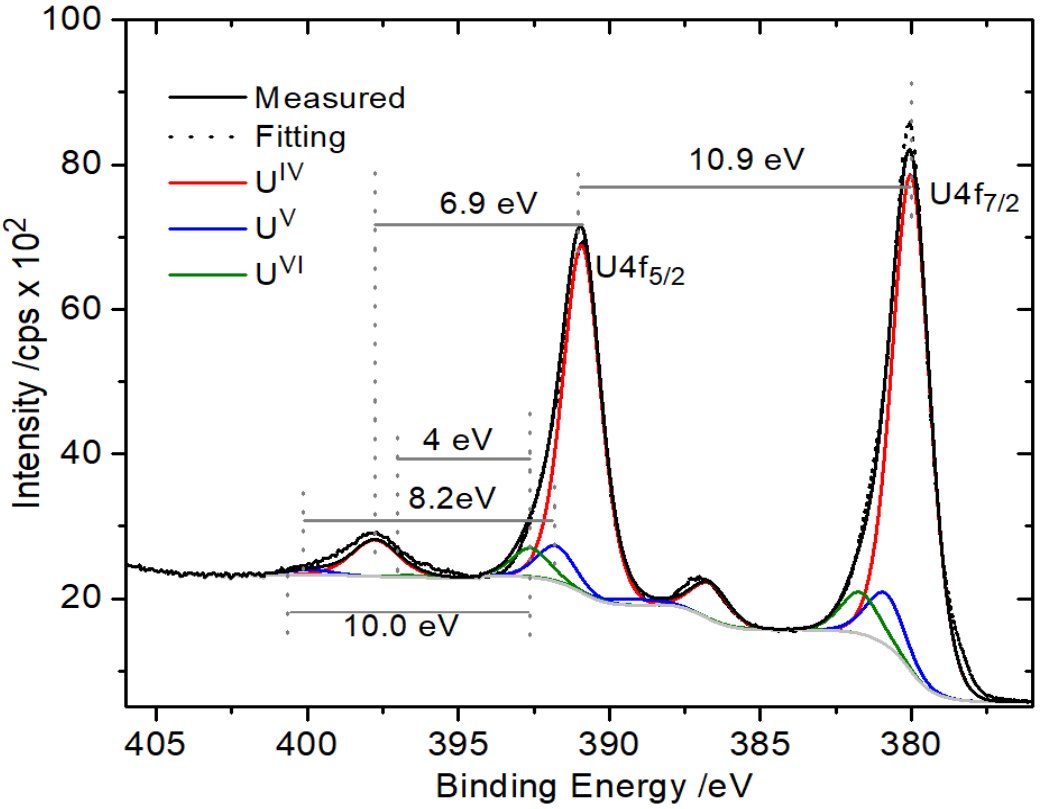

Figure 2.13: High-resolution XPS spectra recorded on the surface of 3 at% SIMFUEL.

2.4 Scanning Electron Microscopy (SEM) and Energy Dispersive X-ray (EDX) Spectroscopy

2.4.1 Principles of SEM/EDX

SEM is an instrument that uses a high energy beam of electrons rather than light to form images, and it can produce high-resolution images of surface morphologies with an excellent depth of field. The resolution of SEM is ~1 nm. The sample surface must be electrically conductive otherwise the electrons will charge the surface. As illustrated in Figure 2.14, the electron source is focused to a fine beam via magnetic scan coils and scanned across the surface of the sample. SEM must be carried out under high vacuum (10^{-6} Torr) to minimize interference from the molecules in air. The electrons are generated by thermionic emission from a metal filament, and accelerated to 0.5 to 30 keV.[18] The electrons reflected from the surface are

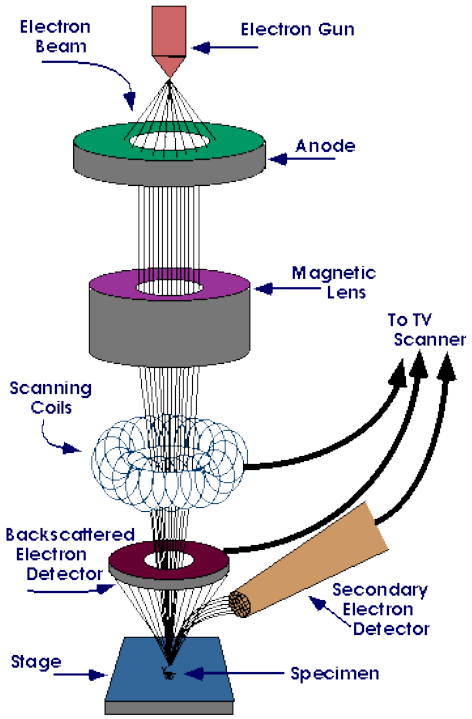

Figure 2.14: Schematic illustration of a Scanning Electron Microscope. (Image source: http://www.purdue.edu/REM/rs/sem.htm)

collected, amplified and plotted as a two-dimensional image of the signal intensity. The intensity of the secondary electrons is mainly determined by the topography of the sample, the electrons can escape the surface if their energy is larger than the work function of 2-6 eV.

The Primary electron beam generates secondary electrons and backscattered electrons. The secondary electrons are generated from inelastic collisions and can be produced within the first few nm of the surface and used to image the topography of the surface. Most secondary electrons come from shallow locations on the sample surface and have a high probability of reaching the detector, thus appearing bright in the image. Electrons from deeper locations are fewer and thus appear darker in the image. Backscattered electrons are electrons elastically scattered with no loss of kinetic energy. The image produced yields some chemical information since the probability of backscattering increases with the atomic number of the element. When the primary beam causes ejection of an electron from an inner shell of an element, an electron from a higher energy level can fill the vacancy in the process emitting an X-ray characteristic of the element from which it came. The X-ray emission signal can be sorted by energy in an energy dispersive X-ray detector. These distributions are characteristic of the elements and site specific and can be obtained by scanning a specific area to produce elemental images showing the spatial distribution of particular elements in the field of view.

2.4.2 SEM/EDX Experimental Details

SEM images were collected before and after electrochemical experiments. The samples were sonicated in and rinsed with Millipore water and then dried in an Ar stream prior to being placed in the microscope. A Hitachi S-4500 (Hitachi, Japan) field emission SEM was used at an electron acceleration voltage of 15 kV (or 10 kV) resulting in a spatial resolution of < 2 nm. Micrographs were recorded at various magnifications (100 – 5000X).

2.5 Raman Spectroscopy

2.5.1 Principles of Raman Spectroscopy

Raman spectroscopy provides information about molecular vibrations that can be used to identify phases. This technique focuses a monochromatic laser source onto a sample and detects the scattered light emitted. The majority of the scattered light is of the same frequency as that from the laser source and is termed Rayleigh scattering. A very small amount of the scattered light is scattered with a frequency different to that of the laser due to interactions between the incident electromagnetic wave and the vibrational energy waves of the molecules in the sample. The shift in wavelength of the inelastically scattered radiation provides chemical and structural information about the molecule being analyzed.

Depending on the vibrational state of the molecule, Raman shifted photons can be of either higher or lower energy. When the energy of the scattered radiation is less than the incident radiation, it is called Stokes radiation and when it is higher it is called anti-Stokes radiation, Figure 2.15.[19] Generally, Raman spectra are plotted with respect to the laser frequency, with the Rayleigh band set at 0 cm^{-1}. The band positions will lie at frequencies which yield information about the vibrational modes in the system.

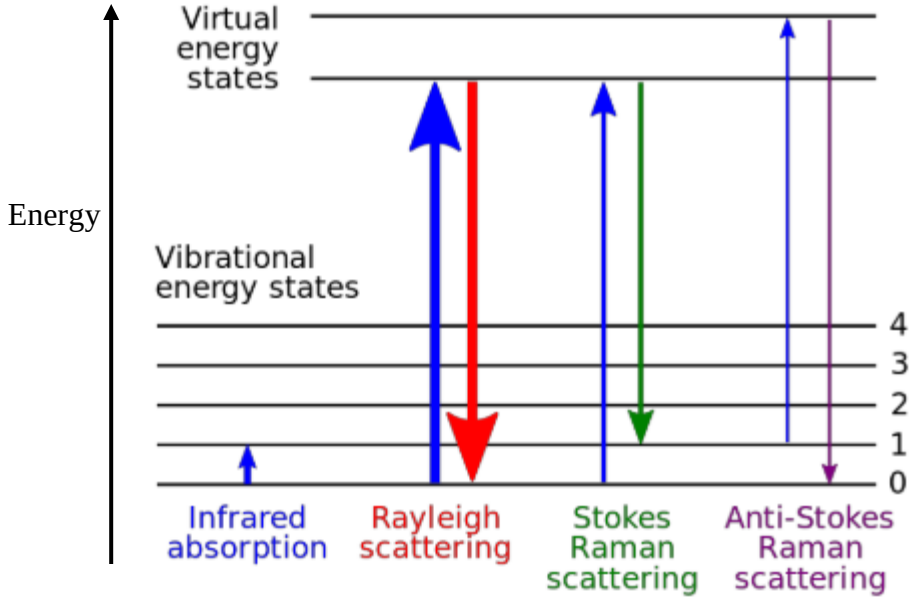

Figure 2.15: Energy level diagram showing the states involved in a Raman signal. The line thickness indicated qualitatively to the signal strength from the different transitions.

2.5.2 Raman Experimental Details

Raman Spectra were obtained using a Renishaw 2000 Laser Raman spectrometer (Renishaw PLC., UK) equipped with a Leica DMLM microscope. Spectra were excited using a He-Ne laser with a wavelength of 632.8 nm. The laser beam was focused to ~2 μm in diameter with a 50x uncoated objective lens on to the electrode mounted on carbon tape attached to a glass slide. The power of the laser beam was kept at 50% to avoid laser heating effects. The spectrometer was calibrated with a standard Si wafer, which has an intense Raman band at 520 cm^{-1}. Spectra were measured over the wavenumber range of 120 to 1400 cm^{-1}. After the measurements, the Gaussian-Lorentzian peak model and a Shirley baseline correction were used to fit the Raman peaks. The deconvolution of the broad band at 500-700 cm^{-1} has been described in detail elsewhere. [5, 8]

2.6 Inductively Coupled Plasma Mass Spectroscopy (ICP-MS) and Inductively Coupled Plasma Atomic Emission Spectroscopy (ICP-AES)

2.6.1 ICP-MS/ICP-AES Principles

Both ICP-AES and ICP-MS are analytical techniques used to determine element concentration at trace level concentrations. Figure 2.16 shows a typical illustration of an ICP-MS instrument. An ICP-MS instrument combines a high-temperature ICP with a mass spectrometer. The solution samples are introduced into a Ar plasma, and the elemental components separated and detected by the mass spectrometer. The solution is nebulized in a spray chamber, with a radio frequency (RF) power generator used to produce an intense electromagnetic field which supplies energy to the induction coil. Most elements in the sample are atomized and ionized in the high temperature plasma (6000-7000 K) as a result of the inelastic collisions between the neutral Ar atoms and the charged particles. The ions are focused by electrostatic lenses as they enter the mass spectrometer where they are filtered under high vacuum by their mass to charge ratio.

Figure 2.17 shows an illustration of the major components in an ICP-AES instrument.[20] The difference between ICP-MS and ICP-AES is the detector. In ICP-AES, the molecules in the sample break into small atoms which then lose electrons and recombine repeatedly in the plasma, each element gives characteristic photon wavelengths. Within the optical chamber, the intensities of the light at all visible wavelengths can be measured simultaneously by photodetectors, allowing the instrument to quickly analyze multiple elements.

2.6.2 ICP-MS/ICP-AES Experimental Details

In this project, the Agilent 7700x ICP-MS and the Perkin Elmer Optima 3300 Dual 24 View ICP-AES in the Biotron Facility (The University of Western Ontario) were used. Prior to sample analysis, the instruments were calibrated with a series of ^{238}U standards. The lower

detection limit for U is 0.02 µg.L^{-1} for ICP-MS and 0.01 mg.L^{-1} for ICP-AES. Samples from experiments were diluted with 2% HNO_3 before injection to achieve the optimal detection range and to prevent precipitation.

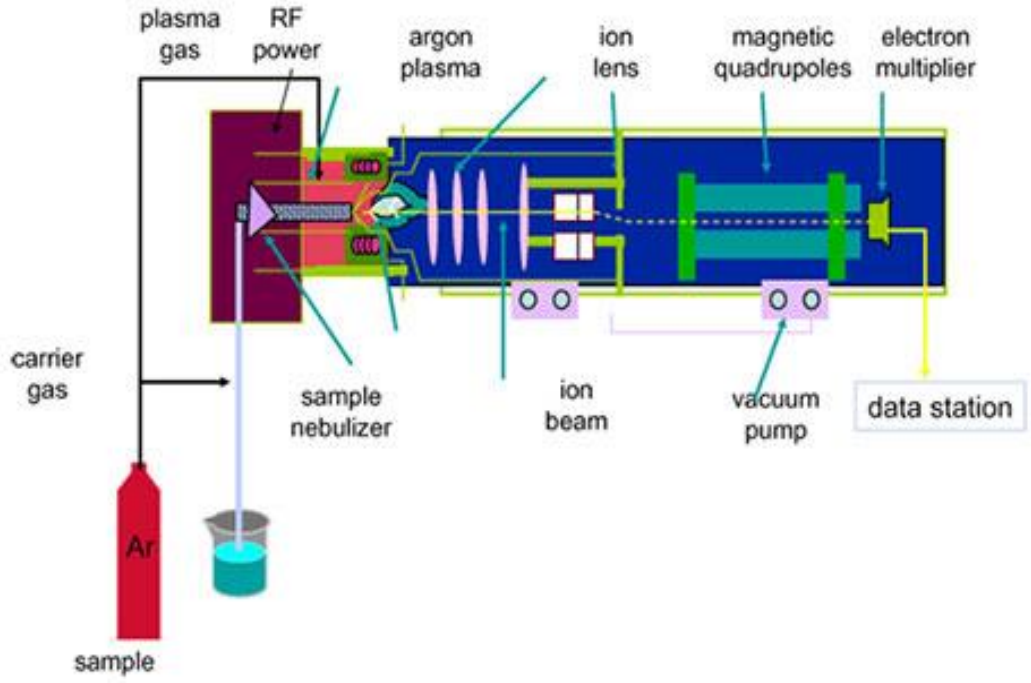

Figure 2.17: Schematic illustration showing the major components of a typical ICP-AES instrument.[19]

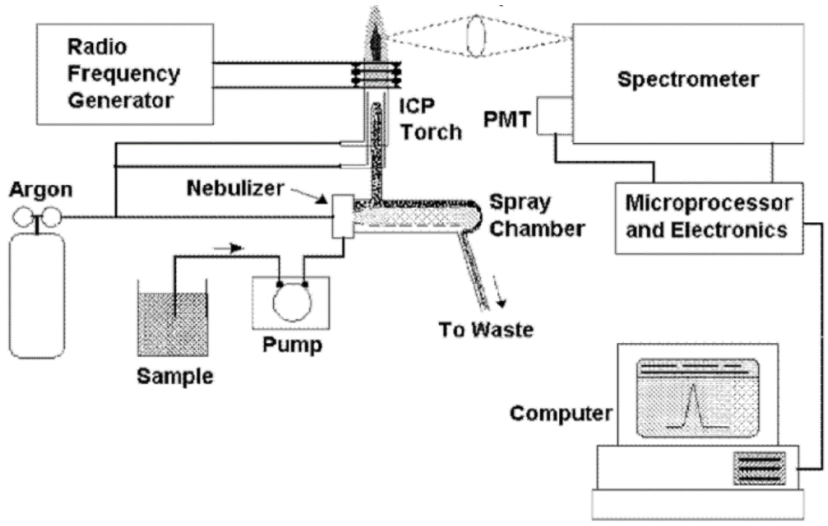

Figure 2.16: Schematic illustration of a typical ICP-MS instrument. (Image source: http://www.emdmillipore.com)

2.7 UV-Vis Spectrophotometry

2.7.1 Principles of UV-Vis Spectrophotometry

Ultraviolet and visible (UV-Vis) absorption spectroscopy measures the attenuation of a beam of light passed through a sample. Absorption spectroscopy uses electromagnetic radiation with a wavelength between 200 nm and 800 nm and is divided into UV (200-400 nm) and visible ranges (400-800 nm).

Figure 2.18 shows the arrangement of a typical UV-Vis instrument. A beam of light generated from the deuterium and tungsten lamp sources is passed through a quartz cuvette which contains the solution. The intensity of the light beam is measured before and after passage through the sample, and the absorbance is calculated using the formula,

$$A = \log I_0/I \qquad \textbf{2.27}$$

where A is the absorbance of the sample, I_0 is the intensity of incident beam, and I is the light intensity after passing though the sample. The relationship between the absorption and compound concentration is described by the Beer-Lambert law,

$$A = \varepsilon \cdot c \cdot l \qquad \textbf{2.28}$$

where ε is the molar absorptivity expressed in units of $L.mol^{-1}.cm^{-1}$, c is the concentration of the sample in $mol.L^{-1}$, and l is the optical path length in cm.

This technique is based on the ability of a molecule to absorb UV and visible light due to electron excitation from the outer shells to a higher energetic level. The characteristic electron transition takes place from the Highest Occupied Molecular Orbital (HOMO) to the Lowest Unoccupied Molecular Orbital (LUMO). The input energy is absorbed at different frequencies which are characteristic of the chemical structure of the absorbing species. An optical

spectrometer measures the wavelengths at which absorption occurs and yields a spectrum of absorbance vs. wavelength.

2.7.2 UV-Vis Experimental Details

All the UV-Vis measurements were performed using a diode array spectrophotometer (BioLogic Science Instruments). H_2O_2 concentrations were determined using the Ghormley tri-iodide method in which I^- is oxidized to I_3^- by H_2O_2 in the presence of ammonium molybdate as a catalyst.[21, 22] The molar absorptivity of I_3^- is 25,500 $L.mol^{-1}.cm^{-1}$ and the measurements were performed in a quartz cuvette with a 1 cm path length. The absorbance at 352 nm was measured, and the detection limit for H_2O_2 using this instrument is 3×10^{-6} $mol.L^{-1}$. H_2O_2 analyses were performed immediately after sampling an experimental solution with solutions containing H_2O_2 covered by commercial grade Al foil to avoid photolytic decomposition.

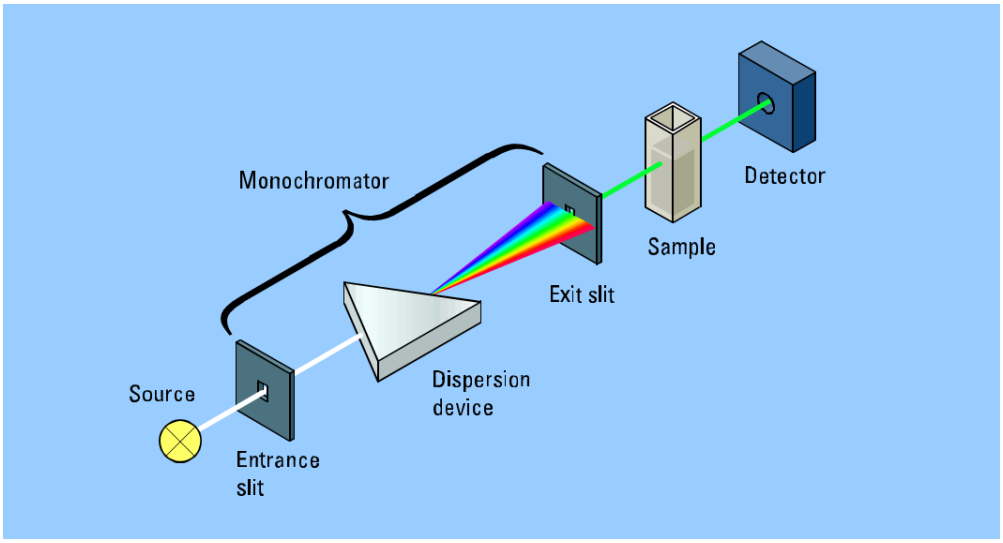

Figure 2.18: Illustration of a diode array UV-Vis spectrophotometer. (Image source: http://faculty.sdmiramar.edu)

2.8 Reference

[1] P.G. Lucuta, R.A. Verrall, H. Matzke, B.J. Palmer, Microstructural features of SIMFUEL — Simulated high-burnup UO_2-based nuclear fuel, Journal of Nuclear Materials, 178 (1991) 48-60.

[2] H. He, P.G. Keech, M.E. Broczkowski, J.J. Noël, D.W. Shoesmith, Characterization of the influence of fission product doping on the anodic reactivity of uranium dioxide, Canadian Journal of Chemistry, 85 (2007) 702-713.

[3] S. Sunder, D. Shoesmith, N. Miller, Electrochemical studies of corrosion of SIMFUEL: simulated used UO_2 fuel, Materials Research Society, Pittsburgh, PA (United States), 1993.

[4] S. Sunder, N.H. Miller, W.H. Hocking, P.G. Lucuta, X-ray photoelectron spectra of SIMFUEL, Journal of Alloys and Compounds, 213-214 (1994) 503-505.

[5] H. He, D. Shoesmith, Raman spectroscopic studies of defect structures and phase transition in hyper-stoichiometric $UO_{(2+x)}$, Phys Chem Chem Phys, 12 (2010) 8108-8117.

[6] H. He, Z. Qin, D.W. Shoesmith, Characterizing the relationship between hyperstoichiometry, defect structure and local corrosion kinetics of uranium dioxide, Electrochimica Acta, 56 (2010) 53-60.

[7] H. He, Z. Ding, D.W. Shoesmith, The determination of electrochemical reactivity and sustainability on individual hyper-stoichiometric UO_{2+x} grains by Raman microspectroscopy and scanning electrochemical microscopy, Electrochemistry Communications, 11 (2009) 1724-1727.

[8] M. Razdan, D.W. Shoesmith, Influence of trivalent-dopants on the structural and electrochemical properties of uranium dioxide (UO_2), Journal of The Electrochemical Society, 161 (2014) H105-H113.

[9] F.L.R. Bard A.J., Electrochemical methods fundamentals and applications second ed., John Wiley & Sons, New York.

[10] C.S. Fadley, D.A. Shirley, Multiplet splitting of metal-atom electron binding energies, Physical Review A, 2 (1970) 1109-1120.

[11] T.B. Scott, G.C. Allen, P.J. Heard, M.G. Randell, Reduction of U(VI) to U(IV) on the surface of magnetite, Geochimica et Cosmochimica Acta, 69 (2005) 5639-5646.

[12] Y.A. Teterin, V.M. Kulakov, A.S. Baev, N.B. Nevzorov, I.V. Melnikov, V.A. Streltsov, L.G. Mashirov, D.N. Suglobov, A.G. Zelenkov, A study of synthetic and natural uranium oxides by X-ray photoelectron spectroscopy, Physics and Chemistry of Minerals, 7 (1981) 151-158.

[13] R. Drot, E. Simoni, M. Alnot, J.J. Ehrhardt, Structural environment of uranium (VI) and europium (III) species sorbed onto phosphate surfaces: XPS and optical spectroscopy studies, Journal of Colloid and Interface Science, 205 (1998) 410-416.

[14] M. Razden, Electrochemical and surface compositional studies on uranium dioxide, PhD Thesis, Chemistry Department, The University of Western Ontario, 2013.

[15] M. Schindler, F.C. Hawthorne, M.S. Freund, P.C. Burns, XPS spectra of uranyl minerals and synthetic uranyl compounds. I: The U 4f spectrum, Geochimica et Cosmochimica Acta, 73 (2009) 2471-2487.

[16] B.G. Santos, H.W. Nesbitt, J.J. Noël, D.W. Shoesmith, X-ray photoelectron spectroscopy study of anodically oxidized SIMFUEL surfaces, Electrochimica Acta, 49 (2004) 1863-1873.

[17] E.S. Ilton, J.-F. Boily, P.S. Bagus, Beam induced reduction of U(VI) during X-ray photoelectron spectroscopy: The utility of the U4f satellite structure for identifying uranium oxidation states in mixed valence uranium oxides, Surface Science, 601 (2007) 908-916.

[18] P.E. Flewitt, R.K. Wild, Physical methods for materials characterisation, CRC Press2017.

[19] E. Smith, G. Dent, Modern Raman spectroscopy: a practical approach, John Wiley & Sons2013.

[20] C. BOSS, K. Fredeen, Concepts, Instruments and techniques in Inductively Coupled Plasma Optical Emission Spectrometry, 2nd ed, PerkinElmerCorp. Norwalk, CT, USA, (1997).

[21] I. Štefanić, J.A. LaVerne, Temperature dependence of the hydrogen peroxide production in the γ-radiolysis of water, The Journal of Physical Chemistry A, 106 (2002) 447-452.

[22] C. Hochanadel, Effects of cobalt γ-radiation on water and aqueous solutions, The Journal of Physical Chemistry, 56 (1952) 587-594.

Chapter 3

3 Anodic Reactions Occurring on Simulated Spent Nuclear Fuel (SIMFUEL) in Hydrogen Peroxide Solutions Containing Bicarbonate/Carbonate – The Effect of Fission Products

3.1 Introduction

The universally accepted concept for the disposal of high level nuclear waste, in particular spent nuclear fuel, is based on multiple barriers including the fuel waste form, durable metal containers, a clay buffer and seals around the container, and a deep geologic repository (DGR).[1] While such a DGR can provide acceptable assurance for long term containment it is necessary to consider the consequences of container failure which could lead to exposure of the fuel to groundwater. Since the spent fuel contains the radioactive fission and activation products, its behaviour in contact with groundwater provides the critical radioactivity source term in assessments of repository safety.[2, 3]

The chemistry/electrochemistry of UO_2 has been studied in a range of proposed repository conditions.[4-11] The redox condition of the groundwater contacting the fuel after container failure is the key factor likely to control the fuel corrosion rate since the solubility of U is orders of magnitude higher for U^{VI} than for the reduced U^{IV} form.[12] If container failure occurs while significant radiation fields exist in the fuel, oxidizing conditions are expected to prevail near the fuel surface as a consequence of water radiolysis.[9, 13, 14]

The radiation-induced dissolution of spent fuel has been investigated both experimentally and computationally,[15-19] and the key oxidant has been shown to be H_2O_2 produced by the alpha radiolysis of the ground water.[13, 20, 21] The fate of H_2O_2 is either to be consumed where it is produced at the fuel surface, or to be transported away from the fuel surface and scavenged

by available reducing species such as Fe^{2+} and H_2 produced by corrosion of the steel containment vessel. Fuel corrosion involves the coupling of UO_2 corrosion and H_2O_2 reduction,[22, 23]

$$H_2O_2 + 2e^- \rightarrow 2OH^- \qquad \textbf{3.1}$$

$$UO_2 \rightarrow UO_2^{2+} + 2e^- \qquad \textbf{3.2}$$

However, H_2O_2 can also undergo oxidation reaction 3.3, and the coupling of reaction 3.1 and 3.3 would lead to H_2O_2 decomposition to produce the alternative oxidant O_2,

$$H_2O_2 \rightarrow O_2 + 2H^+ + 2e^- \qquad \textbf{3.3}$$

While an oxidant, O_2, would react over two orders of magnitude more slowly with UO_2 than the radiolytically produced H_2O_2.[4] As indicated in Figure 3.1, the relative importance of the two anodic reactions will determine the stability of UO_2 in H_2O_2 solutions.

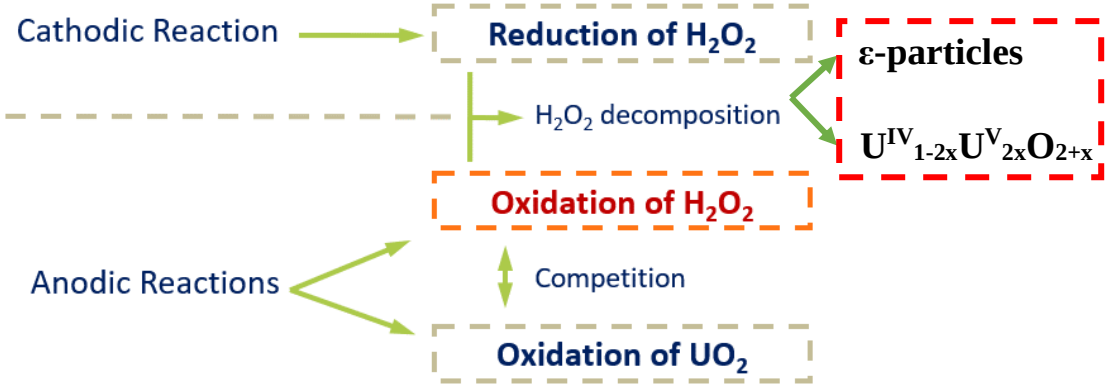

Figure 3.1: Schematic illustration of the possible reactions of H_2O_2 on a UO_2 surface, showing that the H_2O_2 oxidation reaction can be catalyzed by a UO_{2+x} surface or by noble metal (ε) particles.

Attempts have been made to determine the mechanistic balance between UO_2 dissolution and H_2O_2 decomposition under open circuit (corrosion) conditions. At low $[H_2O_2]$ ($< 10^{-4}$ mol.L^{-1}) the corrosion potential (E_{CORR}) increased from ~-0.4 V to ~-0.1 V (vs. SCE) with increasing

[H_2O_2], and recent studies showed that the value of the steady-state E_{CORR} achieved was directly related to the extent of oxidation of the surface, as determined by X-ray photoelectron spectroscopy.[24] Over the intermediate [H_2O_2] range, 10^{-4} to 5×10^{-3} mol.L^{-1}, E_{CORR} rose rapidly to a final steady-state value (~0.1 V), indicating that the first stage of oxidation of the surface from $U^{IV}O_2$ to $U^{IV}_{1-2x}U^{V}_{2x}O_{2+x}$ was rapid. At potentials in this range, both oxidative dissolution as $U^{VI}O_2^{2+}$ and H_2O_2 decomposition are possible. Based on the independence of E_{CORR} on [H_2O_2], it was claimed that the corrosion of the surface and the decomposition of H_2O_2 on the $U^{IV}_{1-2x}U^{V}_{2x}O_{2+x}$ layer were both limited by the slow dissolution of U^{VI} species from a U^{VI} surface layer. XPS measurements confirmed the presence of U^{VI} on the electrode in this potential range.

For [H_2O_2] $\geq 5 \times 10^{-3}$ mol.L^{-1}, E_{CORR} increased approximately linearly with concentration and coverage of the electrode by U^{VI} species increased. Experiments in which the amount of dissolved U^{VI} was measured showed that, at these higher [H_2O_2], dissolution was accelerated [25, 26], and the rate became first order with respect to [H_2O_2]. The increase in dissolution rate coupled to an apparently greater coverage by insulating and potentially blocking surface U^{VI} species was taken as an indication of enhanced dissolution at locally acidified sites on the electrode surface.[27] How these changes influenced the rate and mechanism of H_2O_2 decomposition was not investigated. A similar mechanism was proposed for the influence of α-radiolytically produced H_2O_2 on UO_2 corrosion and H_2O_2 decomposition.[13] It has also been claimed that, in the presence of both H_2O_2 and HCO_3^-/CO_3^{2-} at high concentrations, UO_2 corrosion is accelerated by the formation of a soluble peroxycarbonate complex, $U^{VI}O_2(O_2)_x(CO_3)_y^{2-2x-2y}$.[28, 29]

While the cathodic reduction of H_2O_2 on UO_2 has been investigated, [22, 23, 26, 30, 31] the kinetics of H_2O_2 oxidation and its relative importance when accompanied by the anodic dissolution of UO_2 has received minimal attention. Wu et al. [32] studied the anodic behavior on a SIMFUEL electrode in HCO_3^-/CO_3^{2-} solutions containing various concentrations of H_2O_2. The rates of both anodic reactions were found to be at least partially controlled by the chemical release of U^{VI} surface species as $U^{VI}O_2(CO_3)_x^{(2-2x)+}$ and H_2O_2 oxidation appeared to be the dominant reaction, although a quantitative separation was not achieved. In addition, the role of the noble metal (ε) particles, known to exist in spent fuel and present in the SIMFUEL used,[33, 34] on these anodic reactions remains unknown.

In this study, the mechanisms of both the anodic reactions are investigated. The specific goals are the following: (i) to determine the mechanisms of both reactions; (ii) to determine their relative importance as a function of potential and carbonate concentration ($[CO_3]_{tot}$); and (iii) to elucidate the role played by noble metal (ε) particles in determining the relative importance of anodic dissolution and H_2O_2 decomposition.

3.2 Experimental

3.2.1 Electrode Materials and Preparation and Solutions

SIMFUELs are UO_2 pellets doped with non-radioactive elements to replicate the effects of in-reactor irradiation. [35] Two different SIMFUEL samples were used in this study: one doped with 11 elements (Sr, Y, Ce, Nd, La, Zr, Ba, Pd, Ru, Mo, Rh) to simulate a fuel with both a rare earth doped lattice and noble metal (ε) particles, designated (RE + ε), and a second one not containing the noble metal elements (Pd, Ru, Rh, Mo) and hence free of ε-particles, designated

RE. The SIMFUELs were fabricated and supplied by Canadian Nuclear Laboratories (Chalk River, Canada).

All solutions were prepared with distilled deionized water (resistivity, ρ = 18.2 MΩ cm) purified using a Millipore milli-Q-plus unit to remove organic and inorganic impurities, and subsequently passed through a milli-Q-plus ion exchange column. Experiments were conducted in a 0.1 mol.L^{-1} NaCl solution containing 0.02 mol.L^{-1} H_2O_2 with the pH adjusted to 9.7 with NaOH. $NaHCO_3$ was added to a concentration ($[CO_3]_{tot}$) in the range 0.01 to 0.1 mol.L^{-1}. All chemicals were reagent grade and purchased from Fisher Scientific.

3.2.2 Electrochemical Cell and Equipment

Experiments were conducted using a three-compartment, three-electrode electrochemical cell. The reference electrode was a commercial saturated calomel electrode (SCE) (0.242 V vs. SHE) at 20 ^{o}C. The counter electrode was a Pt foil spot-welded to a Pt wire. The cell was placed in a Faraday cage to minimize interference from external noise. The rotation rate of the rotating disc electrode (RDE) was controlled using an analytical rotator from Pine Instruments (model ASR). All the electrochemical experiments were performed with a Solartron 1287 potentiostat controlled by CorrWare Version 2.7 software. The electrode resistivity (ρ (RE) = 174 ohm.cm; ρ (RE + ε) = 81 ohm.cm) was compensated using the current interrupt procedure. [36]

3.2.3 Electrochemical Experiments

Before each experiment, the SIMFUEL electrode was wet polished with 1200 grit SiC paper and rinsed with Millipore water. The working electrode was then cathodically cleaned at a potential of -1.2 V for 2 minutes prior to each experiment. For potentiostatic experiments, the working electrodes were oxidized for 10 minutes at a potential in the range of 0.1 - 0.4 V until a

steady state current was achieved. In dissolution experiments, the working electrode was held at each potential for one hour.

In these experiments, the electrodes were oxidized for one hour either at the corrosion potential (E_{CORR}) or at a positive applied potential (E) (0.2, 0.3 or 0.4 V). The amount of dissolved U in the solution was then measured and converted into an equivalent charge using Faraday's Law,

$$m = QM/Fn \qquad \textbf{3.4}$$

where m is the mass reacted, Q is the electrochemical charge equivalent to the amount of U dissolved, F is Faraday's constant (96485 $C.mol^{-1}$), and n is the number of electrons involved in the dissolution reaction (2 for $U^{IV} \rightarrow U^{VI}$). After anodic oxidation for one hour, the electrode was quickly transferred to a H_2O_2-free solution for cathodic stripping voltammetry (CSV) to estimate the amount of charge consumed in the production of surface oxidized layers.

3.2.4 Electrode Surface and Solution Analyses

3.2.4.1 Inductively Coupled Plasma Atomic Emission Spectroscopy (ICP-AES)

The concentration of U in the solution was analyzed by Inductively Coupled Plasma Atomic Emission Spectroscopy (ICP-AES). These analyses were performed with a Perkin Elmer Optima 3300 Dual 24 View ICP-AES located in the Biotron facility (Western University). The U emission was monitored at a wavelength of 419 nm, with a detection limit of 0.01 mg L^{-1}. Prior to injection into the spectrometer, samples were mixed with 2% HNO_3 to prevent U precipitation. The calibration standards used were 0.5, 1.0, and 5.0 mg L^{-1} U solutions, and a 2% HNO_3 solution was used as a blank sample.

3.2.4.2 Scanning Electron Microscopy (SEM) and Energy Dispersive X-ray Spectroscopy (EDX)

The surface morphology of the electrode was obtained using a Hitachi S-4500 Field emission scanning electron microscope equipped with a Quartz XOne energy dispersive X-ray analyzer located at Surface Science Western (SSW). Immediately after an experiment, samples were rinsed with Millipore H_2O and dried in an Ar stream prior to being placed in the microscope. The electron beam potential was maintained at 5.0-15 keV and the working distance was 10 mm during image collection resulting in a spatial resolution of < 2 nm. Micrographs were recorded at various magnifications (100 – 5000X).

3.2.5 Raman Spectroscopy

Raman Spectra were obtained using a Renishaw 2000 Laser Raman spectrometer (Renishaw PLC., UK) equipped with a Leica DMLM microscope. Spectra were excited using a He-Ne laser with a wavelength of 632.8 nm. The laser beam was focused to ~2 μm in diameter with a 50x uncoated objective lens on to the electrode mounted on carbon tape attached to a glass slide. The power of the laser beam was kept at 50% to avoid laser heating effects. The spectrometer was calibrated with a standard Si wafer, which has an intense Raman band at 520 cm^{-1}. Spectra were measured over the wavenumber range of 120 to 1400 cm^{-1}. After the measurements, the Gaussian-Lorentzian peak model and a Shirley baseline correction were used to fit the Raman peaks. The deconvolution of the broad band at 500-700 cm^{-1} has been described in detail elsewhere.[37, 38]

3.3 Results and Discussion

3.3.1 Cyclic Voltammetry

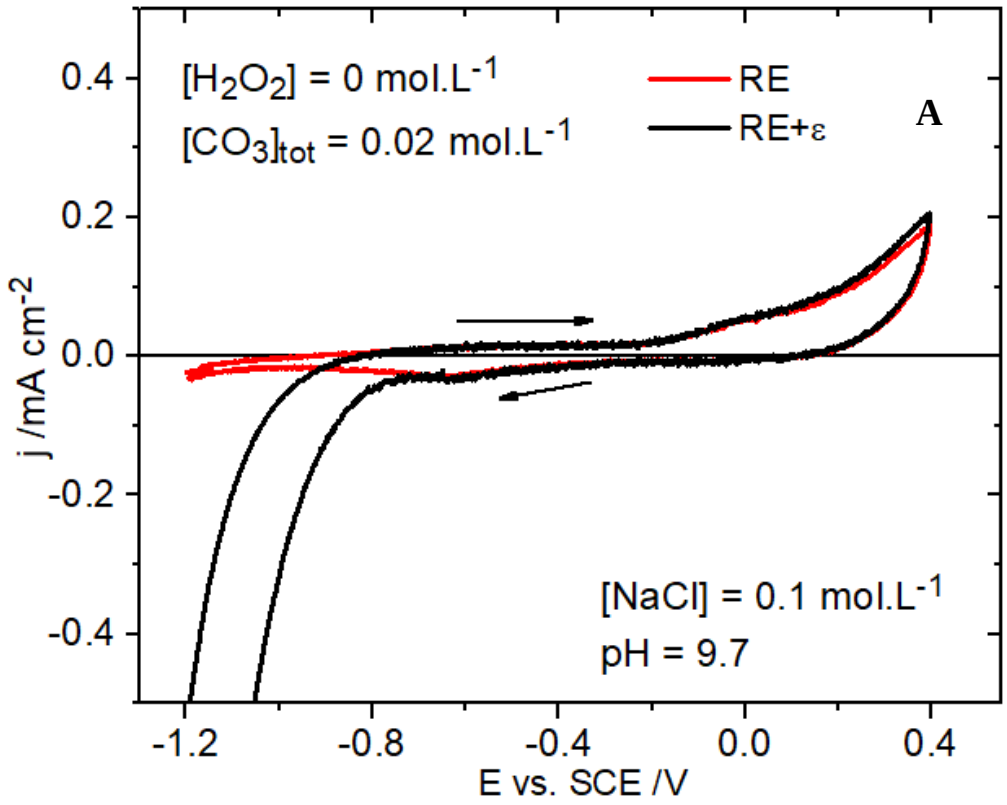

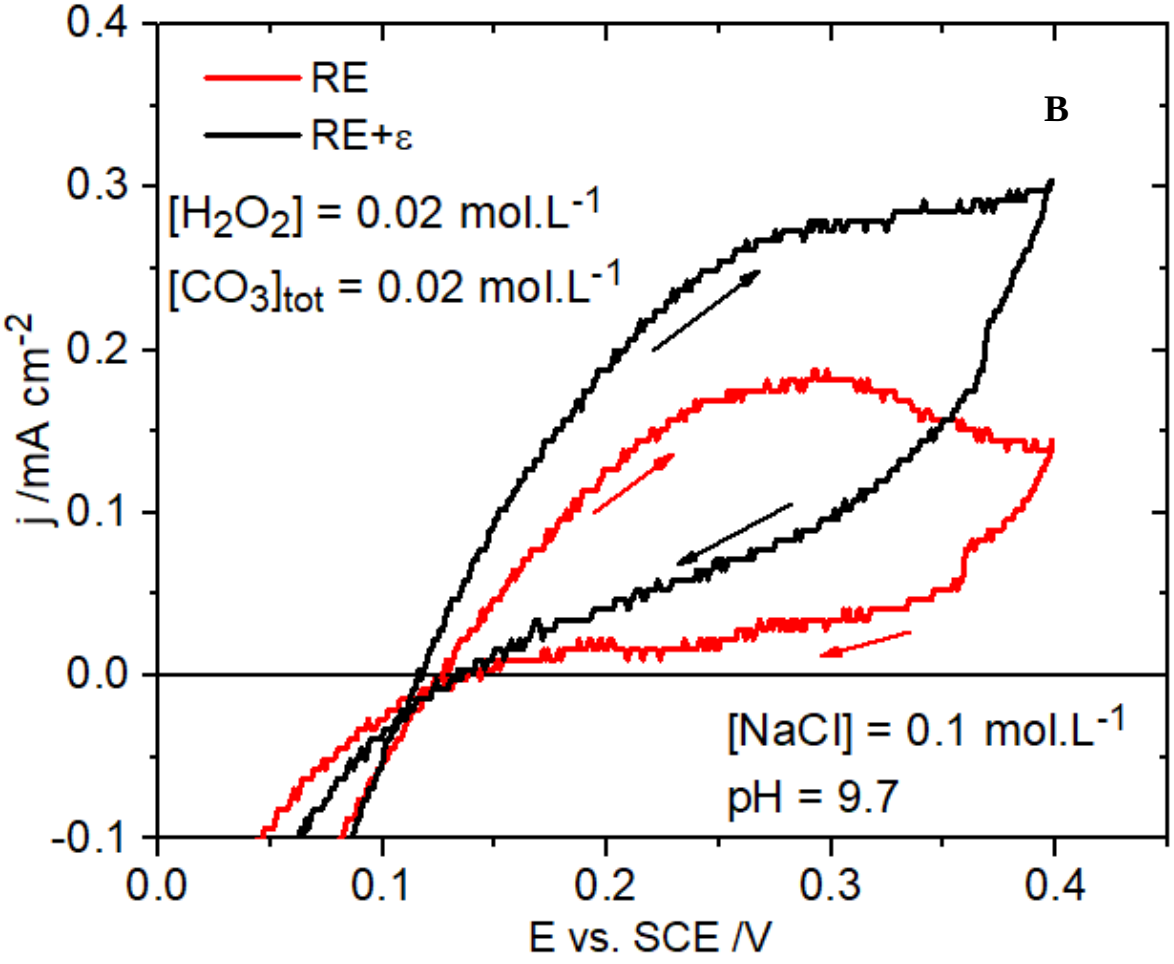

Figure 3.2: CVs recorded on the RE and RE+ε electrodes in an Ar-sparged 0.1 mol.L^{-1} NaCl solution containing 0.02 mol.L^{-1} $NaHCO_3$ with a pH of 9.7, (A) without H_2O_2; (B) with 0.02 mol.L^{-1} H_2O_2: the electrode rotation rate was 16.7 Hz.

Figure 3.2 shows CVs recorded on the two electrodes in a 0.1 mol.L^{-1} NaCl solution containing 0.02 mol.L^{-1} of $NaHCO_3$ (pH = 9.7). In the absence of H_2O_2, Figure 3.2 A, there was no significant difference between the two electrodes in the anodic potential region. However, the cathodic current increased significantly at -0.8 V on the RE + ε electrode due to the catalysis of H_2O reduction on the noble metal (ε) particles. When H_2O_2 was added to the solution, Figure 3.2 B, the anodic current was significantly enhanced and reached a maximum at 0.27 V on the RE electrode with the decreases at positive potential indicating the formation of corrosion products on the UO_2 surface and the inhibition of one or both of the anodic oxidation processes. On the RE + ε electrode, the current was further enhanced and no peak was observed at the positive potential limit of the scan. This enhancement suggested a role for the ε-particles in determining the anodic current over the full potential range.

3.3.2 Characterization of Noble Metal (ε) Particles

3.3.2.1 SEM and EDX

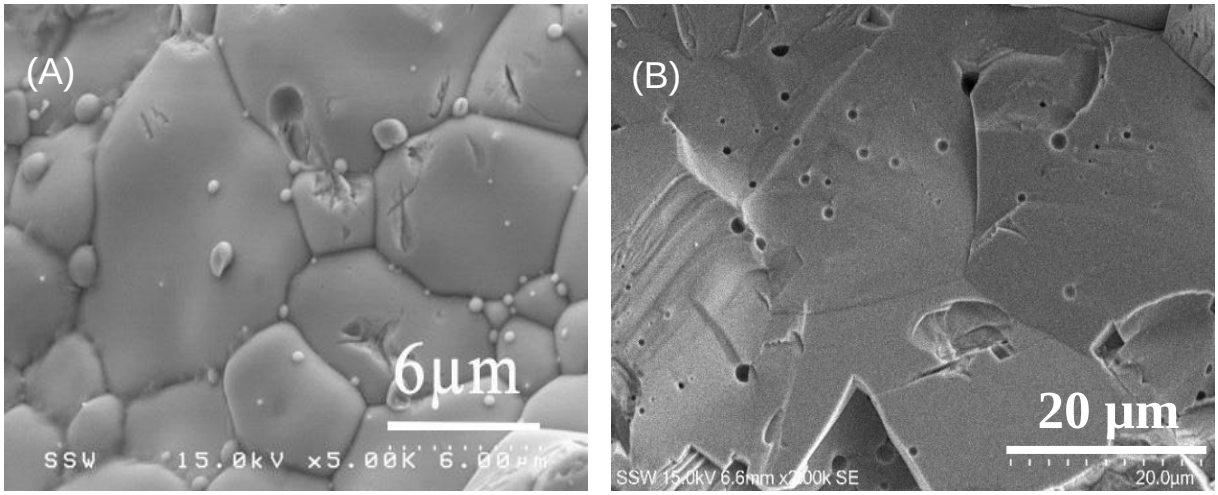

Figure 3.3: SEM images of (A) the RE + ε electrode; (B) the RE electrode.

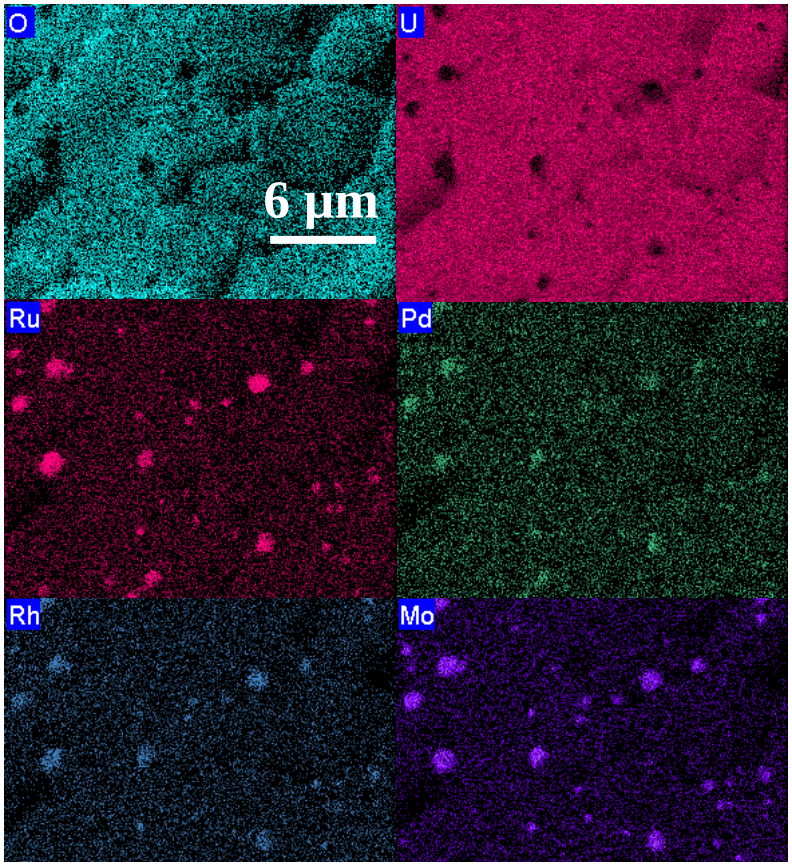

Figure 3.4: EDX maps recorded on the RE+ε electrode showing the distribution of noble metal dopants (Ru, Pd Ru, and Mo).

Figure 3.3 shows the surface morphology of the RE + ε and RE electrodes. The RE + ε electrode (Figure 3.3 A) featured distinct particles mainly residing on grain boundaries and possessed a smaller grain size than the RE electrode. The EDX analyses, Figure 3.4, showed the distinct particles contained Ru, Pd, Rh and Mo, consistent with previous analyses. [35] A more extensive analysis of the composition of a number of ε-particles in the RE + ε electrode showed their composition to be Pd (40 ± 6%), Ru (29 ± 5%), Rh (14 ± 4%) and Mo (16 ± 3%). [39]

3.3.2.2 Raman Analyses

Figure 3.5 shows representative Raman spectra recorded on the RE and RE + ε electrode surfaces. These spectra exhibit a number of bands.[37]

(i) The dominant peak at 445 cm^{-1} can be attributed to the fundamental U-O stretching mode of the fluorite lattice.

(ii) A band at 1150 cm^{-1} (not shown) has been assigned as an overtone (2L-O) of the first order L-O phonon observed at 570-575 cm^{-1}.[40]

(iii) The broad band between 500 and 700 cm^{-1} can be attributed to UO_2 lattice damage, due to the formation of defects caused by lattice doping.

The band in this last region was deconvoluted into three peaks at 540 cm^{-1}, 570 cm^{-1} and 640 cm^{-1}. The peak at 570 cm^{-1} was attributed to a first order phonon (as noted above) while the peak at 540 cm^{-1} was attributed to the creation of oxygen vacancies (O_V) [41, 42] in response to the need for charge compensation due to RE^{III} doping, a process which appears to involve the formation of RE^{III}-O_V clusters.

A peak at 640 cm^{-1} has been commonly assigned to distortion of the anion sublattice associated with a vibrational mode involving clusters of interstitial O atoms in a non-stoichiometric UO_{2+x} lattice. Since the SIMFUELs used in these experiments were sintered and

reduced it was expected to be stoichiometric making this assignment of the peak at 640 cm^{-1} unlikely. It has been suggested [38] this peak can be attributed to a Zr-O_8 complex since Zr^{IV} doping would cause a decrease in the UO_2 lattice parameter, a feature that would be expected to lead to lattice stabilization against anodic oxidation.

Since the peak at 445 cm^{-1} is characteristic of the undisturbed fluorite lattice and the 540 cm^{-1} peak can be attributed to the creation of O_V associated with RE^{III}-doping, the area ratio of these two peaks has commonly been used as a measure of the number of such vacancies. [38] Figure 3.6 shows the peak areas normalized to the area of the peak at 445 cm^{-1}. If it is accepted that the ratio of the 540 cm^{-1} and 445 cm^{-1} peak areas is a measure of the number of O_V created by RE^{III} doping then the RE electrode appeared to have a slightly higher density of O_V than the RE + ε electrode.

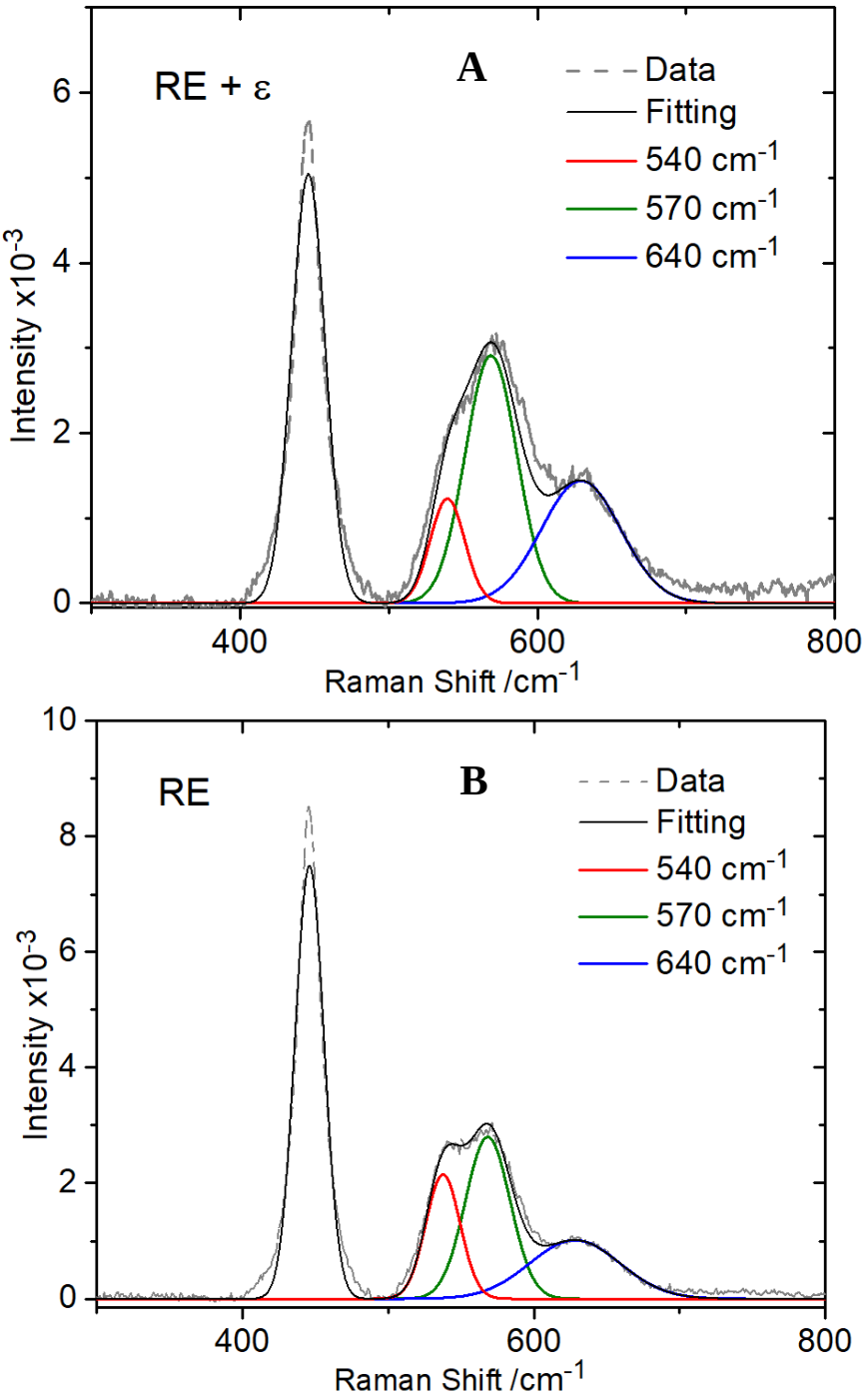

Figure 3.5: Raman spectra recorded on the freshly polished (A) RE + ε and (B) RE SIMFUEL electrodes.

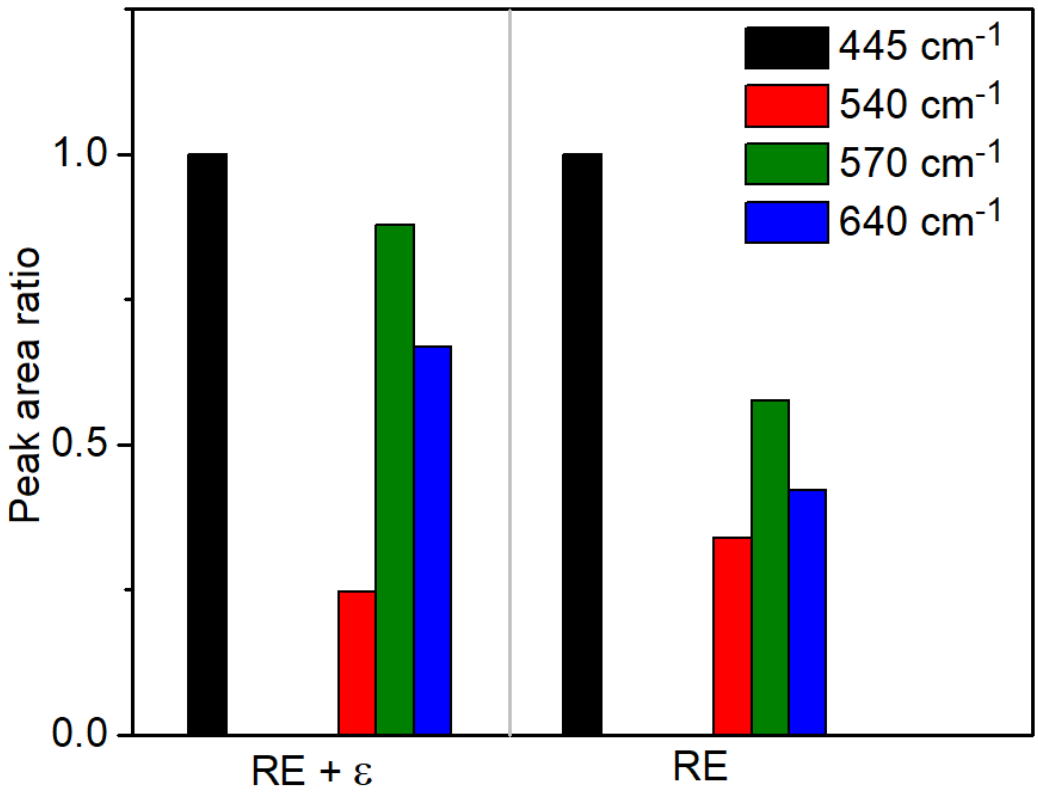

Figure 3.6: Comparison of Raman peak areas normalized to the area of the 445 cm^{-1} peak recorded on the RE + ε and RE electrodes.

3.3.3 Steady-State Currents at Various $[CO_3]_{tot}$

Figure 3.7 shows the current densities recorded on both electrodes over a range of E in a 0.1 $mol.L^{-1}$ of NaCl solution containing 0.1 $mol.L^{-1}$ of $[CO_3]_{tot}$ and 0.02 $mol.L^{-1}$ of H_2O_2. The current reached a steady state value rapidly on both electrodes, but slightly more rapidly on the RE electrode especially at the higher E.

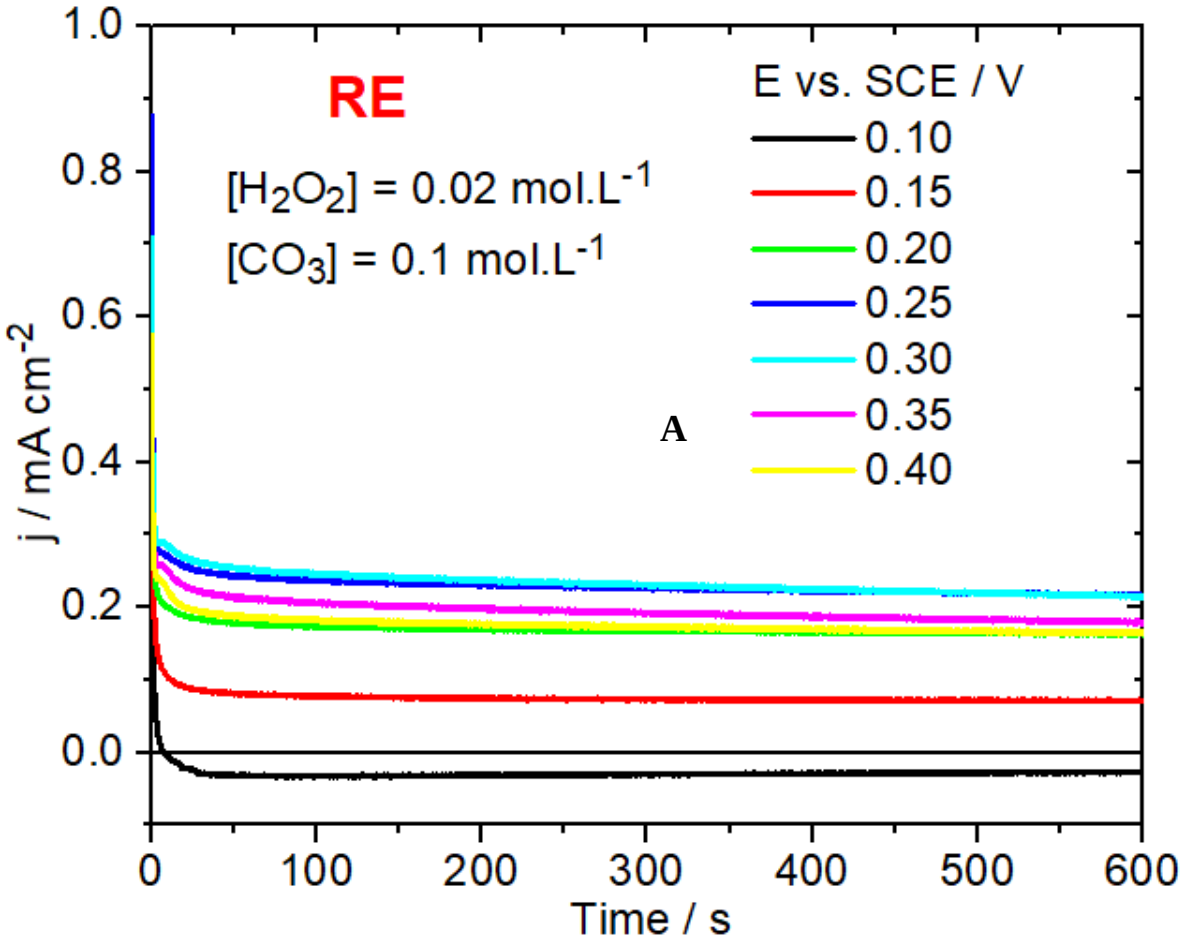
RE
[H2O2] = 0.02 mol.L-1
[CO3] = 0.1 mol.L-1
E vs. SCE / V
0.10
0.15
0.20
0.25
0.30
0.35
0.40
A
j / mA cm-2
Time / s
1.0
0.8
0.6
0.4
0.2
0.0
0
100
200
300
400
500
600

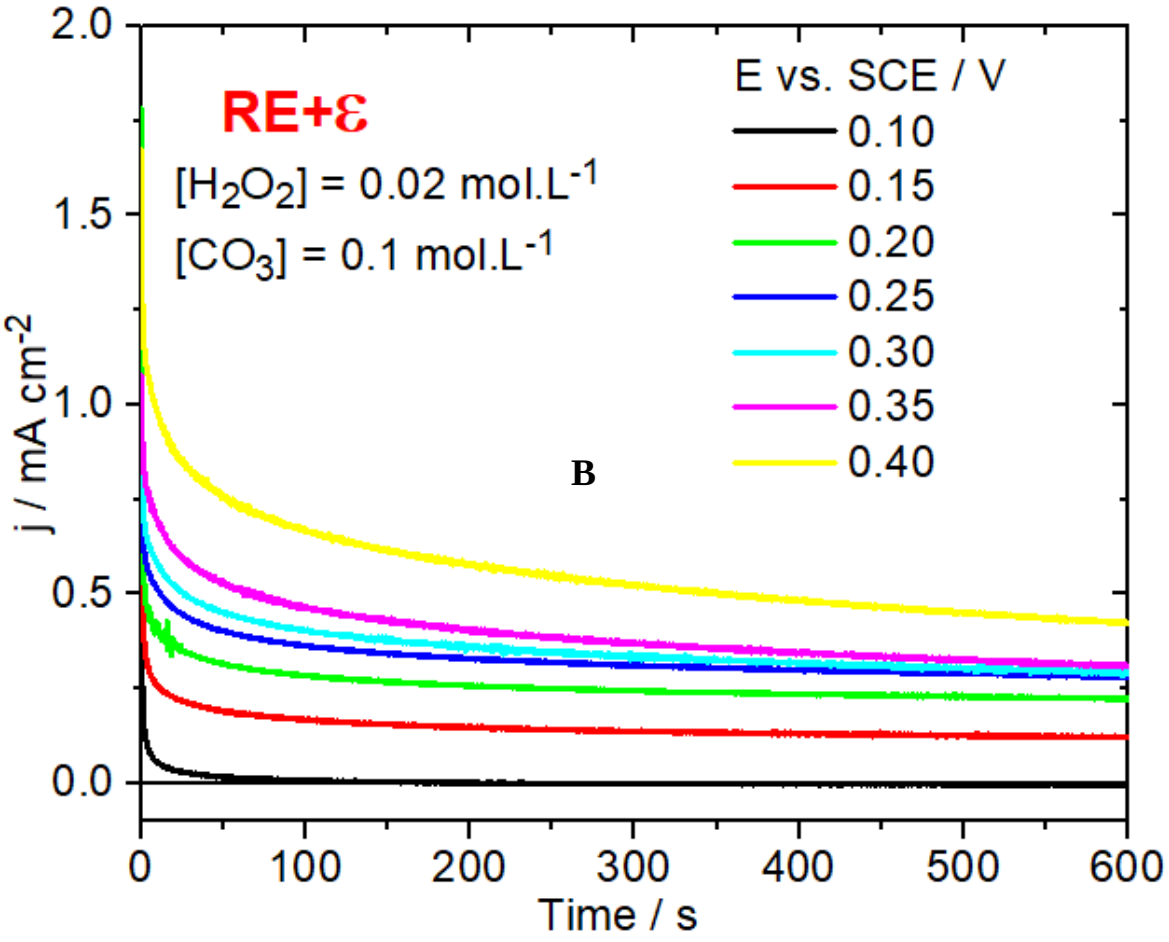

Figure 3.7: Current densities measured at different E for 10 minutes on (A) the RE, and (B) the RE+ε electrodes in an Ar-purged 0.1 mol.L^{-1} NaCl solution containing 0.1 mol.L^{-1} $[CO_3]_{tot}$ and 0.02 mol.L^{-1} H_2O_2: pH = 9.7; electrode rotation rate = 16.7 Hz.

Figure 3.8 A and B show the steady-state currents plotted against E. On the RE electrode the current exhibited the same dependence on E as observed voltammetrically, Figure 3.7, increasing over the low potential range before decreasing again at higher E. The decrease in current beyond the peak became less marked as $[CO_3]_{tot}$ was increased. On the RE + ε electrode the current showed a similar behaviour at low E but any tendency to decrease at more positive E was overcome by a further current increase for E > 0.3V.

Figure 3.8 C shows the difference between the currents (Δj) recorded on the two electrodes,

$$\Delta j = j_{RE + \varepsilon} - j_{RE} \qquad \textbf{3.5}$$

Since the key difference between the two electrodes is the presence of noble metal (ε) particles in the RE + ε electrode, this suggested Δj could be attributed to reactions occurring on these particles not on the UO_2 surface. As will be demonstrated below, the second possibility, that the anodic reactivities of the two doped UO_2 matrices are different can be ruled out. The enhanced currents on the RE + ε, given by Δj, Figure 3.7 C, can be divided into two distinct regions: (i) For $E \leq 0.3V$ the current difference was effectively independent of E and clearly dependent on $[CO_3]_{tot}$; (ii) For $E \geq 0.3V$ the current increased steeply with E but became independent of $[CO_3]_{tot}$.

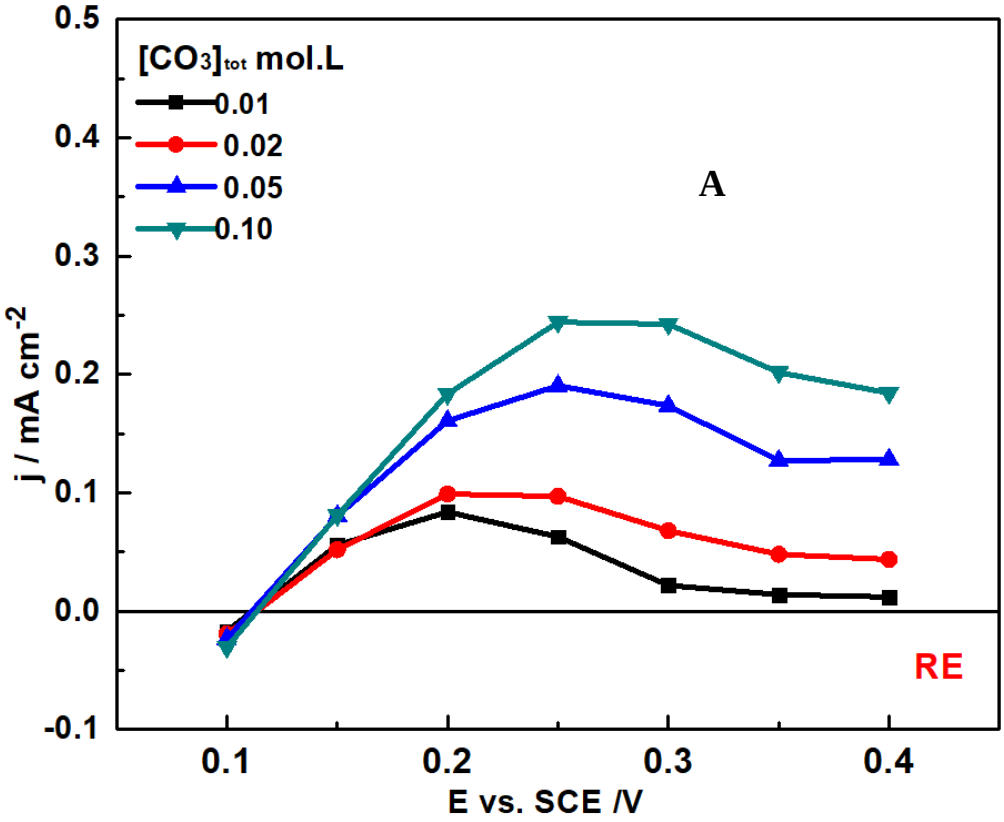
[CO3]tot mol.L
0.01
0.02
0.05
0.10
A
RE
j / mA cm-2
E vs. SCE /V
0.5
0.4
0.3
0.2
0.1
0.0
-0.1
0.1
0.2
0.3
0.4

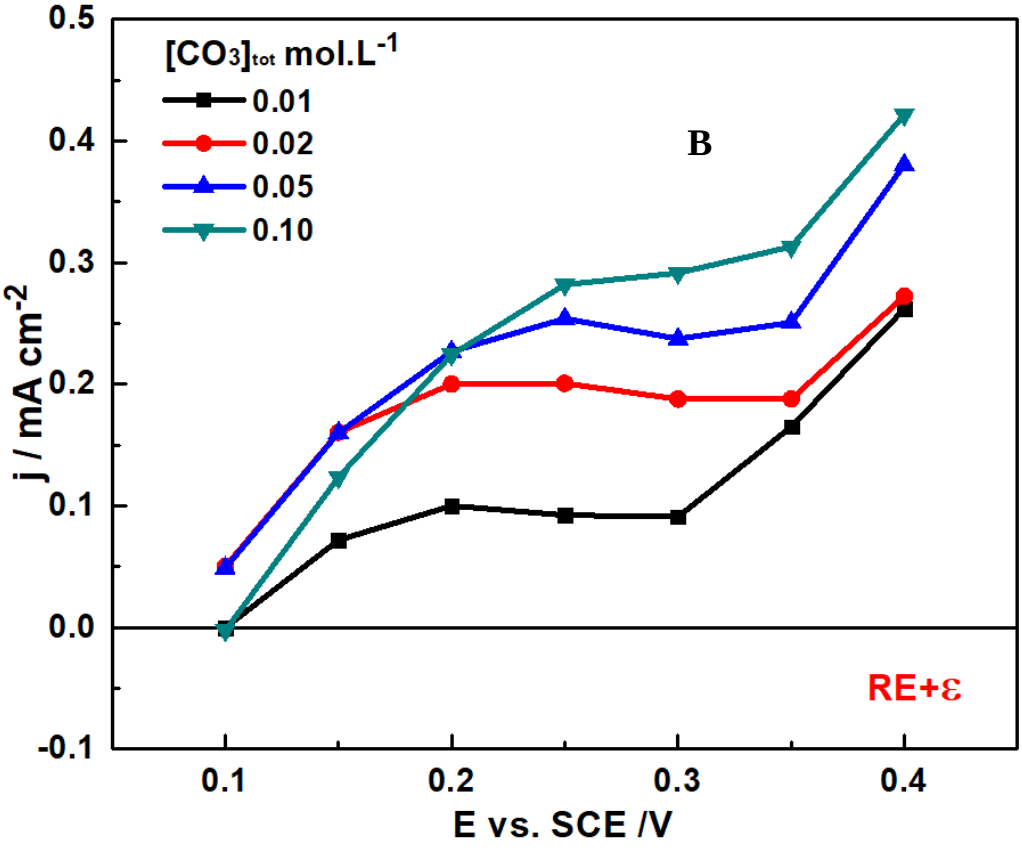
[CO3]tot mol.L-1
0.01
0.02
0.05
0.10
B
RE+ε
j / mA cm-2
E vs. SCE /V
0.5
0.4
0.3
0.2
0.1
0.0
-0.1
0.1
0.2
0.3
0.4

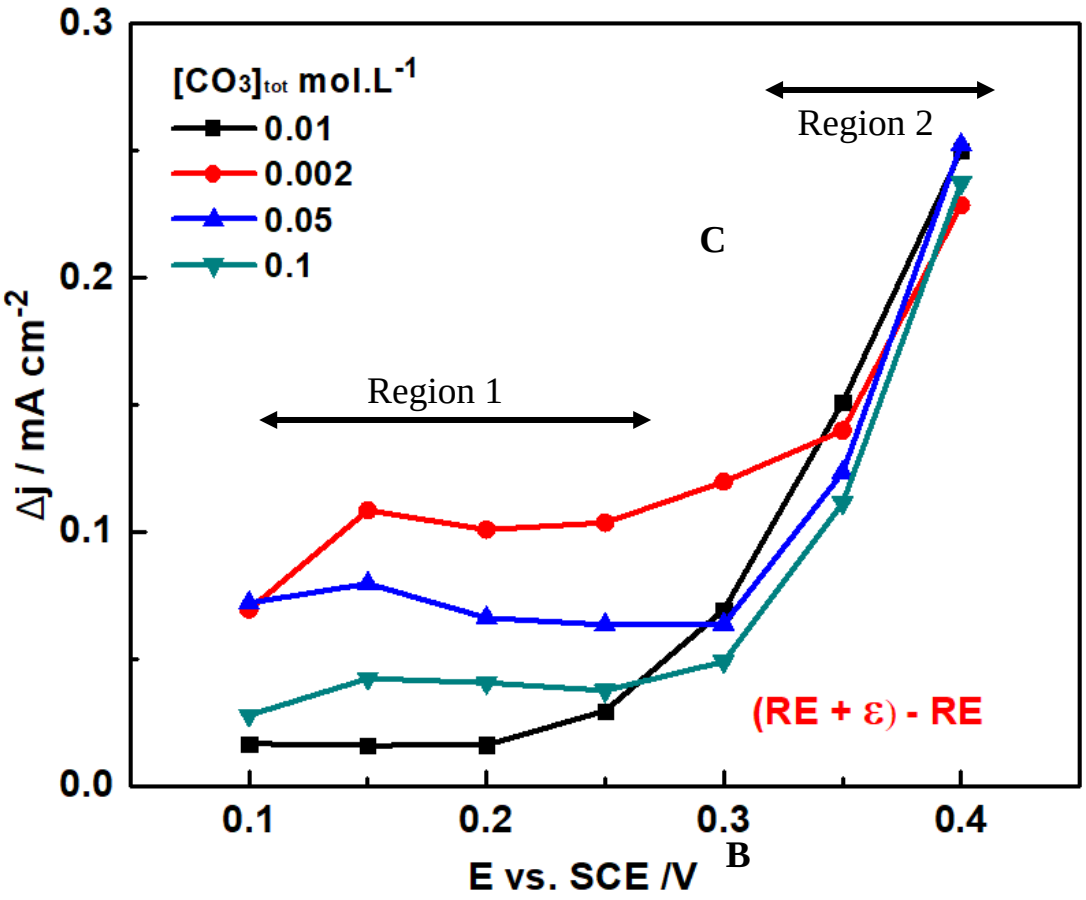

Figure 3.8: Steady-state oxidation current densities as a function of E recorded on the (A) RE and (B) RE+ε electrodes in an Ar-purged 0.1 mol.L^{-1} NaCl solution containing 0.02 mol.L^{-1} H_2O_2, and various $[CO_3]_{tot}$ from 0.01 mol.L^{-1} to 0.1 mol.L^{-1}, (C) calculated current density difference, $j_{(RE+\varepsilon)} - j_{RE}$, determined from (A) and (B); pH = 9.7, electrode rotation rate = 16.7 Hz.

3.3.4 Anodic Dissolution of UO_2

The currents recorded in the potentiostatic experiments, Figure 3.7 and Figure 3.8, contain contributions from both UO_2 and H_2O_2 oxidation. To separate these contributions, the electrodes were potentiostatically oxidized at different applied potentials for 1 hour and the solutions then analyzed for dissolved U. In addition, the charge consumed by the formation of the oxidized surface layers, $U^{IV}_{1-2x}U^{V}_{2x}O_{2+x}$ and $U^{VI}O_3.yH_2O$ and possibly studtite ($U^{VI}O_4.4H_2O$, which could form in the presence of H_2O_2 [19, 42-44]) was determined by cathodic stripping voltammetry. This charge was found to be negligible compared to the total anodic charge consumed and was not, therefore, taken into consideration.

Figure 3.9 shows the amount of U dissolved was almost identical for both electrodes irrespective of the $[CO_3]_{tot}$. Despite the differences in the total amount of charge consumed, obtained by integration of the current over the 1 hour duration of the experiment, the data in Figure 3.9 shows that the extent of U dissolution was similar on the RE and RE + ε electrodes. This demonstrates that the extent of dissolution was uninfluenced by the presence of noble metal (ε) particles, and hence not responsible for the differences in anodic current, Δj (Figure 3.7 C). Also, this similarity in U^{VI} release rates confirmed that the slight differences in the number of RE^{III}-O_V clusters indicated by the Raman analyses had minimal influence on the anodic reactivity of the UO_2 matrix. This is consistent with previous observations on the influence of RE^{III} doping on the anodic reactivity.[45]

SEM micrographs recorded on the RE + ε electrode, Figure 3.10, showed some etching of the surface, possibly with some enhanced grain boundary dissolution. Although not shown, similar changes in surface morphology were observed on the RE electrode.

At E_{CORR}, the amount of U^{VI} dissolved was effectively independent of $[CO_3]_{tot}$, Figure 3.9, indicating that the slow step in the overall dissolution process was the anodic formation of the U^{VI} species from the preformed U^{IV}/U^{V} surface layer

$$U^{IV}O_2 \rightarrow U^{IV}{}_{1-2x}U^{V}{}_{2x}O_{2+x} \rightarrow (U^{VI})_{surf} \rightarrow U^{VI}O_2(CO_3)_y^{(2-2y)+} \qquad \textbf{3.6}$$

At higher E and low $[CO_3]_{tot}$ only a marginal increase in U^{VI} release was observed prior to the inhibition of release at high E (0.3V, 0.4V) when the surface became covered with a $U^{VI}O_3 \cdot yH_2O$ film although the formation of studtite ($U^{VI}O_4 \cdot 4H_2O$) was also possible in the presence of H_2O_2.[19, 42-44] This suppression of dissolution at high E on the RE electrode was consistent with the low currents observed at 0.3/0.4V (Figure 3.8 A) which demonstrate that the

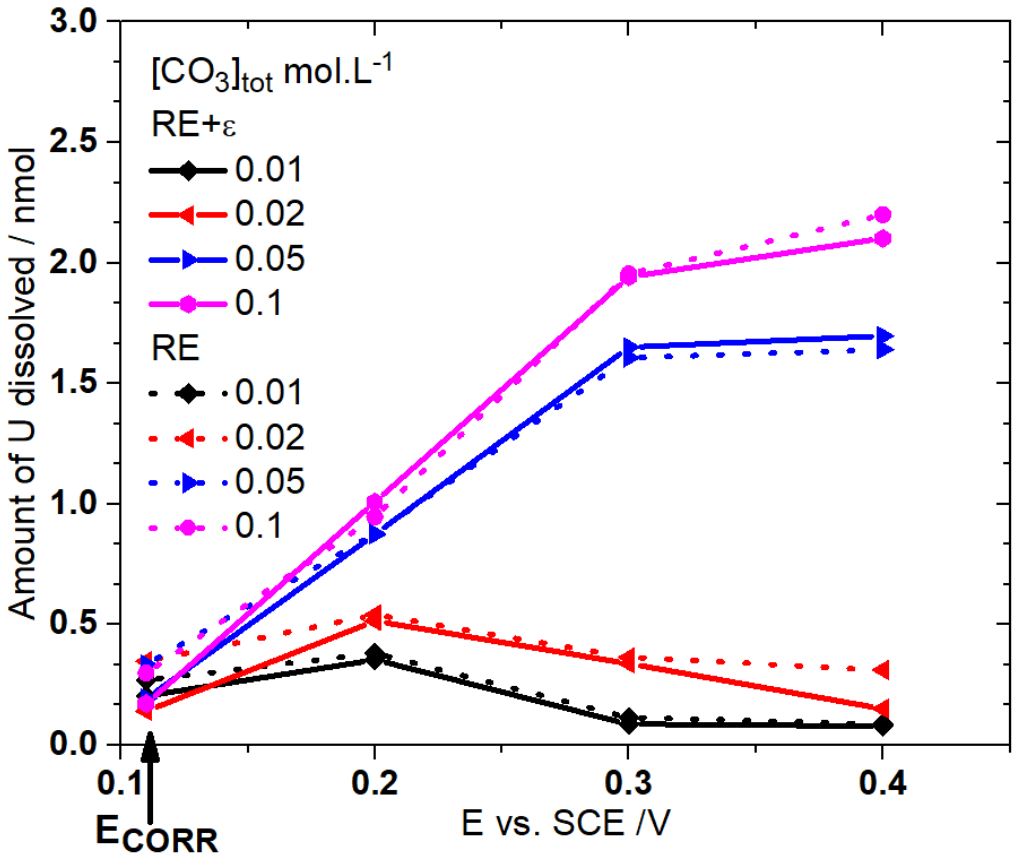

Figure 3.9: The amount of U dissolved at E_{CORR} and various E values (one hour) for both RE and RE+ε electrodes.

anodic oxidation of H_2O_2 was also suppressed at these potentials. By contrast, the suppression of U^{VI} dissolution on the RE + ε electrode under these conditions, Figure 3.9, was not accompanied by a decrease in current, Figure 3.8 B, confirming that the higher currents at 0.3/0.4V were due to an increase in the anodic oxidation of H_2O_2 on the noble metal (ε) particles.

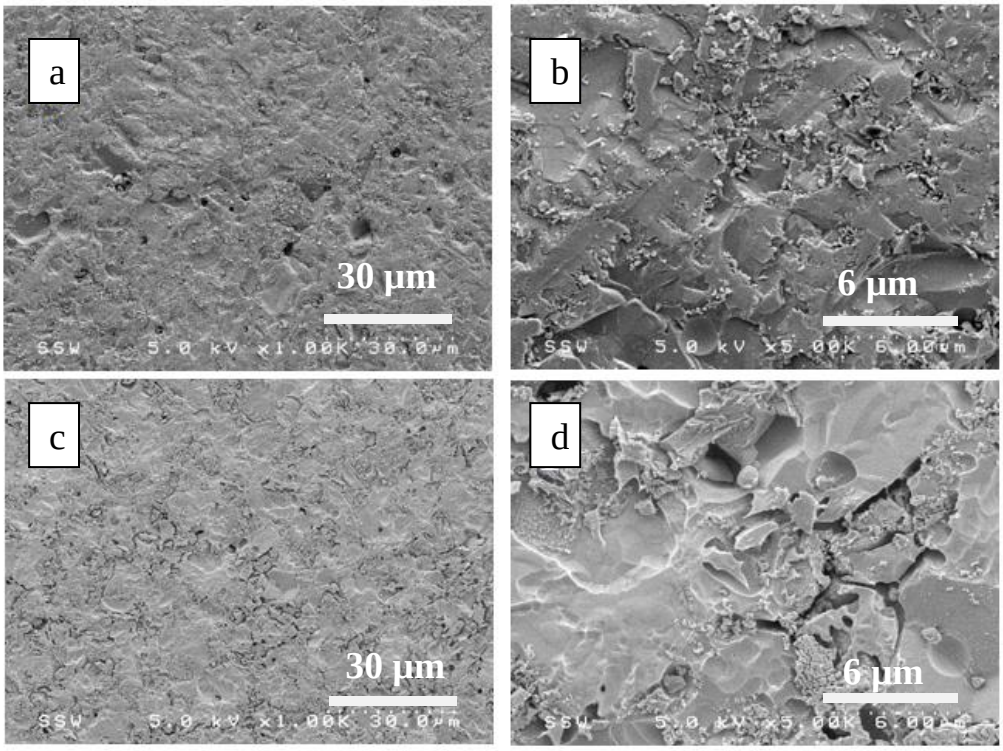

Figure 3.10: SEM micrographs of the RE + ε electrode before and after anodic oxidation at E = 0.35 V for 1 hour in a solution of 0.1 mol.L^{-1} NaCl, 0.02 mol.L^{-1} H_2O_2 and 0.1 mol.L^{-1} $NaHCO_3$ with pH = 9.7: (a) and (b), the freshly polished electrode; (c) and (d) the surface of the electrode after anodic oxidation at 0.35 V for 1 hour.

At higher $[CO_3]_{tot}$, the intermediate $U^{IV}_{1-2x}U^{V}_{2x}O_{2+x}$ layer was considerably thinner and anodic dissolution proceeded more rapidly through U^V/U^{VI} surface intermediates[46]

$$U^{IV}O_2 + HCO_3^- \rightarrow U^VO_2(HCO_3)_{ads} + e^- \quad \textbf{3.7}$$

$$U^VO_2(HCO_3)_{ads} + OH^- \rightarrow U^{VI}O_2(CO_3)_{ads} + H_2O + e^- \quad \textbf{3.8}$$

$$U^{VI}O_2(CO_3)_{ads} + HCO_3^- \rightarrow U^{VI}O_2(CO_3)_2^{2-} + H^+ \quad \textbf{3.9}$$

At $E \leq 0.3V$ the amount of U^{VI} released increased with E indicating control of the dissolution reaction by reaction 3.8. For $E > 0.3V$, the amount released became independent of E but exhibits a dependence on $[CO_3]_{tot}$ consistent with a switch in rate control to the final chemical dissolution (reaction 3.9). It is possible that this dissolution reaction was accelerated by the formation of a soluble peroxycarbonate complex, $U^{VI}O_2(O_2)_x(CO_3)_y^{2-2x-2y}$. The formation of such a species has been shown to accelerate UO_2 dissolution when H_2O_2 and HCO_3^-/CO_3^{2-} concentrations were higher than those employed in this study. [28, 29]

Based on these analyses, the total charge consumed by anodic dissolution (Q_{UO2}) was calculated and compared to the total amount of anodic charge. The ratio of these charges is plotted in Figure 3.11 which provides a measure of the relative importance of U^{VI} dissolution. On the RE electrode the ratio (i.e., the importance of dissolution) increased with E for all $[CO_3]_{tot}$, as indicated by the green arrow, Figure 3.11, with dissolution becoming the dominant reaction at 0.4 V despite the overall decrease in current, Figure 3.8 A, and the suppression of U^{VI} release, Figure 3.9, particularly at low $[CO_3]_{tot}$.

These results confirmed that the formation of U^{VI} surface films strongly suppressed the anodic oxidation of H_2O_2. However, the dependence on $[CO_3]_{tot}$ at both 0.3V and 0.4V, in particular the latter, peaked at intermediate $[CO_3]_{tot}$ (0.02 $mol.L^{-1}$) before decreasing again at higher concentrations, as indicated by the red arrows in Figure 3.11 A. This suggested two influences of HCO_3^-/CO_3^{2-}: (i) at the two low $[CO_3]_{tot}$ an increase leads to a significant promotion of the importance of anodic dissolution, confirming that the increased anodic current can be attributed to an acceleration in the rate of the electrochemical reaction 3.8;

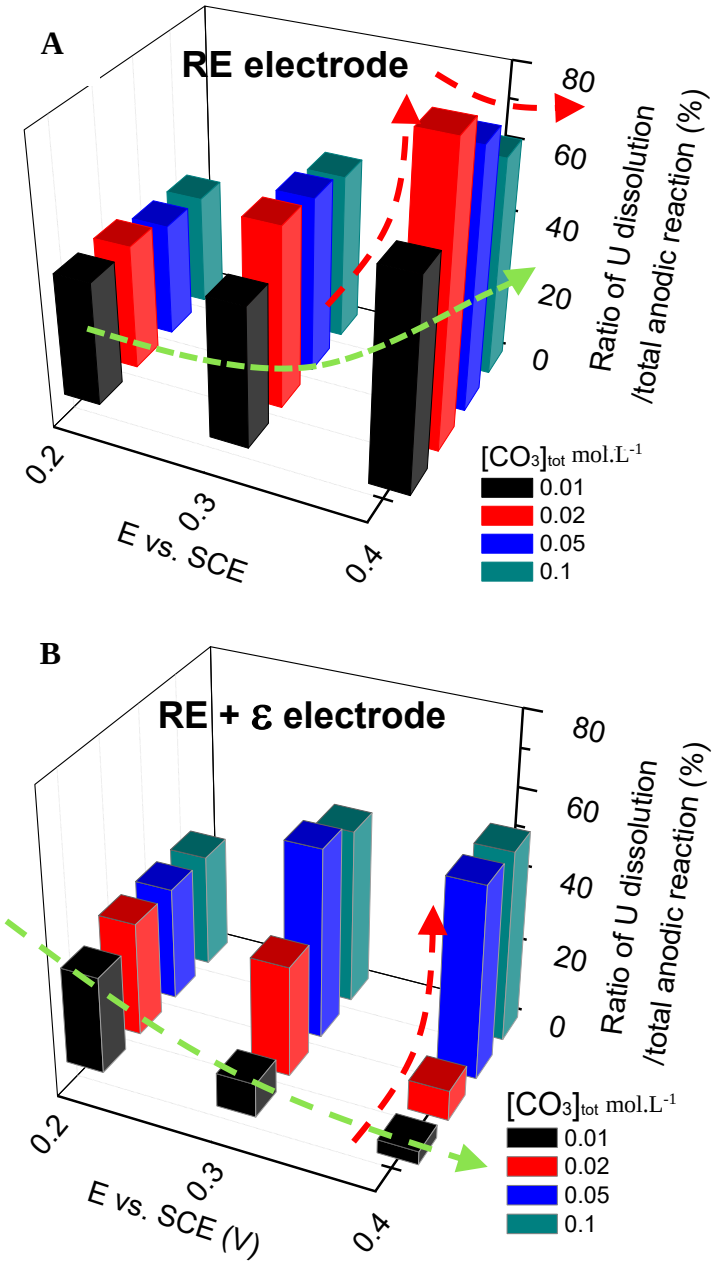

Figure 3.11: The ratio of the charge consumed by UO_2 dissolution to the total electrochemical charge consumed calculated for (A) the RE electrode, and (B) the RE+ε electrode as a function of E and $[CO_3]_{tot}$.

(ii) at the higher $[CO_3]_{tot}$ (0.05 and 0.1 $mol.L^{-1}$) the relative importance of the dissolution reaction was decreased; i.e., the relative importance of the anodic oxidation of H_2O_2 increased,

once the surface U^{VI} layer was rapidly dissolved and the conductive underlying $U^{IV}_{1-2x}U^{V}_{2x}O_{2+x}$ layer exposed.

Significantly different behaviour was observed on the RE + ε electrode. At low $[CO_3]_{tot}$ the ratio decreased to 3.5% as E was increased to 0.4V, as indicated by the green arrow in Figure 3.11. This decrease accompanies the overall decrease in U^{VI} release, Figure 3.9, and the accompanying increase in anodic current, Figure B and C, confirming the dominance of H_2O_2 oxidation under these conditions. Since the surface of the UO_2 matrix remained protected by the U^{VI} surface film at low $[CO_3]_{tot}$, these observations clearly demonstrated that the acceleration of H_2O_2 oxidation was supported on the noble metal (ε) particles. At higher $[CO_3]_{tot}$ the relative importance of U^{VI} dissolution was revived as the U^{VI} surface film dissolved, as indicated by the red arrow in Figure 3.11 B.

3.3.5 The anodic oxidation of H_2O_2

The importance of H_2O_2 oxidation, and the influence of $[CO_3]_{tot}$ and E on it, are demonstrated in Figure 3.12, which shows the anodic charge due to H_2O_2 oxidation (Q_{H2O2}) calculated by subtracting the charge due to UO_2 dissolution (Q_{UO2}) from the total electrochemical charge. At low E (0.2V), Q_{H2O2} increased with $[CO_3]_{tot}$ on both electrodes. This, and the observation that the current for H_2O_2 oxidation on noble metal (ε) particles was enhanced in this potential region 1 (Figure 3.8 C) demonstrated that HCO_3^-/CO_3^{2-} influenced H_2O_2 oxidation in two ways: (i) as discussed above it accelerates U^{VI} dissolution leading to the exposure of the conductive $U^{IV}_{1-2x}U^{V}_{2x}O_{2+x}$ sublayer on which H_2O_2 oxidation could occur; (ii) it accelerated H_2O_2 oxidation on the noble metal (ε) particles in region 1 (Figure 3.8 C).

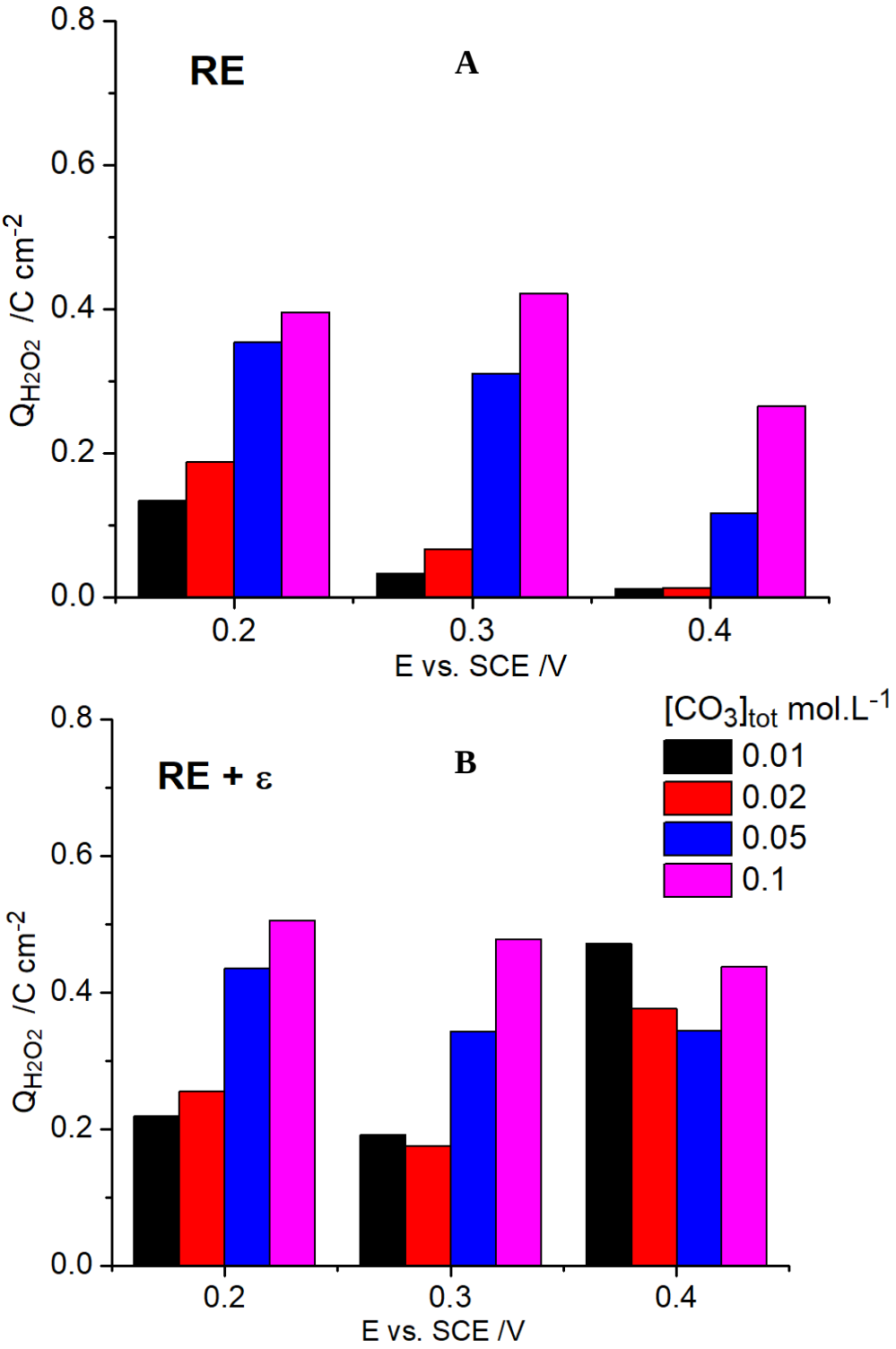

Figure 3.12: The anodic charge due to H_2O_2 oxidation ($Q_{H_2O_2}$) as a function of E on the RE (A) and RE+ε (B) electrodes in a [NaCl] = 0.1 mol.L^{-1} solution containing $[H_2O_2]$ = 0.02 mol.L^{-1} and various $[CO_3]_{tot}$.

This dependence of the current and the charge for H_2O_2 oxidation on $[CO_3]_{tot}$ indicated a carbonate-mediated oxidation of H_2O_2 was occurring on the noble metal (ε) particles in potential region 1 (Figure 3.8 C). The combination of H_2O_2 and HCO_3^-/CO_3^{2-} is known to form a reactive peroxycarbonate species,

$$HCO_3^- + H_2O_2 \rightarrow HCO_4^- + H_2O \qquad \textbf{3.10}$$

a reaction which can catalyze H_2O_2 decomposition and is known to enhance its reactivity.[47] Once formed its anodic oxidation to O_2 and the regeneration of HCO_3^- was rapid on the noble metal (ε) particles,

$$2HCO_4^- \rightarrow 2HCO_3^- + O_2 + 2e^- \qquad \textbf{3.11}$$

On the RE electrode, the ability of HCO_3^-/CO_3^{2-} to revive H_2O_2 oxidation by dissolving the insulating U^{VI} surface layers to expose the underlying catalytic $U^{IV}_{1-2x}U^{V}O_{2+x}$ layer was clear on the RE electrode, Q_{H2O2} increasing with $[CO_3]_{tot}$ at all three potentials.

While the value of Q_{H2O2} also increased with $[CO_3]_{tot}$ on the RE + ε electrode the extent of H_2O_2 oxidation was much greater at 0.4 V than on the RE electrode and the excess current, Δj, showed the reaction was not dependent on $[CO_3]_{tot}$, although it was occurring on the noble metal (ε) particles. This can be attributed to the direct oxidation of H_2O_2 on the noble metal (ε) particles, this reaction having been shown to be catalyzed by oxidized states on the surface of noble metals, [48-52] e.g., Pd^{II} on Pd,

$$Pd + 2H_2O \rightarrow Pd^{II}(OH)_2 + H^+ + 2e^- \qquad \textbf{3.12}$$

$$Pd^{II}(OH)_2 + H_2O_2 \rightarrow Pd^{II}(OH)_2(H_2O_2)_{ads} \qquad \textbf{3.13}$$

$$Pd^{II}(OH)_2(H_2O_2)_{ads} \rightarrow Pd + O_2 + 2H_2O \qquad \textbf{3.14}$$

3.4 Summary

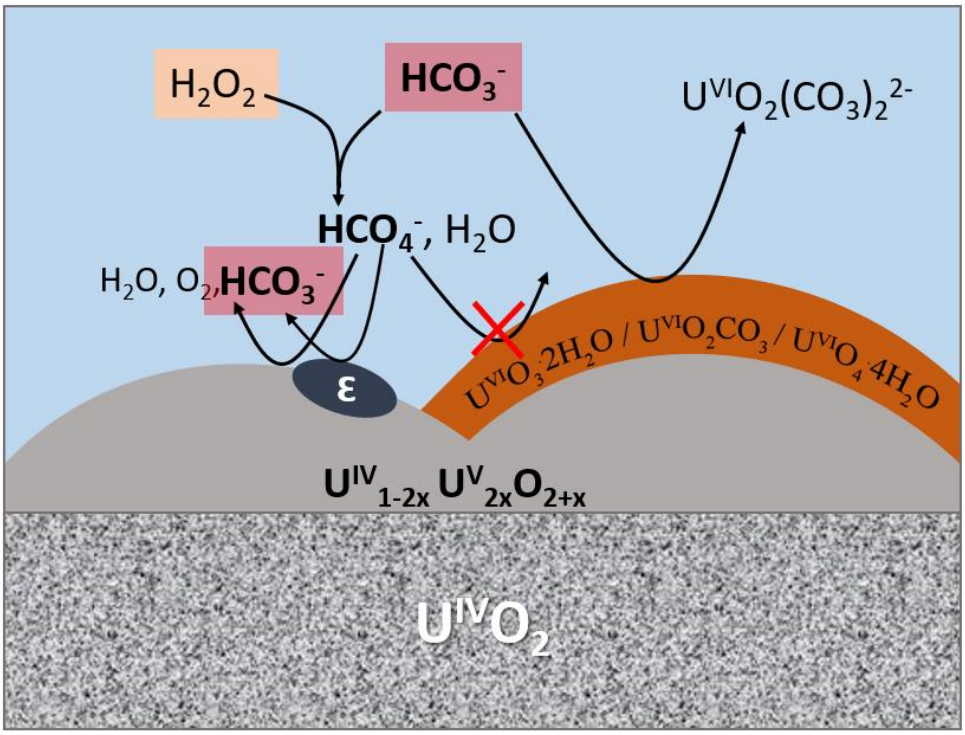

Figure 3.13: Schematic illustration of the major reactions occurring on the RE and RE+ ε electrode surfaces in solutions containing H_2O_2 and CO_3^{2-}/HCO_3^-.

Figure 3.13 shows a schematic summary of the reactions occurring on the various features and surface states on the UO_2/ε-particle surface.

- At all potentials, including E_{CORR}, the surface was covered by a thin conductive $U^{IV}_{1-2x}U^{V}_{2x}O_{2+x}$ layer able to support both anodic dissolution of the UO_2 matrix and anodic oxidation of H_2O_2.
- The balance between these anodic reactions varied with, (i) the presence or absence of noble metal (ε) particles dispersed throughout the fission product-doped UO_2 matrix, (ii) the potential applied, and (iii) the $[CO_3^{2-}]_{tot}$.

- At low $[CO_3]_{tot}$ both anodic reactions were retarded by the growth of insulating U^{VI} surface layers and the rate of the anodic oxidation of H_2O_2 became controlled by the rate of release of U^{VI} to solution to expose the underlying conductive $U^{IV}_{1-2x}U^{V}_{2x}O_{2+x}$ layer.
- The dissolution of this thin U^{VI} layer was accelerated in the presence of HCO_3^-/CO_3^{2-} leading to increases in rate of both anodic reactions.
- The presence of noble metal (ε) particles did not influence the anodic dissolution of the UO_2 matrix but offered an additional pathway for the anodic oxidation of H_2O_2.
- At low potentials in the presence of HCO_3^-/CO_3^{2-}, a peroxycarbonate species, HCO_4^-, was formed and rapidly oxidized H_2O_2 to O_2 on the particles.
- At high potentials H_2O_2 was directly oxidized on the noble metal (ε) particles which were rendered catalytic by their electrochemical oxidation (e.g., $Pd \rightarrow Pd^{II}$).

3.5 Reference

[1] J. McMurry, D. Dixon, J. Garroni, B. Ikeda, S. Stroes-Gascoyne, P. Baumgartner, T. Melnyk, Evolution of a Canadian deep geologic repository: base scenario, Ontario Power Generation Report, (2003) 01200-10092.

[2] F. Garisto, Fourth case study: features, events and processes, Canada: Nuclear Waste Management Organization, (2012).

[3] L. Werme, C. Lilja, Fuel and canister process report for the safety assessment SR-Site, Report TR-10-46,, Swedish Nuclear Fuel and Waste Management Co. (SKB), Stockholm, Stockholm, 2010.

[4] D.W. Shoesmith, Fuel corrosion processes under waste disposal conditions, Journal of Nuclear Materials, 282 (2000) 1-31.

[5] L.H. Johnson, D.W. Shoesmith, Radioactive waste forms for the future: edited by W. Lutze and RC Ewing. Elsevier Science Publishers: North-Holland, Amsterdam 1988.

[6] L.O. Werme, L. Johnson, V. Oversby, F. King, K. Spahiu, B. Grambow, D. Shoesmith, Spent fuel performance under repository conditions: A model for use in SR-Can, SKB2004.

[7] C. Poinssot, C. Ferry, M. Kelm, J. Cavedon, C. Corbel, C. Jegou, P. Lovera, F. Miserque, A. Poulesquen, B. Grambow, Spent fuel stability under repository conditions-final report of the european project, CEA Saclay, 2005.

[8] J. Bruno, Spent Nuclear Fuel, Elements (Quebec), 2 (2006) 343-349.

[9] D. Shoesmith, Used fuel and uranium dioxide dissolution studies–a review, Report NWMO TR-2007-03, Nuclear Waste Management Organization, Toronto, ON, (2007).

[10] H. He, M. Broczkowski, K. O'Neil, D. Ofori, O. Semenikhin, D. Shoesmith, Corrosion of nuclear fuel (UO_2) inside a failed nuclear waste container, Nuclear Waste Management Organization, Toronto, Ontario, (2012).

[11] N. Liu, Z. Zhu, J.J. Noël, D.W. Shoesmith, Corrosion of nuclear fuel inside a failed waste container, Encyclopedia of Interfaical Chemistry: Surface Science and Electrochemistry 2018.

[12] I. Grenthe, J. Fuger, R.J. Konings, R.J. Lemire, A.B. Muller, C. Nguyen-Trung, H. Wanner, Chemical thermodynamics of uranium, North-Holland Amsterdam1992.

[13] J. Wren, D. Shoesmith, S. Sunder, Corrosion behavior of uranium dioxide in alpha radiolytically decomposed water, Journal of the Electrochemical Society, 152 (2005) B470-B481.

[14] K. Spahiu, D. Cui, M. Lundström, The fate of radiolytic oxidants during spent fuel leaching in the presence of dissolved near field hydrogen, Radiochimica Acta, 92 (2004) 625-629.

[15] K. Ollila, V.M. Oversby, Dissolution of unirradiated UO_2 and UO_2 doped with ^{233}U under reducing conditions, Swedish Nuclear Fuel and Waste Management Co., 2005.

[16] B. Muzeau, C. Jégou, F. Delaunay, V. Broudic, A. Brevet, H. Catalette, E. Simoni, C. Corbel, Radiolytic oxidation of UO_2 pellets doped with alpha-emitters (238/239Pu), Journal of Alloys and Compounds, 467 (2009) 578-589.

[17] M. Jonsson, F. Nielsen, O. Roth, E. Ekeroth, S. Nilsson, M.M. Hossain, Radiation induced spent nuclear fuel dissolution under deep repository conditions, Environmental Science & Technology, 41 (2007) 7087-7093.

[18] O. Roth, M. Trummer, M. Jonsson, Factors influencing the rate of radiation-induced dissolution of spent nuclear fuel, Research on Chemical Intermediates, 35 (2009) 465-478.

[19] G. Sattonnay, C. Ardois, C. Corbel, J.F. Lucchini, M.F. Barthe, F. Garrido, D. Gosset, Alpha-radiolysis effects on UO_2 alteration in water, Journal of Nuclear Materials, 288 (2001) 11-19.

[20] C.M. Lousada, M. Trummer, M. Jonsson, Reactivity of H_2O_2 towards different UO_2-based materials: The relative impact of radiolysis products revisited, Journal of Nuclear Materials, 434 (2013) 434-439.

[21] T.E. Eriksen, D.W. Shoesmith, M. Jonsson, Radiation induced dissolution of UO_2 based nuclear fuel – A critical review of predictive modelling approaches, Journal of Nuclear Materials, 420 (2012) 409-423.

[22] J.S. Goldik, H.W. Nesbitt, J.J. Noël, D.W. Shoesmith, Surface electrochemistry of UO_2 in dilute alkaline hydrogen peroxide solutions, Electrochimica Acta, 49 (2004) 1699-1709.

[23] J.S. Goldik, J.J. Noël, D.W. Shoesmith, The electrochemical reduction of hydrogen peroxide on uranium dioxide electrodes in alkaline solution, Journal of Electroanalytical Chemistry, 582 (2005) 241-248.

[24] M. Razden, Electrochemical and surface compositional studies on uranium dioxide, PhD Thesis, Chemistry Department, The University of Western Ontario, 2013.

[25] H. Christensen, E. Bjergbakke, Radiation induced dissolution of UO_2, MRS Proceedings, 84 (1986) 115.

[26] J. Giménez, E. Baraj, M.E. Torrero, I. Casas, J. de Pablo, Effect of H_2O_2, NaClO and Fe on the dissolution of unirradiated UO_2 in NaCl 5 mol kg^{-1}. Comparison with spent fuel dissolution experiments, Journal of Nuclear Materials, 238 (1996) 64-69.

[27] S. Sunder, N.H. Miller, D.W. Shoesmith, Corrosion of uranium dioxide in hydrogen peroxide solutions, Corrosion Science, 46 (2004) 1095-1111.

[28] S.M. Peper, L.F. Brodnax, S.E. Field, R.A. Zehnder, S.N. Valdez, W.H. Runde, Kinetic study of the oxidative dissolution of UO_2 in aqueous carbonate media, Industrial & engineering chemistry research, 43 (2004) 8188-8193.

[29] G.S. Goff, L.F. Brodnax, M.R. Cisneros, S.M. Peper, S.E. Field, B.L. Scott, W.H. Runde, First identification and thermodynamic characterization of the ternary U (VI) species, $UO_2(O_2)(CO_3)_2^{4-}$, in UO_2−H_2O_2−K_2CO_3 solutions, Inorganic chemistry, 47 (2008) 1984-1990.

[30] M. Trummer, S. Nilsson, M. Jonsson, On the effects of fission product noble metal inclusions on the kinetics of radiation induced dissolution of spent nuclear fuel, Journal of Nuclear Materials, 378 (2008) 55-59.

[31] B.G. Santos, J.J. Noël, D.W. Shoesmith, The effect of pH on the anodic dissolution of SIMFUEL (UO_2), Journal of Electroanalytical Chemistry, 586 (2006) 1-11.

[32] G.J.S. Wu L., Shoesmith D. W. , The anodic reactions on simulated spent fuel (SIMFUEL) in H_2O_2 solutions: effect of carbonate/bicarbonate, Journal of Electrochemical Society, 161 (2014) C363-C371.

[33] H. Kleykamp, R. Pejsa, X-ray diffraction studies on irradiated nuclear fuels, Journal of nuclear materials, 124 (1984) 56-63.

[34] H. Kleykamp, The solubility of selected fission products in UO_2 and (U, Pu) O_2, Journal of Nuclear Materials, 206 (1993) 82-86.

[35] P.G. Lucuta, R.A. Verrall, H. Matzke, B.J. Palmer, Microstructural features of SIMFUEL — Simulated high-burnup UO_2-based nuclear fuel, Journal of Nuclear Materials, 178 (1991) 48-60.

[36] M.E. Broczkowski, J.J. Noël, D.W. Shoesmith, The influence of dissolved hydrogen on the surface composition of doped uranium dioxide under aqueous corrosion conditions, Journal of Electroanalytical Chemistry, 602 (2007) 8-16.

[37] H. He, D. Shoesmith, Raman spectroscopic studies of defect structures and phase transition in hyper-stoichiometric $UO_{(2+x)}$, Phys Chem Chem Phys, 12 (2010) 8108-8117.

[38] M. Razdan, D.W. Shoesmith, Influence of trivalent-dopants on the structural and electrochemical properties of uranium dioxide (UO_2), Journal of The Electrochemical Society, 161 (2014) H105-H113.

[39] M. Broczkowski, The effects of hydrogen and temperature on the electrochemistry and corrosion of uranium dioxide, PhD Thesis, Chapter 7, Chemistry DepartmentThe University of Western Ontario, 2008.

[40] T. Livneh, E. Sterer, Effect of pressure on the resonant multiphonon Raman scattering in UO_2, Physical Review B, 73 (2006) 085118.

[41] L. Li, F. Chen, J.-Q. Lu, M.-F. Luo, Study of defect sites in Ce1–xMxO2−δ (x = 0.2) solid solutions using Raman spectroscopy, The Journal of Physical Chemistry A, 115 (2011) 7972-7977.

[42] L. Desgranges, Y. Pontillon, P. Matheron, M. Marcet, P. Simon, G. Guimbretière, F. Porcher, Miscibility gap in the U–Nd–O phase diagram: a new approach of nuclear oxides in the environment?, Inorganic Chemistry, 51 (2012) 9147-9149.

[43] M. Amme, Contrary effects of the water radiolysis product H_2O_2 upon th dissolution of nuclear fuel in natural ground water and deionized water, Radiochimica Acta, 90 (2002) 399-406.

[44] M. Amme, B. Renker, B. Schmid, M.P. Feth, H. Bertagnolli, W. Döbelin, Raman microspectrometric identification of corrosion products formed on UO_2 nuclear fuel during leaching experiments, Journal of Nuclear Materials, 306 (2002) 202-212.

[45] N. Liu, H. He, J.J. Noël, D.W. Shoesmith, The electrochemical study of Dy_2O_3 doped UO_2 in slightly alkaline sodium carbonate/bicarbonate and phosphate solutions, Electrochimica Acta, 235 (2017) 654-663.

[46] P.G. Keech, J.S. Goldik, Z. Qin, D.W. Shoesmith, The anodic dissolution of SIMFUEL (UO_2) in slightly alkaline sodium carbonate/bicarbonate solutions, Electrochimica Acta, 56 (2011) 7923-7930.

[47] T. Wu, J.D. Englehardt, A new method for removal of hydrogen peroxide interference in the analysis of chemical oxygen demand, Environmental Science & Technology, 46 (2012) 2291-2298.

[48] S.B. Hall, E.A. Khudaish, A.L. Hart, Electrochemical oxidation of hydrogen peroxide at platinum electrodes. Part II: effect of potential, Electrochimica Acta, 43 (1998) 2015-2024.

[49] J. Zhang, C. Lin, Z. Feng, Z. Tian, Mechanistic studies of electrodeposition for bioceramic coatings of calcium phosphates by an in situ pH-microsensor technique, Journal of Electroanalytical Chemistry, 452 (1998) 235-240.

[50] L. Gorton, A carbon electrode sputtered with palladium and gold for the amperometric detection of hydrogen peroxide, Analytica Chimica Acta, 178 (1985) 247-253.

[51] J.A. Cox, R.K. Jaworski, Voltammetric reduction and determination of hydrogen peroxide at an electrode modified with a film containing palladium and iridium, Analytical chemistry, 61 (1989) 2176-2178.

[52] D.A. Johnston, M.F. Cardosi, D.H. Vaughan, The electrochemistry of hydrogen peroxide on evaporated gold/palladium composite electrodes. Manufacture and electrochemical characterization, Electroanalysis, 7 (1995) 520-526.

Chapter 4

4 Hydrogen Peroxide Decomposition on Simulated Nuclear Fuel Bicarbonate/Carbonate Solutions

4.1 Introduction

In common with the international community, the Canadian strategy for the disposal of high level nuclear waste is permanent disposal in a deep geologic repository (DGR). The waste form (spent nuclear fuel in the Canadian case) will be sealed in a Cu-coated steel container prior to emplacement in the DGR[1-3]. The durability of these containers is expected to be sufficient to avoid failure until the radiation levels within the fuel decay to innocuous levels, with corrosion models predicting only minimal damage [4]. However, it is judicious to examine the consequences of container failure when the fuel waste form could come into contact with groundwater. Although the groundwater entering the container would be anoxic, the redox conditions within the container, which will control the rate of release of most radionuclides from the fuel, will be controlled by the radiolysis of the groundwater and the corrosion of the inner surface of the steel container [5, 6]. Of the radiolytic oxidants that will be formed, H_2O_2 is expected to have the dominant influence on fuel corrosion [7, 8].

The influence of H_2O_2 on UO_2 corrosion has been extensively studied and much of the earlier literature reviewed [5, 9, 10]. On the corroding UO_2 surface there are two competing anodic reactions which can couple with the cathodic reduction of H_2O_2: the dissolution of $U^{IV}O_2$ as $U^{VI}O_2^{2+}$, and the oxidation of H_2O_2, the latter leading to the decomposition of H_2O_2,

$$2H_2O_2 \rightarrow O_2 + H_2O \qquad \textbf{4.1}$$

Peroxide decomposition has been studied on various metal oxide surfaces and a variety of reaction pathways proposed. Recent studies have demonstrated that the reaction proceeds via a radical mechanism [11-13],

$$(H_2O_2)_{ads} \rightarrow 2(OH^{\bullet})_{ads} \qquad \textbf{4.2}$$

$$(H_2O_2)_{ads} + (OH^{\bullet})_{ads} \rightarrow H_2O + (HO_2^{\bullet})_{ads} \qquad \textbf{4.3}$$

$$2(HO_2^{\bullet})_{ads} \rightarrow H_2O_2 + O_2 \qquad \textbf{4.4}$$

Decomposition on oxides which can sustain reversible redox transformations can be catalyzed by these transformations [14, 15]. On $U^{IV}O_2$ surfaces the balance between $U^{IV}O_2$ dissolution and H_2O_2 decomposition varied depending on the composition of the oxide. Thus, while the overall reactivity remained the same, 14% of the H_2O_2 was consumed by dissolution on $U^{IV}O_2$ compared to ~ 2% on SIMFUEL[16] ($U^{IV}O_2$ doped with non-radioactive elements including rare earth elements to simulate in-reactor burn-up[17]). This difference has been attributed to differences in the redox reactivities of $U^{IV}O_2$ and SIMFUEL [8], although the presence of potentially catalytic noble metal (ε) particles in the SIMFUEL was not addressed. The stabilization of the $U^{IV}O_2$ matrix against dissolution by rare earth doping has been subsequently demonstrated electrochemically [18-21]. Corrosion potential (E_{CORR}) measurements suggest that H_2O_2 decomposition may be controlled by the kinetics of the cathodic

reaction [22] although the behaviour on the $U^{IV}O_2$ surface is strongly influenced by its chemical composition.

In this study we have investigated the corrosion of SIMFUEL in NaCl solutions containing various concentrations of HCO_3^-/CO_3^{2-} and H_2O_2 with a primary emphasis on determining the mechanisms and relative importance of $U^{IV}O_2$ dissolution and H_2O_2 decomposition. A combination of electrochemical, and surface and solution analytical methods have been applied.

4.2 Experimental

4.2.1 Materials

The UO_2 electrodes were cut from 3 at.% SIMFUEL manufactured by Atomic Energy Canada Limited (now Canadian Nuclear Laboratories, Chalk River, Ontario, Canada). SIMFUELs are $U^{IV}O_2$ pellets doped with 11 non-radioactive elements (Ba, Ce, La, Sr, Mo, Y, Zr, Rh, Pd, Ru, Nd) to replicate the chemical effects of in-reactor irradiation and have been well characterized and studied [17]. These dopants are categorized into two groups: (1) elements which are distributed throughout the $U^{IV}O_2$ matrix and can influence the structure and electrical conductivity; and (2) elements (Pd, Ru, Rh, Mo) which segregate as noble metal (ε) particles and are generally distributed along grain boundaries. The distribution and composition of these particles has been described elsewhere[23, 24].

4.2.2 Electrodes and Solutions

Electrodes were polished on wet 1200 SiC paper and rinsed with Type I water prior to experiments. All solutions were prepared with Type 1 water (ρ = 18.2 Mohm.cm), purified using a Millipore Milli-Q Plus unit and deaereated with Ar (ultra-high purity, Praxair) for at least 1 h

prior to an experiment. Ar purging was then continued throughout an experiment. Experiments were conducted in a 0.1 mol.L^{-1} NaCl solution containing various $NaHCO_3$ (0.005 to 0.05 mol.L^{-1}) and H_2O_2 (0.001 mol.L^{-1} to 0.02 mol.L^{-1}) concentrations. The solution pH was adjusted to 9.7 using 0.2 mol.L^{-1} NaOH solution, and measured using an Orion model 250A pH meter and an Orion 91-07 Triode pH/ATC probe. All chemicals were reagent grade and purchased from Fisher Scientific. All experiments were performed at room temperature.

4.2.3 Electrochemical Cell and Procedures

A one-compartment 40 mL cell was used to minimize the UO_2 surface area to solution volume ratio enabling more accurate measurements of H_2O_2 consumption and the extent of U dissolution. A saturated Ag/AgCl reference electrode was placed in the main compartment and a Pt wire counter electrode was used separated from the main cell body by a high-density glass frit. The cell was placed in a Faraday cage to minimize interference from external electrical noise and covered with Al foil to avoid photolytic decomposition of the H_2O_2. All electrochemical experiments were performed with a Solartron 1480 Multistat controlled by CorrWare Version 2.7 software.

The electrode was polarized to a potential of -1.2 V (vs. saturated Ag/AgCl) for 20 s to cathodically remove air-formed oxides. Polarization resistances (R_P) were obtained from the slopes of current-potential scans over the range $E_{CORR} \pm 10$ mV. Electrodes for X-ray photoelectron spectroscopic (XPS) analyses were removed from the cell, rinsed with Type 1 water, dried in an Ar stream, and immediately sealed in an evacuated plastic box for rapid transfer to the spectrometer.

4.2.4 Scanning Electron Microscopy (SEM) and Energy Dispersive X-ray (EDX) Analyses

The surface morphology of electrodes was observed using a Hitachi S-4500 field emission scanning electron microscope (SEM) equipped with a Quartz XOne energy dispersive X-ray (EDX) analysis system. An electron beam voltage of 20 kV was used and the working distance was 10 mm during image collection resulting in a spatial resolution of < 2 nm.

4.2.5 X-ray Photoelectron Spectroscopy (XPS)

XPS analyses were performed on a Kratos Axis NOVA spectrometer using a monochromatic Al K_α X-ray source (1486.6 eV). The instrument work function was calibrated to give a binding energy of 83.96 eV for the Au $4f_{7/2}$ line for metallic Au and the spectrometer dispersion was adjusted to give a binding energy (BE) of 932.62 eV for the Cu $2p_{3/2}$ line of metallic Cu. Survey scans were recorded over the energy range 0-1100 eV on an analysis area of 300 x 700 μm^2 with a pass energy of 160 eV. Spectra were charge-corrected when necessary using the C 1s peak set to be at 285.0 eV. Spectra were analyzed using CasaXPS software (version 2.3.14).

High resolution scans were performed for the spectral region including the $U4f_{5/2}$ and U $4f_{7/2}$ peaks and their satellites, using a pass energy of 20 eV with a step size of 0.05 eV. All spectra were fitted using a 50% Gaussian and 50% Lorentzian routine with a Shirley background correction. The 4f peaks were used to quantify the U oxidation states (U^{IV}, U^{V}, U^{VI}) using curve fitting procedures and binding energies discussed elsewhere [25-27]. The resolved components in both the U4f peaks and the associated satellite structures were used to calculate the total proportions of each oxidation state. The positions and shapes of the satellite structures were used to confirm the validity of the analyses as described in published literature.[28-31].

4.2.6 Inductively-Coupled Plasma Mass Spectrometry (ICP-MS)

Dissolved U concentrations were determined by ICP-MS with an Agilment 7700 x ICP-MS using both “He gas” and “No gas” modes. The solutions were diluted by a factor of 1000 using 2% HNO_3 prior to analysis to minimize matrix effects. The instrument has a detection limit of 0.02 µg/L for U and was calibrated using a series of U standards.

4.2.7 UV-Vis Spectrophotometry

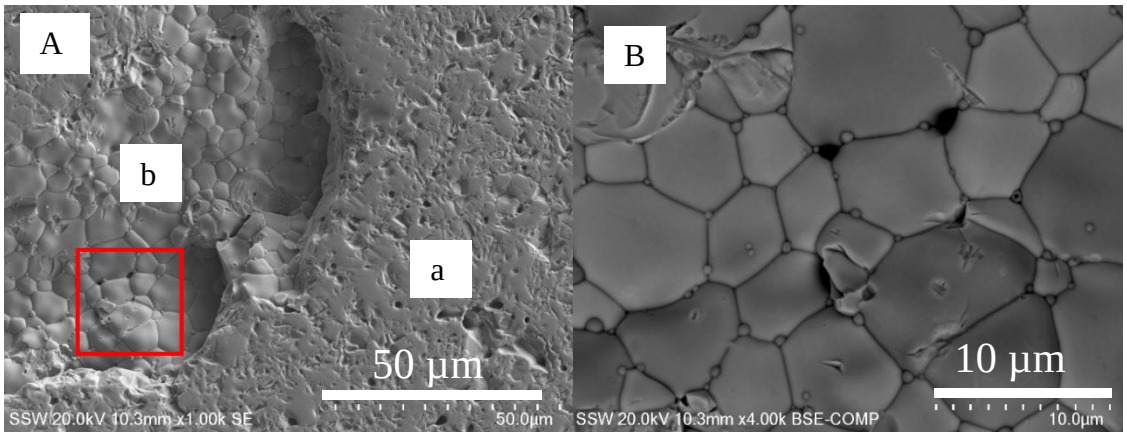

Figure 4.1: SEM images of a 3 at.% SIMFUEL specimen. A: (a) the polished surface; (b) smooth large UO_2 grains untouched by the polishing procedure: B: showing the presence of ε-particles on the grain boundaries, image B is the magnification of the red box highlighted area in image (A).

H_2O_2 concentrations were measured with an Ultra-Violet/visible (UV-Vis) spectrophotometer. The measurements were performed using a BioLogic Science Instrument MOS 450 diode array UV-vis Spectrophotometer using the Ghormley tri-iodide method [32, 33]. The absorbance at 352 nm was measured with a detection limit for H_2O_2 of 3 x 10^{-6} mol.L^{-1}. Analyses were performed immediately after sampling with the vial containing the extracted solution covered with Al foil.

4.3 Results

4.3.1 SEM/EDX Analysis

Figure 4.1 shows the surface morphology of a freshly polished and sonicated 3 at.% SIMFUEL doped with noble metal (ε) particles. In Figure 4.1 A, area (a) shows the general surface to be rough with residual sintering voids. Locations untouched by polishing, area (b), show undamaged UO_2 grain features. Figure 4.1 B shows the UO_2 large and smooth grains with diameters in the range 3 to 10 µm. The small particles decorating the grain boundaries have been shown previously to be noble metal (ε) particles containing Mo, Pd, Ru and Rh [23, 24].

4.3.2 Hydrogen Peroxide Decomposition in HCO_3^-/CO_3^{2-} Solutions

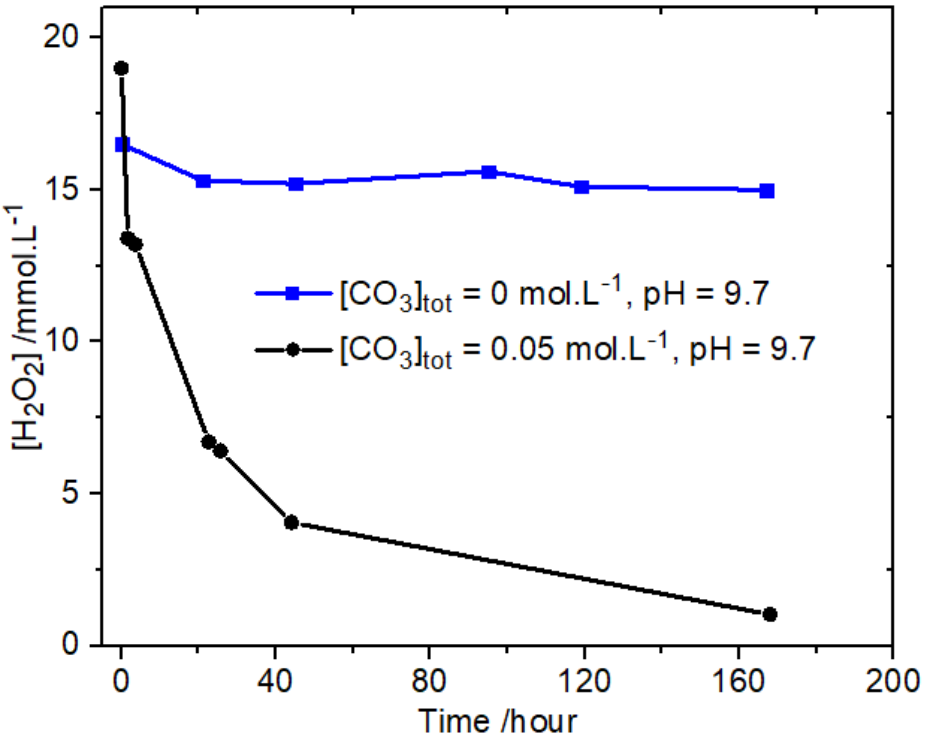

Figure 4.2: H_2O_2 concentration as a function of time: $[H_2O_2]$ = 0.016 mol.L^{-1} in both experiments (pH adjusted to 9.7).

The effect of HCO_3^-/CO_3^{2-} on the homogeneous decomposition of H_2O_2 is shown in Figure 4.2. In the absence of HCO_3^-/CO_3^{2-}, the $[H_2O_2]$ decreased by ~ 10% in 7 days. This decrease was not unexpected since H_2O_2 decomposition is known to occur in alkaline solution with or without the presence of metal catalysts.[34-38] Littauer et al.[38] proposed that H_2O_2 decomposes in strong alkaline (pH = 12) solutions through the formation of perhydroxyl ions (HO_2^-) which then catalyze H_2O_2 decomposition via reactions 4.5 and 4.6,

$$H_2O_2 + OH^- \rightarrow HO_2^- + H_2O \qquad \textbf{4.5}$$

$$HO_2^- + OH^- \rightleftharpoons O_2 + H_2O + 2e^- \qquad \textbf{4.6}$$

This reaction can occur in the absence of metallic or oxide catalysts[36] at a rate determined by both the total alkalinity and $[H_2O_2]$.

In the HCO_3^-/CO_3^{2-} solution, the $[H_2O_2]$ decreased markedly over the 168 h duration of the experiment, demonstrating a catalytic influence of HCO_3^-/CO_3^{2-} irrespective of any influence of alkalinity. Raman Spectroscopy has been used to demonstrate the formation of peroxycarbonate ions when HCO_3^-/CO_3^{2-} was present in H_2O_2 solutions in the pH range 7.0 to 9.5 [39]. The H_2O_2 decomposition rate in HCO_3^-/CO_3^{2-} solutions has been shown to be a maximum at pH values between 11.5 and 11.7 [40], when the solution is dominated by CO_3^{2-}. It was proposed that the reaction proceeded via steps 4.7 and 4.8,

$$CO_3^{2-} + H_2O_2 \rightarrow CO_4^{2-} + H_2O \qquad \textbf{4.7}$$

$$CO_4^{2-} + HO_2^- \rightarrow HCO_3^- + H_2O + O_2 \qquad \textbf{4.8}$$

At the pH of 9.7 used in our experiments, the solution would be ~ 40% CO_3^{2-} making it essential to consider the homogeneous decomposition process when evaluating the influence of $U^{IV}O_2$ on the heterogeneous decomposition of H_2O_2.

4.3.3 H_2O_2 Decomposition on SIMFUEL

In the presence of a SIMFUEL electrode, the total decrease in $[H_2O_2]$ ($\Delta[H_2O_2]_{tot}$) can be attributed to both homogeneous decomposition in solution ($\Delta[H_2O_2]_{sol}$) and consumption on the SIMFUEL surface ($\Delta[H_2O_2]_{UO_2}$). The latter includes both heterogeneous decomposition and consumption by $U^{IV}O_2$ corrosion. The total amount of H_2O_2 decomposed ($\Delta[H_2O_2]_{tot}$) can be corrected for homogeneous decomposition by comparing H_2O_2 consumption in the presence and absence of a $U^{IV}O_2$ electrode, and is given by

$$\Delta[H_2O_2]_{UO_2} = \Delta[H_2O_2]_{tot} - \Delta[H_2O_2]_{sol} \qquad \textbf{4.9}$$

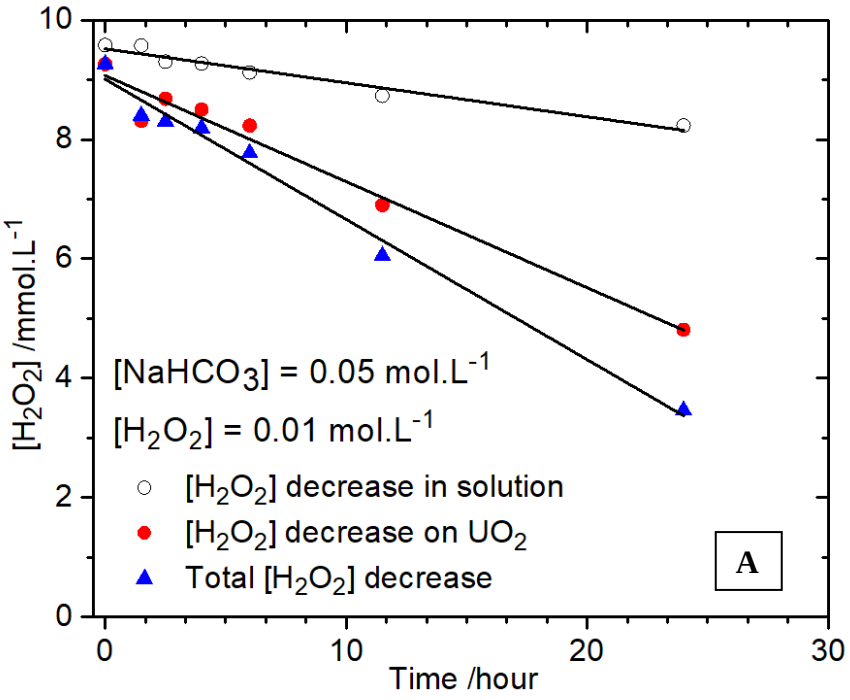
10
8
6
4
2
0
0
10
20
30
[H2O2] /mmol.L-1
Time /hour
[NaHCO3] = 0.05 mol.L-1
[H2O2] = 0.01 mol.L-1
[H2O2] decrease in solution
[H2O2] decrease on UO2
Total [H2O2] decrease
A

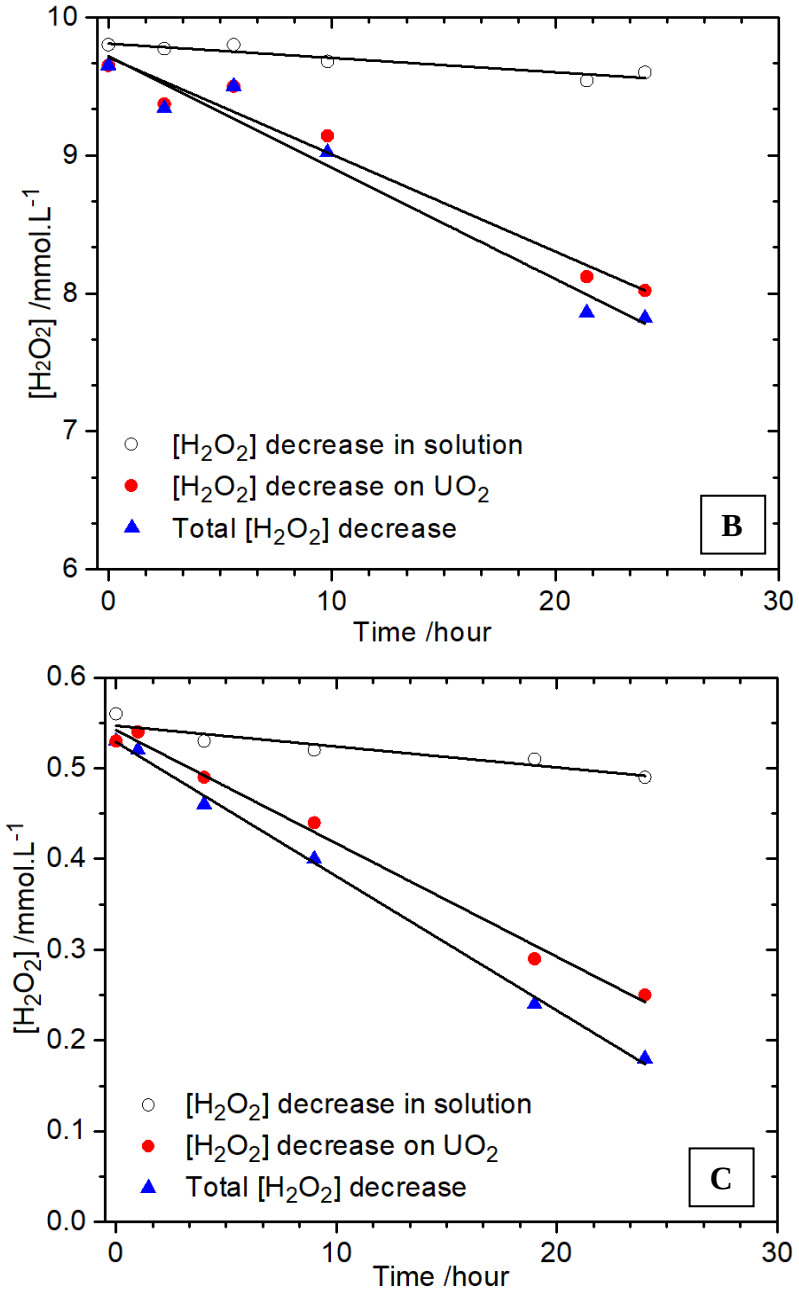

Figure 4.3: $[H_2O_2]$ as a function of time in solutions containing various $[H_2O_2]$ and $[CO_3]_{tot}$; Hollow circle – no SIMFUEL present; blue triangle – SIMFUEL present; Red circle – decrease in $[H_2O_2]$ by reaction on SIMFUEL. (A) $[H_2O_2]$ = 0.01 mol.L^{-1}, $[CO_3]_{tot}$ = 0.05 mol.L^{-1} ; (B)) $[H_2O_2]$ = 0.01 mol.L^{-1}, $[CO_3]_{tot}$ = 0.01 mol.L^{-1}; (C)) $[H_2O_2]$ = 0.0005 mol.L^{-1}, $[CO_3]_{tot}$ = 0.05 mol.L^{-1}. All the solutions contained 0.1 mol.L^{-1} of NaCl, pH =9.7.

In a solution containing $[H_2O_2]$ = 0.01 mol.L^{-1} and $[CO_3]_{tot}$ = 0.05 mol.L^{-1}, Figure 4.3 A, approximately 48% of the available H_2O_2 was consumed. Since 14% was consumed by homogeneous decomposition ($\Delta[H_2O_2]_{sol}$), the majority was consumed by either decomposition on, or reaction with, the SIMFUEL ($\Delta[H_2O_2]_{UO2}$). When the $[CO_3]_{tot}$ was decreased by a factor of 5 to 0.01 mol.L^{-1}, only minimal homogeneous decomposition was observed, Figure 4.3 B, confirming the acceleration of this reaction by CO_3^{2-}. In this solution, while reaction on the SIMFUEL surface was the dominant process, the overall consumption of H_2O_2 was decreased. A comparison of the results in Figure 4.3 A and B indicates a significant role for HCO_3^-/CO_3^{2-} in accelerating the reactions on the SIMFUEL surface. At a higher $[CO_3]_{tot}$, but lower $[H_2O_2]$, the fractions of the H_2O_2 consumed homogeneously and heterogeneously, Figure 4.3 C, were similar to those observed at the same $[CO_3]_{tot}$ and higher $[H_2O_2]$, Figure 4.3 A. These results confirm the importance of HCO_3^-/CO_3^{2-} in both the homogeneous and heterogeneous reactions.

4.3.4 Corrosion Potential (E_{CORR}) and Polarization Resistance (R_P) Measurements

A series of corrosion experiments was conducted in 0.1 mol.L^{-1} NaCl containing various $[CO_3]_{tot}$ and $[H_2O_2]$. E_{CORR} was monitored over an exposure period of 24 h and a series of R_P measurements conducted at 1 h intervals. Three examples of E_{CORR} and R_P plots (as a function of time) are shown in Figure 4.4. All three sets of values exhibit similar, but quantitatively different, behaviour. E_{CORR} rapidly increased to ~ 0.15 V (not observable on the plots) before decaying to less positive values, while R_P values decreased over approximately the first 5 h before increasing steadily over the remainder of the experiment.

Since the anodic oxidation of both UO_2 and H_2O_2 are supported by the cathodic reduction of H_2O_2,

$$I_{CORR} + I_{H2O2} = \sum I_A = -I_C \qquad \textbf{4.10}$$

where I_{CORR} is the current due to $U^{IV}O_2$ dissolution and I_{H2O2} that due to the anodic oxidation of H_2O_2. However, since R_P^{-1} is proportional to the total interfacial charge transfer rate, it does not distinguish between the relative rates of the two reactions.

The initial decrease in R_P indicates an acceleration of the interfacial reaction rate over the first 5 h followed by a decrease as R_P increases at longer times. Figure 4.4 A and B show the influence of changing the $[CO_3]_{tot}$ by a factor of 5 in solutions containing the same $[H_2O_2]$ (0.01 $mol.L^{-1}$). In the more concentrated HCO_3^-/CO_3^{2-} solution, Figure 4.4 A, E_{CORR} decreased steadily as the H_2O_2 was consumed, Figure 4.3 A. This indicates that the long term increase in R_P can be attributed to the consumption of $[H_2O_2]$, but this cannot explain the initial decrease in R_P. When the $[CO_3]_{tot}$ was decreased, Figure 4.4 B, the decrease in E_{CORR} and long term increase in R_P are relatively minor indicating a considerably lower rate of H_2O_2 consumption, Figure 4.3 B. Despite the identical $[H_2O_2]$, the overall rate of its consumption (R_P^{-1}) is lower at lower $[CO_3]_{tot}$.

Since we would not expect HCO_3^-/CO_3^{2-} to influence the rate of H_2O_2 decomposition on noble metal particles, the difference in H_2O_2 consumption rate can be attributed to the influence of HCO_3^-/CO_3^{2-} on the rate of the processes occurring on the $U^{IV}O_2$ surface. Lower E_{CORR} values coupled with increased interfacial rates indicates that the dominant effect of a decrease in $[CO_3]_{tot}$ is to suppress the rate of anodic reactions. This hypothesis appears borne out by the values recorded at high $[CO_3]_{tot}$/low $[H_2O_2]$, Figure 4.4 C, the E_{CORR}/R_P behaviour being similar to that recorded at high $[CO_3]_{tot}$/high $[H_2O_2]$ with the exception that the R_P values are considerably higher at the lower $[H_2O_2]$.

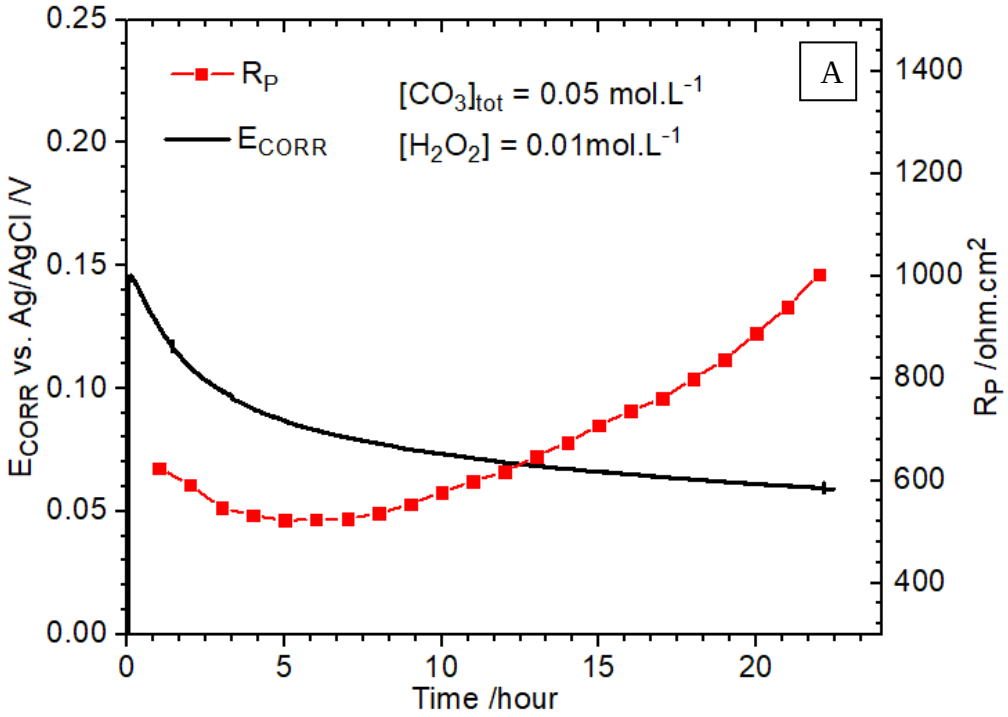
A
R_P
E_{CORR}
$[CO_3]_{tot}$ = 0.05 mol.L^{-1}
$[H_2O_2]$ = 0.01mol.L^{-1}
E_{CORR} vs. Ag/AgCl /V
R_P /ohm.cm^2
Time /hour
0.25
0.20
0.15
0.10
0.05
0.00
1400
1200
1000
800
600
400
0
5
10
15
20

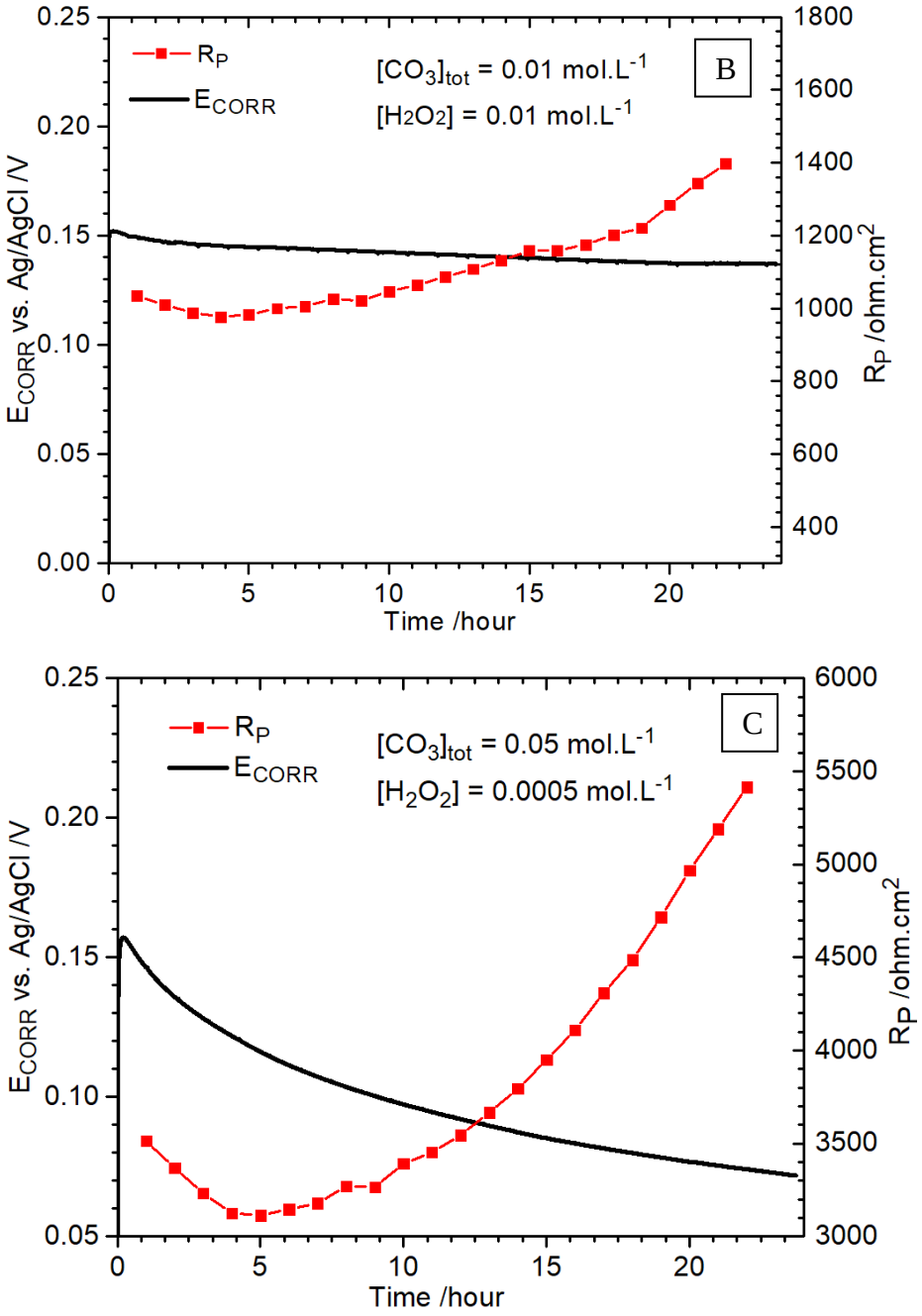

Figure 4.4: Corrosion potential (E_{CORR}) and polarization resistance (R_P) measurements as a function of time in solutions containing different $[H_2O_2]$ and $[CO_3]_{tot}$. The curves show E_{CORR} (black line) and the connected squares show the R_P values measured every hour. All the solutions contain 0.1 mol.L^{-1} of NaCl (pH = 9.7).

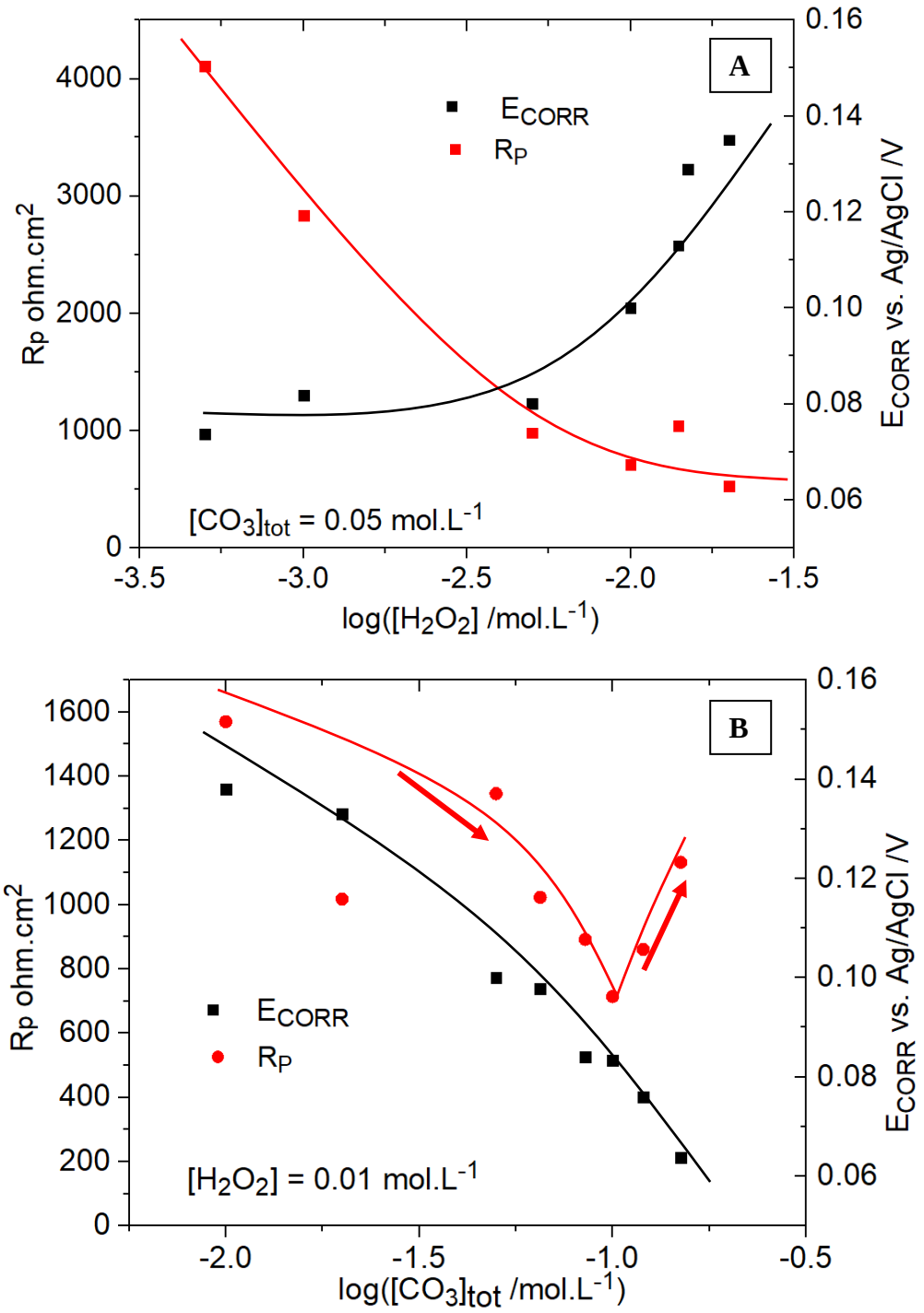

Figure 4.5: R_P and E_{CORR} values recorded after 16 hours of exposure: A-as a function of $[H_2O_2]$; B-as a function of $[CO_3]_{tot}$. All the solutions contain 0.1 mol.L^{-1} of NaCl, pH = 9.7.

Figure 4.5 (A and B) show the changes in R_P and E_{CORR} recorded over a wider range of $[H_2O_2]$ (A) and $[CO_3]_{tot}$ (B). The interfacial reaction rate (R_P^{-1}), the rate of H_2O_2 consumption, increases rapidly with increasing $[H_2O_2]$ at low $[H_2O_2]$ while E_{CORR} remains effectively constant. At higher $[H_2O_2]$, the rate approaches a concentration-independent value while E_{CORR} increases markedly. Since these experiments were conducted in a solution containing 0.05 mol.L^{-1} HCO_3^- /CO_3^{2-} the electrode surface should be relatively free of U^{VI} species (see below) allowing H_2O_2 consumption to proceed uninhibited.

Similar changes in E_{CORR} with $[H_2O_2]$ were observed previously on an undoped UO_2 not containing noble metal (ε) particles [9] suggesting the present observations can be attributed to reactions occurring predominantly on the UO_2 surface not on the noble metal (ε) particles. Although no rates were measured in this previous study, it was proposed that the behaviour at low $[H_2O_2]$, when E_{CORR} was independent of $[H_2O_2]$, could be attributed to the dominance of H_2O_2 decomposition over UO_2 corrosion, with the increase in E_{CORR} at higher $[H_2O_2]$ indicating an increased importance of the anodic dissolution of UO_2. The results presented here show that if such a change in the importance of the individual reactions occurs at higher $[H_2O_2]$, it does not lead to any increase in the consumption rate of H_2O_2.

The influence of $[CO_3]_{tot}$ on E_{CORR} and the interfacial rate involves two distinct stages, Figure 4.5 B. While E_{CORR} decreases over the full concentration range investigated, the consumption rate first increases with $[CO_3]_{tot}$ (for concentrations $\leq$ 0.1 mol.L^{-1}) before decreasing again at higher $[CO_3]_{tot}$ (as indicated by the arrows in the figure).

4.3.5 XPS Analysis of UO_2 Surface Composition

XPS spectra were recorded on SIMFUEL specimens exposed to solutions containing 0.01 mol.L^{-1} H_2O_2 and two different $[CO_3]_{tot}$. Figure 4.6 shows the background corrected and fitted U4$f_{7/2}$ peaks deconvoluted to determine the relative amounts of U^{IV}, U^{V} and U^{VI} in the electrode surface. The exposure times were chosen to yield measurements of surface composition after the initial acceleration in the interfacial rate (4 h, Figure 4.4) and after an

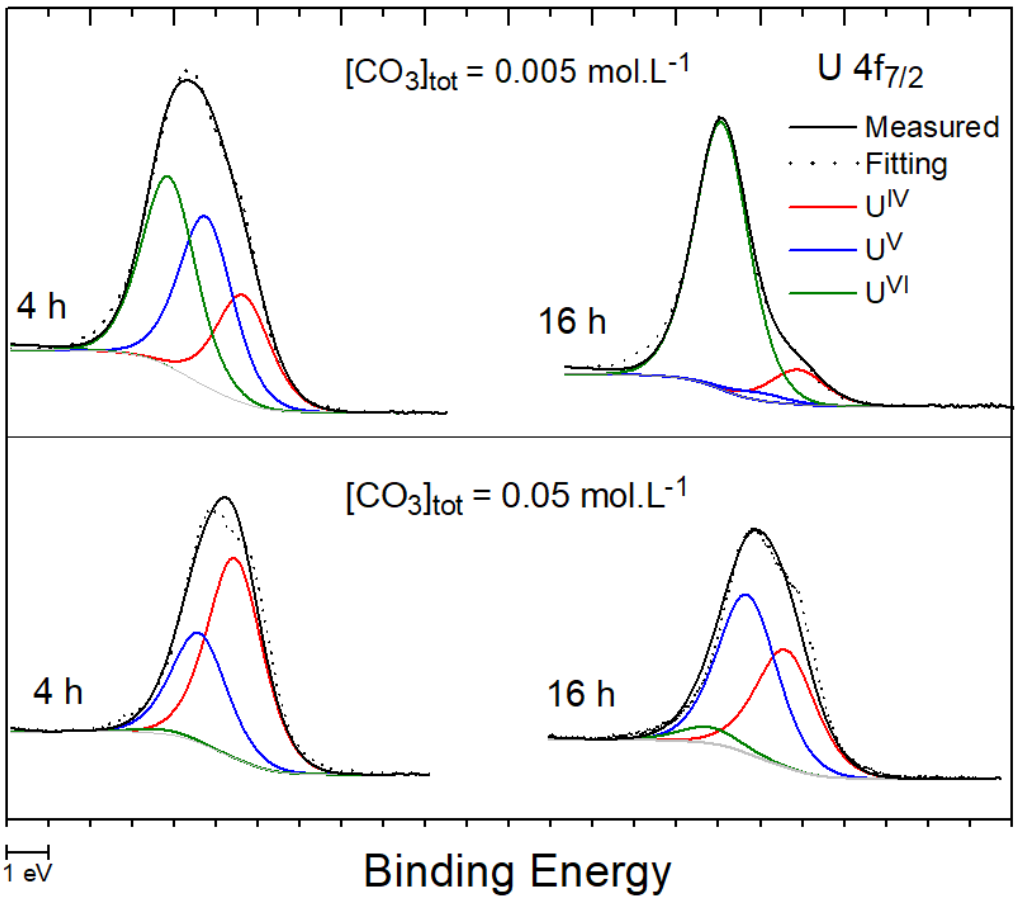

Figure 4.6: The U$f_{7/2}$ peak recorded on SIMFUEL surfaces (dashed line), deconvoluted into contributions from U^{IV}, U^{V} and U^{VI}, after various exposure periods to solutions containing different 0.01 mol.L^{-1} H_2O_2 and HCO_3^-/CO_3^{2-} concentrations. All solutions contained 0.1 mol.L^{-1} NaCl (pH = 9.7).

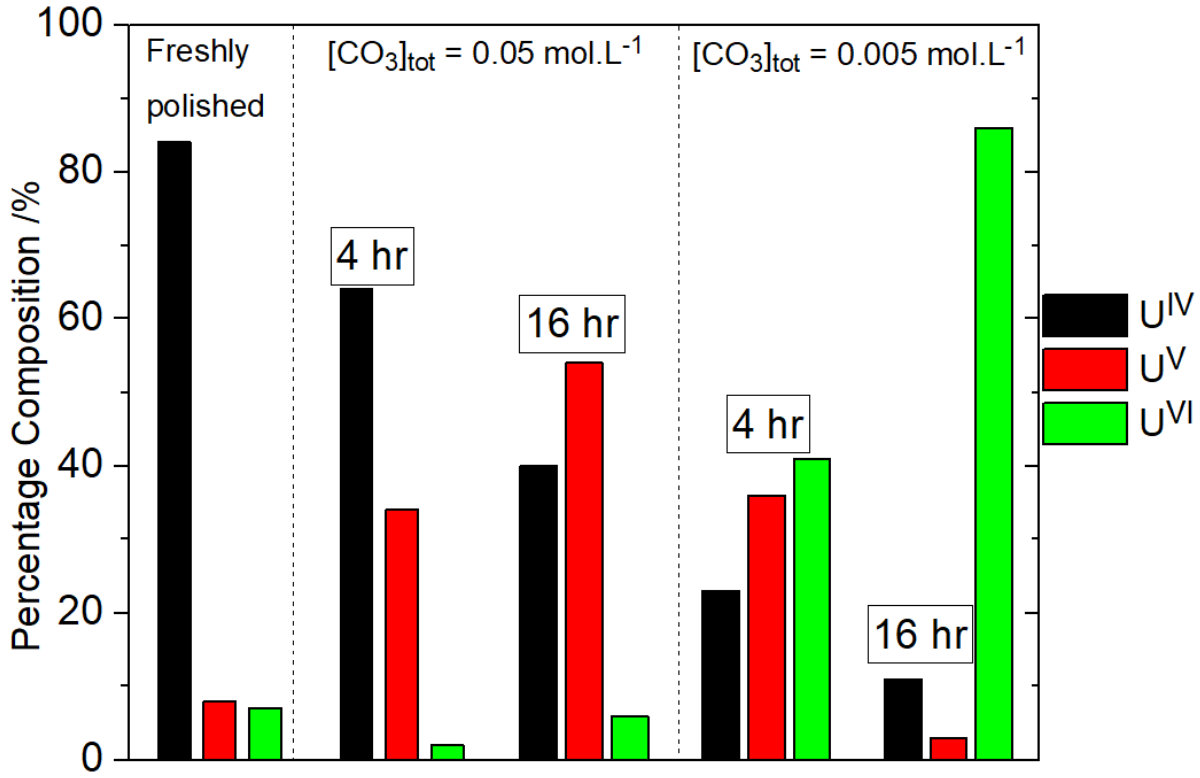

Figure 4.7: Percentage of U oxidation states in the SIMFUEL surface after exposure to a 0.01 mol.L^{-1} H_2O_2 solution obtained by deconvolution of the U4f$_{7/2}$ peaks in XPS spectra , Figure 6.

extended exposure period (16 h, Figure 4.4) when the interfacial rate had slowed considerably due to the consumption of H_2O_2. Figure 4.7 compares the fractions of the individual oxidation states (expressed as percentages) in the exposed electrode surfaces to values measured on a freshly polished electrochemically reduced surface.

For the freshly polished and reduced electrode only minor amounts of oxidized states (U^V and U^{VI}) are present as expected after this treatment. After exposure to the more concentrated HCO_3^-/CO_3^{2-} solution (0.05 mol.L^{-1}) the U^V content of the surface increases substantially after 4h

and even more so after 16h while the U^{VI} content remains minor. When considered in conjunction with the R_P values for a high $[CO_3]_{tot}$/high $[H_2O_2]$ solution (Figure 4.4 A) these analyses show that an acceleration in rate (decrease in R_P) accompanies this initial oxidation of the surface to $U^{IV}_{1-2x}U^{V}_{2x}O_{2+x}$ and that a predominantly U^{IV}/U^{V} surface is sustained at longer times when consumption of H_2O_2 proceeds, as indicated by the increase in R_P. These results confirm that the optimum surface composition to support H_2O_2 decomposition is a mixed U^{IV}/U^{V} surface, offering strong evidence that the decomposition reaction is catalyzed by a reversible U^{IV}-U^{V} redox transformation in the $U^{IV}O_2$ surface.

When the $[CO_3]_{tot}$ was reduced by an order of magnitude the surface after 4 h again exhibited a significant U^{V} content, consistent with the formation of the $U^{IV}_{1-2x}U^{V}_{2x}O_{2+x}$ layer, but also contained a substantial U^{VI} content. After 16h the surface composition was totally dominated by U^{VI}. When considered in conjunction with the R_P values recorded in the low $[CO_3]_{tot}$/high $[H_2O_2]$ solution (Figure 4.4 B) these analyses show that, while the initial formation of the $U^{IV/}U^{V}$ layer accelerates the consumption of H_2O_2, it is muted and eventually suppressed by the accumulation of U^{VI} surface species at longer exposure times. This would account for the small increase in R_P accompanied by only a marginal decrease in E_{CORR} (Figure 4.4 B).

4.3.6 UO_2 Dissolution Experiments

Up to this juncture, only the overall consumption of H_2O_2 has been measured. To determine the relative importance of the two reactions responsible for H_2O_2 consumption, a series of experiments was conducted, over an exposure period of 24 h, to determine the amount of dissolved U and the total amount of H_2O_2 consumed. The analyzed amount of U can then be used to calculate the fraction of the consumed H_2O_2 used in UO_2 corrosion. The O_2 produced by

decomposition could also act as an oxidant for UO_2, but at a rate 200 times slower than H_2O_2 [41]. This slow rate, and the continuous purging of the solution with Ar, means any influence of O_2 can be neglected. The surface films formed ($U^{IV}_{1-2x}U^{V}_{2x}O_{2+x}$, U^{VI} oxide/hydroxide/carbonate) will also consume negligible amounts of H_2O_2 since they are, at most, only a few nanometres thick.

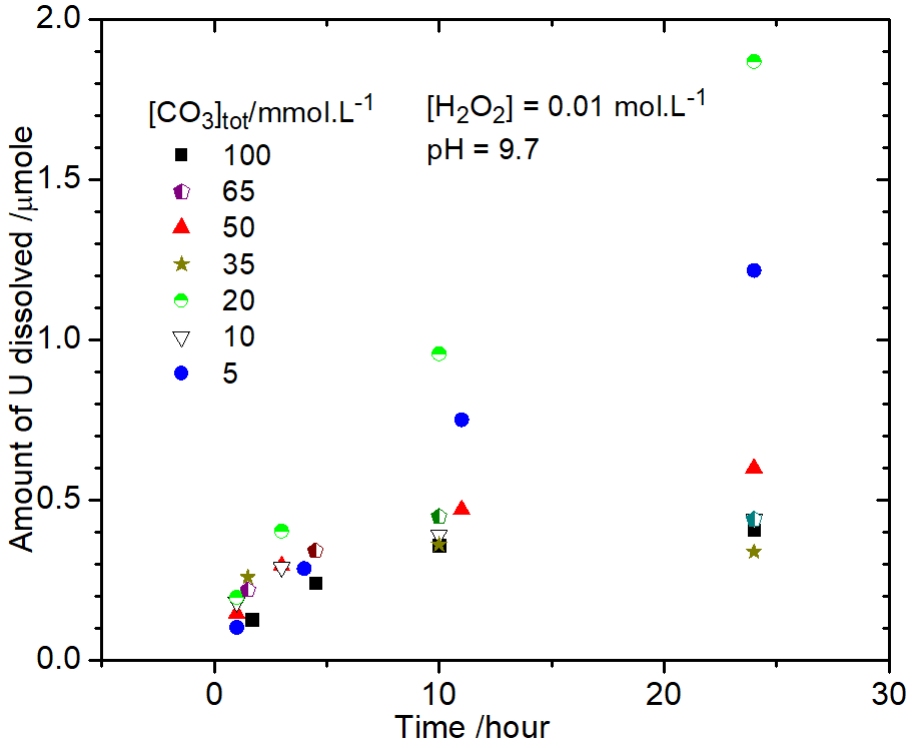

Figure 4.8: The amount of dissolved U measured as a function of time in 0.01 mol L^{-1} H_2O_2 solutions containing different $[CO_3]_{tot}$ as a function of time.

Figure 4.8 shows the influence of $[CO_3]_{tot}$ on U dissolution over a 24 h exposure period in a solution containing 0.01 mol.L^{-1} H_2O_2. At high $[CO_3]_{tot}$ (35 to 100 mmol.L^{-1}) the amount of U released increases over the first ~ 10 hours before reaching a plateau value indicating release has stopped. At lower $[CO_3]_{tot}$, in particular 5 and 10 mmol.L^{-1}, U release did not plateau but continued unabated. At the higher $[CO_3]_{tot}$, the release coincides with the earlier exposure period

over which R_P values, Figure 4.4, decrease indicating an acceleration in H_2O_2 consumption as the surface is oxidized to $U^{IV}_{1-2x}U^{V}_{2x}O_{2+x}$. At the lower $[CO_3]_{tot}$ when the U release increased, the rate of H_2O_2 consumption will be substantially lower, Figure 4.3 B and Figure 4.4 B, and the XPS analyses show the surface will be partially blocked by the accumulation of U^{VI}.

Table 4-1 shows the ratio of the amount of H_2O_2 causing dissolution to the total amount consumed corrected for that consumed by homogeneous decomposition. These fractions confirm that the great majority of H_2O_2 is consumed by decomposition with only a small fraction used to cause UO_2 corrosion. These results are consistent with those of Nilsson et al.[16] who found only 0.2% of the H_2O_2 consumed on a SIMFUEL surface caused UO_2 dissolution.

Table 4-1: The amount U dissolved in different $[CO_3]_{tot}$ solutions and the calculated fraction of H_2O_2 used to oxidize U ($[H_2O_2]_{dis}$) over the total $[H_2O_2]$ ($[H_2O_2]_{tot}$)

$[CO_3]_{tot}$ (mmol.L^{-1})	U dissolved in 24 hours (µmol)	$[H_2O_2]_{dis}/[H_2O_2]tot$ (%)
5	1.22	0.41
10	0.44	0.15
20	1.87	0.62
35	0.34	0.11
50	0.60	0.20
65	0.44	0.15
100	0.40	0.14

4.3.7 Discussion

In aqueous HCO_3^-/CO_3^{2-} solutions containing a SIMFUEL specimen (electrode), decomposition is the dominant route for H_2O_2 consumption. This process can proceed both homogeneously and heterogeneously. Under the conditions employed in the present study (pH = 9.7, 0.005 mol.L^{-1} ≤ [CO3]tot ≤ 0.2 mol.L^{-1}; 0.001 mol.L^{-1} ≤ $[H_2O_2]$ ≤ 0.02 mol.L^{-1}) approximately 10 to 15% of the H_2O_2, depending on $[CO_3]_{tot}$, is decomposed homogeneously via

the formation of a peroxycarbonate (CO_4^{2-}) intermediate. This reaction is strongly dependent on pH and would be less significant at a lower pH value.

The dominant reaction consuming H_2O_2 is its catalytic decomposition on the SIMFUEL surface, only a small fraction (< 4% depending on $[CO_3]_{tot}$) being consumed by UO_2 corrosion for a $[H_2O_2]$ of 0.01 mol.L^{-1}. These values are consistent with those measured by Nilsson et al.[16] and considerably lower than the 14% measured on undoped UO_2 containing no noble metal particles. This difference has been shown to be due to the rare earth (RE^{III}) doping of the UO_2 lattice which leads to the formation of RE^{III}-O_V clusters and a reduction in the availability of the oxygen vacancies (O_V) required to accommodate the incorporation of the O interstitial ions which begin the process of destabilizing the UO_2 matrix[19, 20, 42].

On first immersion, the reduced SIMFUEL surface is oxidized to $U^{IV}_{1-2x}U^{V}_{2x}O_{2+x}$, a reaction which precedes the eventual further oxidation and dissolution as $U^{VI}O_2^{2+}$ [29, 43]. However, such a dissolution process is transitory with decomposition becoming the sole observable reaction after a few hours. The formation of this layer is accompanied by a decrease in E_{CORR} and an increase in the H_2O_2 decomposition rate. This combination, and the switching off of the U release to solution, indicates a depolarization of the anodic dissolution reaction to produce $U^{VI}O_2^{2+}$ and demonstrates that the overall decomposition reaction, which proceeds via radical intermediates (reactions 4.2 to 4.4), is catalyzed by the reversible redox transformation occurring on the $U^{IV}_{1-2x}U^{V}_{2x}O_{2+x}$ surface; i.e., reactions 4.1 and 4.2 in the schematic illustration in Figure 4.9. This would require that the reduction of U^{V} to U^{IV} (reaction 4.2, Figure 4.9) be more rapid than the further oxidation to U^{VI} via the sequence of reactions leading to dissolution as $U^{VI}O_2(CO_3)_y^{(2-2y)+}$ (reaction 4.3 to 4.5, Figure 4.9).

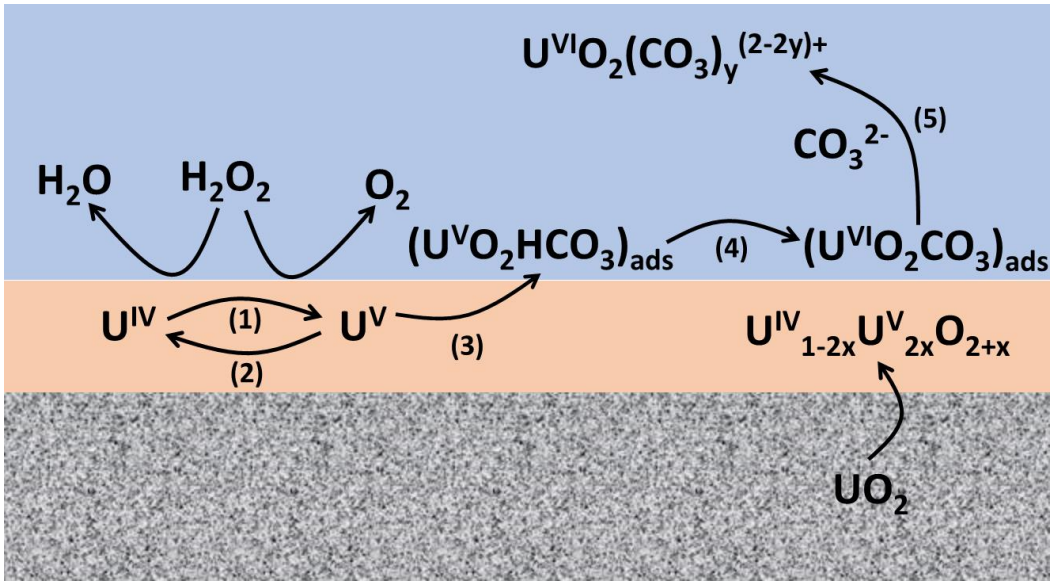

Figure 4.9: A schematic illustration of the reactions involving H_2O_2 on a UO_2 surface.

The E_{CORR} and R_P measurements demonstrate that the rate of decomposition is accelerated by an increase in $[CO_3]_{tot}$ except at high $[CO_3]_{tot}$ (> 0.1 mol.L^{-1}). The primary function of HCO_3^- /CO_3^{2-} is to complex and dissolve surface U^{VI} species ($(U^{VI}O_2CO_3)_{ads}$) formed by oxidation of the catalytic surface (reactions 4.4 and 4.5, Figure 4.9) preventing their accumulation on, and blockage of, the catalytic surface sites. It is also possible (but not shown in Figure 4.9) that heterogeneous decomposition involves the peroxycarbonate species (CO_4^{2-}) formed in the solution which has been shown to be readily oxidizable on SIMFUEL surfaces.

At high $[CO_3]_{tot}$ (> 0.1 mol.L^{-1}) (Figure 4.5 B) the decomposition rate begins to decrease again with increasing $[CO_3]_{tot}$. This is most likely due to the more rapid formation of the surface adsorbed carbonate complex state in the $U^{IV}_{1-2x}U^V_{2xO2+x}$ surface (reactions 4.3 and 4, Figure 4.9)[44]. This would facilitate the release of U^{VI}, a reaction controlled by the chemical

dissolution of U^{VI} surface species (reaction 4.5, Figure 4.9). This sequence of reactions would extract the U^{V} species from the catalytic surface layer by anodic oxidation and inhibit the matrix reduction reaction (reaction 4.2, Figure 4.9) required to complete the decomposition process.

When the $[CO_3]_{tot}$ becomes too low to prevent the accumulation of U^{VI} species on the catalytic surface layer, Figure 4.6. H_2O_2 consumption is suppressed as shown by the R_P values in Figure 4.3 B. Under these conditions, the surface U^{VI} species is likely to be a uranyl oxide, $U^{VI}O_3 \bullet 2H_2O$, or possibly studtite, $U^{VI}O_4 \bullet 4H_2O$[22]. Interestingly, when H_2O_2 decomposition becomes partially blocked in this manner, there is a slight increase in the release of soluble $U^{VI}O_2^{2+}$ to the solution.

For $[H_2O_2] \leq 0.01$ mol.L^{-1} and a sufficient $[CO_3]_{tot}$ to maintain access to the catalytic layer, H_2O_2 decomposition occurs under redox buffered conditions typified by an increase in rate (R_P^{-1}) with $[H_2O_2]$ while E_{CORR} remains constant, Figure 4.4 A. Similar behavior was previously observed on undoped UO_2 [9] containing no noble metal (ε) particles indicating that the role of the ε-particles in H_2O_2 decomposition is probably minor, although this remains to be demonstrated.

Under redox buffered conditions, the equilibrium potentials for the two half reactions exhibit a similar dependence on $[H_2O_2]$ which are opposite in sign. Thus, providing both reactions are rapid, as would be the case on the catalytic $U^{IV}_{1-2x}U^{V}_{2x}O_{2+x}$ layer, the rate, but not E_{CORR}, would change with $[H_2O_2]$, as observed.

However, for $[H_2O_2] \geq 0.01$ mol.L^{-1} the interfacial rate (the H_2O_2 consumption rate, but not necessarily the decomposition rate) becomes constant while E_{CORR} increases. This would be

expected to influence the relative kinetic importance of UO_2 corrosion and H_2O_2 decomposition by accelerating the sequence of reactions (3 to 5 in Figure 4.9) leading to anodic dissolution of the UO_2 matrix while retarding the transformation of U^V to U^{IV} (reaction 2, Figure 4.9), the redox reaction catalyzing the decomposition cathodic half reaction. This claim is consistent with our electrochemical results[24], which demonstrated that an increase in potential led to a much larger fraction of the anodic current (up to 40%) going to the anodic dissolution reaction.

4.4 Summary

-In aqueous HCO_3^-/CO_3^{2-} solutions in the presence of SIMFUEL, H_2O_2 consumption proceeds by homogenous decomposition in solution and by reaction with the SIMFEUL surface.

- Homogenous decomposition to O_2 and H_2O proceeds through a peroxycarbonate (CO_4^{2-}) intermediate with a rate dependent on both $[CO_3]_{tot}$ and pH.

- On the SIMFUEL surface, H_2O_2 decomposition is the dominant reaction, with only minor to negligible amount of UO_2 corrosion occurring. The stability of the SIMFUEL surface can be attributed to the stabilization of the $U^{IV}O_2$ matrix by RE^{III} doping.

- Surface decomposition proceeds via a radical mechanism and is catalyzed by the reversible $U^{IV} \rightleftharpoons U^V$ redox transition in a $U^{IV}_{1-2x}U^V_{2x}O_{2+x}$ surface.

- The primary function of HCO_3^-/CO_3^{2-} is to complex and dissolve U^{VI} surface species which prevents their accumulation to form an insulating layer which blocks decomposition on the catalytic surface layer.

- When the surface is maintained free of U^{VI} species, H_2O_2 decomposition proceeds under redox buffered conditions on the catalytic surface.

- At high $[CO_3]_{tot}$ ($\geq$ 0.1 mol.L^{-1}) and/or high $[H_2O_2]$ ($\geq$ 0.1 mol.L^{-1}), the decomposition rate decreases due to the more rapid formation of U^{VI} surface species which can be transferred to solution as $U^{VI}O_2(CO_3)_y^{(2-2y)+}$ by a chemical dissolution reaction.

- The role of noble metal (ε) particles in the SIMFUEL on H_2O_2 decomposition appears to be minor although this remains to be conclusively demonstrated.

4.5 References

[1] P.G. Keech, P. Vo, S. Ramamurthy, J. Chen, R. Jacklin, D.W. Shoesmith, Design and development of copper coatings for long term storage of used nuclear fuel, Corrosion Engineering, Science and Technology, 49 (2014) 425-430.

[2] D.S. Hall, P.G. Keech, An overview of the Canadian corrosion program for the long-term management of nuclear waste, Corrosion Engineering, Science and Technology, 52 (2017) 2-5.

[3] T. Standish, J. Chen, R. Jacklin, P. Jakupi, S. Ramamurthy, D. Zagidulin, P. Keech, D. Shoesmith, Corrosion of copper-coated steel high level nuclear waste containers under permanent disposal conditions Electrochimica Acta, 211 (2016) 331-342.

[4] G. Kwong, Status of corrosion studies for copper used fuel containers under low salinity conditions, Report NWMO TR-2011-14, Nuclear Waste Management Organization, Toronto, ON, (2011).

[5] D. Shoesmith, Used fuel and uranium dioxide dissolution studies–a review, Report NWMO TR-2007-03, Nuclear Waste Management Organization, Toronto, ON, (2007).

[6] N. Liu, Z. Zhu, J.J. Noël, D.W. Shoesmith, Corrosion of nuclear fuel inside a failed waste container, Encyclopedia of Interfaical Chemistry: Surface Science and Electrochemistry 2018.

[7] E. Ekeroth, O. Roth, M. Jonsson, The relative impact of radiolysis products in radiation induced oxidative dissolution of UO_2, Journal of Nuclear Materials, 355 (2006) 38-46.

[8] C.M. Lousada, M. Trummer, M. Jonsson, Reactivity of H_2O_2 towards different UO_2-based materials: The relative impact of radiolysis products revisited, Journal of Nuclear Materials, 434 (2013) 434-439.

[9] S. Sunder, N.H. Miller, D.W. Shoesmith, Corrosion of uranium dioxide in hydrogen peroxide solutions, Corrosion Science, 46 (2004) 1095-1111.

[10] T.E. Eriksen, D.W. Shoesmith, M. Jonsson, Radiation induced dissolution of UO_2 based nuclear fuel – A critical review of predictive modelling approaches, Journal of Nuclear Materials, 420 (2012) 409-423.

[11] C.M. Lousada, A.J. Johansson, T. Brinck, M. Jonsson, Mechanism of H_2O_2 decomposition on transition metal oxide surfaces, The Journal of Physical Chemistry C, 116 (2012) 9533-9543.

[12] A. Barreiro Fidalgo, B. Dahlgren, T. Brinck, M. Jonsson, Surface reactions of H_2O_2, H_2, and O_2 in aqueous systems containing ZrO_2, The Journal of Physical Chemistry C, 120 (2016) 1609-1614.

[13] C.M. Lousada, M. Yang, K. Nilsson, M. Jonsson, Catalytic decomposition of hydrogen peroxide on transition metal and lanthanide oxides, Journal of Molecular Catalysis A: Chemical, 379 (2013) 178-184.

[14] D. Fu, X. Zhang, P.G. Keech, D.W. Shoesmith, J.C. Wren, An electrochemical study of H2O2 decomposition on single-phase γ-FeOOH films, Electrochimica Acta, 55 (2010) 3787-3796.

[15] S.-S. Lin, M.D. Gurol, Catalytic Decomposition of hydrogen peroxide on iron oxide: kinetics, mechanism, and implications, Environmental Science & Technology, 32 (1998) 1417-1423.

[16] S. Nilsson, M. Jonsson, H_2O_2 and radiation induced dissolution of UO_2 and SIMFUEL pellets, Journal of Nuclear Materials, 410 (2011) 89-93.

[17] P.G. Lucuta, R.A. Verrall, H. Matzke, B.J. Palmer, Microstructural features of SIMFUEL — Simulated high-burnup UO_2-based nuclear fuel, Journal of Nuclear Materials, 178 (1991) 48-60.

[18] M. Razdan, M. Trummer, D. Zagidulin, M. Jonsson, D.W. Shoesmith, Electrochemical and surface characterization of uranium dioxide containing rare-earth oxide (Y_2O_3) and metal (Pd) particles, Electrochimica Acta, 130 (2014) 29-39.

[19] M. Razdan, D.W. Shoesmith, Influence of trivalent-dopants on the structural and electrochemical properties of uranium dioxide (UO_2), Journal of The Electrochemical Society, 161 (2014) H105-H113.

[20] N. Liu, H. He, J.J. Noël, D.W. Shoesmith, The electrochemical study of Dy_2O_3 doped UO_2 in slightly alkaline sodium carbonate/bicarbonate and phosphate solutions, Electrochimica Acta, 235 (2017) 654-663.

[21] N. Liu, J. Kim, J. Lee, Y.-S. Youn, J.-G. Kim, J.-Y. Kim, J.J. Noël, D.W. Shoesmith, Influence of Gd doping on the structure and electrochemical behavior of UO2, Electrochimica Acta, 247 (2017) 496-504.

[22] L. Wu, D.W. Shoesmith, An electrochemical study of H_2O_2 oxidation and decomposition on simulated nuclear fuel (SIMFUEL), Electrochimica Acta, 137 (2014) 83-90.

[23] M. Broczkowski, The effects of hydrogen and temperature on the electrochemistry and corrosion of uranium dioxide (UO_2), Ph.D. Thesis, Chapter 7, Department of ChemistryThe University of Western Ontario, 2008.

[24] Z. Zhu, L. Wu, J.J. Noël, D.W. Shoesmith, Anodic reactions occurring on simulated nuclear fuel (SIMFUEL) in hydrogen peroxide solution containing bicarbonate/carbonate – the effect of fission products, (2018).

[25] R. Drot, E. Simoni, M. Alnot, J.J. Ehrhardt, Structural environment of uranium (VI) and europium (III) species sorbed onto phosphate surfaces: XPS and optical spectroscopy studies, Journal of Colloid and Interface Science, 205 (1998) 410-416.

[26] A. Froideval, M. Del Nero, R. Barillon, J. Hommet, G. Mignot, pH dependence of uranyl retention in a quartz/solution system: an XPS study, Journal of Colloid and Interface Science, 266 (2003) 221-235.

[27] T.B. Scott, G.C. Allen, P.J. Heard, M.G. Randell, Reduction of U(VI) to U(IV) on the surface of magnetite, Geochimica et Cosmochimica Acta, 69 (2005) 5639-5646.

[28] E.S. Ilton, J.-F. Boily, P.S. Bagus, Beam induced reduction of U(VI) during X-ray photoelectron spectroscopy: The utility of the U4f satellite structure for identifying uranium oxidation states in mixed valence uranium oxides, Surface Science, 601 (2007) 908-916.

[29] B.G. Santos, H.W. Nesbitt, J.J. Noël, D.W. Shoesmith, X-ray photoelectron spectroscopy study of anodically oxidized SIMFUEL surfaces, Electrochimica Acta, 49 (2004) 1863-1873.

[30] M. Schindler, F.C. Hawthorne, M.S. Freund, P.C. Burns, XPS spectra of uranyl minerals and synthetic uranyl compounds. I: The U 4f spectrum, Geochimica et Cosmochimica Acta, 73 (2009) 2471-2487.

[31] M. Razdan, D.S. Hall, P.G. Keech, D.W. Shoesmith, Electrochemical reduction of hydrogen peroxide on SIMFUEL (UO_2) in acidic pH conditions, Electrochimica Acta, 83 (2012) 410-419.

[32] I. Stefanic, Temperature dependence of the hydrogen peroxide production in the γ-radiolysis of water, Journal of physical chemistry, (2002).

[33] C.J. Hochanadel, Effects of Cobalt y-radiation on Water and Aqueous Solution (1952).

[34] J. Abbot, D.G. Brown, Kinetics of iron-catalyzed decomposition of hydrogen peroxide in alkaline solution, International Journal of Chemical Kinetics, 22 (1990) 963-974.

[35] W.D. Nicoll, A.F. Smith, Stability of dilute alkaline solutions of hydrogen peroxide, Industrial & Engineering Chemistry, 47 (1955) 2548-2554.

[36] O. Spalek, J. Balej, I. Paseka, Kinetics of the decomposition of hydrogen peroxide in alkaline solutions, Journal of the Chemical Society, Faraday Transactions 1: Physical Chemistry in Condensed Phases, 78 (1982) 2349-2359.

[37] R. Venkatachalapathy, G.P. Davila, J. Prakash, Catalytic decomposition of hydrogen peroxide in alkaline solutions, Electrochemistry Communications, 1 (1999) 614-617.

[38] K.C.T. E. L. Littauer, Catalytic decomposition of hydrogen peroxide in alkaline solution, Journal of Electrochemical Society, 126 (1979) 1924-1927.

[39] J. Flanagan, D.P. Jones, W.P. Griffith, A.C. Skapski, A.P. West, On the existence of peroxocarbonates in aqueous-solution Journal of the Chemical Society-Chemical Communications, (1986) 20-21.

[40] J.A. Navarro, M.A. de la Rosa, M. Roncel, F.F. de la Rosa, Carbon dioxide-mediated decomposition of hydrogen peroxide in alkaline solutions, Journal of the Chemical Society, Faraday Transactions 1: Physical Chemistry in Condensed Phases, 80 (1984) 249-253.

[41] D.W. Shoesmith, Fuel corrosion processes under waste disposal conditions, Journal of Nuclear Materials, 282 (2000) 1-31.

[42] M. Razdan, Shoesmith D.W., The electrocheical reacivity of 6.0 wt.% Gd doped UO_2 in aquous carbonate-bicarbonate solutions, Journal of The Electrochemical Society, 4 (2014) H225-H234.

[43] B.G. Santos, J.J. Noël, D.W. Shoesmith, The effect of pH on the anodic dissolution of SIMFUEL (UO_2), Journal of Electroanalytical Chemistry, 586 (2006) 1-11.

[44] P.G. Keech, J.S. Goldik, Z. Qin, D.W. Shoesmith, The anodic dissolution of SIMFUEL (UO_2) in slightly alkaline sodium carbonate/bicarbonate solutions, Electrochimica Acta, 56 (2011) 7923-7930.

Chapter 5

5 The Kinetics of Hydrogen Peroxide Reduction on UO_2 Electrodes

5.1 Introduction

The prospects for the long-term containment of nuclear spent fuel are very good. However, it's judicious to assume some containers will fail before the radiation fields have decayed to uranium ore levels. It is also reasonable to assume that the container failure leading to wetting of the fuel would not occur until β/γ radiation fields had become insignificant. Hence, a clear understanding of the influence of H_2O_2, the key oxidizing product of α-radiolysis, is important to elucidate the full mechanism of UO_2 corrosion. In previous chapters, it was found that H_2O_2 can cause UO_2 corrosion, but also undergo decomposition to H_2O and O_2. This means it will be both anodically oxidized and cathodically reduced. In previous chapters, the anodic oxidation and decomposition of H_2O_2 have been studied. However, the key reaction supporting both anodic oxidation reactions (H_2O_2 and UO_2) is the cathodic reduction of H_2O_2.

The kinetics of H_2O_2 reduction on UO_2 surfaces has been shown to be dependent on the chemical state of the surface with X-ray photoelectron spectroscopy (XPS) studies showing reduction is blocked when insulating U^{VI} layers are present but proceeds rapidly on surfaces comprised of U^{IV}/U^{V} sites [1, 2]. Goldik et al. [1-4] interpreted the kinetics using the mechanism proposed by Presnov and Trunov [5-7] for O_2 reduction on transition metal oxides and adopted by Hocking et al. to explain O_2 reduction on UO_2. According to this theory electron transfer to adsorbed O_2 molecules occurs at donor-acceptor relay (DAR) sites comprising U^{IV} and U^{V} atoms, one on the surface and the other in the sub-surface adjacent layer. The cathodic reduction of O_2 is slow on UO_2 but accelerated by oxidation of the surface to $U^{IV}_{1-2x}U^{V}_{2x}O_{2+x}$ which

provides the donor-acceptor relay (DAR) sites (adjacent U^{IV}-U^{V} sites) which catalyze an electron relay process[8, 9]. The kinetics of H_2O_2 reduction are considerably faster than those of O_2 reduction due to the ability of H_2O_2 to create, rather than rely on pre-existing, DAR sites.

On SIMFUEL surfaces, which contain noble metal (ε) particles, the kinetics of O_2 reduction is catalyzed on the particle surfaces. However, electrochemical studies indicate only a minor influence of ε-particles (6 at.% SIMFUEL) on H_2O_2 reduction[3], since the rate on the DAR sites is already high. Goldik et al. demonstrated that the kinetics of the H_2O_2 cathodic reduction reaction varied with [H_2O_2] and the degree of oxidation of the UO_2 surface[2]. The presence of corrosion products suppressed the H_2O_2 reduction reaction by blocking the DAR sites (U^{IV}/U^{V}) with insulating U^{VI} species[1]. The influence of carbonate on H_2O_2 reduction kinetics has also been studied on UO_2 surfaces and it was proposed that carbonate can also coordinate with the DAR sites and inhibit the H_2O_2 redox reaction[4]. This is not unexpected as carbonate can also interfere with the O_2 reduction reaction on a UO_2 surface.[10, 11]

In this chapter, an extensive electrochemical and surface analytical study was performed to examine the cathodic activity of different UO_2 electrodes in alkaline H_2O_2 solutions. The primary goal was to determine the effects of non-stoichiometry and fission product dopants on the kinetics of the H_2O_2 reduction reaction.

5.2 Experimental

5.2.1 Materials

Six different electrodes were used in this study, including 3 at.% SIMFUEL doped with 11 elements (Sr, Y, Ce, Nd, La, Zr, Ba, Pd, Ru, Rh, Mo) to simulate in-reactor irradiation, UO_{2+x} (x = 0.002, 0.05 and 0.1), 6.0 wt.% Gd_2O_3 (rare-earth) doped UO_2 (Gd-UO_2) and 12.9 wt.%

Dy_2O_3 (rare-earth) doped UO_2 (Dy-UO_2). The SIMFUEL and UO_{2+x} materials were fabricated by Atomic Energy of Canada Limited (now Canadian Nuclear Laboratories, Chalk River, Canada), Dy-UO_2 and Gd-UO_2 were provided by Cameco (Port Hope, Canada). The non-stoichiometric UO_{2+x} samples were produced by annealing UO_2 powder in a CO/CO_2 atmosphere with a controlled composition at different temperatures and for various times according to the Ellingham diagram.[12, 13] The SIMFUEL, Gd-UO_2 and Dy-UO_2 pellets were sintered and reduced to produce high density stoichiometric UO_2 material. Rotating disc electrodes (RDE) were constructed from cylindrical slices approximately 2-3 mm thick and 12 mm in diameter. Prior to each experiment, the electrode was wet polished with 1200 SiC paper and rinsed with Millipore water (18.2 MΩ.cm).

5.2.2 Electrochemical Cell and Procedures

A three-compartment electrochemical cell was used in all experiments. A saturated calomel electrode (SCE) was used as the reference. The counter electrode was a Pt mesh spot welded to a Pt wire. The ohmic drop between the reference electrode and working electrode (UO_2 samples) was minimized by using a Luggin capillary. The cell was placed in a Faraday cage to prevent interference from external noise. The electrodes were cathodically cleaned at -1.2 V vs. SCE for 2 minutes to reduce air-formed films.

A Solartron 1287 potentiostat was used to apply potentials and record the current responses. The potential scan rate was 10 $mV.s^{-1}$. Corrware software was used to control the instrument and analyze data. The rotation rate of the working electrode (WE) was controlled using an analytical rotator from Pine Instrument (model ASR).

5.2.3 Solution Preparation

All solutions were prepared with deionized water with a resistance of 18.2 MΩ.cm, purified using a Millipore Milli-Q Plus unit, to remove organic and inorganic impurities, and then passed through a Milli-Q-plus ion exchange column. All experiments were conducted at room temperature and purged with Ar (ultra-high purity, Praxair) for at least 30 minutes prior to experiments. Purging was then continued throughout each experiment. Experiments were performed in a 0.1 mol.L^{-1} NaCl solution with the pH adjusted to 9.7 using NaOH solution. When required $NaHCO_3$, Na_2SO_4 and H_2O_2 were added at a desired concentration. All chemicals were reagent grade and purchased from Fisher Scientific.

5.2.4 X-ray Photoelectron Spectroscopy (XPS)

XPS analyses were performed on a Kratos Axis NOVA spectrometer using a monochromatic Al K_α X-ray source (1486.6 eV). The instrument work function was calibrated to give a binding energy of 83.96 eV for the Au $4f_{7/2}$ line for metallic Au, and the spectrometer dispersion was adjusted to give a binding energy (BE) of 932.62 eV for the Cu $2p_{3/2}$ line of metallic Cu. Survey scans were recorded over the energy range 0-1100 eV on an analysis area of 300 x 700 μm^2 with a pass energy of 160 eV. Spectra were charge-corrected when necessary using the C 1s peak set to be at 285.0 eV. Spectra were analyzed using CasaXPS software (version 2.3.14). The procedures used to record and fit high resolution spectra have been described in Chapter 4.

Other surface characterization techniques, such as scanning electron microscopy/energy-dispersive x-ray spectroscopy (SEM/EDX), X-ray diffraction, and Raman spectroscopy, have been conducted on Gd-UO_2, Dy-UO_2 [14, 15], $UO_{2.002}$, $UO_{2.05}$, $UO_{2.1}$[16, 17], and SIMFUEL[17, 18].

5.3 Results

5.3.1 XPS

The fractions of U^{IV}, U^{V} and U^{VI}, obtained by deconvolution of high resolution XPS spectra are listed in Table 5-1. As expected for the non-stoichiometric UO_{2+x} samples the fraction of U^{IV} decreases, and those of U^{V} and U^{VI} increase as the degree of non-stoichiometry (x) increases from 0.002 to 0.05. However, a decrease in U^{V} and U^{VI} content was observed when x was increased from 0.05 to 0.1. This is not unexpected as the stoichiometry of the individual UO_{2+x} grains in this material are very non-uniform making an analysis of the stoichiometry variable from analysis to analysis.[12] The fraction of oxidized U states (U^{V}, U^{VI}) in the two RE (III)-doped specimens (Dy-UO_2, Gd-UO_2) are similar. These electrodes have been extensively characterized using SEM, EDX and Raman Spectroscopy which show that the RE^{III}-dopants, i.e. Dy and Gd, are evenly distributed within UO_2 matrix.[15] The fractions of U^{V} and U^{VI} in the 3 at.% SIMFUEL surface are lower than those in the Dy-UO_2 and Gd-UO_2 electrodes, consistent with a significantly lower RE(III) doping level.

Table 5-1: The fraction of U oxidation states (U^{IV}, U^{V} and U^{VI}) on the surface of UO_2 electrodes after polishing and sonication.

Electrodes	U^{IV} (%)	U^{V} (%)	U^{VI} (%)	References
$UO_{2.002}$	93.5	1.3	5.2	
$UO_{2.05}$	64	25	11	
$UO_{2.1}$	75	17	8	
3 at.% SIMFUEL	84	9	7	
Dy-UO_2	76	12	12	[15]
Gd-UO_2	73	19	8	[15]

5.3.2 The Effects of H_2O_2 and Diffusion

Figure 5.1 A compares CVs recorded on the Gd-UO_2 electrode in 0.1 mol.L^{-1} NaCl (pH = 9.7) with and without added H_2O_2. The potential was scanned from a cathodic limit of -1.2 V to 0.4 V and back. While the anodic current exhibited only a marginal increase after addition of 0.02 mol.L^{-1} H_2O_2, as expected based on the results in Chapter 3, the cathodic current increased markedly. The current on the reverse scan was enhanced suggesting that the cathodic reduction was accelerated slightly by the anodic oxidation process at positive potentials. The current plateau for E < -0.8 V suggests the establishment of transport control.

Figure 5.1 B compares the currents recorded on a static and a rotated Gd-UO_2 electrode. The recorded currents with and without electrode rotation were very similar in the potential range from ~ 0V to – 0.4 V, suggesting a reaction controlled by interfacial processes. However, for more negative potentials, the current became dependent on electrode rotation rate, confirming

a strong contribution from H_2O_2 transport to the electrode surface. The hysteresis in current between the forward and reverse scans remained at low potentials but was inverted in the potential range -0.4 V to 0 V.

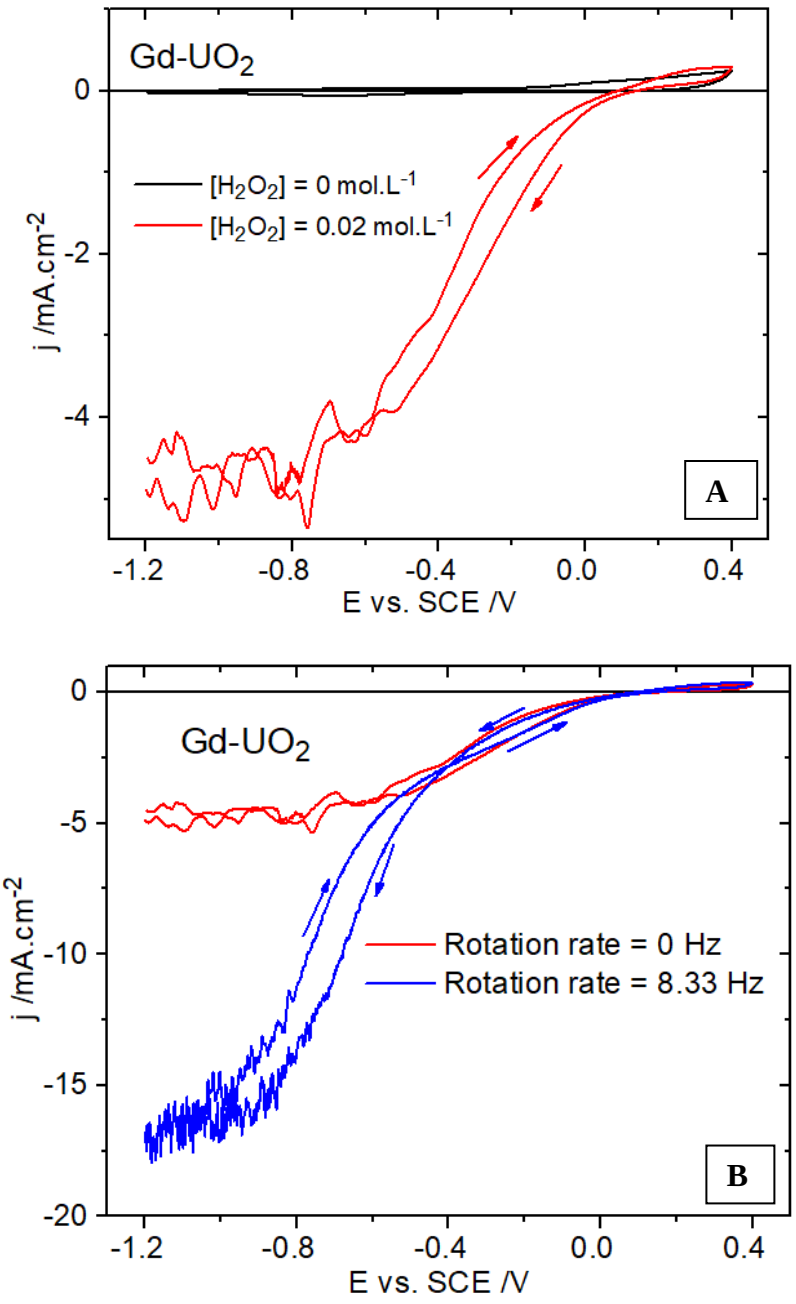

Figure 5.1: CVs recorded on Gd-UO_2 (A) [H_2O_2] = 0 mol.L^{-1}, no electrode rotation (black line), [H_2O_2] = 0.02 mol.L^{-1}, and no electrode rotation (red line); (B) 0.02 mol.L^{-1} H_2O_2 with a rotation rate of 8.33 Hz (blue line) and without electrode rotation (red line). All solutions contained 0.1 mol.L^{-1} of NaCl and 0.05 mol.L^{-1} of $NaHCO_3$, pH = 9.7, scan rate = 10 mV.s^{-1}.

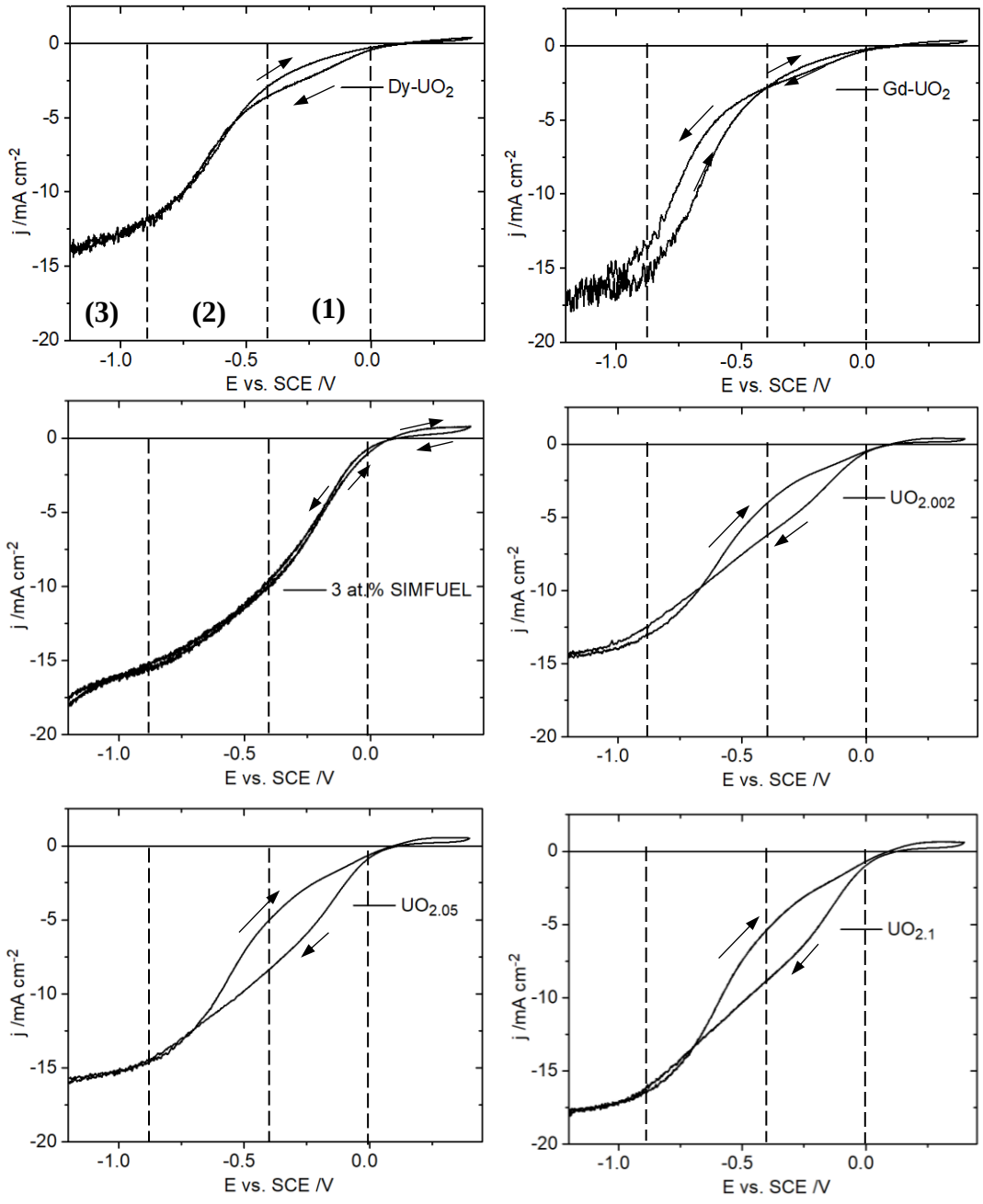

Figure 5.2: CVs recorded on UO_2 electrodes, Dy-UO_2, Gd-UO_2, 3 at.% SIMFUEL, $UO_{2.002}$, $UO_{2.05}$ and $UO_{2.1}$, in a 0.1 mol.L^{-1} of NaCl solution containing 0.02 mol.L^{-1} of H_2O_2, and 0.05 mol.L^{-1} of $NaHCO_3$ (pH = 9.7): electrode rotation rate = 8.33 Hz: scan rate = 10 mV.s^{-1}. The dashed lines define regions of different behaviour on the forward scans.

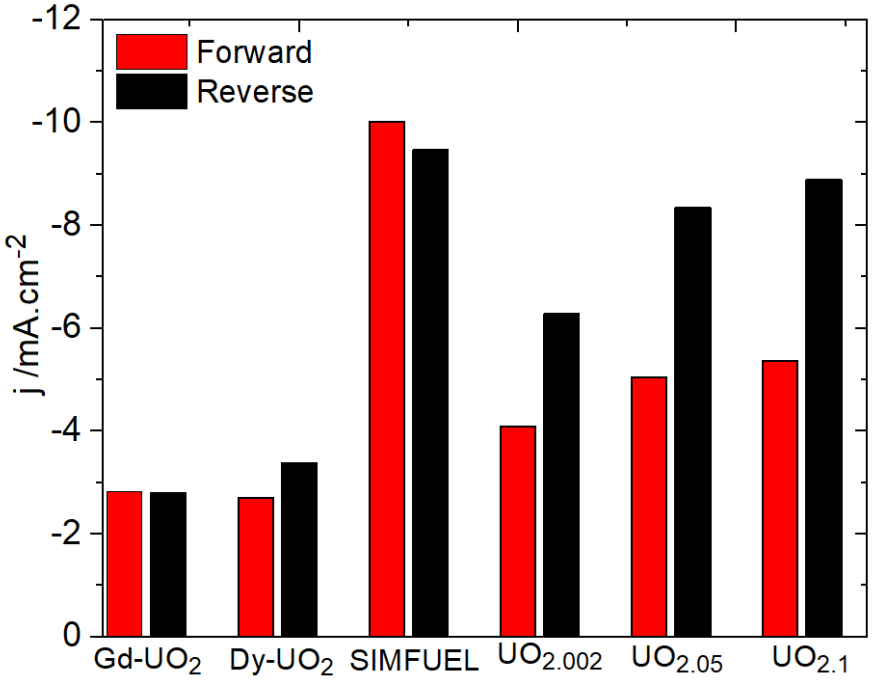

Figure 5.3: Cathodic currents measured at -0.4 V on UO_2 electrodes on forward and reverse scans (from Figure 5.2).

Figure 5.2 shows CVs recorded on all 6 UO_2 electrodes over the potential range from -1.2 V to 0.4 V. For the RE(III)-doped electrodes the cathodic current profile on the forward scan could be divided into distinct sections: (1) from 0 to ~ -0.4 V the current increased only slowly with potential; (2) from -0.4 V to -0.8 V the current was strongly dependent on potential; (3) for E < -0.8 V the current tended towards a potential-independent plateau. On the reverse scan the current was slightly enhanced in region 1. Similar, but not as well defined, stages were observed for the three non-stoichiometric electrodes, with the current in the potential range 0 V to ~ -0.6 V significantly enhanced on the reverse scan, the extent of enhancement appearing to increase with the degree of non-stoichiometry. For the SIMFUEL electrode, little hysteresis was observed

between the forward and reverse scans and the current was more potential-dependent in the region 0 V to -0.4 V than on the other electrodes.

The differences in behaviour of the electrodes was most marked in the potential region 0 V to -0.5 V. This is illustrated in Figure 5.3 which shows the currents measured at -0.4 V on the forward and reverse scans for all electrodes. For the RE(III)-doped electrodes the currents were small and only marginally influenced by the scan to positive potentials indicating only a minor to negligible modification of the kinetics of H_2O_2 due to the anodic oxidation of UO_2. For the three non-stoichiometric electrodes the current in this region were higher on the forward scan and significantly enhanced on the reverse scan, the $UO_{2.1}$ electrode exhibiting the largest currents. These electrodes, while exhibiting non-uniform compositions, with some areas being more non-stoichiometric than others, have been shown to become more anodically reactive as the degree of non-stoichiometry (x in UO_{2+x}) increased [12, 19]. The large current on the forward scan for the SIMFUEL electrode suggested either the lightly RE(III)- doped lattice was highly reactive for H_2O_2 reduction or the ε-particles play a role in the reduction reaction. As for the RE(III)-doped electrodes there is little influence of a scan to positive potentials.

Figure 5.4 shows CVs recorded on the Gd-UO_2 and $UO_{2.05}$ electrodes from an initial potential of -1.2 V to various positive potential limits. These plots confirmed that the hysteresis observed between the forward and reverse scans could be attributed to changes in the oxidized state of the electrode surfaces incurred as the potential limit was made more positive. Similar scans were performed on all the electrodes and demonstrated, as shown for the two electrodes in Figure 5.4, that retraceable currents were observed, providing the potential was not scanned to > -0.3 V; i.e., the complications due to anodic oxidation were avoided. This was consistent with

previous XPS analyses which showed that the threshold for observable oxidation of UO_2 was approximately -0.4 V to -0.3 V[14, 15, 20].

5.3.3 H_2O_2 Reduction

Figure 5.5 shows CVs recorded to an anodic limit of -0.3 V on the Gd-UO_2, SIMFUEL and $UO_{2.1}$ electrodes at various electrode rotation rates. For Gd-UO_2 and SIMFUEL, three distinct regions of behaviour were observed: (a) the current was dependent on potential and independent of electrode rotation rate indicating activation-controlled behaviour; (b) the current was dependent on both potential and electrode rotation rate indicating reduction was under mixed activation-diffusion control; and (c) the current was almost independent of potential but strongly dependent on rotation rate consistent with a transition to transport control. As indicated by the length of the arrows in Figure 5.5 A and Figure 5.5 B the relative importance of these three regions was different for the two electrodes. For the Gd-UO_2 electrode, the activation-controlled region (a) extended to much lower potentials than for the SIMFUEL; while for SIMFUEL regions (b) (mixed activation/diffusion control) and (c) (apparent diffusion control) never became clearly separated. On the $UO_{2.1}$ electrode, Figure 5.5 C, only regions (a) and (b) were observed, with the dependence of the current on rotation rate being minor in region (b).

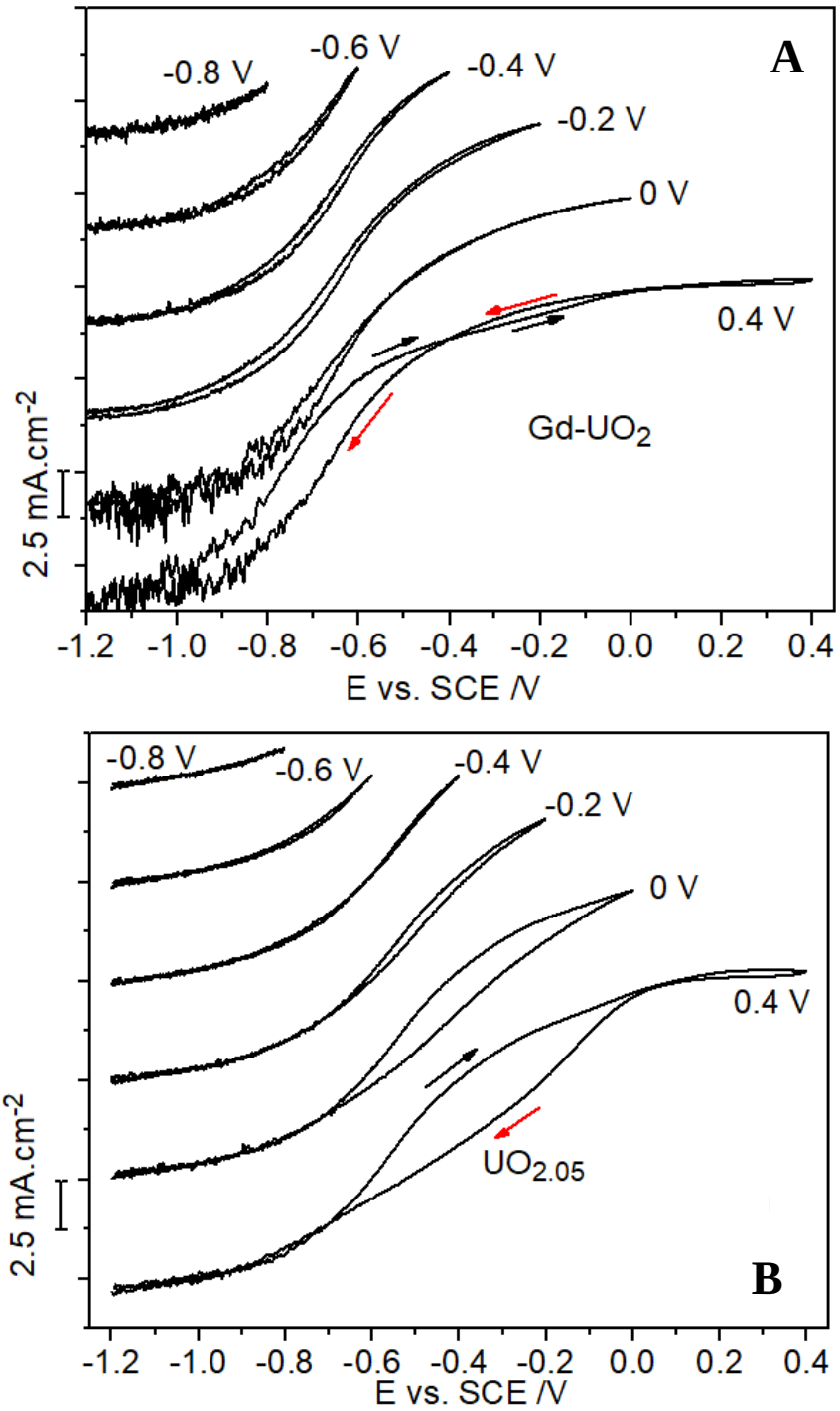

Figure 5.4: CVs recorded on (A) the Gd-UO_2 electrode and (B) the $UO_{2.05}$ electrode from -1.2 V to different positive potential limits in a solution containing 0.1 mol.L^{-1} of NaCl, 0.05 mol.L^{-1} $NaHCO_3$ and 0.02 mol.L^{-1} of H_2O_2 (pH = 9.7): electrode rotation rate = 8.33 Hz. The curves are offset by 5 mA.cm^{-2} for clarity.

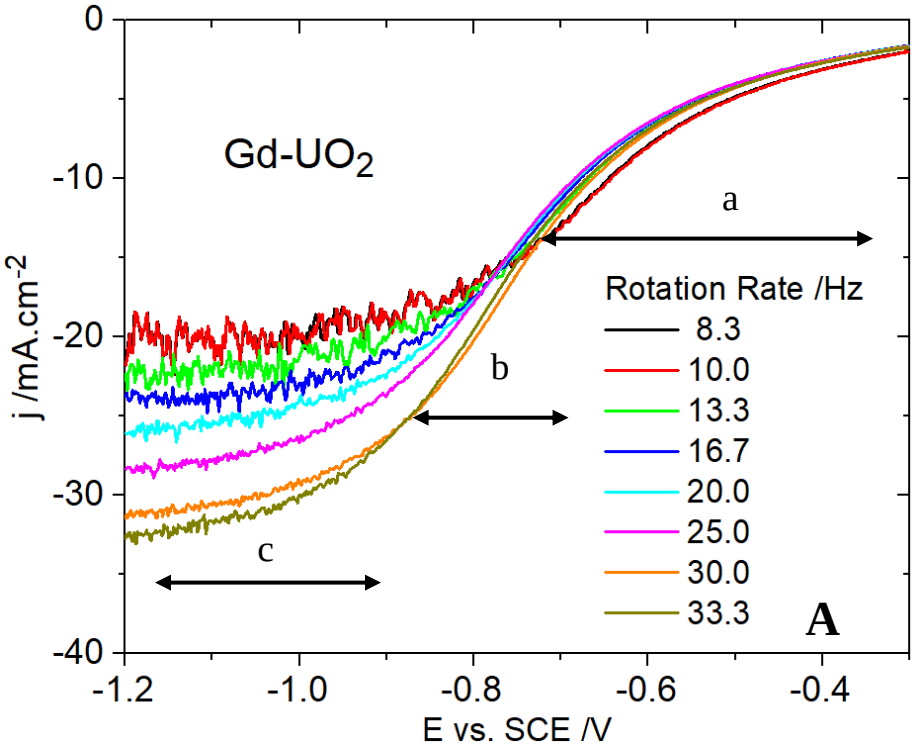
Gd-UO2
a
b
c
Rotation Rate /Hz
8.3
10.0
13.3
16.7
20.0
25.0
30.0
33.3
A
j /mA.cm-2
E vs. SCE /V
0
-10
-20
-30
-40
-1.2
-1.0
-0.8
-0.6
-0.4

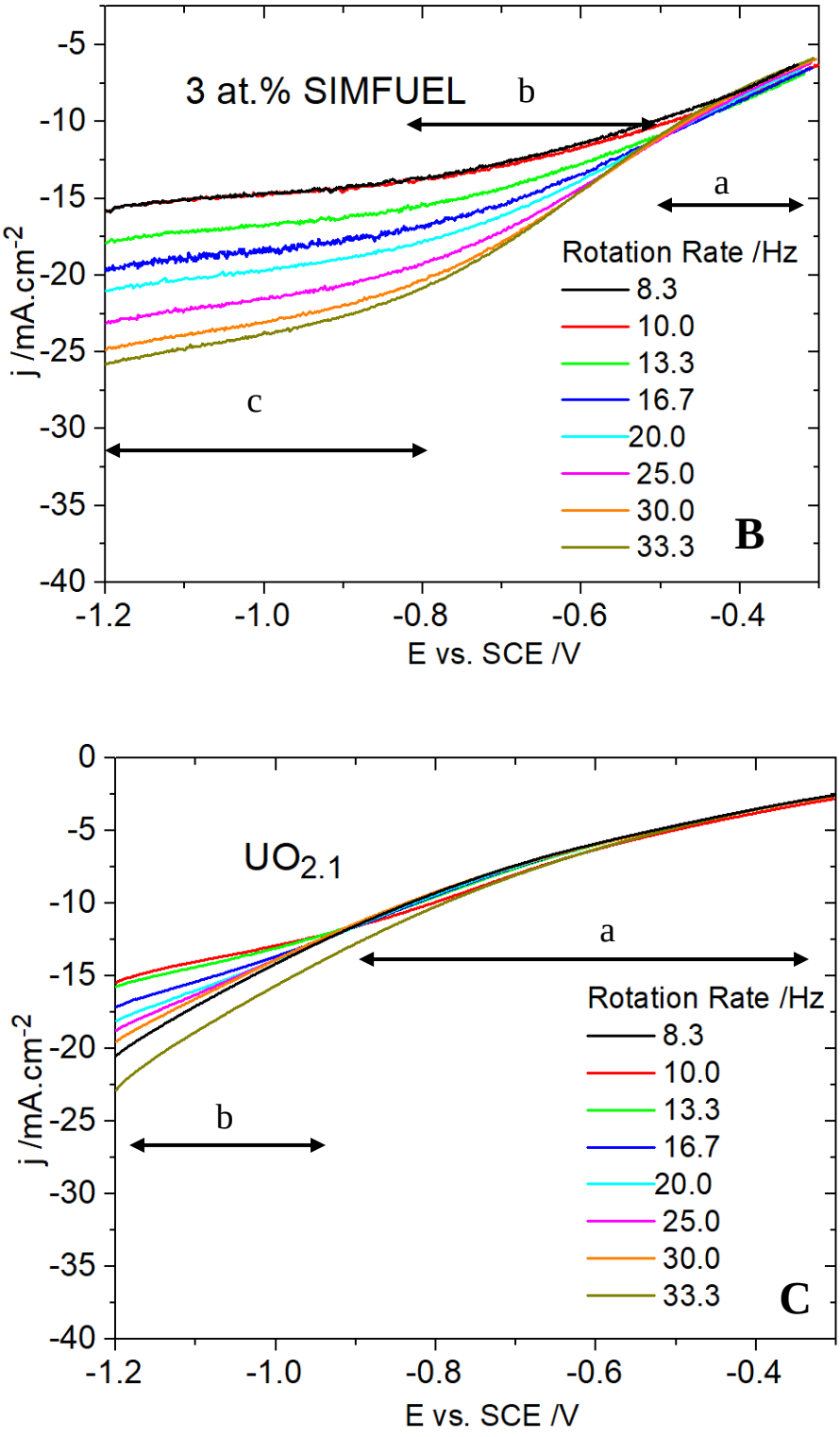

Figure 5.5: CVs recorded from -1.2V to -0.3V on (A) the Gd-UO_2, (B) the 3 at.% SIMFUEL and (C) $UO_{2.1}$, at various electrode rotation rates in a 0.1 mol.L^{-1} of NaCl solution (pH 9.7), $[H_2O_2]$ = 0.02 mol.L^{-1} and $[CO_3]_{tot}$ = 0.05 mol.L^{-1}.

5.3.4 Tafel Plots

Figure 5.6 shows Levich plots for H_2O_2 reduction currents recorded at -1.1 V, a potential in the apparently diffusion controlled region (c), Figure 5.5. However, despite the absence of a clear diffusion controlled region on the $UO_{2.1}$ electrode, a Levich plot for $UO_{2.1}$ was included in Figure 5.6 for comparison. The diffusion-limited cathodic current as a function of electrode rotation rate (ω) is given by the Levich equation [21],

$$j_d = \xi n F A c_b D^{2/3} \nu^{-1/6} \omega^{1/2} \qquad \textbf{5.1}$$

where j_d is the diffusion controlled current, n is the number of electrons transferred (n = 2), F is the Faraday constant (96485 C.mol^{-1}), A is the geometric surface area of the electrode (cm^2), c_b is the bulk concentration of H_2O_2 (mol.L^{-1}), D is diffusion coefficient of H_2O_2 (1.32×10^{-5} cm^2.s^{-1}[22]), ν is the kinematic viscosity of the electrolyte (1.013×10^{-2} cm^2.s^{-1} [23]) and ξ is a numerical coefficient given by[24]

$$\xi = \frac{1.5553}{1 + 0.2980(Sc)^{-1/3} + 0.14514(Sc)^{-2/3}} \qquad \textbf{5.2}$$

where Sc is the Schmidt number, Sc = ν/D.

While all the electrodes exhibited linear plots, comparison of the measured currents to those calculated from equation 5.1 showed that, on all electrodes, total diffusion control of the reaction was not achieved. Since the currents were almost independent of potential in this region this behaviour indicates they are partially controlled by a chemical reaction step. On the SIMFUEL, $UO_{2.002}$ and $UO_{2.05}$ electrodes the currents, and their dependence on electrode rotation rate were very similar. By contrast the currents on the two RE(III)-doped electrodes were significantly lower, with the currents on the heavily doped Dy-UO_2 being the lowest. The

currents measured on the $UO_{2.1}$ electrode were also very low and almost independent of rotation rate.

The currents measured for potentials ≤ -0.7V; i.e., in regions (b) and (c) for most electrodes (Figure 5.5) exhibited mixed kinetic-diffusion control. The currents were corrected for the transport contribution using the Koutećky-Levich (K-L) equation,

$$\left(\frac{1}{-j}\right)^{1/m} = \left(\frac{1}{-j_k}\right)^{1/m} + \frac{(-j)^{1-1/m}}{B\sqrt{\omega}} \qquad \textbf{5.3}$$

where m is the reaction order, j_k is the kinetic current, and B is a constant given by

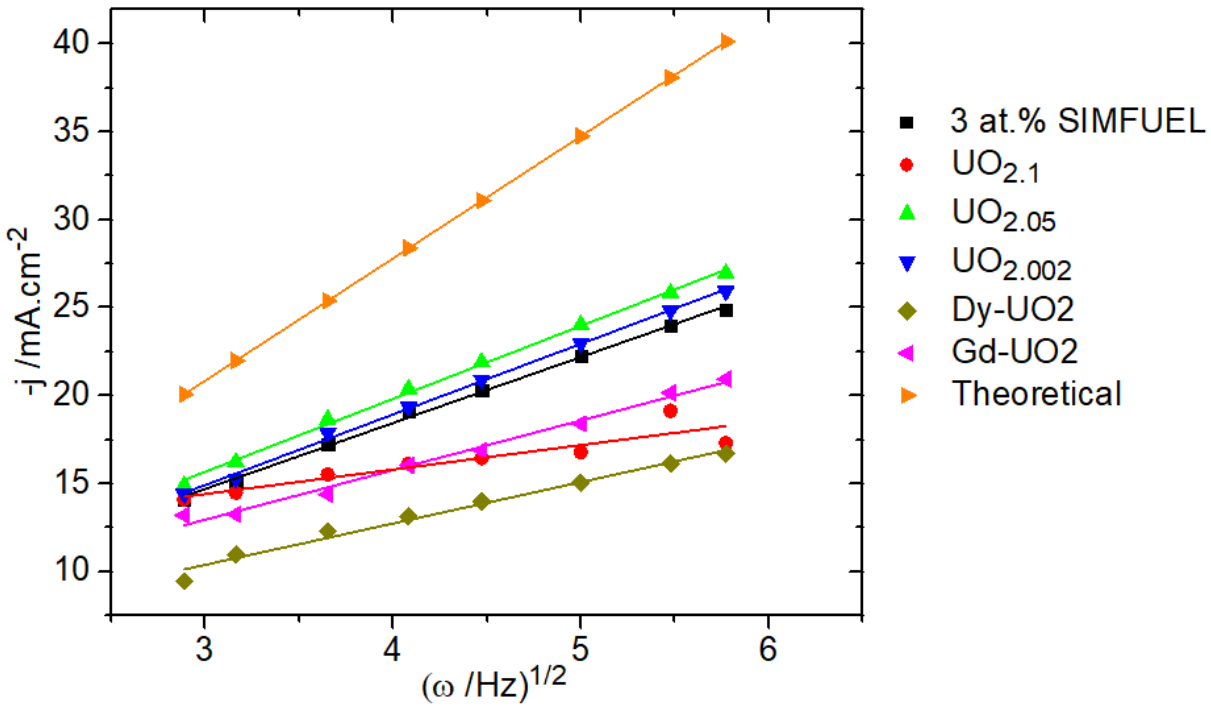

Figure 5.6: Levich plots of the current densities measured at -1.1 V for the 6 different UO_2 electrodes in a 0.1 mol.L^{-1} of NaCl solution containing 0.02 mol.L^{-1} of H_2O_2 and 0.05 mol.L^{-1} of $NaHCO_3$ (pH = 9.7). The theoretical curve was calculated for this [H_2O_2] using the Levich equation (1.1).

$$B = n\xi FAc_b D^{2/3} \nu^{-1/6} \qquad \textbf{5.4}$$

Figure 5.7 shows an example of K-L plots of the H_2O_2 reduction currents recorded on the Dy-UO_2 electrode with the assumption that the reaction order m = 1. While arbitrary, application of the K-L equation is known to be insensitive to the assumed reaction order. This has been discussed in detail previously [2]. The measured currents can be corrected for the contribution from diffusion by extrapolation of these plots to $\omega^{-1/2} = 0$ to yield the kinetic current, j_k. Figure 5.8 A shows the log of the kinetic currents, obtained from K-L plots, plotted as a function of potential for all the electrodes. With the exception of the Gd-UO_2 and $UO_{2.1}$ electrodes, two regions of behaviour were observed: (1) over the potential range -0.3 V to ~ -0.9 V, log j_k increased relatively steeply with potential; (2) for E < -0.9 V, log j_k became considerably less potential dependent. This behaviour was similar to that previously observed for experiments performed on a number of SIMFUELs [3].

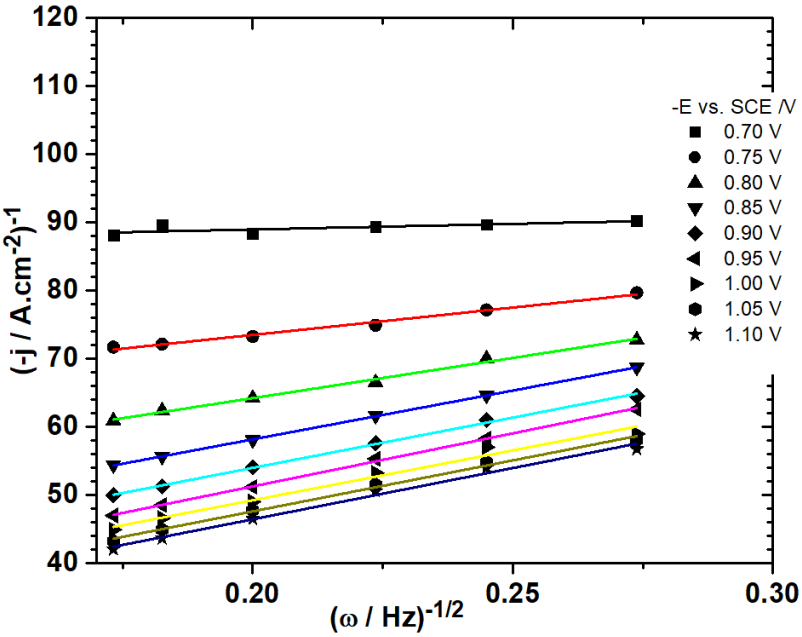

Figure 5.7: Koutećky-Levich plots of currents measured on the Dy-UO_2 electrode in a 0.1 mol.L^{-1} NaCl solution containing 0.02 mol.L^{-1} of H_2O_2 and 0.05 mol.L^{-1} of $[CO_3]_{tot}$ (pH = 9.7). The reaction was assumed to be first order with respect to H_2O_2.

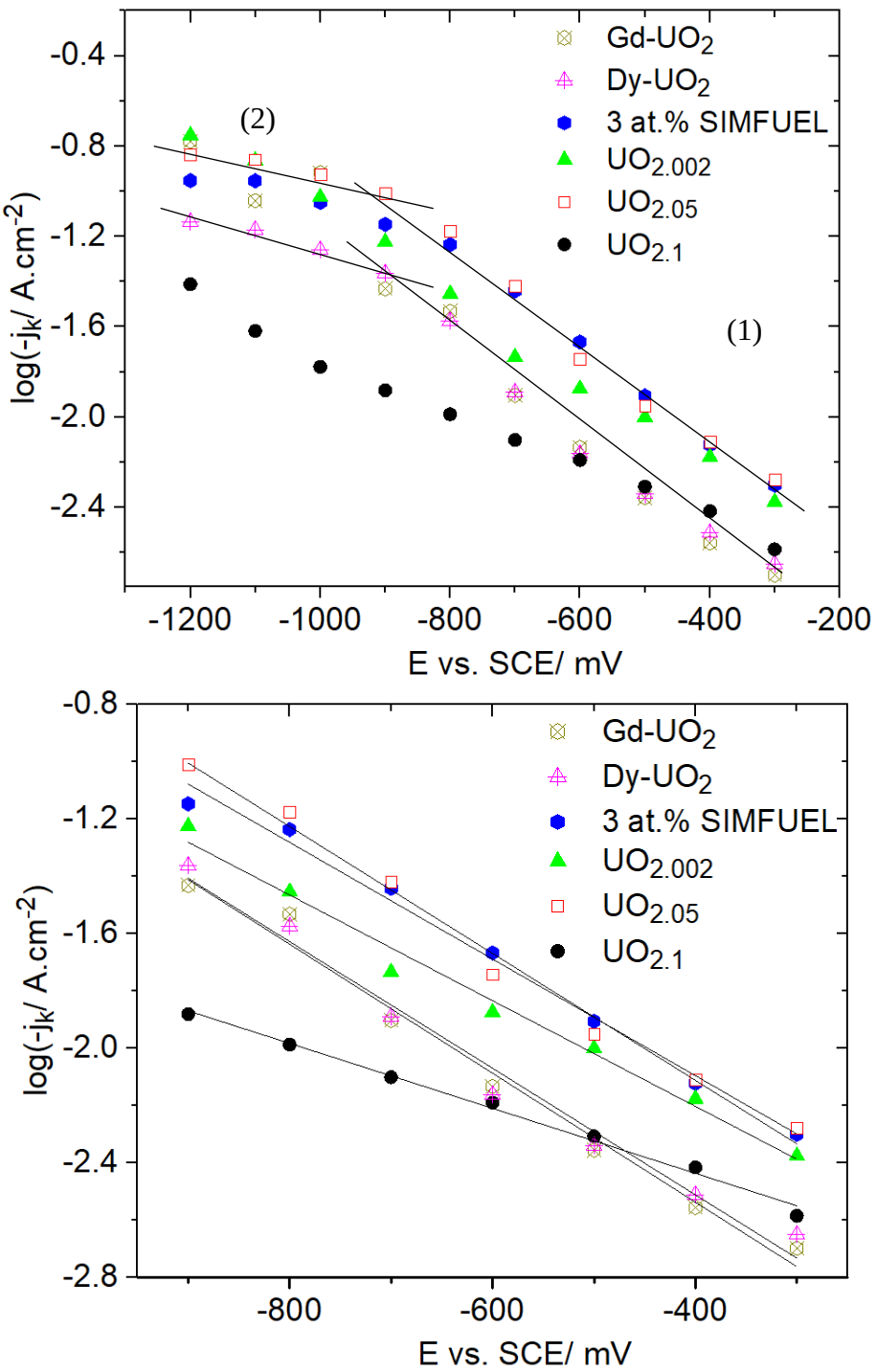

Figure 5.8: (A) Plots of the kinetic current (j_k) recorded on all 6 UO_2 electrodes in a 0.1 mol.L^{-1} of NaCl solution contains 0.02 mol.L^{-1} of H_2O_2 and 0.05 mol.L^{-1} of $NaHCO_3$ (pH = 9.7. The plotted lines are guides not fits. (B) Linear fits to the currents in the potential region -0.9V to -0.3V.

For the non-stoichiometric electrodes, the currents measured on the $UO_{2.002}$ and $UO_{2.5}$ electrodes were similar with regions 1 and 2 better defined for the $UO_{2.05}$ electrode than for the $UO_{2.002}$ electrode. On the $UO_{2.1}$ electrode, the currents were substantially lower and less potential-dependent, and no clear transition between regions 1 and 2 was observed. Fits to the currents in region 1 were used to obtain Tafel slopes, Figure 5.8 B, which are summarized in Table 5-2. These slopes were large, particularly in the case of the $UO_{2.1}$ electrode.

Table 5-2: Tafel slopes measured on all 6 electrodes in a 0.1 mol.L^{-1} of NaCl solution containing 0.02 mol.L^{-1} H_2O_2, and two different $[CO_3]_{tot}$ (pH = 9.7). The currents in the potential region from -0.3 V to -0.9 V were used for these calculations.

	$[CO_3]_{tot}$ = 0.05 mol.L^{-1}	***$[CO_3]_{tot}$ = 0.01 mol.L^{-1}***
Electrode	**Tafel slope mV/decade**	**Tafel slope mV/decade**
Dy-UO_2	-453	-363
$UO_{2.05}$	-450	-476
$UO_{2.002}$	-540	-461
3 at.% SIMFUEL	-490	-592
Gd-UO_2	-444	-331
$UO_{2.1}$	-877	-741

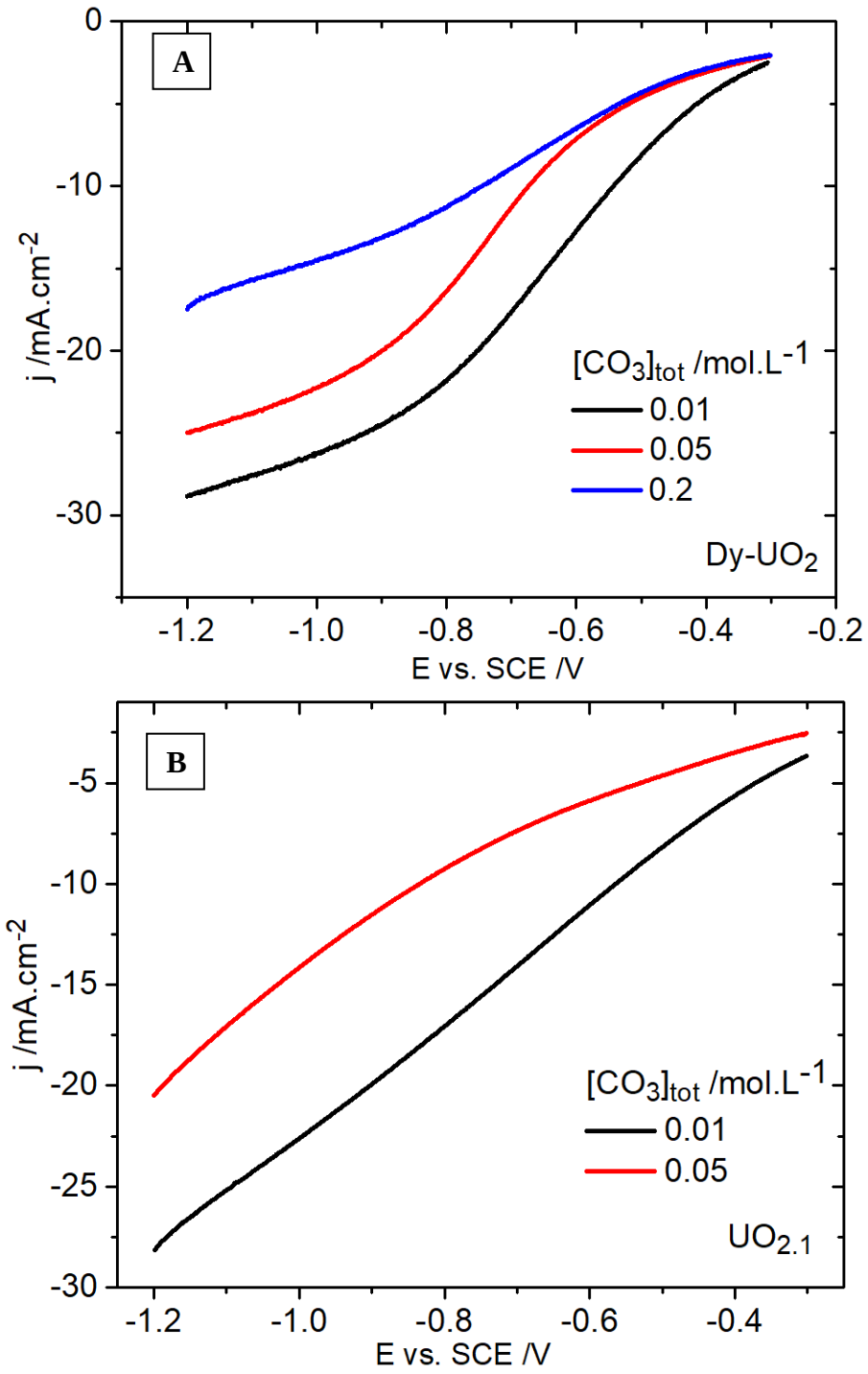

Figure 5.9: CV scans recorded from -1.2V to -0.3V on the $UO_{2.1}$ and Dy-UO_2 electrodes in a 0.1 mol.L^{-1} of NaCl containing 0.02 mol.L^{-1} of H_2O_2 (pH = 9.7) and various $[CO_3]_{tot}$.

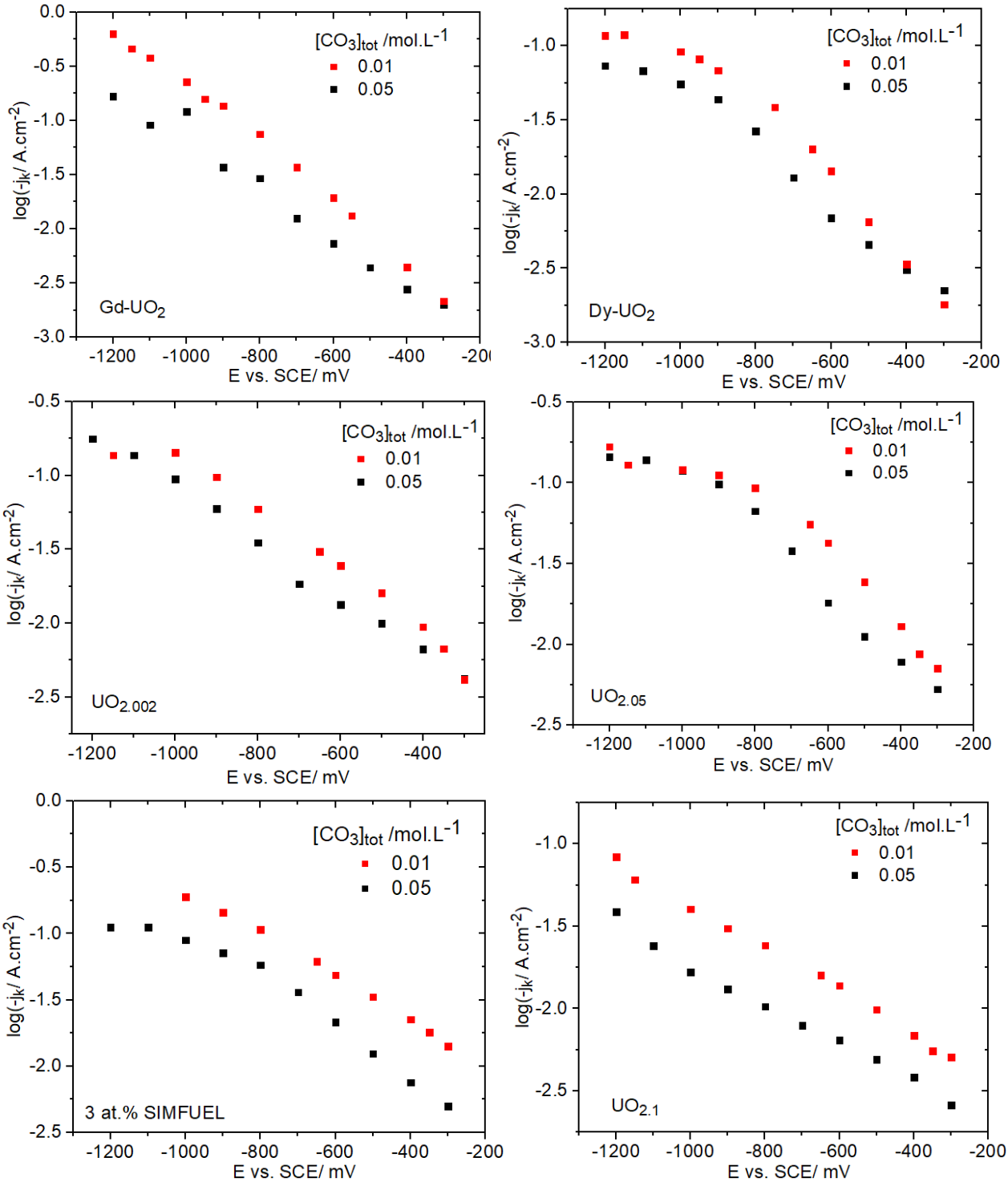

Figure 5.10: Plots of kinetic currents (j_k) as a function of potential recorded on all 6 electrodes in a 0.1 mol.L^{-1} NaCl solution containing 0.02 mol.L^{-1} of H_2O_2 (pH = 9.7) and two different $[CO_3]_{tot}$.

5.3.5 The Influence of HCO_3^-/CO_3^{2-} and SO_4^{2-}

Figure 5.9 shows that the reduction currents recorded on both the Dy-UO_2 and $UO_{2.1}$ electrodes were significantly increased if the $[CO_3]_{tot}$ was decreased. As best observed on the Dy-UO_2 electrode, the suppression of the current by HCO_3^-/CO_3^{2-} was more marked at more negative potentials.

Figure 5.10 shows log i_k vs E plots for all the electrodes in solutions containing two different $[CO_3]_{tot}$, and the Tafel slopes, obtained by fitting the currents in the potential range -0.3 V t0 -0.9 V (Region 1), are listed in Table 5-2. For the Re(III)-doped electrodes the currents were increased and the Tafel slopes decreased by a decrease in $[CO]_{tot}$; i.e., the currents became more potential-dependent. For the Dy-UO_2 electrode the transition from region 1 (-0.3 V to -0.9 V) to region 2 (< -0.9 V) was clearly defined at both $[CO_3]_{tot}$, while, for the Gd-UO_2 electrode, region 2 was poorly defined, the currents in this region being considerably higher than on the Dy-UO_2 electrode. For the SIMFUEL, the currents were decreased at higher $[CO_3]_{tot}$ in both potential regions although the Tafel slope appeared to be slightly increased. Considering the large values, this increased Tafel slope was probably not significant. For the $UO_{2.002}$ and $UO_{2.05}$ electrodes the currents in region 1 were increased and the Tafel slopes decreased as $[CO_3]_{tot}$ was decreased. However, the currents in region 2 remained unchanged. For the $UO_{2.1}$ electrode the currents were suppressed but the transition from region 1 to region 2 was still not observed.

Current measurements were also made in solutions containing $[SO_4^{2-}]$ similar to the $[CO_3]_{tot}$ used. The currents recorded for H_2O_2 reduction at three potentials in the -1.2 V to -0.3 V range, Figure 5.12 confirmed that SO_4^{2-} exhibited an almost negligible effect on the kinetics of H_2O_2 reduction demonstrating that the influence of HCO_3^-/CO_3^{2-} was specific to this anion.

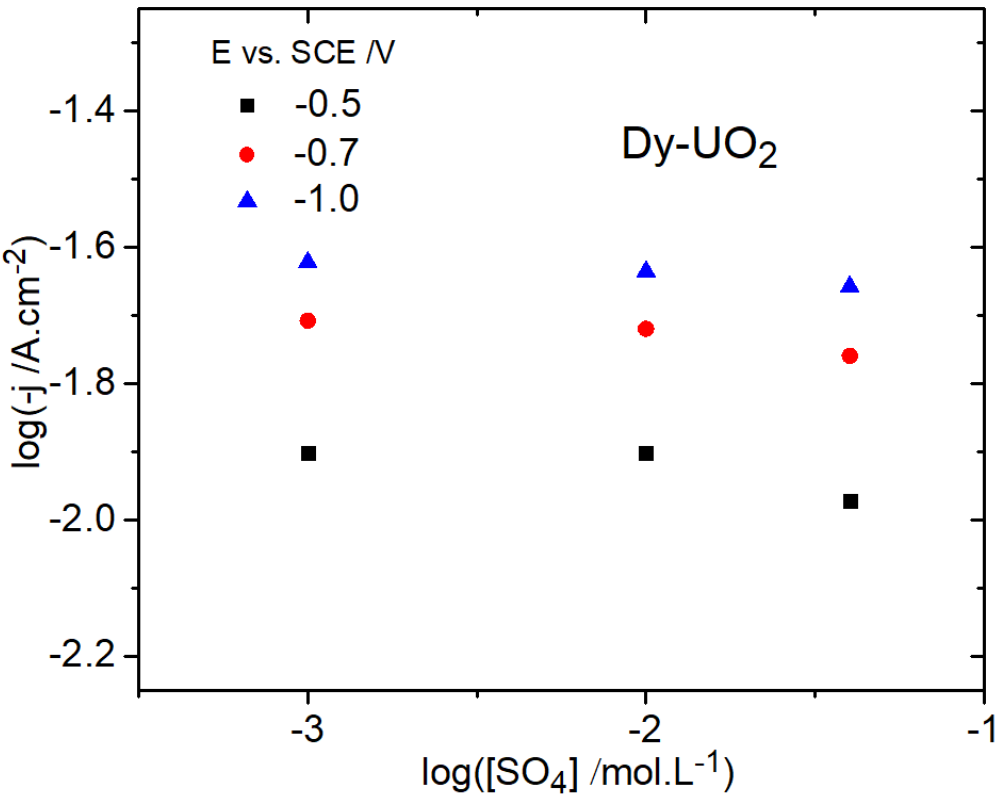

Figure 5.11: H_2O_2 reduction currents recorded on the Dy-UO_2 electrode measured in a 0.1 mol.L^{-1} NaCl solution containing 0.02 mol.L^{-1} H_2O_2 (pH = 9.7) as a function of $[SO_4]_{tot}$.

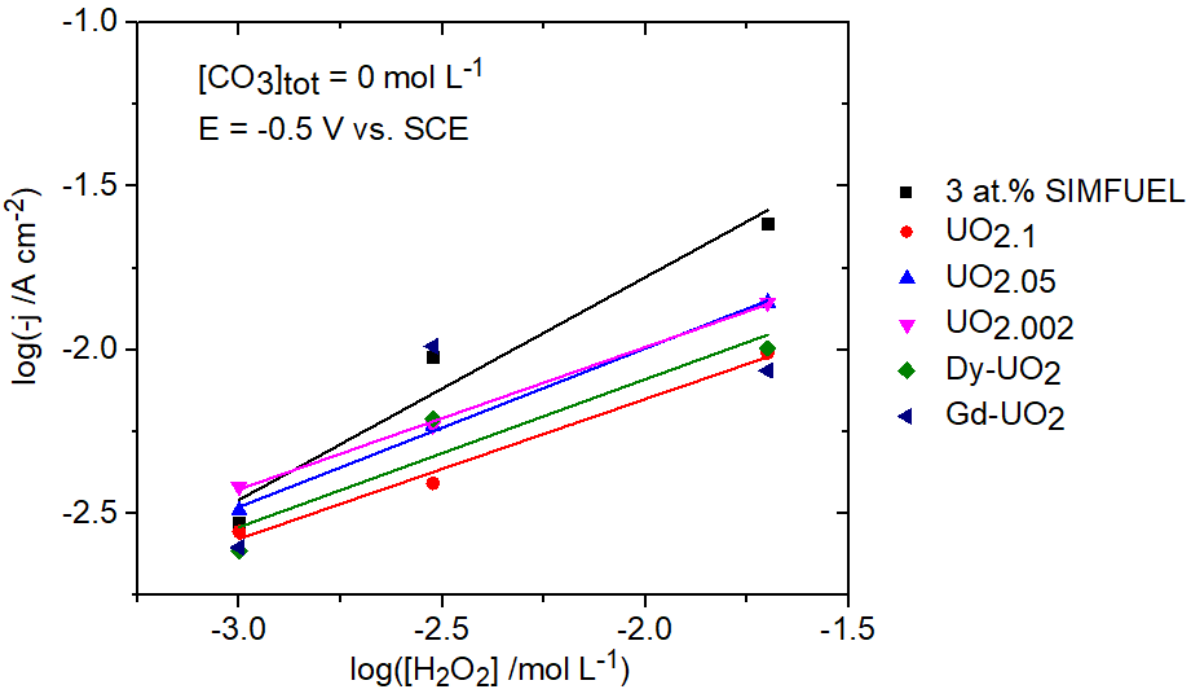

Figure 5.12: Kinetic currents (j_k) for H_2O_2 reduction on the 6 electrodes at a potential of -0.5 V as a function of [H_2O_2] in a 0.1 mol.L^{-1} of NaCl solution (pH = 9.7).

Figure 5.12 shows kinetic currents measured at -0.5 V on the 6 electrodes in carbonate-free solutions containing various [H_2O_2]. This potential was chosen since it was in region 1 when the currents were potential-dependent (i.e., in the Tafel region). Except for SIMFUEL, the reaction orders with respect to H_2O_2 were in the range 0.43 to 0.48. For SIMFUEL a slightly higher reaction order of 0.68 was obtained. Attempts to measure reaction orders at a potential of -1.1 V (i.e., in the potential range within which the current became chemically controlled) yielded values between 1.0 to 1.5, although currents measured on the two RE-doped electrodes were erratic and no meaningful values were obtained. It is possible that at the high potentials, in solutions unbuffered by HCO_3^-/CO_3^{2-}, the local pH at the electrode surface differed from the set solution value to an extent dependent on the electrode rotation rate. Goldik et al.[2] showed that the current for H_2O_2 reduction was sensitive to pH for values ≥ 12.

5.4 Discussion

In previous studies on SIMFUEL Goldik et al. [1, 3, 4] adopted the kinetic analysis developed for H_2O_2 on Cu by Vazquez et al. [25] and Cere et al. [26]. The transition from a potential-dependent current at low cathodic overpotentials to a chemically-controlled current at high cathodic overpotentials was interpreted as a two step reaction involving first the chemical oxidation of the UO_2 surface by H_2O_2 with a reaction rate constant of k_c,

$$2(U^{IV}\text{-}U^{V}) + H_2O_2 \xrightarrow{k_c} 2(U^{V}\text{-}U^{V}) + 2OH^- \qquad \textbf{5.5}$$

followed by the electrochemical regeneration of U^{IV}-U^{V} with a rate constant k_e

$$2(U^{V}\text{-}U^{V}) + 2e^- \xrightarrow{k_e} 2(U^{IV}\text{-}U^{V}) \qquad \textbf{5.6}$$

Although not explicitly represented in this sequence of reactions, the availability of O_V is required to accommodate and release O ions from interstitial sites in the UO_2 fluorite lattice [32]. The Tafel slope for reaction **5.6** is defined by the rate constants and given by

$$\frac{d\log(-j_k)}{dE} = \frac{-\alpha_c F}{2.303RT}\left(\frac{X}{1-X}\right) \qquad \textbf{5.7}$$

where $x = \frac{c_b k_c}{k_e}$, α_c is the transfer coefficient for the electrochemical reaction.

In addition, the reaction order (m) with respect to H_2O_2 is also related to the rates of these two reactions (i.e., to X) by the relationship,

$$m = \left(\frac{\partial \log(-j_k)}{\partial \log c_b}\right)_E = \frac{1}{1+X} \qquad \textbf{5.8}$$

Using these relationships, the large Tafel slopes and fractional reaction orders can be explained in terms of the relative rates of these two reactions. If the rate of the chemical reaction is fast $(c_b k_c \gg k_e)$, then $X \to \infty$, and the reaction would be completely electrochemically controlled

with a Tafel slope of $\frac{-\alpha_c F}{2.303RT}$, assuming rate control by the first electron in the overall two electron process. Additionally, the reaction order (m) would tend to 0. Conversely, if the chemical reaction was slow ($c_b k_c \ll k_e$), X would tend to 0, the Tafel slope become extremely large, and the reaction order approach 1.

The applicability of this chemical-electrochemical mechanism was clear in our results. When the overall reaction was under mixed chemical/electrochemical control in potential region 1 (-0.3 V to -0.9 V), large Tafel slopes and fractional reaction orders were observed on all electrodes. When the potential-dependent rate constant, k_e, became large in region 2 (< -0.9 V), the current became less dependent, and in some cases independent, on potential and the reaction order increased to ≥ 1, consistent with control by the chemical reaction. With the exception of $UO_{2.1}$, all the electrodes exhibited similar behaviour, with log j_k – E plots exhibiting the two regions of behaviour consistent with a transition from electrochemical to chemical control as the potential was increased. Since all the currents were measured for the same [H_2O_2], the differences in behaviour, which were subtle but distinct, reflected the differences in the rate constants for the chemical and electrochemical reactions.

For the RE-doped electrodes, the absolute currents measured in region 1 were effectively identical but lower than for the other electrodes indicating no significant difference in the electron transfer rates; i.e., providing the chemical oxidation rate was not rate-determining, the kinetics for H_2O_2 reduction were similar. However, in region 2, when the electrochemical rate was high, the current for the Dy-UO_2 electrode became almost independent of potential while that for the Gd-UO_2 electrode continued to increase. This indicated that the chemical reaction step (the creation of U^V sites, reaction 5.5) was more rapid on the less heavily-doped Gd-UO_2. This was consistent with the higher availability of oxygen vacancies (O_V), which are necessary

for the creation of the required DAR sites, in the more lightly doped electrode. Previous Raman spectroscopic studies have shown that RE-doping limited the availability of O_Vs due to the formation of Re^{III}-O_V clusters [14, 15], but did not unequivocally detect a measurable difference in the number of O_V in these two electrodes.

For the SIMFUEL, the currents were higher than for the RE(III)-doped electrodes, Figure 5.3, but the Tafel slope remained large, Table 5-2. This indicated no observable change in the mechanism but an increase in overall reactivity. This increase persisted over both potential regions; i.e., was independent of the potential and, therefore, not changed as the kinetics evolved from electrochemical to chemical control. Possible explanations for this behaviour include; either (a) a more reactive UO_2 matrix due to the lower RE(III) doping level, and/or (b) an additional H_2O_2 reduction reaction on the noble metal (ε) particles. Raman spectroscopy [14,15] confirms that this electrode had a higher number density of O_V which would support a higher rate of the chemical step; i.e., a more reactive matrix. However, it is presently not possible to distinguish this effect from that of the catalyzed reduction on the particles.

For the non-stoichiometric UO_{2+x} electrodes the behaviour on the $UO_{2.002}$ and $UO_{2.05}$ electrodes was similar with the $UO_{2.002}$ exhibiting a slightly lower Tafel slope, possibly related to the lower conductivity of this electrode [19]. In region 2, the currents were effectively identical, suggesting no measurable difference in the rate of the chemical oxidation of the UO_2 surface. The $UO_{2.1}$ electrode exhibited the lowest currents for any of the electrodes and had the largest Tafel slope. Additionally, there is no observable transition from mixed electrochemical-chemical control (region 1) to chemical control (region 2). This indicated that both reactions were slow with the extremely large Tafel slope indicating a very slow chemical oxidation step. However, the inability to separate these regions could have reflected the heterogeneous non-stoichiometry

of this electrode. Energy dispersive X-ray and Raman spectroscopic analyses [16] showed some locations were close to stoichiometric while others approached, and possibly exceeded, a composition of $UO_{2.25}$. One possibility was that the variations in non-stoichiometry in this electrode led to some locations rendered unreactive due to the dominance of cubooctahedral clusters and distortions of the fluorite lattice[16].

The suppression of the H_2O_2 reduction current by an increase in $[CO_3]_{tot}$ clearly indicated an influence of this anion on the reduction process since a similar suppression was not observed for SO_4^{2-}. Previous studies have shown that both O_2 reduction (on UO_2) and H_2O_2 reduction (on SIMFUEL) were suppressed in the presence of HCO_3^-/CO_3^{2-}[4, 10, 11, 27]. For O_2 reduction, the mechanism did not change as indicated by the similar Tafel slopes and reaction orders observed at different $[CO_3]_{tot}$ but some H_2O_2 was released to the solution consistent with the subsequent H_2O_2 reduction step being also retarded. It was proposed that this was due to the competition for adsorption at DAR sites between H_2O_2 and HCO_3^-/CO_3^{2-} anions. [4]

The results obtained in this study showed HCO_3^-/CO_3^{2-} suppressed the current in both potential regions 1 and 2 for the SIMFUEL and RE(III)-doped electrodes but only in region 1 for the $UO_{2.002}$ and $UO_{2.05}$ electrodes. This suggested that, for these two non-stoichiometric oxides, HCO_3^-/CO_3^{2-} suppressed the rate of the electrochemical reduction step, the reduction of U^V, without influencing the rate of its chemical formation. This suggested the key influence of this anion was to stabilize the intermediate U^V state on the surface of the electrode. This affinity of HCO_3^-/CO_3^{2-} for oxidized surface states on UO_2 surfaces at negative potentials has been discussed in detail previously.[4, 28, 29] In H_2O_2 solutions it was also possible that the peroxycarbonate (HCO_4^-) ions formed when both H_2O_2 and HCO_3^-/CO_3^{2-} were present in the solution stabilized U^V by forming $UO_2(HCO_4)_{ads}$ surface species which are kinetically slow to

reduce and lead to a decrease in available DAR sites for H_2O_2 reduction[30]. Presently, it is not possible to distinguish between these possibilities. The absence of any influence of SO_4^{2-} on the kinetics of H_2O_2 reduction was not surprising since XPS studies have shown SO_4^{2-} ions had no observable effects on the surface composition of UO_2.[28, 29, 31]

The results in Figure 5.3 showed that the influence of anodic oxidation influenced the kinetics of H_2O_2 reduction to different degrees depending on the electrode. For the RE-doped electrodes the marginal influence of anodic oxidation was consistent with the known resistance to oxidation of these materials [16-18, 22, 32]. This could be attributed to the elimination of available O_V by the formation of RE^{III}-O_V clusters which decreased the extent of formation of the U^V species required in the catalytic DAR sites. Raman studies[15] showed this O_V elimination process was slightly less effective for the Dy-UO_2 electrode than the Gd-UO_2 electrode which would account for the slightly greater effect of anodic oxidation on the latter.

For the non-stoichiometric electrodes, the kinetics of H_2O_2 reduction was stimulated on all three electrodes as indicated by the increased currents on the reverse scans, with the catalytic effect increasing in the order

$$UO_{2.002} < UO_{2.05} < UO_{2.1}$$

These electrodes, while possessing non-uniform compositions, have also been shown to exhibit an enhanced anodic reactivity which increased as the degree of non-stoichiometry increased [12, 19]. As shown in this study, this increase in reactivity with degree of non-stoichiometry was not observed in the absence of anodic oxidation. A more detailed analysis is required if these effects are to be elucidated. For the SIMFUEL electrode anodic oxidation did not lead to an observable catalysis of the H_2O_2 reduction reaction. It was possible that any effect, which would be expected

to be quite small (as observed for the RE(III)-doped electrodes), was obscured by the currents for H_2O_2 reduction on the ε-particles.

SEM/EDX analyses of these electrodes, coupled with current-sensing AFM measurements [17] showed wide variations in the distribution of non-stochiometric locations whose conductivity tended to increase with the degree of non-stoichiometry. For the $UO_{2.002}$ electrode, these analyses showed a generally random distribution of O interstitial ions in the matrix which led to lattice distortions and a slightly enhanced anodic reactivity [32]. This would involve the creation of the U^V surface species required to catalyze the H_2O_2 reduction reaction when the potential was subsequently made negative. Similar analyses of the $UO_{2.05}$ showed a distinct separation into conducting (non-stochiometric) and non-conducting locations. Since the overall anodic reactivity of this electrode was greater than that of the $UO_{2.002}$ electrode the enhanced creation of DAR sites would account for the enhanced kinetics of the H_2O_2 reduction reaction after anodic oxidation, Figure 5.3.

For the $UO_{2.1}$ electrode there was a marked separation into conducting and non-conducting locations, with well-developed, anisotropically conducting ridges and enhanced grain boundary conductivity. On this electrode surface compositions varied from close to stoichiometric to ~ $UO_{2.33}$ which was close to U_3O_7 a phase within which significant fluorite lattice distortions were observed.[12, 16] While scanning electrochemical microscopy (SECM) measurements showed larger reduction currents for the redox mediator, ferrocenemethanol, were observed on more highly non-stoichiometric locations it is not immediately obvious these sites would also be the most active sites for H_2O_2 reduction. The overall reactivity of this electrode was suppressed (compared to the $UO_{2.002}$ and $UO_{2.05}$ electrodes, Figure 5.8) [19]

5.5 Summary and Conclusions

- The electrochemical reduction of H_2O_2 has been studied on a range of UO_2 electrodes including RE(III)-doped and non-stoichiometric electrodes and a SIMFUEL.
- On all electrodes reduction proceeded via a sequence of two reactions, the chemical oxidation of the surface creating U^V sites followed by the electrochemical reduction of the surface back to its original U^{IV} state.
- After correcting for transport effects, the rate of reduction decreased in the order $UO_{2.002}$ ~ $UO_{2.5}$ ~ SIMFUEL > Gd-UO_2 ~ Dy-UO_2 > $UO_{2.1}$
- The rate was suppressed on the RE(III)-doped electrodes by the stabilization of RE(III)-O_V clusters which decreased the availability of the O_V required during oxidation of U^{IV} surface states to U^V.
- On SIMFUEL, reduction may be catalyzed on the surfaces of the noble metal (ε) particles present in this electrode.
- HCO_3^-/CO_3^{2-}, in the concentration range 0.01 to 0.05 mol.L^{-1}, suppressed the reduction rate by stabilizing the U^V surface state required to catalyze the reduction reaction thereby inhibiting its reduction back to the original U^{IV} state.

5.6 References

[1] J.S. Goldik, H.W. Nesbitt, J.J. Noël, D.W. Shoesmith, Surface electrochemistry of UO_2 in dilute alkaline hydrogen peroxide solutions, Electrochimica Acta, 49 (2004) 1699-1709.

[2] J.S. Goldik, J.J. Noël, D.W. Shoesmith, The electrochemical reduction of hydrogen peroxide on uranium dioxide electrodes in alkaline solution, Journal of Electroanalytical Chemistry, 582 (2005) 241-248.

[3] J.S. Goldik, Noel J.J., Shoesmith D.W., The effects of simulated fission products in the reduction of hydrogen peroxide on simulated nuclear fuel electrodes, Journal of The Electrochemical Society, 153 (2006) E151-E159.

[4] J.S. Goldik, J.J. Noël, D.W. Shoesmith, Surface electrochemistry of UO_2 in dilute alkaline hydrogen peroxide solutions, Electrochimica Acta, 51 (2006) 3278-3286.

[5] A. Trunov, V. Presnov, Oxygen electroreduction on semiconductor catalysis II: processes at oxide semiconductor-electrolyte interface Elektrokhimiya, 11 (1975) 77-84.

[6] A. Trunov, V. Presnov, Oxygen electroreduction on semiconductor catalysis III: the importance of 3d electrodes of oxide semiconductor Elektrokhimiya, 11 (1975) 290-292.

[7] V. Presnov, A. Trunov, Oxygen Electroreduction on Semiconductor Catalysts I: General Approach and Processes in the Semiconductor, Elektrokhimiya, 11 (1975) 71-76.

[8] D. Shoesmith, F. King, A mixed potential model for the prediction of the effects of alpha radiolysis, precipitation and redox processes on the dissolution of used nuclear fuel, Ontario Power Generation Report, (1998) 01200-00038.

[9] D.W. Shoesmith, Fuel corrosion processes under waste disposal conditions, Journal of Nuclear Materials, 282 (2000) 1-31.

[10] W. Hocking, J.S. Betteridge, D.W. Shoesmith, The cathodic reduction of oxygen on uranium dioxide in dilute alkaline aqueous solution, Atomic Energy of Canada Limited Report, 1991.

[11] W.H. Hocking, J.S. Betteridge, D.W. Shoesmith, The cathodic reduction of oxygen on uranium dioxide in dilute alkaline aqueous solution, Journal of Electroanalytical Chemistry, 379 (1994) 339-351.

[12] H. He, Z. Qin, D.W. Shoesmith, Characterizing the relationship between hyperstoichiometry, defect structure and local corrosion kinetics of uranium dioxide, Electrochimica Acta, 56 (2010) 53-60.

[13] T.B. Lindemer, T.M. Besmann, Chemical thermodynamic representation of 〈$UO_{2\pm x}$〉, Journal of Nuclear Materials, 130 (1985) 473-488.

[14] M. Razdan, Shoesmith D.W., The electrocheical reacivity of 6.0 wt.% Gd doped UO_2 in aquous carbonate-bicarbonate solutions, Journal of The Electrochemical Society, 4 (2014) H225-H234.

[15] M. Razdan, D.W. Shoesmith, Influence of trivalent-dopants on the structural and electrochemical properties of uranium dioxide (UO_2), Journal of The Electrochemical Society, 161 (2014) H105-H113.

[16] H. He, D. Shoesmith, Raman spectroscopic studies of defect structures and phase transition in hyper-stoichiometric $UO_{(2+x)}$, Phys Chem Chem Phys, 12 (2010) 8108-8117.

[17] H. He, M. Broczkowski, K. O'Neil, D. Ofori, O. Semenikhin, D. Shoesmith, Corrosion of nuclear fuel (UO_2) inside a failed nuclear waste container, Nuclear Waste Management Organization, Toronto, Ontario, (2012).

[18] H. He, P.G. Keech, M.E. Broczkowski, J.J. Noël, D.W. Shoesmith, Characterization of the influence of fission product doping on the anodic reactivity of uranium dioxide, Canadian Journal of Chemistry, 85 (2007) 702-713.

[19] H. He, R.K. Zhu, Z. Qin, P. Keech, Z. Ding, D.W. Shoesmith, Determination of Local Corrosion Kinetics on Hyper-Stoichiometric UO_{2+x} by Scanning Electrochemical Microscopy, Journal of The Electrochemical Society, 156 C87-C94.

[20] B.G. Santos, H.W. Nesbitt, J.J. Noël, D.W. Shoesmith, X-ray photoelectron spectroscopy study of anodically oxidized SIMFUEL surfaces, Electrochimica Acta, 49 (2004) 1863-1873.

[21] F.L.R. Bard A.J., Electrochemical methods fundamentals and applications second ed., John Wiley & Sons, New York.

[22] V.G. Prabhu, L.R. Zarapkar, R.G. Dhaneshwar, Electrochemical studies of hydrogen peroxide at a platinum disc electrode, Electrochimica Acta, 26 (1981) 725-729.

[23] CRC Handbook of Chemistry and Physics, Internet Version 2005, CRC Press, Boca Raton, FL.

[24] J. Newman, Schmidt number correction for the rotating disk, The Journal of Physical Chemistry, 70 (1966) 1327-1328.

[25] M.V. Vazquez, S.R. de Sanchez, E.J. Calvo, D.J. Schiffrin, The electrochemical reduction of hydrogen peroxide on polycrystalline copper in borax buffer, Journal of Electroanalytical Chemistry, 374 (1994) 179-187.

[26] S. Ceré, M. Vazquez, S.R. de Sánchez, D.J. Schiffrin, Surface redox catalysis and reduction kinetics of hydrogen peroxide on copper–nickel alloys, Journal of Electroanalytical Chemistry, 470 (1999) 31-38.

[27] D.W. Shoesmith, J.S. Betteridge, W.H. Hocking, The cathodic reduction of oxygen on n-type UO_2 in dilute alkaline aqueous solution, Journal of Electroanalytical Chemistry, 406 (1996) 69-81.

[28] S. Sunder, D.W. Shoesmith, M.G. Bailey, G.J. Wallace, Anodic oxidation of UO_2: Part II. electrochemical and X-ray photoelectron spectroscopic studies in alkaline solutions, Journal of Electroanalytical Chemistry and Interfacial Electrochemistry, 150 (1983) 217-228.

[29] D.W. Shoesmith, S. Sunder, M.G. Bailey, G.J. Wallace, F.W. Stanchell, Anodic oxidation of UO_2 IV. X-ray photoelectron spectroscopic and electrochemical studies of film growth in carbonate-containing solutions, Applications of Surface Science, 20 (1984) 39-57.

[30] Z. Zhu, L. Wu, J.J. Noël, D.W. Shoesmith, Anodic reactions occurring on simulated nuclear fuel (SIMFUEL) in hydrogen peroxide solution containing bicarbonate/carbonate – the effect of fission products, (2018).

[31] D.W. Shoesmith, S. Sunder, M.G. Bailey, G.J. Wallace, Anodic oxidation of UO_2. V. electrochemical and X-ray photoelectron spectroscopic studies of film-growth and dissolution in phosphate-containing solutions, Canadian Journal of Chemistry, 66 (1988) 259-265.

[32] N. Liu, H. He, J.J. Noël, D.W. Shoesmith, The electrochemical study of Dy_2O_3 doped UO_2 in slightly alkaline sodium carbonate/bicarbonate and phosphate solutions, Electrochimica Acta, 235 (2017) 654-663.

Chapter 6

6 Model for UO_2 Corrosion Inside a Failed Waste Container under Permanent Disposal Conditions – Sensitivity Analyses

6.1 Introduction

While containers for high level nuclear waste are designed to avoid failure after emplacement in a deep geologic repository (DGR), it is judicious to examine the consequences if failure should occur. Assuming containers fail after 1000 years of emplacement in a DGR the groundwater contacting the fuel would be anoxic since available oxidants will have been consumed by microbial reactions and the container corrosion process. Thus, the key source of oxidants inside a failed container would be water radiolysis caused by the α radiation fields associated with the spent fuel wasteform. H_2O_2 has been identified as the main radiolytic oxidant likely to cause UO_2 corrosion by oxidizing UO_2 to the much more soluble UO_2^{2+}, resulting in the release of radionuclides from the fuel matrix.[1, 2]

Two corrosion fronts will exist within a failed container: one on the fuel surface driven by radiolytic oxidants, and a second on the carbon steel surface sustained by H_2O reduction to produce the potential redox scavengers Fe^{2+} and H_2. These two fronts will be coupled since, for instance, Fe^{2+} and H_2O_2 would be expected to react via the Fenton reaction.

Extensive studies have shown that dissolved H_2 can suppress fuel corrosion,[3-10] which will counterbalance the tendency of H_2O_2 to accelerate it.[11-15] The presence of noble metal (ε) particles in the fuel, generated during in-reactor irradiation, can catalyze both reactions by acting as micro-galvanic anodes/cathodes within the UO_2 matrix.[10, 15, 16] Broczkowski et al.[7] monitored the influence of H_2 on the corrosion potential of UO_2 specimens with/without ε-particles, and showed that a lower corrosion potential was observed when ε-particles were

present, which is indicative of a slower corrosion process. This effect was confirmed by Trummer et al.[9], who showed that the dissolution of U was totally supressed by increasing the Pd weight percentage in UO_2 samples to 3% when H_2 was present. These experiments confirm that the activation of H_2 by noble metals is the key mechanism in the inhibition of UO_2 corrosion.

Goldik et al.[16] studied the kinetics of H_2O_2 reduction on SIMFUELs containing ε-particles using electrochemical methods, and found that the kinetic activity increased with the number density of noble metal particles in the SIMFUELs. Trummer et. al. [9] showed the dissolution of U was catalyzed when Pd was present in the UO_2 matrix, with the rate constant for oxidation of UO_2 by H_2O_2 increasing by ~ 2 orders of magnitude.

Over the past few years we have been developing a model for fuel corrosion inside a failed container[17]. Most recently, this model has been expanded from one to two dimensional to determine the influence of complex geometries[18] on fuel corrosion. This is necessary since the fuel pellets are fractured due to thermal stress during in-reactor irradiation and during the cooling process when the fuel is removed from the reactor. Liu et al.[19] demonstrated that the effects of radiolytically produced H_2 ($(H_2)_{int}$) and H_2 from steel corrosion ($(H_2)_{ext}$) are strongly influenced by the geometrical dimensions of the fracture.

In this study, these model calculations have been extended to include a number of additional effects:

(i) More complex defect shapes including pores and fractures with different dimensions;

(ii) A non-uniform number and distribution of ε-particles within fractures in the fuel;

(iii) The influence of O_2, a H_2O_2 decomposition product, on the fuel corrosion rate.

6.2 Model Description

As a consequence of in-reactor fission, the fuel undergoes a number of microstructural and compositional changes, with the key processes likely to influence the fuel reactivity being the doping of the UO_2 lattice with rare earth (RE^{III}) elements and the creation of noble metal (ε) particles. Since RE^{III} doping increases the conductivity of the lattice [20] it can lead to galvanic coupling of the UO_2 matrix to the noble metal particles. These particles can then act as microgalvanically-coupled anodes and cathodes which can control the redox conditions on the fuel surface and, hence, the corrosion rate of the fuel.

The reactions presently included in the model are shown in Figure 6.1.

(1) The production of key alpha radiolysis products, H_2O_2 and H_2. A simplified model was used to calculate the [H_2O_2] and [H_2], with other minor radiolysis products, such as OH and H radicals, not included. This simplified model has been compared to a complete water radiolysis model.[18] Using the simplified model, the calculated concentrations of dissolved UO_2^{2+} increased by only ~20% at the base of fractures in the fuel, making its use a conservative approach which does not underestimate the fuel corrosion behaviour.[18]

(2) UO_2 oxidation and dissolution caused by H_2O_2 reduction on the UO_2 surface (reaction 2a)[21] and on the microgalvanically-coupled catalytic ε-particles (reaction 2b).[9]

(3) The oxidation of H_2 leading to the suppression of UO_2 corrosion through different pathways: (i) reaction 3a - the reduction of U^{VI}/U^{V} to U^{IV} by H_2 oxidation on ε-particles [22]; (ii) reaction 3b - the reduction of UO_2^{2+} to UO_2 by H_2 in aqueous solution[23]; reaction 3c - the reduction of UO_2^{2+} adsorbed on the UO_2 surface by H_2 oxidation on ε particles.[10]

(4) The consumption of the dominant oxidant, H_2O_2, by reaction with Fe^{2+} in the Fenton reaction (reaction 4).[24]

(5) The catalytic recombination of the radiolytically produced H_2O_2 and H_2 on the ε-particles (reaction 5). [25]

(6) The decomposition of H_2O_2 to H_2O and O_2 catalyzed by the reversible U^{IV}/U^{V} redox transformation in the fuel surface (reaction 6). [21]

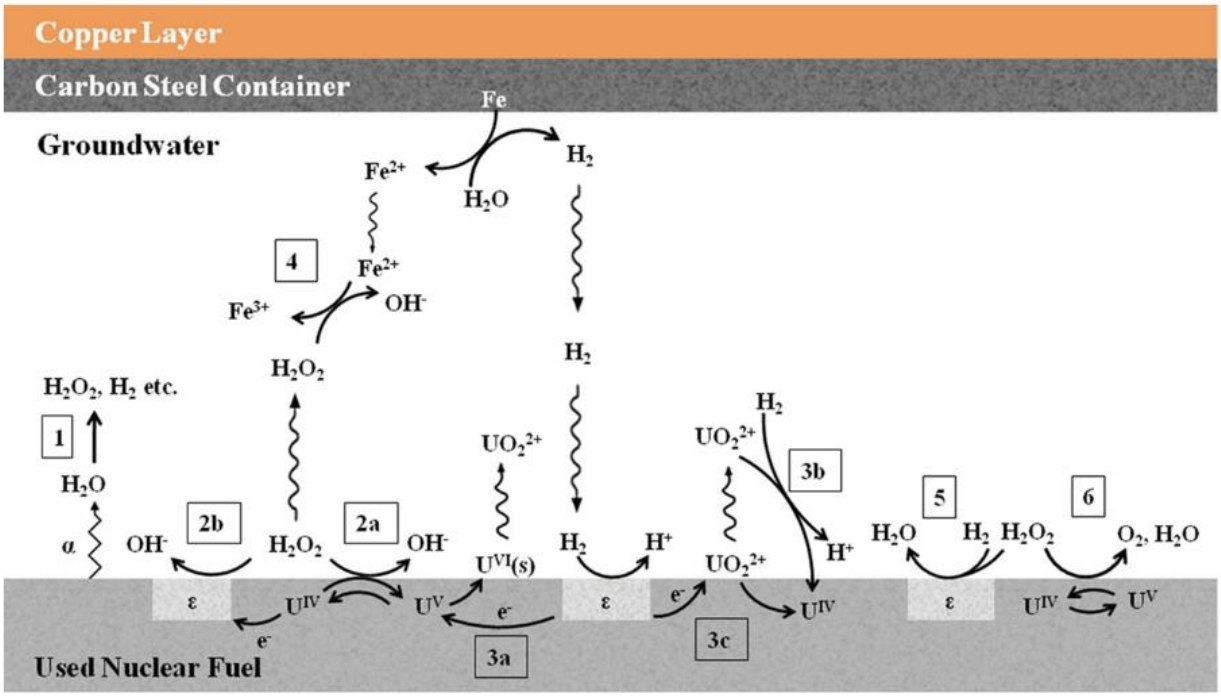

Figure 6.1: Key reactions involved in the radiolytic corrosion of spent fuel inside a failed container.

The effects of corrosion product deposition (such as $UO_3 \cdot 2H_2O$), which can effectively block the further corrosion of UO_2, are not included in the model. This simulates the likely groundwater scenario in which dissolved UO_2^{2+} species are prevented from accumulating on the fuel surface by complexation with carbonate/bicarbonate ions present at a sufficiently high concentration in the groundwater.

In the model, the rates of these processes are described by a series of one-dimensional diffusion reaction equations. This model is then numerically simulated using COMSOL Multiphysics (commercially available software) based on the finite element method. The model was developed using the chemical engineering module and the dilute species transport module of COMSOL Multiphysics (version 4.3.0.151, COMSOL Inc.). The parameter values adopted in the model have been discussed elsewhere. [17-19, 26] The default values of the simulation parameters are listed in Table 6-1. The parameters were maintained at the default values for all calculations unless otherwise stated. The dose rate used in calculations was 9.03×10^{5} $Gy.a^{-1}$ which corresponds to CANDU fuel with a burn-up of 220 $MKW.kg.U^{-1}$ (a unit describing the absorption of one joule of radiation energy per kilogram of matter per year) at 1000 years after discharge from the reactor.[27]

Table 6-1: Default values of simulation parameters used in model calculations

Parameter	Value	Reference
Diffusion layer thickness	10^{-3} m	[26]
Radiation zone thickness	1.3×10^{-5} m	[27]
Alpha radiation dose rate	9.03×10^{5} Gy.a^{-1}	[27]
UO_2 oxidation rate constant in H_2O_2	1×10^{-8} m.s^{-1}	[21]
H_2O_2/UO_2 surface reaction rate constant on ε-particles	6.92×10^{-6} m.s^{-1}	[9]
H_2/U^{VI} surface reaction rate constant on ε-particles	4×10^{-7} m.s^{-1}	[22]
H_2/UO_2^{2+} bulk reaction rate constant	3.6×10^{-9} L.mol^{-1}.s^{-1}	[23]
H_2/H_2O_2 surface reaction rate constant on ε-particles	2.2×10^{-5} m.s^{-1}	[25]
Fe^{2+} bulk reaction rate constant	1×10^{6} L.mol^{-1}.s^{-1}	[24]
H_2O_2 homogenous decomposition rate constant	8.29×10^{-8} s^{-1}	[28]
H_2O_2 surface-catalyzed decomposition rate constant	6.14×10^{-8} m.s^{-1}	[21]

6.2.1 The Influence of ε-particle Distribution

In previous model simulations, ε-particles were assumed to be uniformly distributed when simulating the radiolytic corrosion of UO_2 inside a fracture in a fuel pellet.[19] However, fission reactions are concentrated in the outer rim of fuel pellets leading to a high density of fission products, including ε-particles, at these locations but a much lower density at deeper locations within the pellet. To simulate this situation a linear gradient of particles was assumed with the coverage (area density) of the particles linearly distributed between the surface and the interior of a pellet; i.e., the coverage by ε-particles decreases linearly as the fracture deepens,

$$s = 0.01 + s_0 \times y \qquad \textbf{6.1}$$

where s represents the ε-particle coverage at location y (unit: m), $y \leq 0$ (at the fracture mouth, y = 0). For example, for a fracture with a depth of 6 mm, $s_0 = 1\ m^{-1}$, the coverage on the fracture bottom linearly decreases to 0.4% from 1% at the fracture mouth.

6.2.2 The Influence of Fracture Geometry

The influence of geometry was studied by changing the defect geometry from a 2-D fracture to a 3-D cylindrical pore, Figure 6.2. The fracture geometry in the fuel pellet was specified by width (a) and depth. To build the pore model, the width was replaced by a radius parameter (r), where r = a/2, and a is the width.

6.2.3 The Influence of H_2O_2 Decomposition to Produce the Alternative Oxidant, O_2

The primary radiolytic oxidant causing fuel corrosion is H_2O_2 since its reaction rate is 200 x higher than the alternative oxidant, O_2. However, it has been demonstrated experimentally that H_2O_2 decomposition to O_2 and H_2O occurs rapidly on UO_2 surfaces which would make O_2 the dominant oxidant likely to cause fuel corrosion. Lousada et al.[29] suggested that the impact of H_2O_2 on oxidative UO_2 dissolution decreases in the presence of fission products which can facilitate the H_2O_2 decomposition. Hence, the impact ratio of other molecular water radiolysis oxidants, e.g. O_2, would increase. Under α-radiation induced water radiolysis, the impact of H_2O_2 contributes to 65.97% of U dissolution with 99.8% of H_2O_2 decomposed on SIMFUEL surface. It was calculated that O_2 has an impact ratio of 30.10% based on previously published reaction rate constant between O_2 and UO_2[1]. This study concluded that O_2 is no longer negligible when the majority of H_2O_2 decomposes. The results in Chapter 4 of this thesis are consistent with the values of H_2O_2 being found to decompose.

A number of studies have shown that O_2 reduction is catalyzed on noble metal particles; i.e., on SIMFUEL surfaces[9, 30, 31]. Trummer et al.[9] suggested that, in an O_2-containing solution, an increase in Pd weight percent, indicating an enhanced fuel burn-up level, resulted in a higher dissolution rate of UO_2. This was attributed to catalysis of O_2 reduction which accelerated the UO_2 corrosion. The experimentally determined reaction rate constant for O_2 reduction on a UO_2 electrode doped with 3 wt.% Pt was determined to be 10^{-7} $m.s^{-1}$. Reaction (6.2) is included in the model calculations to take into account the catalyzing effects of ε-particles on O_2 reduction and UO_2 corrosion,

$$1/2O_2 + UO_2 \xrightarrow{k\_O_2\_eps} UO_3 \qquad \textbf{6.2}$$

where $k\_O_2\_eps = 10^{-7}$ $m.s^{-1}$.[9]

6.3 Results and Discussion

6.3.1 Influence of Defect Geometry

Figure 6.3 shows H_2 and H_2O_2 concentration profiles for the pore model. Both $[H_2]$ and $[H_2O_2]$ decrease with distance from the base of the pore as a consequence of diffusive losses as the pore opening is approached. At deep locations (0.5 and 1 mm from the base), there is no significant difference between $[H_2]$ and $[H_2O_2]$, Figure 6.3 A. However, at greater distances from the base (≥3 mm) the $[H_2O_2]$ reaches a plateau, Figure 6.3 B, and becomes independent of pore depth, while the $[H_2]$ increases linearly with distance from the base, Figure 6.3 A. The UO_2 corrosion rate (expressed as a flux of UO_2^{2+} leaving the wall of the pore at that location) increases with pore depth for shallow pores and then decreases for pore depths ≥ 3 mm, Figure 6.3 C. This increase in corrosion rate as the pore deepens from 0.5 to 3 mm, can be attributed to the increase in $[H_2O_2]$ with the accumulation of radiolytically produced H_2 ($[H_2]_{rad}$) at the base of

deeper pores leading to the suppression of fuel corrosion. This calculation is supported by experiments performed on UO_2 in irradiated water in which the accumulation of radiolytically produced H_2 in a closed system suppressed U dissolution by a factor of one third compared to the accumulation in an open system.[32]

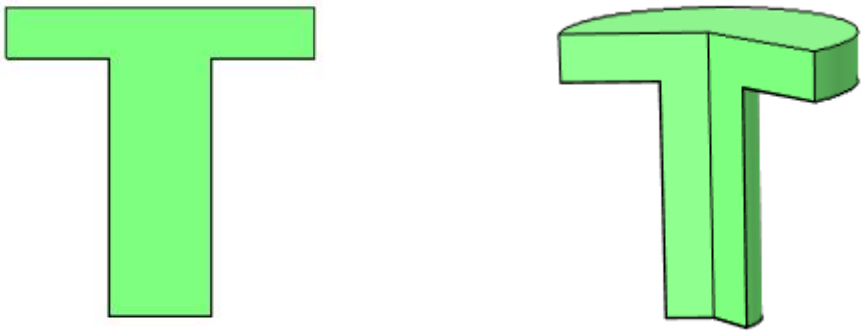

Figure 6.2: The 2-D fracture (A) and 3-D pore defect (B) in a fuel pellet.

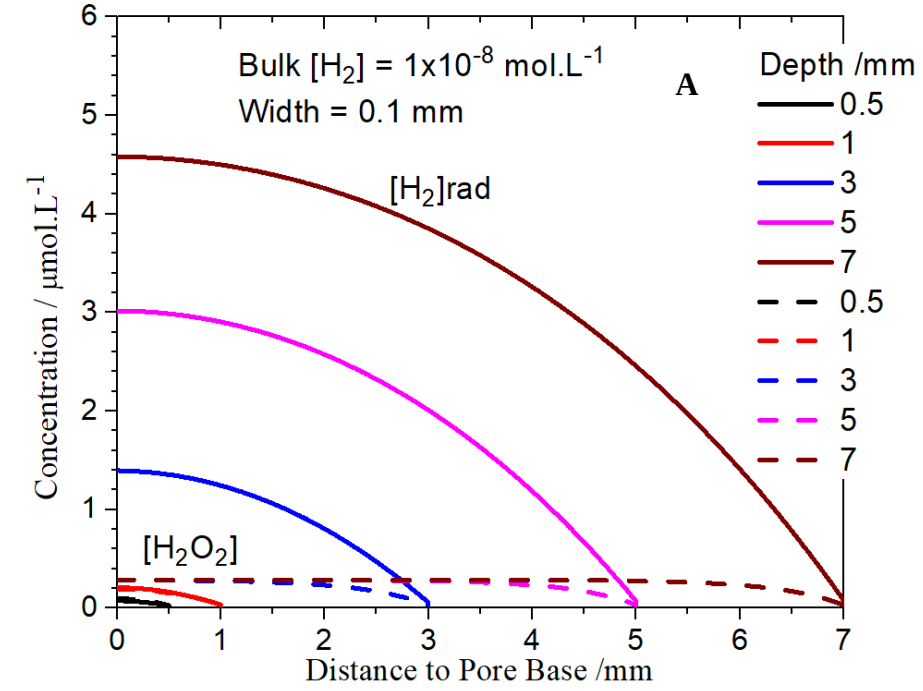
Bulk [H2] = 1x10-8 mol.L-1
Width = 0.1 mm
A
Depth /mm
0.5
1
3
5
7
0.5
1
3
5
7
[H2]rad
[H2O2]
Concentration / µmol.L-1
Distance to Pore Base /mm

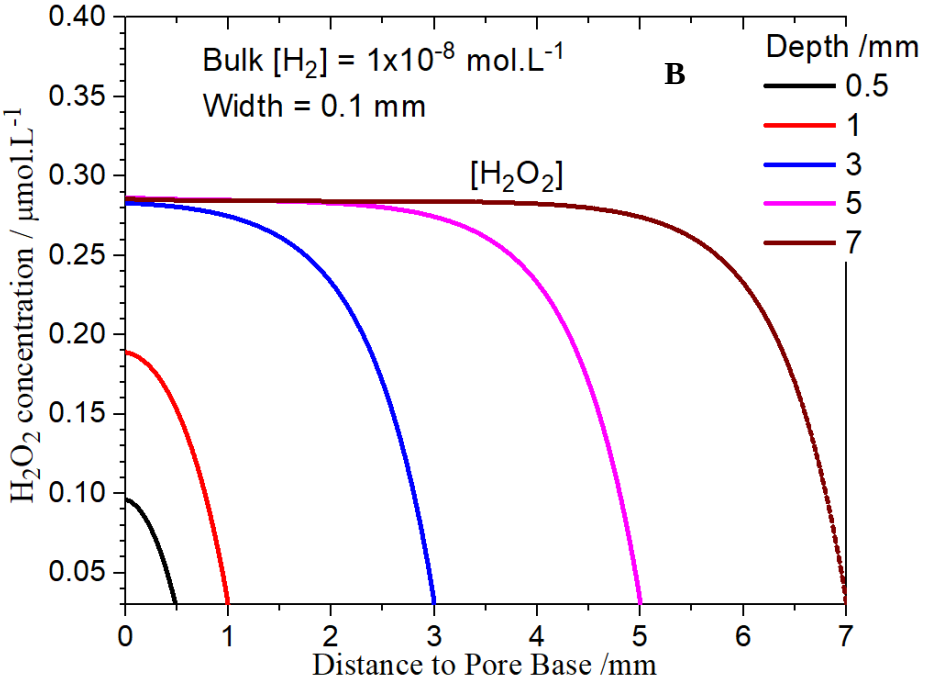
Bulk [H2] = 1x10-8 mol.L-1
Width = 0.1 mm
B
Depth /mm
0.5
1
3
5
7
[H2O2]
H2O2 concentration / µmol.L-1
Distance to Pore Base /mm

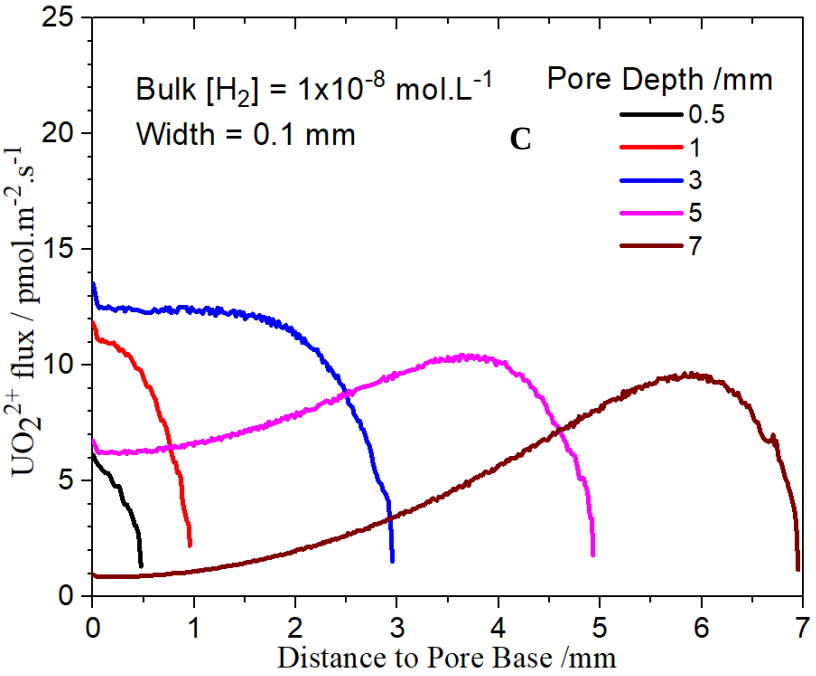

Figure 6.3: The influence of pore depth on (A) Concentration profiles for [H_2] and [H_2O_2] : (B) enhanced concentration profile for H_2O_2; (C) the calculated UO_2^{2+} flux (UO_2 corrosion rate) in the direction normal to the wall of the pore as a function of the distance from the base of the pore, Pore width = 0.1 mm. Bulk [H_2] = 10^{-8} mol.L^{-1}; all other parameters have the default values (Table 6-1).

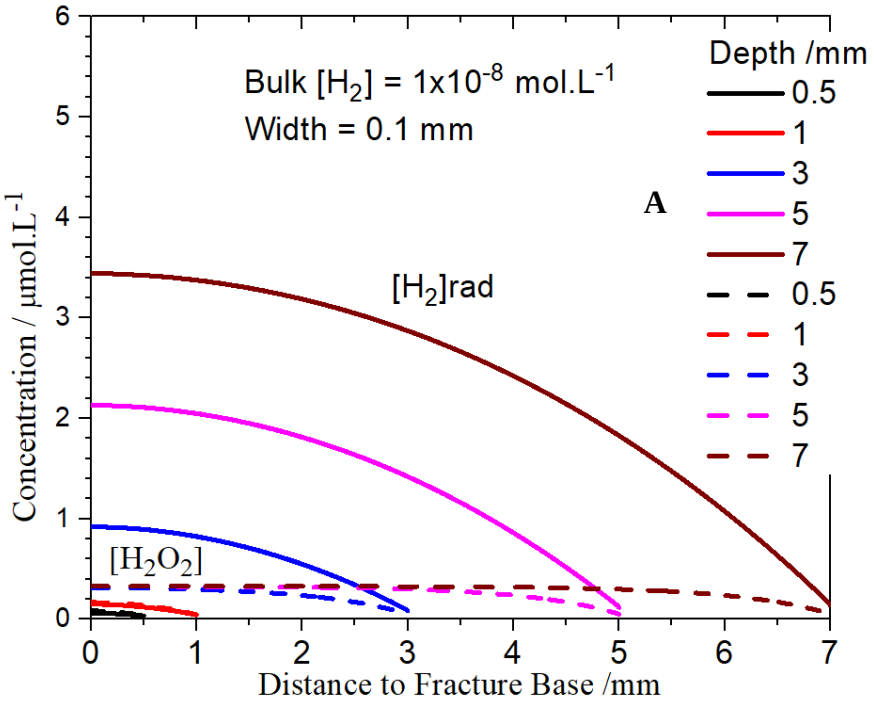
Bulk [H2] = 1x10-8 mol.L-1
Width = 0.1 mm
A
Depth /mm
0.5
1
3
5
7
0.5
1
3
5
7
[H2]rad
[H2O2]
Concentration / µmol.L-1
Distance to Fracture Base /mm

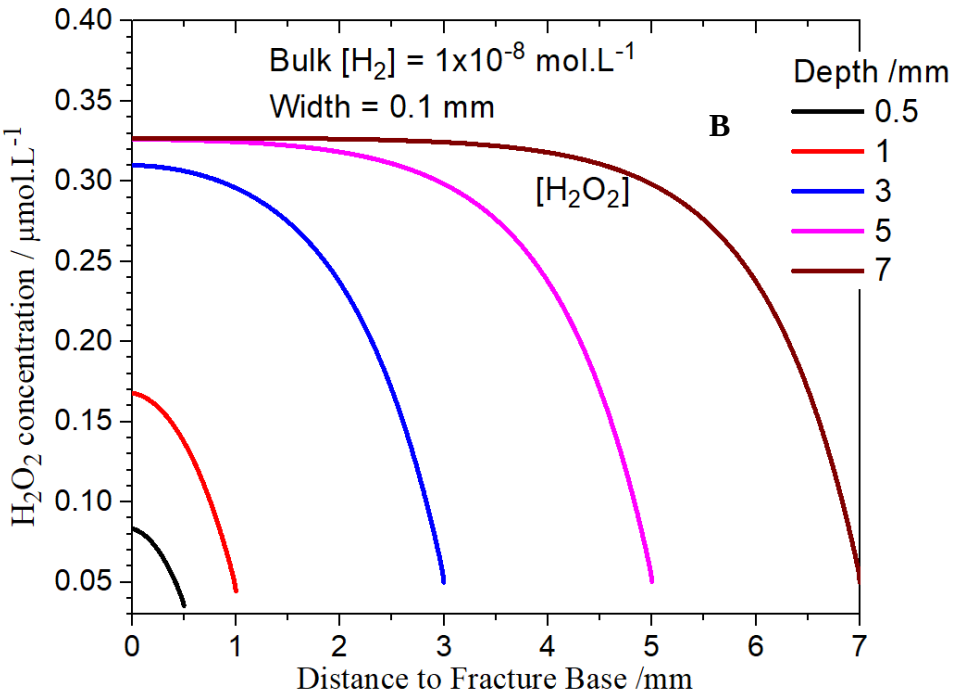
Bulk [H2] = 1x10-8 mol.L-1
Width = 0.1 mm
B
Depth /mm
0.5
1
3
5
7
[H2O2]
H2O2 concentration / µmol.L-1
Distance to Fracture Base /mm

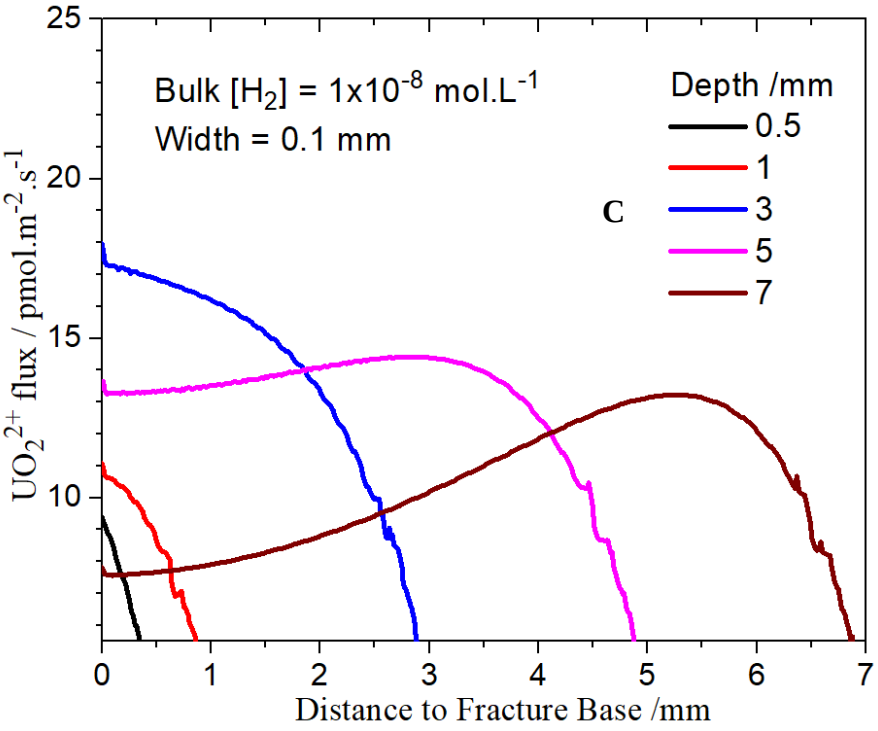

Figure 6.4: The influence of fracture depth on the concentration profiles for (A) $[H_2]$ and $[H_2O_2]$; (B) enhanced concentration profiles for H_2O_2; (C) the calculated UO_2^{2+} flux (UO_2 corrosion rate) in the direction normal to the wall of a fracture as a function of the distance from the base of a fracture: pore width = 0.1 mm, bulk $[H_2] = 10^{-8}$ mol.L^{-1}, all other parameters have the default values (Table 6-1).

Similar calculations were performed for the fracture geometry, Figure 6.4 A and B show the same trends are obtained for both the pore and the fracture models, the corrosion rate being significantly suppressed by $[H_2]$ for depths ≥ 3mm. Comparison of the two sets of data shows corrosion rates within a pore are slightly lower than those in a fracture.

Figure 6.5 shows the calculated critical $[H_2]$ ($[H_2]_{crit}$) for a range of fracture (A) and pore (B) dimensions. The critical H_2 concentration ($[H_2]_{crit}$) is the amount of H_2 required from steel corrosion to completely inhibit fuel corrosion at all locations within a fracture or a pore. For wide fractures (width > 0.6 mm), $[H_2]_{crit}$ increases as the fracture depth increases, while for

narrow fractures (width < 0.6 mm) it first increases then decreases as the fracture deepens suggesting a significant suppression of fuel corrosion by the local accumulation of radiolytic H_2 at deep locations. A similar behaviour was observed for the pore geometry, Figure 6.5 B, but with a slightly lower demand for H_2 from steel corrosion in shallow pores compared to shallow fractures. For both geometries, an upper limit for $[H_2]_{crit}$ of 5.7 $\mu mol.L^{-1}$ is sufficient to suppress corrosion, irrespective of fracture/pore dimensions. This value is calculated to be ~17 times more than the $[H_2]_{crit}$ required to suppress corrosion on a planer surface without defects. Thus, if the corrosion of the steel container can produce more than 5.7 $\mu mol.L^{-1}$ of H_2, the corrosion of CANDU spent fuel with a burn-up of 220 $MWh.kg.U^{-1}$ could be totally suppressed.

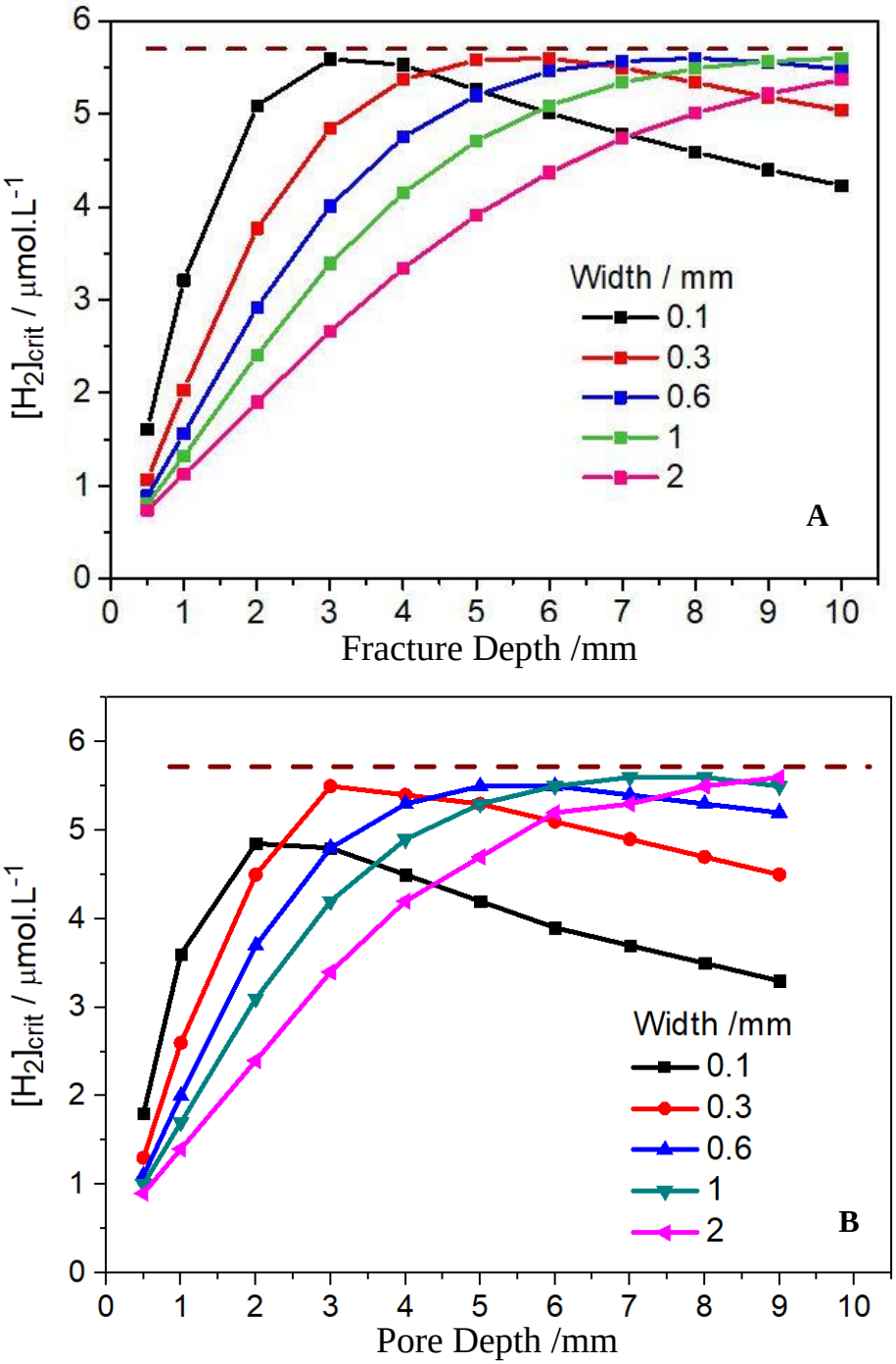

Figure 6.5: Critical $[H_2]$ ($[H_2]_{crit}$) for two different types of defect (A: fracture, B: pore) with different widths and depths. The dashed line indicates an upper limit for $[H_2]_{crit}$.

The fracturing of the fuel pellets, due to thermal stress during the in-reactor irradiation and the cooling process after discharge from the reactor, leads to complex fracture geometries in the spent fuel. Previously, we investigated the influence on corrosion of fractures with a uniform width from the bottom to the top (Figure 6.6 left), although more complex defect geometries are possible (Figure 6.6, middle and right).

Figure 6.7 compares the corrosion rates in fractures with the different geometries shown schematically in Figure 6.6. The resulting corrosion rates (UO_2^{2+} flux in the direction normal to the wall of fractures) are not particularly sensitive to the different geometries. The calculated corrosion rate for an "open" fracture (top width (0.6 mm) and bottom width (0.1 mm)) is similar to the rate calculated for a uniform fracture (width (0.1 mm). For a "closed" fracture (top width = 0.1 mm and bottom width = 0.6 mm), the corrosion rate is increased in deeper fractures; i.e., by ~20% at the depth of 5 mm, compared with the rate calculated for a uniform fracture. This can be attributed to the accumulation of H_2O_2 within the fracture, its loss by diffusion out of the fracture being limited.

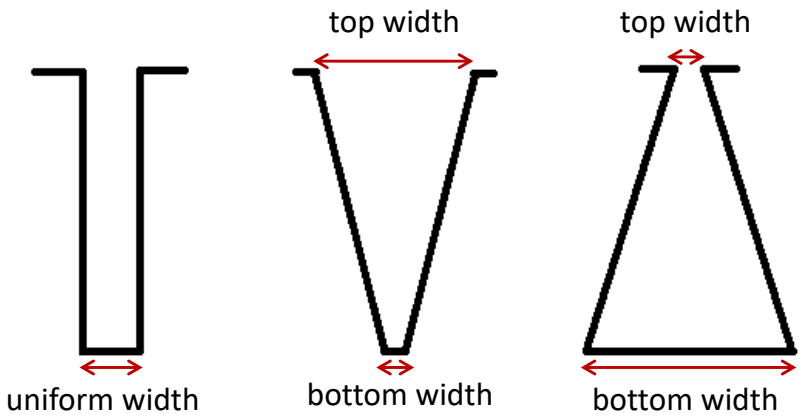

Figure 6.6: Illustration of fracture geometries.

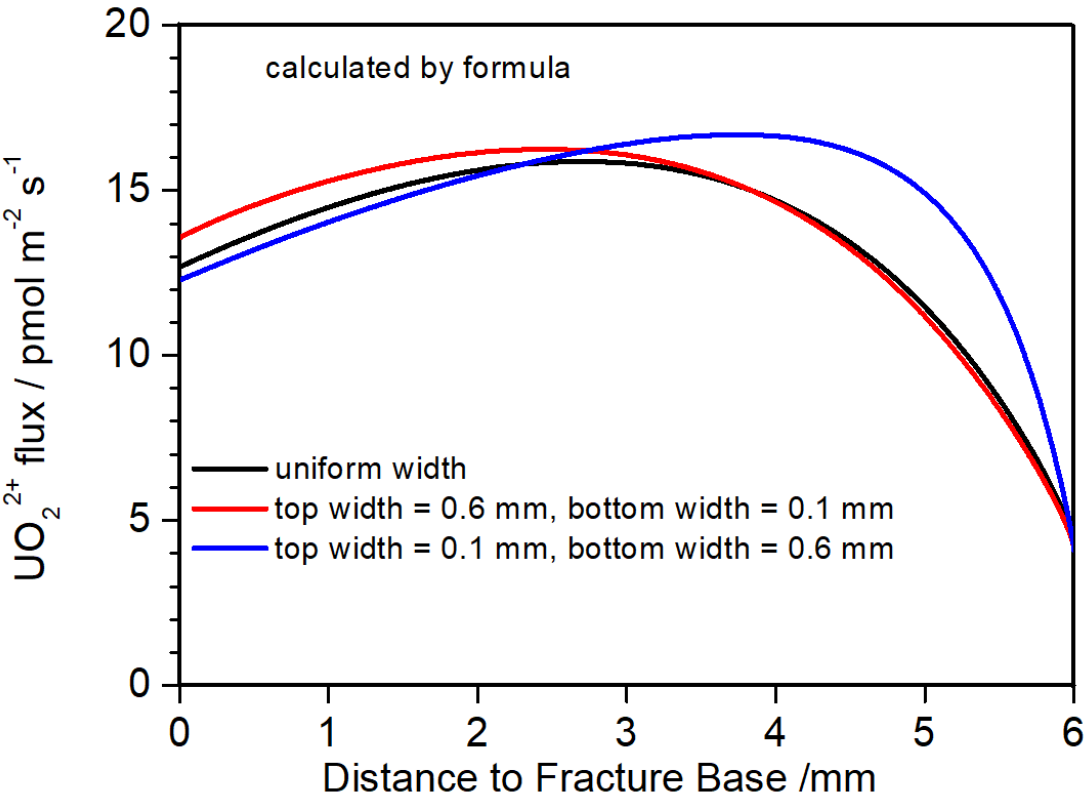

Figure 6.7: The calculated flux of UO_2^{2+} (equivalent to the fuel corrosion rate in the direction normal to the wall of a fracture) as a function of the distance to the base of the fracture: Black line, uniform fracture, width = 0.1 mm, depth = 6 mm; red line, top width = 0.6 mm, bottom width = 0.1 mm, depth = 6 mm; blue line, top width = 0.1 mm, bottom width = 0.6 mm, depth = 6 mm. All other model parameters have the default values (Table 6-1).

6.3.2 The Effects of ε-particle Coverage and Distribution

To simulate the enhanced burn up in the outer regions of the fuel[33], a linear variation in ε-particle coverage along a fracture wall was adopted (equation 6.1). The ε-particle coverage was assumed to decrease from the outer surface of the pellet to deep locations inside the fracture.

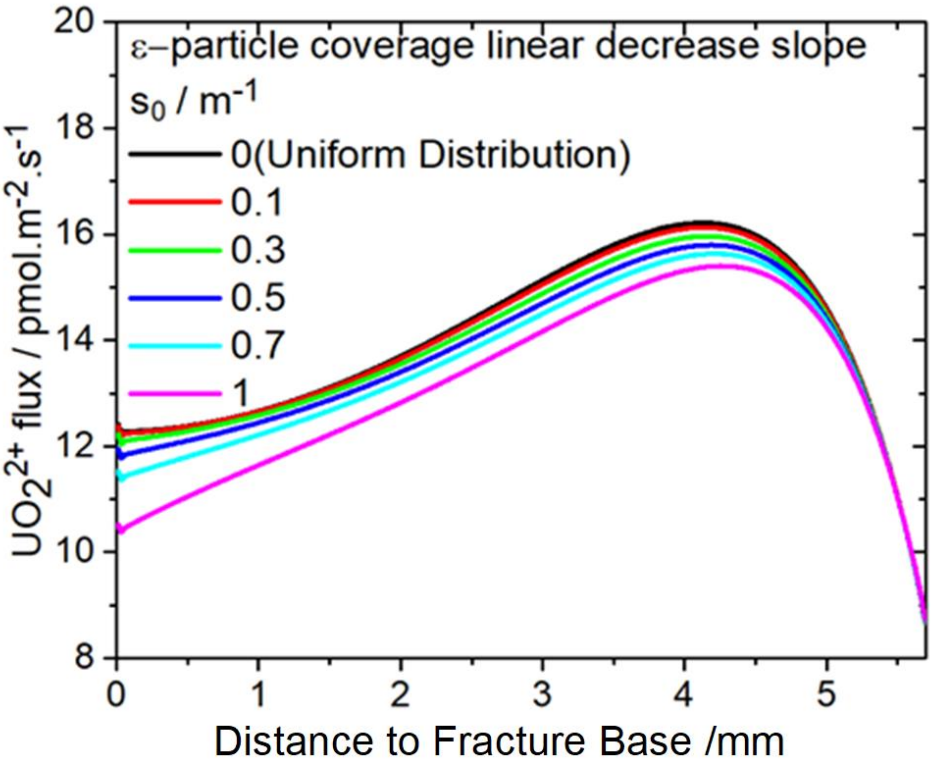

Figure 6.8: The UO_2 flux profile as a function of distance to the fracture base for a variety of ε-particle distributions. When the slope s_0 = 0, ε-particles uniformly cover 1% of the surface and fracture wall. All other model parameters have the default values (Table 6-1).

Figure 6.8 shows the fuel corrosion rate increases as a function of distance from the base of a fracture consistent with a lower rate at deep locations due to the accumulation of radiolytic H_2. As with other calculations, the steep decrease in rate as the mouth of the fracture is approached

can be attributed predominantly to the diffusive loss of H_2O_2 from the fracture. As the coverage with ε-particles deep in the fracture is decreased (i.e., s_0 (equation 6.1) is increased) the corrosion rate at deep locations is only slightly decreased. This reflects the dual and opposite influences of the particles, which catalyze both the reduction of H_2O_2 (reaction 2b, Figure 6.1), which would increase the corrosion rate, and the oxidation of H_2 (reactions 3a and 3c, Figure 6.1) which would decrease it. The lowest corrosion rate at the bottom of the fracture is observed for the lowest number of ε-particles. The slight decrease in rate as the number of ε-particles is decreased at deep locations indicates that the ε-particle effect on H_2O_2 reduction is slightly more important than its influence on H_2 oxidation.

Figure 6.9 shows the critical H_2 concentration ($[H_2]_{crit}$) required to completely suppress corrosion as a function of fracture depth in a narrow (A) and a wide (B) fracture for a uniform distribution of ε-particles ($s_o = 0$) and for a linear decrease in ε-particle coverage ($s_o = 1$). For the uniform distribution, the H_2 requirement decreases slightly. For a decreased number of ε-particles at deep locations (Figure 6.9 A), the H_2 requirement increases to 10 $\mu mol.L^{-1}$ which is twice the maximum amount required for a linear distribution, calculated to be 5.7 $\mu mol.L^{-1}$ (Figure 6.5 A). This reflects the lower rates of reactions 3a and 3c (Figure 6.1) at deep locations, resulting in a higher demand for H_2 from steel corrosion.

For a wide fracture, the $[H_2]_{crit}$ values are higher. As the number of ε-particles decreases the demand for external H_2 increases insignificantly for shallow fractures. The absence of ε-particles at the base of a deep wide fracture leads to a very significant increased demand for external H_2. The difference in demand between narrow and wide fractures can be attributed to the need to suppress corrosion over a wider surface area of corroding fuel in the wide fracture.

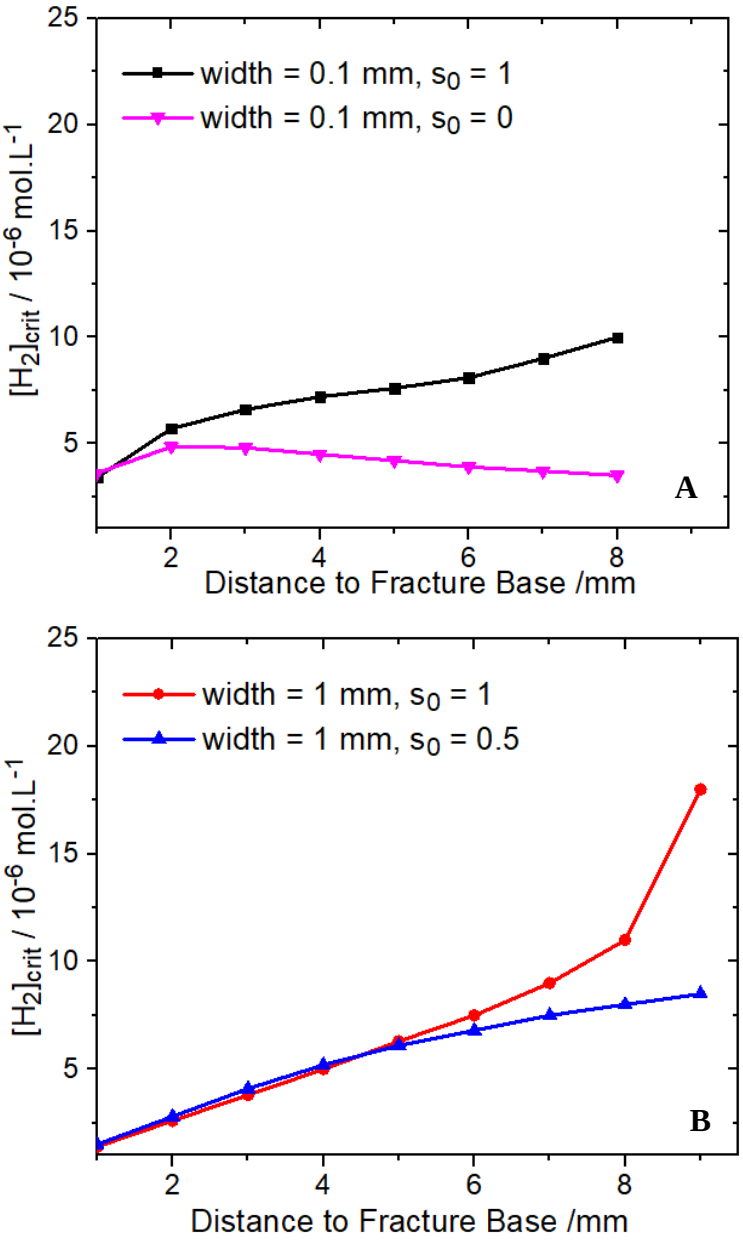

Figure 6.9: Critical H_2 concentration ($[H_2]_{crit}$) as a function of fracture depth for narrow (A) and wide (B) fractures as the number of ε-particles changes along the fracture wall. Black line and dots – number of ε-particles decreases to 0% at the base of a fracture: Pink line and dots - uniform distribution of ε-particles: Red line and dots – number of ε-particles decreases to 0% on the fracture bottom: Blue line and dots – number of ε-particles decreases to 0.5% at the base of a fracture.

6.3.3 UO_2 Corrosion by O_2

In this study, a wide range of H_2O_2 decomposition ratios (to the alternative oxidant O_2 and H_2O) were adopted to determine the consequences of fuel corrosion by reaction with O_2. The decomposition ratio is defined as the fraction of the radiolytically-produced H_2O_2 leading to UO_2 corrosion, with the remaining fraction decomposing to produce O_2. The values used in calculations ranged from 0.14, the value measured by Pehrman and Jonsson[21] on UO_2 containing no ε-particles to 0.006, a value close to that measured on SIMFUEL in our experiments, Chapter 4.

Figure 6.10 A and B show the decrease in $[H_2O_2]$ and the corresponding increase in $[O_2]$ for this range of decomposition ratios calculated as a function of fracture depth. The higher concentrations at the base of the fractures reflect the lesser amounts of oxidant lost by transport from the fracture at deeper locations. At the base of the fracture, the $[O_2]$ increases by a factor of 3 as the fraction of H_2O_2 decomposed increases from 86% (R = 0.14) to 99.5% (R = 0.005); i.e., R = 0.14 and 0.005, respectively, where R is the dissolution fraction. The corresponding decrease in $[H_2O_2]$ is by a factor of 75. This difference in the changes in concentration reflects the greater reactivity of H_2O_2 compared to that of O_2. As a consequence, the fuel corrosion rate decreases significantly as the more reactive H_2O_2 is converted into the 200x less reactive O_2.

This calculation neglects the catalytic effect of ε-particles on O_2 reduction. When this effect is taken into account, the UO_2 corrosion rate is insignificantly affected at a dissolution fraction 0.14, since H_2O_2 remains the dominant oxidant. However, when the very large majority of the H_2O_2 is decomposed (99.5%) the fuel corrosion rate is increased (by a factor of 2) when this catalytic effect is included but remains extremely low, this is consistent with previous studies. At locations closer to the mouth of the fracture any influence of ε-particles on the

kinetics of O_2 reduction becomes negligible, since the majority of the O_2 is transported out of the fracture and the suppression of corrosion by H_2 from steel corrosion dominates the fuel corrosion rate.

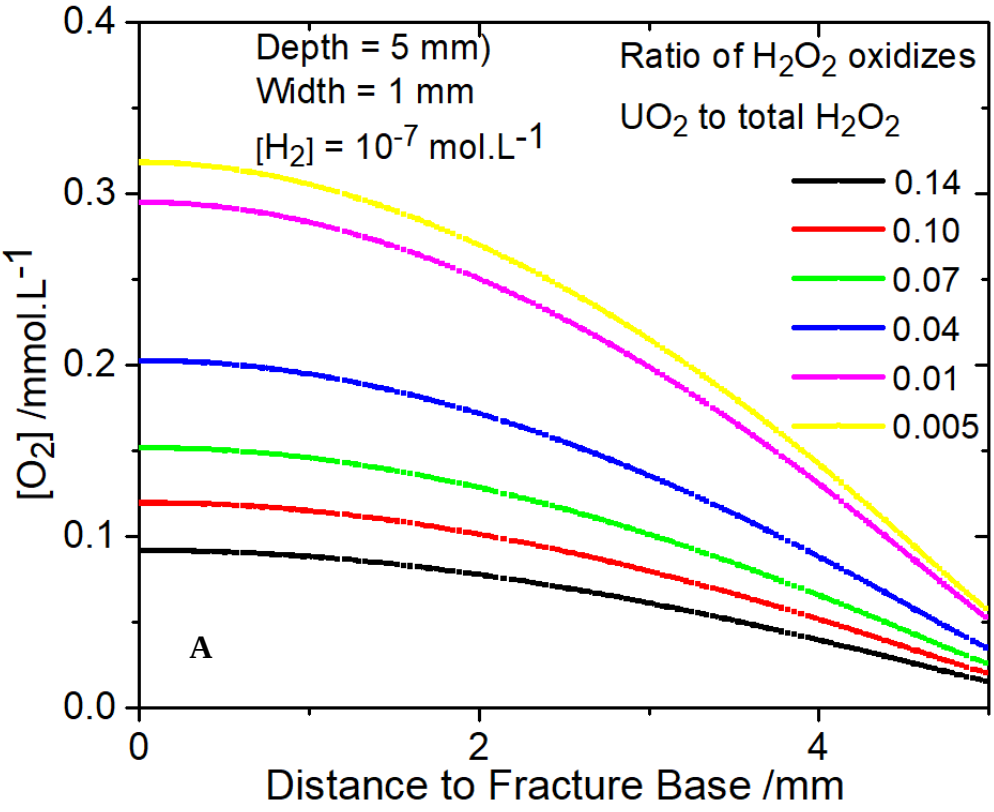

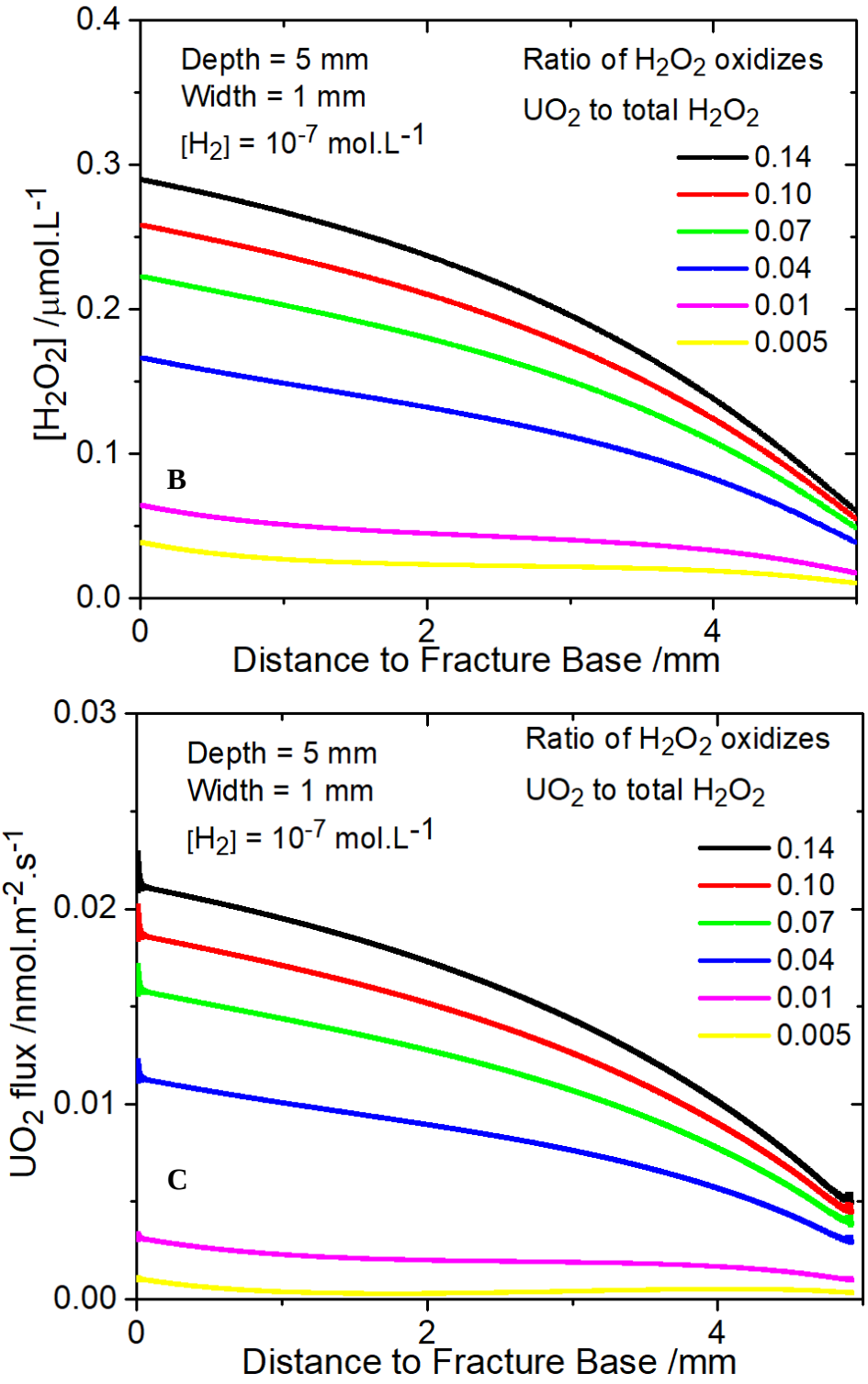

Figure 6.10: The [O_2] (A), [H_2O_2] (B) profiles along the central line of a fracture for different dissolution fractions (R). (C) UO_2 corrosion rate. All other model parameters have the default values (Table 6-1).

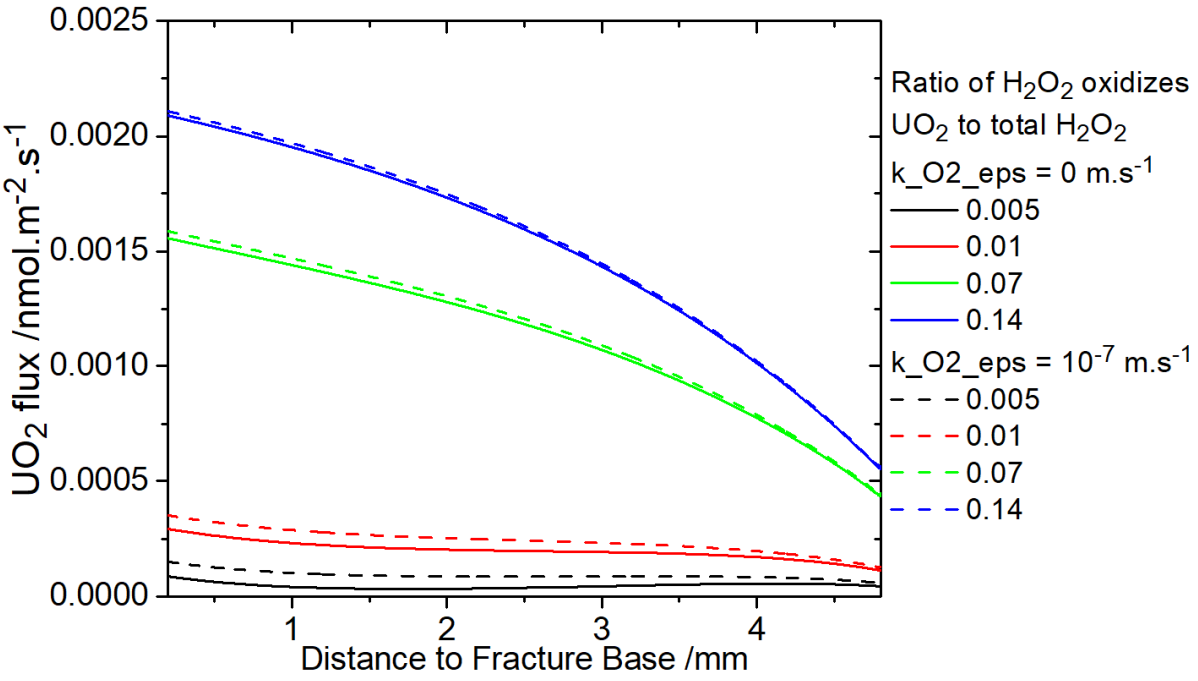

Figure 6.11: The UO_2 corrosion rate as a function of decomposition taking into account catalysis of O_2 reduction on ε-particles. Fracture width = 1 mm; fracture depth = 5 mm, and the bulk $[H_2] = 10^{-7}$ mol.L^{-1}. All other model parameters have the default values.

6.4 Summary and Conclusions

Various defect geometries including pores and fractures with various geometries exert only a minor influence on the rate of fuel corrosion. These minor effects reflect slight variations in the amount of radiolytic H_2O_2 trapped within defects (pores, fractures).

Since the in-reactor fission process occurs predominantly in the outer rim of fuel pellets calculations were performed in which the distribution of ε-particles was varied from the outer to the inner regions of a fracture. Since these particles catalyze both H_2O_2 reduction, which increases the fuel corrosion rate, and H_2 oxidation, which decreases the rate, only a minor net effect on the overall corrosion rate is observed. This indicates that the change in number of ε-particles has a slightly larger effect on H_2O_2 reduction than on H_2 oxidation. When the number of ε-particles at deep locations is decreased the amount of H_2 required to completely suppress corrosion at deep locations increases by a factor of 2 to 3.

The extent of H_2O_2 decomposition to the considerably less reactive O_2 (and H_2O) causes a significant decrease in fuel corrosion rate since the slowly reacting O_2 is dominantly lost by transport out of the defect. Whether or the catalytic effect of the ε-particles on O_2 reduction has only a minimal effect on the corrosion rate.

6.5 References

[1] E. Ekeroth, O. Roth, M. Jonsson, The relative impact of radiolysis products in radiation induced oxidative dissolution of UO_2, Journal of Nuclear Materials, 355 (2006) 38-46.

[2] D.W. Shoesmith, Fuel corrosion processes under waste disposal conditions, Journal of Nuclear Materials, 282 (2000) 1-31.

[3] D. Shoesmith, The role of dissolved hydrogen on the corrosion/dissolution of spent nuclear fuel, Nuclear Waste Management Organization Technical Report NWMO-TR-2008-19. Toronto, Canada, (2008).

[4] D. Cui, J. Low, K. Spahiu, Environmental behaviors of spent nuclear fuel and canister materials, Energy & Environmental Science, 4 (2011) 2537-2545.

[5] P. Carbol, K. Spahiu, The effect of dissolved hydrogen on the dissolution of 233 U doped UO 2 (s) high burn-up spent fuel and MOX fuel, Swedish Nuclear Fuel and Waste Management Co., 2005.

[6] S. Röllin, K. Spahiu, U.B. Eklund, Determination of dissolution rates of spent fuel in carbonate solutions under different redox conditions with a flow-through experiment, Journal of Nuclear Materials, 297 (2001) 231-243.

[7] M.E. Broczkowski, J.J. Noël, D.W. Shoesmith, The influence of dissolved hydrogen on the surface composition of doped uranium dioxide under aqueous corrosion conditions, Journal of Electroanalytical Chemistry, 602 (2007) 8-16.

[8] M. Broczkowski, J. Noël, D. Shoesmith, The inhibiting effects of hydrogen on the corrosion of uranium dioxide under nuclear waste disposal conditions, Journal of Nuclear Materials, 346 (2005) 16-23.

[9] M. Trummer, O. Roth, M. Jonsson, H_2 inhibition of radiation induced dissolution of spent nuclear fuel, Journal of Nuclear Materials, 383 (2009) 226-230.

[10] S. Nilsson, M. Jonsson, On the catalytic effect of Pd(s) on the reduction of UO_2^{2+} with H2 in aqueous solution, Journal of Nuclear Materials, 374 (2008) 290-292.

[11] M. Broczkowski, P. Keech, J. Noël, D. Shoesmith, Corrosion of uranium dioxide containing simulated fission products in dilute hydrogen peroxide and dissolved hydrogen, Journal of the Electrochemical Society, 157 (2010) C275-C281.

[12] J.S. Goldik, H.W. Nesbitt, J.J. Noël, D.W. Shoesmith, Surface electrochemistry of UO_2 in dilute alkaline hydrogen peroxide solutions, Electrochimica Acta, 49 (2004) 1699-1709.

[13] E. Ekeroth, M. Jonsson, Oxidation of UO_2 by radiolytic oxidants, Journal of Nuclear Materials, 322 (2003) 242-248.

[14] S. Sunder, N.H. Miller, D.W. Shoesmith, Corrosion of uranium dioxide in hydrogen peroxide solutions, Corrosion Science, 46 (2004) 1095-1111.

[15] S. Nilsson, M. Jonsson, H_2O_2 and radiation induced dissolution of UO_2 and SIMFUEL pellets, Journal of Nuclear Materials, 410 (2011) 89-93.

[16] J.S. Goldik, Noel J.J., Shoesmith D.W., The effects of simulated fission products in the reduction of hydrogen peroxide on simulated nuclear fuel electrodes, Journal of The Electrochemical Society, 153 (2006) E151-E159.

[17] L. Wu, Z. Qin, D.W. Shoesmith, An improved model for the corrosion of used nuclear fuel inside a failed waste container under permanent disposal conditions, Corrosion Science, 84 (2014) 85-95.

[18] L. Wu, N. Liu, Z. Qin, D.W. Shoesmith, Modeling the radiolytic corrosion of fractured nuclear fuel under permanent disposal conditions, Journal of The Electrochemical Society, 161 (2014) E3259-E3266.

[19] N. Liu, L. Wu, Z. Qin, D.W. Shoesmith, Roles of radiolytic and externally generated H_2 in the corrosion of fractured spent nuclear fuel, Environmental science & technology, 50 (2016) 12348-12355.

[20] I. Hastings, Structures in irradiated UO_2 fuel from Canadian reactors, Atomic Energy of Canada Limited(AECL), Report AECL-MISC-249, (1982).

[21] R. Pehrman, M. Trummer, C.M. Lousada, M. Jonsson, On the redox reactivity of doped UO_2 pellets – influence of dopants on the H_2O_2 decomposition mechanism, Journal of Nuclear Materials, 430 (2012) 6-11.

[22] M. Trummer, S. Nilsson, M. Jonsson, On the effects of fission product noble metal inclusions on the kinetics of radiation induced dissolution of spent nuclear fuel, Journal of Nuclear Materials, 378 (2008) 55-59.

[23] E. Ekeroth, M. Jonsson, T.E. Eriksen, K. Ljungqvist, S. Kovács, I. Puigdomenech, Reduction of UO_2^{2+} by H_2, Journal of Nuclear Materials, 334 (2004) 35-39.

[24] F.J. Millero, S. Sotolongo, The oxidation of Fe(II) with H_2O_2 in seawater, Geochimica et Cosmochimica Acta, 53 (1989) 1867-1873.

[25] S. Nilsson, M. Jonsson, On the catalytic effects of UO_2(s) and Pd(s) on the reaction between H_2O_2 and H_2 in aqueous solution, Journal of Nuclear Materials, 372 (2008) 160-163.

[26] L. Wu, Y. Beauregard, Z. Qin, S. Rohani, D.W. Shoesmith, A model for the influence of steel corrosion products on nuclear fuel corrosion under permanent disposal conditions, Corrosion Science, 61 (2012) 83-91.

[27] F. Garisto, D. Barber, E. Chen, A. Inglot, C. Morrison, Alpha, beta and gamma dose rates in water in contact with used CANDU fuel, Report NWMO TR-2009-27, Nuclear Waste Management Organization, Toronto, ON, (2009).

[28] A. Elliot, Rate constants and g-values for the simulation of the radiolysis of light water over the range 0-300 deg C, Atomic Energy of Canada Ltd., 1994.

[29] C.M. Lousada, M. Trummer, M. Jonsson, Reactivity of H_2O_2 towards different UO_2-based materials: The relative impact of radiolysis products revisited, Journal of Nuclear Materials, 434 (2013) 434-439.

[30] J.S. Betteridge, N.A.M. Scott, D.W. Shoesmith, L.E. Bahen, W.H. Hocking, P.G. Lucuta, Effects of hyperstoichiometry and fission products on the electrochemical reactivity of UO_2 nuclear fuel, Canada, 1997, pp. 30.

[31] P.S.D. Brito, C.A.C. Sequeira, Cathodic oxygen reduction on noble metal and carbon electrodes, Journal of Power Sources, 52 (1994) 1-16.

[32] A. Traboulsi, J. Vandenborre, G. Blain, B. Humbert, J. Barbet, M. Fattahi, Radiolytic Corrosion of Uranium Dioxide: Role of Molecular Species, The Journal of Physical Chemistry C, 118 (2014) 1071-1080.

[33] J. Bruno, Spent Nuclear Fuel, Elements (Quebec), 2 (2006) 343-349.

Chapter 7

7 Summary and Future Work

7.1 Summary

The primary goal of this thesis was to provide a detailed understanding of the mechanism of spent nuclear fuel corrosion inside a failed groundwater-containing container using both experimental and computational approaches.

In chapter 3, the effects of noble metal (ε) particles on the two possible anodic reactions, UO_2 corrosion and H_2O_2 oxidation, were studied in HCO_3^-/CO_3^{2-} solutions. It was found that the balance between these anodic reactions was controlled by ε-particles dispersed throughout the fission product-doped UO_2 matrix, the potential applied, and the $[CO_3]_{tot}$. Both reactions were suppressed by the formation of U^{VI} surface films. When the formation of these films was prevented at higher HCO_3^-/CO_3^{2-} concentrations both reactions occurred readily on the sublayer of $U^{IV}_{1-2x}U^{V}_{2x}O_{2+x}$. When present, noble metal (ε) particles supported H_2O_2 oxidation over the full potential range. At low potentials, the peroxycarbonate (HCO_4^-) species formed was rapidly oxidized on the particles. At high potentials H_2O_2 could be directly oxidized on the noble metal particles rendered catalytic by preoxidation (e.g., Pd to Pd^{II}).

In chapter 4, an attempt was made to separate H_2O_2 decomposition and H_2O_2 consumption due to UO_2 corrosion. It was found that in aqueous HCO_3^-/CO_3^{2-}, H_2O_2 consumption proceeded by both homogenous decomposition in solution and by heterogeneous reaction with the SIMFUEL surface. Homogenous decomposition to O_2 and H_2O proceeded through a peroxycarbonate (CO_4^{2-}) intermediate in HCO_3^-/CO_3^{2-} solutions which was consistent with the results in chapter 3. On the SIMFUEL surface, H_2O_2 decomposition was the dominant reaction,

and only minor to negligible amounts of UO_2 corrosion occurred. This was due to the stability of SIMFUEL surface. The primary function of HCO_3^-/CO_3^{2-} was to complex and dissolve U^{VI} surface species which prevented their accumulation to form an insulating layer which blocked decomposition on the catalytic $U^{IV}_{1-2x}U^{V}_{2x}O_{2+x}$ surface layer. When the surface was maintained free of U^{VI} species, H_2O_2 decomposition proceeded under redox buffered conditions on the catalytic surface. The role of noble metal (ε) particles in the SIMFUEL matrix on H_2O_2 decomposition appeared to be minor although this remains to be conclusively demonstrated.

In chapter 5, the electrochemical reduction of H_2O_2 was studied on a range of UO_2 electrodes including RE(III)-doped and non-stoichiometric electrodes, and on a SIMFUEL. On all electrodes reduction proceeded via a sequence of two reactions: the chemical oxidation of the surface created U^V sites followed by the electrochemical reduction of the surface back to its original U^{IV} state. After correcting for transport effects, the rate of reduction decreased in the order $UO_{2.002}$ ~ $UO_{2.5}$ ~ SIMFUEL > Gd-UO_2 ~ Dy-UO_2 > $UO_{2.1}$. The reduction rate was suppressed on the RE(III)-doped electrodes by the formation of RE(III)-O_V clusters within the UO_2 matrix which decreased the availability of the O_V required for UO_2 oxidation. On the SIMFUEL electrode, reduction may be catalyzed on the surfaces of the noble metal (ε) particles present in this electrode. HCO_3^-/CO_3^{2-}, in the concentration range 0.01 to 0.05 $mol.L^{-1}$, suppressed the reduction rate by stabilizing the U^V surface state required to catalyze the reduction reaction thereby inhibiting its reduction back to the original U^{IV} state.

In chapter 6, the results of a series of computational analyses were presented on the effects of defect geometries, ε-particle distribution and H_2O_2 decomposition on the UO_2 corrosion rate. The defect geometries in the form of pores and fractures exerted only a minor influence on the rate of fuel corrosion. These minor effects reflected slight variations in the amount of radiolytic

H_2O_2 trapped within defects (pores, fractures). Since the in-reactor fission process occurs predominantly in the outer rim of fuel pellets, calculations were performed in which the distribution of ε-particles was varied from the outer to inner region of a fracture. Since these particles catalyzed both H_2O_2 reduction, which increased the fuel corrosion rate, and H_2 oxidation, which decreased the rate, only a minor net effect on the overall corrosion rate was observed which indicated that the change in number of ε-particles had only a slight effect. When the number of ε-particles at deep locations was decreased the amount of H_2 required to completely suppress corrosion at deep locations increased by a factor of 2 to 3. The extent of H_2O_2 decomposition to the considerably less reactive O_2 (and H_2O) caused a significant decrease in fuel corrosion rate since the slowly reacting O_2 was dominantly lost by transport out of the defect. The catalytic effect of the ε-particles on O_2 reduction had only a minimal effect on the corrosion rate.

7.2 Future Work

- While it has been demonstrated that H_2O_2 decomposition is the dominant reaction as opposed to UO_2 corrosion, the effects of ε-particles and RE(III)-dopants on H_2O_2 decomposition remain unclear. A series of experimental studies on SIMFUELs with different degrees of simulated burnup is required to elucidate this effect.
- The relative kinetics of H_2O_2 reactions on ε-particles and RE(III)-doped UO_2 electrodes could be investigated using a combination of Raman Spectroscopy and Scanning Electrochemical Microscopy.
- The results in chapter 5 showed that the kinetics of H_2O_2 reduction on non-stochiometric UO_{2+x} varied with x. However, the composition of these electrodes is non-uniform across

the surface. As a consequence, the results to date show only an average influence of non-stoichiometry. A similar study on electrodes with a more uniform distribution of composition is required to elucidate the real influence of non-stoichiometry.

- In HCO_3^-/CO_3^{2-} solutions a role of the peroxycarbonate (CO_4^-) ion has been demonstrated. However, the importance of this ion under conditions representing the anticipated conditions inside a failed container has not been demonstrated. A series of studies as a function of $[H_2O_2]$, $[CO_3]_{tot}$ and pH is required to establish a database which can be used to determine, by extrapolation, the importance of this ion under failed container conditions.
- Many possible influences of conditions inside a failed container remain to be investigated. The importance of variations in groundwater composition, the deposition of corrosion products and the corrosion of the steel vessel can be assessed using model calculations.

Curriculum Vitae

Ziyan Zhu

EDUCATION

Ph.D., Western University 2014-2018

B.Sc., Honors Specialization in Chemistry, Western University 2009-2014

PUBLICATIONS

- Nazhen Liu, **Ziyan Zhu**, Linda Wu, Zack Qin, James J. Noel, David W. Shoesmith, Predicting Radionuclide Release Rates from Spent Nuclear Fuel inside a Failed Waste Disposal Container Using a Finite Element Model, Corrosion, 2018.
- Nazhen Liu, **Ziyan Zhu**, James J. Noel, David W. Shoesmith, Encyclopedia of Interfacial Chemistry: Surface Science and Electrochemistry, 2017.
- Nastaran Kazemi-Zanjani, Pierangelo Gobbo, **Ziyan Zhu**, Mark S. Workentin, François Lagugné-Labarthet, High-resolution Raman Imaging of Bundles of Single-walled Carbon Nanotubes by Tip-enhanced Raman Spectroscopy., Can. J. Chem., 2015, Vol. 93, No. 1, p51-59.

PRESENTATIONS AND CONFERENCES

Spent Fuel Workshop, Sheffield, UK 2018

- **Ziyan Zhu**, James J. Noël, David W. Shoesmith, Electrochemical Study of Simulated Spent Nuclear Fuel (SIMFUEL) Corrosion in Groundwater Conditions (oral presentation)

NACE Southern Ontario Student Section Symposium, Hamilton, Canada 2017

- **Ziyan Zhu**, Malin Ly, James J. Noël, David W. Shoesmith, Kinetics of Hydrogen Peroxide Reduction on UO_2 Electrodes (Poster)

Canadian Chemistry Conference and Exhibition, Toronto, Canada 2017

- **Ziyan Zhu**, James J. Noël, David W. Shoesmith, Hydrogen Peroxide Decomposition on UO_2 SIMFUEL in Carbonate Solutions (Oral presentation)

NACE Northern Area Eastern Conference, Toronto, Canada 2016

- **Ziyan Zhu**, James J. Noël, David W. Shoesmith, Hydrogen Peroxide Decomposition on UO_2 SIMFUEL in Carbonate Solutions (oral presentation)

Fallona Interdisciplinary Showcase, London, Canada 2016

- **Ziyan Zhu**, James J. Noël, David W. Shoesmith, Hydrogen Peroxide Decomposition on UO_2 SIMFUEL in Carbonate Solutions

University Network of Excellence in Nuclear Engineering, Waterloo, Canada 2016

- **Ziyan Zhu**, James J. Noël, David W. Shoesmith, Hydrogen Peroxide Decomposition on UO_2 SIMFUEL in Carbonate Solutions (**Poster-third place winner**)

Gordon Corrosion Conference, New London, US

- **Ziyan Zhu**, James J. Noël, David W. Shoesmith, Hydrogen Peroxide Decomposition on UO_2 SIMFUEL in Carbonate Solutions (poster)

Spent Fuel Workshop, Stockholm, Sweden 2016

- **Ziyan Zhu**, James J. Noël, David W. Shoesmith, Hydrogen Peroxide Decomposition on UO_2 SIMFUEL in Carbonate Solutions (oral presentation)

National Association of Corrosion Engineers (NACE), Vancouver, Canada 2016

- **Ziyan Zhu**, James J. Noël, David W. Shoesmith, Hydrogen Peroxide Decomposition on UO_2 SIMFUEL in Carbonate Solutions (poster)

  UNENE Workshop, Waterloo, Canada 2015

- **Ziyan Zhu**, Linda Wu, James J. Noël, David W. Shoesmith, The Corrosion of Simulated Nuclear Fuel (SIMFUEL) in Hydrogen Peroxide Solutions- Effects of Fission Products (poster)

  NACE Northern Area Eastern Conference, Ottawa, Canada 2015

- **Ziyan Zhu**, Linda Wu, James J. Noël, David W. Shoesmith, The Corrosion of Simulated Nuclear Fuel (SIMFUEL) in Hydrogen Peroxide Solutions- Effects of Fission Products (poster)

Awards

- Western Graduate Research Scholarship
- NACE Travel Awards 2016
- Student Poster Competition Award – 3nd Place, University Network of Excellence in Nuclear Engineering, Waterloo, 2016